# Investigation of magnetic resonance imaging biomarkers of radiation effects on healthy mice brain tissue and Glioblastoma treatment

**Abdulrahman Hussain Qaisi**

This thesis is submitted in fulfilment of the requirements for the Degree of Doctor of Philosophy

**College of Medical, Veterinary and Life Science**

**Institute of Neuroscience and Psychology**

**Glasgow Experimental MRI Centre,**

**University of Glasgow,**


University of Glasgow

**November 2019**

# Abstract


## Introduction

In the field of clinical oncology, radiotherapy is one of the most extensively applied anticancer treatments. However, the ionizing radiation (IR) is absorbed not only by the targeted cells, but also by the surrounding normal cells as well. Consequently, patients may experience symptoms associated with a damage to normal tissues a few weeks, months or years after a course of radiotherapy. We applied a right brain hemisphere radiation technique for mice that mimics radiation exposure during radiotherapy. We investigated several possible brain imaging biomarkers for radiation-induced damage, such as demyelination, axonal injury and inflammation, at different time points post-irradiation (IR). Because Glioblastoma Multiform (GBM) can provoke a more infiltrative phenotype in GBM cells which survive treatment, scans of the brain were obtained using different Magnetic Resonance Imaging (MRI) modalities, including Diffusion Tensor Imaging (DTI), T2 weighted high resolution and T2 mapping) at several time points (pre-IR and 15, 50, 90 and 180 days post-IR). We also investigated the ability of MRI to assess the early stage effect of ionising radiation treatment on the invasiveness of an infiltrative rodent GBM model by using T2 weighted imaging.

## Aims of this thesis:

Our research focussed on investigating a range of established and novel MRI methods as an imaging biomarkers of radiation-induced brain injury. In the future, this may help with the early identification of patients likely to later suffer from reduced cognitive functioning. It will also facilitate the identification of treatment options to address infiltration during radiotherapy, that will have the potential to improve future treatment outcomes.

## The thesis is structured as follows:

The body of the thesis consists of eight chapters. The background to the thesis, presented in the first two chapters, consists of a broad literature review (Mechanisms of radiotherapy associated cognitive decline in patients with brain tumours) and MRI physics (Theoretical aspects of Magnetic Resonance Imaging). The six results chapters are presented in the format of a typical peer reviewed

scientific paper, namely, introduction, methods, results and discussion, and conclusions. A brief description of each chapter follows:

**Chapter 1: Mechanisms of radiotherapy associated cognitive decline in patients with brain tumours**

In this review we present an outline of the use of radiation therapy on the Central Nervous System and its adverse effects on the brain. The review also includes a focus on the neurocognitive effects of radiotherapy and their classification based on the time of clinical expression. The advanced MRI techniques which are used for brain imaging are also discussed.

**Chapter 2: Theoretical aspects of Magnetic Resonance Imaging**

This chapter contains a description of the basic theories of MRI physics and the MRI sequences that were applied in this research.

**Chapter 3: Infiltrative rodent GBM model**

In this preliminary study, we assessed the ability of MRI to probe the early stage effects of ionizing radiation treatment on the invasiveness of an infiltrative rodent GBM model. The aim of this study was to assess the ability of MRI (T2 weighted imaging) to probe early stage effects of ionizing radiation (IR) treatment on the invasiveness of an infiltrative rodent GBM model.

**Chapter 4: Exploratory study**

The aim of the exploratory study was to detect the acute effects of radiation-induced brain injury using quantitative MRI. We tested the ability of T2 mapping and diffusion weighted imaging with multiple *b*-values to detect the acute effects of radiation.

**Chapter 5: Preliminary findings using MRI to detect radiation-induced brain injury in mice**

Building on the findings from Chapter-4 and using a large group size, this study aimed to relate the changes identified in long observation time diffusion MRI experiments, to the micro-structural changes identified using histology.

**Chapter 6: Efficient gradient calibration based on diffusion MRI**

During the development of the long observation time, stimulated echo DTI sequence, we noticed some problems with the data, for example, FA measurements of water phantoms were not zero. To ensure these errors were not a result of poor gradient calibration, we calibrated the gradients using a diffusion MRI method.

**Chapter 7: Minimising observation time related errors on DTI**

In this chapter, we describe our investigation to determine which imaging parameters were important and how errors could be minimised. We investigated the effects using phantom measurements and derived a correction for *b*-matrices to apply to the in-vivo DTI data acquired (see Chapter-8).

**Chapter 8: Diffusion MRI monitoring of specific structures in the irradiated mouse brain**

The results obtained in Chapter-5 demonstrate the occurrence of radiation-induced changes in white matter (WM) regions (e.g.fimbria) using long observation time diffusion MRI measurements. Due to the directionality of WM, an in-vivo DTI study was performed. Errors in long observation time DTI measurements were reduced by implementing the results from Chapters 6 and 7.

# Table of Contents

# List of Tables

# List of Figures

# Acknowledgement

I would like to extend a huge thank you to my supervisors Dr. William Holmes, Prof. Anthony Chalmers and Dr. Antoine Vallatos for giving me the opportunity to do this PhD, for carefully reading my thesis, and for their encouragement. I am greatly indebted to the close supervision provided by Dr. William Holmes who always had an open door for constructive criticism. I'd like to extend a huge thank you to my supervisor, Prof. Anthony Chalmers, for taking me on as part of his lab team, and for his indispensable help and advice throughout my PhD project. Special thanks to Dr. Antoine Vallatos, for his invaluable advice, support and guidance, and for being such a good friend, without all of which I would not have been able to finish my thesis.

I would like to thank also Jim Mullin who always offered a helping hand before and during the setup of MRI experiments and also for his skills in solving problems. Special thanks are also extended to Lindsay Gallagher and Linda Carberry for all their hard work and help with animals, experiments and scanning. I really could not have done it without their help.

I would like to thank my friends Haitham, Mohammad and Samantha for many helpful discussions and help with my research.

In Prof. Anthony Chalmers' lab, warm thanks are due to Dr. Karin Williams, Dr. Joanna Birch, Dr. Rodrigo Gutierrez Quintana, Dr. Apostolos Zarros, Katrina Stevenson, Dr. David Walker, Dr. Mark Jackson and Maria Clara Liuzzi, who offered me much appreciated support and their extensive knowledge and advice regarding histology and statistics.

I also wish to express my love and gratitude to my beloved wife, kids and my parents for their understanding and encouragement throughout the duration of my studies.

In the southern part of the Earth (Australia), I would like to thank Mr. Roy Short for all his proofreading help and prompt responses throughout my Masters and PhD programs.

# Author's Declaration

I hereby certify that this research is entirely my own work and has not been taken from the work of others save and to the extent that such work has been cited and acknowledged within the text of my work.

# Definitions/Abbreviations

| | |
|---|---|
| **CNS** | Central Nervous System |
| **MRI** | Magnetic Resonance Imaging |
| **CRT** | Cranial Radiotherapy |
| **WM** | White Matter |
| **GM** | Grey Matter |
| **MRC** | Medical Research Council |
| **WBI** | Whole Brain Irradiation |
| **ICRU** | International Commission on Radiation Units and Measurement |
| **GTV** | Gross Tumour Volume |
| **CTV** | Clinical Target Volume |
| **ITV** | Internal Tumour Volume |
| **PTV** | Planning Target Volume |
| **OARs** | Organ at Risk |
| **ROS** | Reactive Oxygen Species |
| **PDX** | Patient-Derived Xenografts |
| **SGZ** | Subgraular Zone |
| **MWM** | Morris Water Maze |
| **O-2A** | Oligodendrocytes type-2 astrocytes |
| **GFAP** | Glial Fibrillary Acidic Protein |
| **CBF** | Cerebral Blood Flow |
| **CBV** | Cerebral Blood Volume |
| **DCE** | Dynamic Contrast- Enhanced |
| **DTI** | Diffusion Tensor Imaging |
| **NSC** | Neuronal Stem Cells |
| **SDG** | Subependymal of the Dentate Gyrus |
| **CT** | Computed Tomography |
| **PET** | Positron Emission Tomography |
| **BBB** | Blood Brain Barrier |
| **Gd-T1w** | Gadoliniumd-T1 weighted |
| **DWI** | Diffusion Weighted Imaging |
| **ASL** | Arterial Spin Labelling |
| **rCBV** | Relative Cerebral Blood Volume |
| **ROI** | Region of Interest |
| **NAA** | N-AcetylAspartate |
| **Cr** | Creatine |
| **Cho** | Choline |
| **MI** | Myo-insitol |
| **MRS** | Magnetic Resonance Spectroscopy |
| **FA** | Fractional Anisotropy |
| **ALL** | Acute Lymphoblastic Leukaemia |
| **SVZ** | Sub-Ventricular Zone |
| **GBM** | Glioblastoma Multiform |
| **SE** | Spin Echo |
| **STE** | Stimulated Echo |
| **NMR** | Nuclear Magnetic Resonance |
| **μ** | Magnetic moment |
| ***I*** | Nuclear Spin |
| **γ** | Gyromagnetic ratio |

| | |
|---|---|
| $B_0$ | External magnetic field |
| $\omega_0$ | Larmor frequency |
| **T** | Tesla |
| $M_0$ | Net magnetization |
| **K** | Boltzmann constant |
| **ΔE** | Energy separation between two energy levels |
| ***h*** | Plank's constant |
| **RF** | Radiofrequency |
| **θ** | The flip angle |
| **FID** | Free Induction Decay |
| **T1** | Longitudinal relaxation |
| **T2** | Transverse relaxation |
| **TE** | Echo Time |
| **TR** | Repetition Time |
| $\overline{X^2}$ | Mean squared displacement |
| **Δ** | Time of diffusion |
| **D** | Diffusion coefficient |
| **PGSE** | Pulse Gradient Spin Echo |
| **δ** | The gradient duration |
| **G** | The gradient strength |
| ***b*** | *b* value (factor) |
| **ADC** | Apparent Diffusion Coefficient |
| $\lambda_1$ | Axial diffusivity |
| $\lambda_2$ | Radial diffusivity |
| $\lambda_3$ | Radial diffusivity |
| **MD** | Mean diffusivity |
| **CSF** | Cerebrospinal fluid |
| **α** | Alpha rays |
| **β** | Beta rays |
| **γ** | Gamma rays |
| **SARRP** | Small Animal Radiation Platform |
| **Gy** | Gray |
| **CBCT** | Cone Beam CT |
| **DKI** | Diffusion Kurtosis Imaging |
| **DWI** | Diffusion Weighted Imaging |
| **SNR** | Signal to Noise Ratio |
| **H&E** | Haematoxylin and Eosin |
| **LFB** | Luxol fast blue |
| **GCC** | Gradient Calibration Constant |
| $CuSO_4.5H_2O$ | Copper sulphate |
| **EPI** | Echo Planner Imaging |
| **ΔN** | The population differences, between the parallel and anti-parallel states |
| **2D** | Two dimensional |
| $B_0$ | Static Magnetic Field |
| **CA3** | Cornu Ammonis |
| **D** | Diffusion |
| **DNA** | Deoxyribonucleic Acid |
| **DSC** | Dynamic Susceptibility Contrast |
| **Dw GSP** | Diffusion weighted spoiler gradient |
| **DW-MRI** | Diffusion Weighted MRI |
| **FOV** | Field of View |

| | |
|---|---|
| **fWBI** | Fractionated Whole Brain Irradiation |
| **Gss** | Slice selection gradient |
| ***J*** | Vector or the net flux |
| **MSME** | Multiple Spin Echo Multiple Echo |
| **$M_{xy}$** | Transverse magnetisation |
| **PFA** | Paraformaldehyde |
| **RARE** | Rapid Acquisition with Relaxation Enhancement |
| **$S_0$** | Signal when zero gradient is applied |
| **SAR** | Specific Absorption Rate |
| **SE-DTI** | Spin Echo-DTI |
| **SRS** | Stereotactic Radiosurgery |
| **STEAM** | Stimulated Echo Acquisition Mode |
| **STE-DTI** | Stimulated Echo-DTI |
| **T** | Temperature |
| **T2-FLAIR** | T2-weighted-Fluid Attenuated Inversion Recovery |
| **z** | Longitudinal Magnetisation |
| **ε** | Eigenvectors |
| **λ** | **Eigenvalues** |

# Chapter 1

# Chapter-1 Mechanisms of radiotherapy associated cognitive decline in patients with brain tumours

## 1.1 Introduction

Radiotherapy is recognised as one of the most important non-invasive modalities for the treatment of cancer. In the United States in 2004, nearly 1 million of the ~1.4 million people who developed cancer were treated with radiotherapy (Barnett *et al.*, 2009). Each year approximately 10.9 million people worldwide are diagnosed with cancer and approximately 50% require radiotherapy, with 60% of those patients being treated with curative intent (Barnett *et al.*, 2009). However, the total safe radiation dose that can be administered to the tumour is limited by the risk of injury to normal tissue that is within the radiation volumes (Robbins *et al.*, 2012). Advancements in radiation technologies, have resulted in increased quality of life as well as increased life expectancy for patients with brain tumours (Jacob *et al.*, 2018). With this improved survival rate, the negative impact of radiation-induced brain damage and associated neurocognitive dysfunction are being recognised. There is growing evidence that cognitive dysfunction is a major problem associated with cancer treatments, including chemotherapy and radiotherapy, and that this is not attributed to stress, fatigue and depression alone (Lenzi *et al.*, 2004)(Hurria *et al.*, 2006). Hence, strategies aimed at toxicity reduction are important (Barnett *et al.*, 2009).

## 1.2 Radiation therapy for Central Nervous System (CNS) Tumours

Surgery, chemotherapy and radiotherapy are the current options for treating brain tumours. These treatments are often used together and most patients, nowadays, receive all of them. The choice of treatment depends mainly on factors such as type and grade of brain tumour, location and size, age of the patient and general health. Radiotherapy treatment usually follows surgery, however, patients who cannot have surgery have only radiotherapy instead. Prior to the 1970s, it was generally thought that the human brain was radioresistant (Greene-Schloesser *et al.*, 2012). However, brain tumour cells are killed by radiotherapy with high energy x-rays (photons) or protons (Miszczyk *et al.*, 2018). Neurocognitive and

neurological alterations after treatment of brain tumours are associated with ionising radiation which suggests that radiotherapy can damage the brain (DeAngelis, 2001). The human brain is sensitive to radiation therapy, for example, endothelial cells that line the walls of blood vessels are the cells most sensitive to radiation (Johnson *et al.*, 1985). Arteriosclerotic injury can be a response to the damage of endothelial cells (Hopewell, 1998). Studies using Magnetic Resonance Imaging (MRI) in childhood acute lymphoblastic leukaemia (ALL) survivors, who were treated with cranial radiotherapy (CRT), shows a reduction in both WM and grey matter (GM) volume, damage to brain tissue microstructure and associated cognitive deficits (Reddick *et al.*, 2006),(Armstrong *et al.*, 2013).

Taking advantage of the fact that normal tissues can repair damage in about eight hours post-radiotherapy treatment, radiotherapy can be delivered in low to moderate daily doses. However, tumour cells do not behave like normal cells that reproduce effectively, hence, eventually tumour cells die. As a result, the tumour will get smaller and no further tumour growth is expected, due to the destruction of tumour cells (Hubenak *et al.*, 2014).

Fractionated radiotherapy, where the full dose of radiation is fractionated into a small number of doses called fractions, is normally given to most glioma patients. The main benefit of fractionating the dose, is that healthy cells are allowed to recover between treatments (Arnold *et al.*, 2018). In both humans and animals, the radiation dosing regime plays an important role in specific pathologies (Marsh *et al.*, 2010)(Armstrong *et al.*, 2004)(Padovani *et al.*, 2012). Fractionated radiotherapy is of particular benefit when treating the brain, which tolerates multiple small fractions much better than large fractions. CNS disorders can arise after a single dose of more than 30 Gray (Gy), while WM necrosis will not occur at fractionated doses until they exceed 60 Gy (Greene-schloesser and Robbins, 2012). The benefit of increasing the radiotherapy dose from 50 to 60 Gy was initially suggested by the findings of studies on sequential dosing (Walker, Strike and Sheline, 1979). The dose and response to treatment was established in a Medical Research Council (MRC) randomised trial of different radiotherapy doses in the treatment of grade three and four astrocytoma. In this study radiotherapy was given post-operatively. Patients were randomised to receive 45 Gy in 20 fractions over four weeks, while the second group was randomised to receive 60 Gy in 30 fractions over six weeks. The second group had a median survival benefit of three

months compared with the first treatment group in which the dosage was unsuccessful (Bleehen and Stenning S P, 1991). No further survival benefit from a 10 Gy boost following 60 Gy Whole Brain Irradiation (WBI) was confirmed by the Chang et al. 1983 study (Chang *et al.*, 1983). Currently, as treatment for high grade glioma, fractionated external beam radiotherapy, at a dose of 60 Gy, in 30 daily fractions, is given at a precisely localised volume including the enhanced tumour mass and a 2-5 cm margin (Brada, 2006).

Experiments in rats have shown that a single intracranial dose of 25 Gy led to an initial early drop in oligodendrocyte numbers, followed by a variable pattern of oligodendrocyte markers for several months and, finally, an apparently permanent decline between 12 and 15 months post-irradiation (Panagiotakos *et al.*, 2007). Furthermore, 15 months post-irradiation, WM demyelination was observed in the corpus callosum, fimbria, external capsule and deep WM (Panagiotakos *et al.*, 2007).

### 1.2.1 Tumour volumes in radiotherapy planning

Reports have been issued by The International Commission on Radiation Units and Measurement (ICRU) (Reports 50 and 62, 1993, 1999) to define the appropriate volumes that are useful for radiotherapy planning. The target volume definition is separated into four distinct volumes, as shown in Figure 1.1(c). The Gross Tumour Volume (GTV) is defined as the malignant growth of the visible tumour, while the Clinical Target Volume (CTV) is a sub-clinical region including the GTV and margin around the GTV where there may be microscopic involvement. Internal Tumour Volume (ITV) is the volume surrounding CTV that accounts for the movement and change in CTV/GTV. The Planning Target Volume (PTV) is defined by margins that must be added around the CTV or GTV to balance, for external treatment, inaccurate movements of the organ, tumour and patient and any other inaccuracies due to beam and patient setup. Hence, the bias with a sub-optimal GTV will be enlarged from the corresponding PTV leading to unnecessarily increase the volume of healthy tissue irradiated.

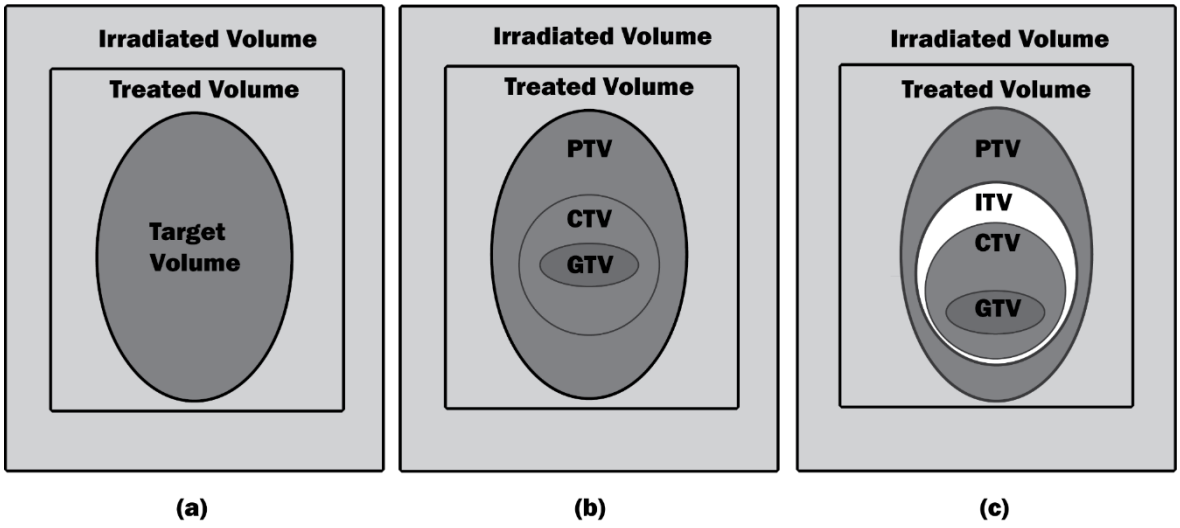


**Figure 1.1: Volume defined by ICRU Reports 50 and 62. Gross Tumour Volume (GTV), Internal Target Volume (ITV), Planning Target Volume (PTV), treated volume and irradiated volume. (adapted from (Purdy, 2008)).**

Normal tissues whose radiation sensitivity may influence treatment planning or prescribed dose are defined as Organs at Risk (OARs)(Purdy, 2008). During brain tumour irradiation, normal tissues are irradiated, in addition to the tumour. However, there is a wide variation in the radio-sensitivity of normal tissues and susceptibility to changes in fraction size. Consequently, the volume of the normal tissues must be defined clearly (Briere *et al.*, 2017). The chiasma, lens, optic nerve, retina, parotid and thyroid glands the in frontal lobe of the brain are examples of normal tissues at risk during brain radiotherapy (Nazemi-Gelyan *et al.*, 2015).

### 1.2.2 Radiation-induced brain injury

Following brain tumour radiotherapy treatments, the adverse effects of radiotherapy on the brain are very different in adults and children. Because children are at high risk of developing late sequelae after radiation therapy, children may develop intellectual deterioration which, in turn, may lead to cognitive decline later or dementia in long-term survivors (Taphoorn and Klein, 2004), diminished endocrine function and changed social behaviour (Danoff *et al.*, 1982). This review will focus on the neurocognitive effects of radiotherapy on adult patients with brain tumours and the pathophysiological mechanisms of radiotherapy induced CNS injury.

Radiation-induced brain injury is classified in terms of acute, early delayed and delayed injury based on the time of clinical presentation (Tofilon and Fike, 2000)(Figure 1.2).

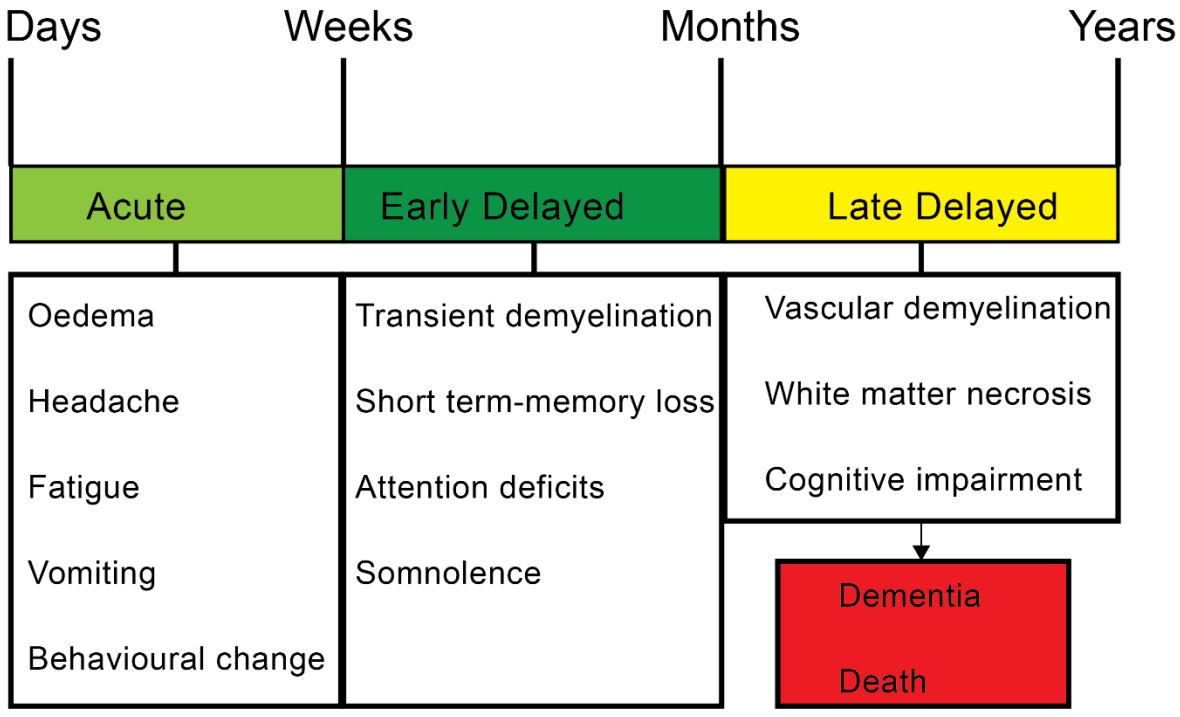


**Figure 1.2: Schematic clinical presentation of radiation induced brain injury (modified from** (Greene-Schloesser *et al.*, 2012)**).**

Acute radiation-induced brain injury is characterised by patients presenting with headache, fatigue and vomiting. If this occurs, it becomes apparent within a few days or weeks of treatment, usually due to accumulating fluid (oedema) in the

brain. Another common acute adverse effect of radiotherapy on brain is cerebral oedema (McTyre, Scott and Chinnaiyan, 2013). Recent advances in radiotherapy treatments in conjunction with the use of steroids have significantly improved patients well-being and reduced the occurrence of acute symptoms (Greene-Schloesser *et al.*, 2012) (Dietrich *et al.*, 2008).

Early delayed brain injury occurs from 1-6 months post-radiation and is thought to be a result of demyelination. Early delayed adverse effects are usually characterised by fatigue, somnolence and cognitive dysfunction. In addition, slower information processing speed, memory, word retrieval deficits and decreased fine motor dexterity are further characteristics of early delayed radiation effects (Crossen *et al.*, 2019)(Acres, 1941)(Hospital *et al.*, 1996). While these early injuries can result in severe reactions, they are normally reversible and can resolve spontaneously (Greene-Schloesser *et al.*, 2012).

Late delayed radiation-induced brain injury is usually observed 6 months or more post-irradiation and is histopathologically characterised by vascular abnormalities, demyelination and WM necrosis (Schultheiss and Stephens, 2009). These injuries are irreversible and may be progressive. Late radiation-induced brain injury is also characterised by reduction in the proliferation of glial cells (Van Der Maazen *et al.*, 1993) and/or vascular endothelial cells (Calvo *et al.*, 1988). The main cause of WM necrosis is the loss of these cells, particularly glial cells, which are thought to cause necrosis earlier than loss of endothelia cells. Risk factors in delayed radiation brain injury are the volume of radiated tissue, radiation dose, concomitant chemotherapy, patient age and the co-morbidity vascular risk factors (Correa, 2010).

To study the radiobiology and the advancement of clinical oncology, animal modelling is essential in the provision of preclinical data (Koontz, Verhaegen and Ruysscher, 2017). In fact, there is a limited data from clinical studies on the effects induced by radiation on the anatomical structures (Nagesh *et al.*, 2008). Deficits in sensory and neurocognitive functions can be a result of dysfunction in WM structures, including the corpus callosum (Douglas H. Smith, 2003)(Okamoto *et al.*, 2007). Consequently, early detection of neuroanatomical changes may enable replanning of therapy, helping to avoid further damage to at-risk regions

(Nagesh *et al.*, 2008). In the study of both tumour and normal tissue radiobiology, mouse models, in particular, are mostly utilised due to their cost effectiveness and versatility (Koontz, Verhaegen and Ruysscher, 2017). Preclinical studies have provided beneficial insight into the pathogenesis of radiation-induced brain injury (Ngen *et al.*, 2016)(Yang *et al.*, 2017), which provides a significant opportunity for diagnostic and therapeutic studies. Further, imaging studies of preclinical models can be directly correlated to histology. In fact, several preclinical studies in adult rodent brains have shown a persistent and marked reduction in neurogenesis (Fike, Rosi and Limoli, 2009), neuroinflammation with astrocytes and microglia activation (Schindler *et al.*, 2008) and progressive loss of cognitive function following single dose of radiation (Raber *et al.*, 2004).

In the development of new therapies for glioblastoma, preclinical mouse models are recognised as an essential model for analysing both the biology of glioblastoma as well as analysing and evaluating the potential of new therapeutic targets (And, 2017). Xenograft and genetically engineered mouse models are the two current preclinical glioblastoma models. Glioblastoma xenograft models are classified into two categories: glioblastoma cell-line xenograft and patient-derived xenografts (PDX). U87, U251, T98G and A178 are the most commonly used glioblastoma cell-lines and are commercially available. PDX has the advantage of retaining the features of the primary brain tumour both genetically and histologically. Therefore, in translation research it is used extensively and it is a recent focus of glioblastoma research (Vleeschouwer, 2017). Furthermore, the PDX model can be used to better predict the drug response of the patient's tumour (Choi *et al.*, 2014).

By contrast, there is a growing awareness that patients who have received fractionated WBI (fWBI) can have significant cognitive impairment at more than 6 months post-irradiation. This is despite the absence of detectable abnormalities, identified as a signal intensity abnormality in WM, when using conventional MR imaging in some patients (Constine *et al.*, 1988) (Sundgren *et al.*, 2009). Cognitive impairment contributes to a significant decrease in a patient's quality of life. In clinical trials, a patient's quality of life is recognised as second only to survival (Greene-Schloesser *et al.*, 2012). Reports from preclinical research suggest that decreased neurogenesis following mouse brain irradiation may contribute to impaired cognitive function (Greene-Schloesser, Moore and Robbins, 2013)(Peiffer

*et al.*, 2014). The neurogenesis zone is the most sensitive part in the brain and radiation effects occurs here without histological abnormalities. The subgraular zone (SGZ) of the hippocampus and sub-ventricle-zone (SVZ) are the main brain regions for neurogenesis (Schultheiss *et al.*, 1995)(Yang *et al.*, 2017). Animal models can develop impaired cognitive functions without obvious histological changes because cells within the SGZ are responsible for cognitive function (Raber *et al.*, 2004) (Yazlovitskaya *et al.*, 2006)(Chan *et al.*, 2012)(Abayomi, 1996). Mice are widely used to develop radiation-induced brain injury models, because of their biological similarities to humans and the lower costs incurred than for other rodents (Yang *et al.*, 2017). Another advantages of mouse models is the ability to study complex behaviours associated with neurodevelopmental disabilities (Crawley, 2008) including learning and memory(Li *et al.*, 2009)(Jiang *et al.*, 2010). In preclinical study, the Morris Water Maze (MWM) is used to test the hippocampal dependent learning that includes both spatial memory and long-term spatial memory (Morris, 1981). The MWM is a widely method used method for assessing these cognitive processes in mice (Crawley, 2008).

### 1.2.3 Parenchymal hypothesis of radiation-induced brain injury

The process of radiation-induced brain injury is highly complex and interactive and includes multiple tissue elements (Sundgren and Cao, 2009). Histological presentation of radiation effect on CNS is naturally dominated by demyelination that involves oligodendrocytes, a target cell population. In fact, the CNS is involved in different cellular phenotypes, networking to form a highly integrated system. Hence, after radiation, not only will oligodendrocytes be affected but also astrocytes, microglia, neurons and the endothelial cells that line the blood vessels (Tofilon and Fike, 2000).

#### 1.2.3.1 Oligodendrocytes

Oligodendrocytes play a vital role in the formation of the myelin sheath. Oligodendrocytes type-2 astrocytes (O-2A), exposed to WBI , lose their ability to expand and differentiate into mature oligodendrocytes (Martin C. Raff, Robert H. Miller and Mark Noble, 1983). It has been hypothesised that demyelination and WM necrosis is a result of radiation-induced loss of (O-2A) progenitor cells, resulting in failure to replace oligodendrocytes (Martin C. Raff, Robert H. Miller

and Mark Noble, 1983). Further, the impact of radiation on the number of, and proliferation potential of, mature oligodendrocytes shows a reduction in the number of mature oligodendrocytes 15 months post-irradiation, concomitantly with myelin loss (Panagiotakos *et al.*, 2007).

#### 1.2.3.2 Microglia

In the normal brain, microglia take the place of microphages in providing the immune surveillance of the CNS. Microglia actively monitor the microenvironment to ensure homeostasis of the CNS (Stollg and Jander, 1999). Neurotrophins expressed by microglia selectively regulate microglial function, proliferation and secretion of neurotrophic factors that promote neuronal survival (Elkabes, DiCicco-Bloom and Black, 1996). Microglia become activated after injury and are characterised by the rounding of the cell body, proliferation, increased production of reactive oxygen species (ROS), cytokines and chemokines that mediate neuroinflammation and retraction of cell processes (Pocock and Liddle, 2001)(Lee *et al.*, 2010). The potential contribution of specific types of cells to promote pro-inflammatory mediators in the brain after irradiation is still unclear. However, microglia are the first immune cells in the brain to release pro-inflammatory genes when they are activated by various stimulants (Block, Zecca and Hong, 2007). Radiation-induced brain injury has been linked to the activation of microglia post-irradiation, due to upregulation of pro-inflammatory genes (Acharya *et al.*, 2016).

#### 1.2.3.3 Neurons

Research using animal models has demonstrated that there is an increase in apoptosis, which is a result of therapeutic irradiation (Tada *et al.*, 2000)(Peißner *et al.*, 1999), and a decrease in both stem/precursor and proliferation cells into neurons within the neurogenesis of the hippocampus (Tada *et al.*, 2000)(Parent *et al.*, 1999)(Snyder, Kee and Wojtowicz, 2001). Preclinical studies of hippocampal function support the hypothesis that the reduction in neurogenesis contributes to the cognitive deficits which experienced by patients after cranial radiation therapy (Hodges *et al.*, 1998).

### 1.2.3.4 Astrocytes

Approximately 50% of the glial cell population in the brain is comprised of astrocytes (Hansson, 1988). Astrocytes play a vital role in the protection of endothelial cells and neurons from oxidative injury (Wilson, 1997) (Figure 1.3). In response to injury, astrocytes undergo proliferation, exhibit hypertrophic nuclei/cell bodies and also overexpress glial fibrillary acidic protein (GFAP)(Zhou *et al.*, 2011). Irradiation of both rat and mouse brains results in increased GFAP protein levels, both 24 hours post-irradiation (acute) and, chronically, up to 4-5 months post-irradiation (Chiang, McBride and Withers, 1993).

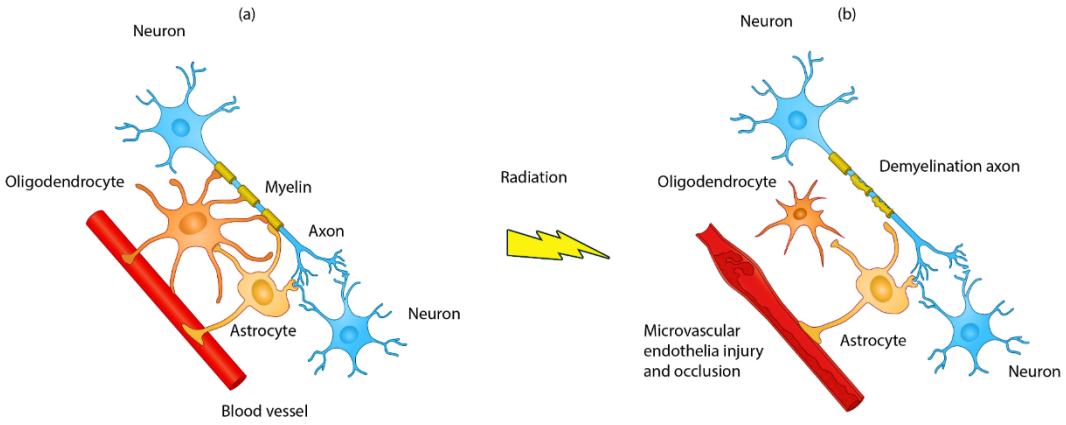


**Figure 1.3: Image shows vasculopathy and oligodendrocyte damage as a result of radiation-induced WM damage. (a) In a healthy brain, essential connectivity for cortical function is provided by WM, while oligodendrocytes play a vital role in establishing and maintaining myelin around WM axons. (b) Death of oligodendrocyte cells, due to radiation, leads to loss of myelin sheath integrity. Further, damage to the feeding microvessels not only affects WM, but also has negative effects on astrocytes that provide metabolic and functional support to neurons. (Modified from** (Makale *et al.*, 2016)**).**

### 1.2.3.5 Cerebral blood flow and cerebral blood volume

Limited reports are available about how change cerebral blood flow (CBF) and the cerebral blood volume (CBV) in the normal brain change after irradiation. Those reports that are available, indicate that there are changes in CBF and CBV which might be dose dependent (Hahn *et al.*, 2009)(Lee *et al.*, 2005)(Jain, Scarpace and Rock, 2007). In a prospective study of ten patients who underwent partial brain radiotherapy using Dynamic Contrast Enhanced (DCE) MRI to predict radiation-induced neurocognitive dysfunction, Cao et al.(2009), found that the permeability

of vascular volumes and the blood brain barrier (BBB) increased significantly in the regions irradiated with a high dose during radiotherapy. This decreased after radiotherapy (Cao *et al.*, 2009). This study suggests that delayed alterations in verbal learning might be predicted by early changes in cerebral vasculature (Cao *et al.*, 2009).

#### 1.2.3.6 White matter

Degenerative structural changes in WM are usually the result of cerebral vascular injury. The time lag between vascular injury and demyelination in WM and necrosis decreases with increased radiation dose (Reinhold *et al.*, 1990). One of the important determinants of cognitive impairment after traumatic brain injury is WM disruption. However, conventional neuroimaging underestimates its extent. By contrast, diffusion tensor imaging (DTI) can provide a validated and sensitive way of identifying the impact of, for example, axonal injury (Kinnunen *et al.*, 2011). Recently, it has become possible to the study WM disruption using DTI (Arfanakis *et al.*, 2002)(Assaf and Pasternak, 2008). DTI Data from tensor models are used to estimate the number of water diffusion in a different direction at each time points in the image. Hence, WM distribution can be quantified using DTI metrics such as fractional anisotropy (Basser and Pierpaoli, 1996)(Basser and Pierpaoli, 1998).

### 1.2.4 Radiation-induced cognitive impairment

Neurocognitive functions are linked to attention, memory, language perception, decision making and problem solving. Many of these functions are controlled by specific regions or neuronal pathways in the brain. A neurocognitive deficit is an impairment or reduction in cognitive function when a definable physical change has occurred in the brain, as in the case of a brain tumour. Cognitive impairment has been observed after brain radiotherapy and this can alter the quality of life and the neurocognitive function of a long-term survivor. Indeed, cognitive function has been recognised as an independent predictor of survival rate in brain tumour patients (Abayomi, 2002)(Butler, Rapp and Shaw, 2006). Deficits in hippocampal-dependent functions, such as memory loss, learning and spatial information processing, are observed mainly in long-term survivors (Brown *et al.*, 2004)(Meyers *et al.*, 2004) exposed to brain irradiation. The symptoms of

neurocognitive impairment include memory loss and loss of attention as well executive function deficits sever enough to meet the criteria of dementia (Chang *et al.*, 2007)(Armstrong *et al.*, 2000). The hippocampus is recognised as one of the OARs during radiotherapy treatment which should be included in experimental treatment plans (Marsh *et al.*, 2012). Recently, it has become technically possible and dosimetrically feasible to create hippocampal sparing treatment plans with appropriate target volumes (Kazda *et al.*, 2014). According to studies of animal models of human amnesia and histopathological findings in the irradiated brain, vascular injury that leads to hypoxia and ischemia in the hippocampal is likely to be the result of cranial irradiation(Abayomi, 2002). Furthermore, in the irradiated brain, the characteristic histological changes have been observed to be the most pronounced in the hippocampal regions (Crompton and Layton, 1958), where the changes in vascular conclusion result in ischemia and hypoxia (Hopewell *et al.*, 1986).

#### 1.2.4.1 Time course of cognitive decline

The development of cognitive decline 6 months after radiotherapy treatment is recognised as progressive and irreversible (Greene-schloesser *et al.*, 2012)(Connor *et al.*, 2016). Neurocognitive decline following radiotherapy occurs in a biphasic pattern, starting with a transient cognitive decline at approximately 4 months post-radiation treatment which is then followed by transient improvement. However, 12 months or more post-radiation therapy, progressive or irreversible deterioration in cognitive functioning starts to appear. It is very important to note that, during this time period, cognition might also be affected by tumour progression (Makale *et al.*, 2016). Based on studies of rodents subjected to global ischemia and irradiation, it has been hypothesised that cognitive dysfunction post irradiation is the result of ischaemia hippocampal damage. This hypothesis is supported by the evidence that the irradiated brain manifests histopathological changes, which closely mimic those found in the brain following global ischemia (Volpe and Hirst, 1983)(Squire, Amaral and Press, 1990).

#### 1.2.4.2 Anatomical structures and cognitive function

The CNS is comprised of GM and WM. GM contains the cell bodies, dendrites and axon terminals of neurons. WM matter is made of myelin rich axons connecting

regions of GM to each other. Axonal damage and demyelination are the hallmarks of WM injury, with WM being more susceptible to radiation damage than GM. Both axial damage and demyelination play different roles in neurological function. Clinical evidence suggests that limited radiation-therapy induces lower demyelination, which can cause fewer cognitive deficits, whereas extensive demyelination is associated with more severe cognitive dysfunction (Schultheiss *et al.*, 1995). The largest commissure structure consisting of WM tract is the corpus callosum. Impaired cognition and processing speed are associated with corpus callosum damage (Moretti *et al.*, 2005).

The hippocampus is involved in learning, retrieval of information, cooperation in learning and formation of new memories. Within the hippocampus, the critical neurological centre for learning and memory is the SGZ (Izquierdo and Medina, 1997)(Yazlovitskaya *et al.*, 2006). In the Granular Zone of the dentate gyrus within the hippocampus are the so-called Neuronal Stem Cells (NSC), which are responsible for such functions. In the brain, NSC are the brain cells possessing mitotic potential (Kazda *et al.*, 2014)(Figure 1.4). In different parts of the hippocampus, mitotically active NSC are located particularly in the SVZ and Sub ependymal of the Dentate Gyrus (SDG) and migrate to the granular zone of the hippocampus. Some studies suggest that NSC migrate from the hippocampus to faraway areas in the brain to replace damaged astrocytes and oligodendrocyte cells (Lin *et al.*, 2015)(Sawada, Matsumoto and Sawamoto, 2014). These neuronal stem cells are more sensitive to various injuries including radiation-induced apoptosis (Barani, Benedict and Lin, 2007)(Saad and Wang, 2015). A study in mice found that the breakage of double strand DNA in NSC precursors was induced by ionising radiation which, in turn, led to apoptosis (Barazzuol *et al.*, 2015). The loss of NSC due to irradiation leads to a reduction in cognitive function. It was considered that later memory impairment in patients who underwent WBI therapy was the result of damage to NSC (Abayomi, 2009). Consequently, the formation of new neurons can be blocked by doses lower than 2 Gy and impair the hippocampal-dependent memory function (Saad and Wang, 2015).

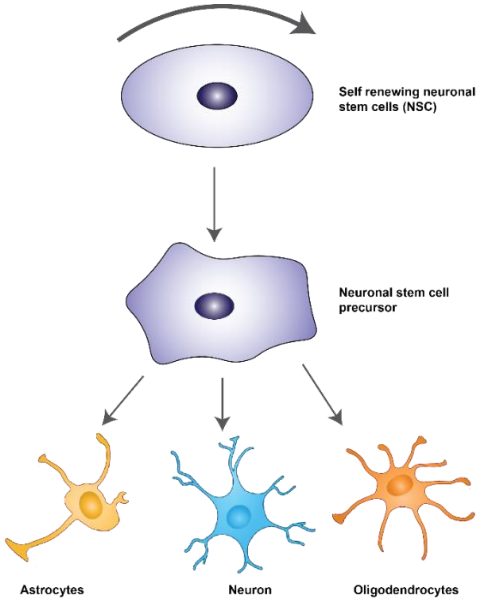


**Figure 1.4: Image shows neurogenesis of the NSC. (Modified from** (Dietrich *et al.*, 2008)**).**

Studies have also shown that GBM tends to arise in and recur in areas like SVZ, where the active neurogenesis is more common in these regions (Kimura *et al.*, 2013). A study of a radiation dose that was increased to 70 Gy demonstrated no overall survival benefit in the higher dose group, however, it showed better survival with patients who had received a higher radiation dose to the ipsilateral SVZ (Kusumawidjaja *et al.*, 2016). Contradictory to the previous studies results, a study by Elicin *et.al* (2014) Showed that there was no benefit, or an even worse outcome, when increasing the radiation dose to SVZ. Consequently, irradiation of SVZ remains controversial, and this will need to be addressed in the future prospective study trials (Allhenn, Shetab Boushehri and Lamprecht, 2012).

Furthermore, loss or structural reorganisation of dendritic spines plays a vital role in learning and memory deficits. Hence, at the synaptic level, changes in the spine's density and morphology can account for functional differences (Segal, 2010). Spine density and morphology in the hippocampus are altered by cranial irradiation, which is time dependent and region specific (Cameron *et al.*, 1993). Consequently, the observed changes or structural reorganisation of dendritic spines post-irradiation therapy suggests that the distribution of neuronal circuity might play a role in radiation-induced cognitive impairment (Chakraborti *et al.*, 2012).

#### 1.2.4.3 Cytotoxicity and neuroinflammation

Radiation deposits energy into cellular molecules causing physical changes to the extracellular matrix, proteins, lipids and DNA of living cells (Burns *et al.*, 2016). This damage activates the brain's innate immune system causing activation of microglia (Leach *et al.*, 2001). Inflammatory cytokines are produced by activated microglia. It is believed that they propagate an ongoing cascade of chronic inflammation and that this is correlated with the impairments in hippocampal neurogenesis and cognitive functions (Monje *et al.*, 2007). A preclinical study on mice also showed that radiation provokes microglia pyroptosis (Liao *et al.*, 2017). Linkermann *et al.* (2014) found a close relationship between the development of pyroptosis and the activation of inflammasomes (Linkermann *et al.*, 2014). Inflammasomes, in particular the NLRC4 inflammasome, have been recognised as a key sensor of bacteria that infect macrophage cells such as microglia (Jamilloux *et al.*, 2013)(Miao *et al.*, 2006).

#### 1.2.4.4 Cognitive impairment and white matter degeneration

A hallmark of radiation-induced brain injury is WM atrophy (Burns *et al.*, 2016). As a result of their high metabolic demand and mitochondrial content, oligodendrocytes are more sensitive to radiation which, in turn, leads them to be more susceptible to oxidative stress and bioenergetic failure (Szerlip *et al.*, 2011). WM injury and radiation necrosis are also related to superimposed microvascular injury (Ishii *et al.*, 2009). WM plays an important role in the cognitive tasks of working memory and executive function. Hence, degeneration of WM is recognised as one of the major contributors to cognitive impairment (Panagiotakos *et al.*, 2007). The importance of WM integrity and its relationship to cognitive performance has been proven in the study by Kinnunen et al. (2011) which examined WM damage and its role in cognitive impairment after traumatic brain injury (Kinnunen *et al.*, 2011). Consequently, imaging biomarkers of WM injury could play a vital role in predicting cognitive decline follow radiotherapy (Chapman *et al.*, 2016).

## 1.3 Cognitive impairment in brain tumour survivors after radiotherapy treatment

Of adult brain tumour patients who survive more than 6 months post-irradiation, 50-90% are reported to experience cognitive impairment, including dementia (Crossen *et al.*, 1994)(Meyers and Brown, 2006). Radiotherapy has been regarded as the main cause of cognitive decline in those patients and also in children treated with radiotherapy who later developed intellectual deterioration. Indeed, cognitive deficits were first reported in children treated for brain tumours or for acute leukaemia as a result of the neurotoxic side effects of radiation on the developing brain (Taphoorn and Klein, 2004).

This cognitive impairment is marked by reduced spatial memory, verbal memory and attention. Further, approximately 49% of patients treated with (fWBI) described significant cognitive impairment at two years post-treatment, experiencing problems with novel problem-solving ability. Unfortunately, this issue is ongoing and its incidence continues to rise over time (Roman and Sperduto, 1995)(Twijnstra *et al.*, 1987). Occasionally, radiation-induced cognitive impairment progresses to dementia, when patients start to experience memory loss, urinary incontinence and ataxia (Vigliani *et al.*, 1999) and fWBI patients who survive more than two years have an increasing risk of developing dementia over time (Scott *et al.*, 1999). Nowadays, due to the improvements in advanced radiotherapy technology, brain tumour patients survive longer than in the past, however, the number of patients who experience radiation-induced brain injury is growing rapidly.

### 1.3.1 High-grade brain tumours

In patients with high grade malignancies, the short time to tumour recurrence and short-term survival are the main reasons for the limited ability to quantify the onset, progression and delayed cognitive impairment due to radiotherapy treatment (Correa, 2010). In glioma patients, cognitive decline appears several weeks earlier than radiographic evidence (Brown *et al.*, 2006). More pronounced cognitive decline has been identified in patients with tumour progression compared with patients who remain stable. It is thought that the decline is due to antiepileptics and corticosteroids (Bosma *et al.*, 2007).

### 1.3.2 Low-grade brain tumours

In low-grade glioma patients, several studies have documented that cognitive dysfunction is due to the tumour itself rather than radiotherapy treatment being the primary or even a key factor (MJB *et al.*, 1994)(Torres *et al.*, 2003). However, different studies have suggested that both partial and WBI are associated with cognitive dysfunction resulting from low-grade brain tumours several years post-treatment (Douw *et al.*, 2009). Hence, the significant side effects of radiation therapy in patients suffering from low-grade gliomas should not be disregarded (Brown *et al.*, 2003). One study found that long term-memory decline and encephalopathy were more severe in patients who had received radiotherapy postresection (Surma-aho and Jääskeläinen, 2001). Consequently, the prominent side effects of radiotherapy should be considered when planning the management of low-grade glioma patients. Indeed, there are findings that, compared with low-grade glioma patients who did not receive radiotherapy, for low-grade glioma patients treated with radiotherapy, any experience of greater neurocognitive decline than in the former group was dose dependent (Laack *et al.*, 2005). Consequently, neurocognitive deficits for patients with low-grade glioma are particularly concerning for those who are quite young and actively engaged in family and work (Sherman *et al.*, 2016).

## 1.4 The use of advanced MRI techniques in brain tumours

There is a progressive increase in survival rates after radiotherapy treatment as a result of the development of irradiation techniques development. While this improvement has led to a reduction in the acute effects of radiation therapy, late effects remain a concern (Robbins *et al.*, 2012). There are currently no validated imaging biomarkers to determine who will, or will not, develop radiation-induced brain injury, cognitive impairment or favourable treatment outcomes. Radiobiology research recognises the importance of developing interventions to identify and prevent injury to the normal brain (Robbins *et al.*, 2012). Radiation-induced late effects occur within the closed cranial cavity, hence, non-invasive imaging techniques should play a vital role in studying the late effects of brain tumour radiotherapy treatment. Radiation-induced cognitive impairment can occur in the absence of radiographic evidence of gross anatomical changes. Consequently, imaging techniques such as conventional MRI, ultrasounds, and X-

ray Computed Tomography (CT) are not likely to provide valuable information regarding the onset and progression of radiation-induced cognitive impairment. However, brain function and physiological properties can be interrogated by advanced MRI and Positron Emission Tomography (PET).

Based on the MRI pulse sequence used, different tissue properties can be used to probe various molecular, cellular, microanatomical and physiological characteristics of normal and tumorous tissues. PET uses radioligands containing positron emitting atoms to interrogate functional properties of normal and tumorous tissues. Theoretically, imaging biomarkers can be found by those non-invasive imaging techniques, given their ability to probe the onset and progression of radiation-induced cognitive impairment (Greene-Schloesser *et al.*, 2012). The following review will focus on conventional and novel MRI techniques that can be used to gather information about biology, cell structure and vascular dynamics allowing brain tumours to be characterised.

## 1.4.1 Standard MRI sequences in GBM

### 1.4.1.1 Gadolinium enhanced T1-Weighted images

Disruption in the BBB is shown by gadolinium signal enhancement on the Gadolinium-T1 weighted (Gd-T1w) contrast (Scott *et al.*, 2002). Paramagnetic contrast agents enhance shorten the T1 relaxation times of tissue, resulting in signal enhancement on T1 weighted images where the contrast agent molecules can leak past the BBB into the interstitial space (Falk Delgado *et al.*, 2019).

BBB breakdown is recognised as a key feature of brain tumours and also in non-neoplastic conditions (Villanueva-Meyer, Mabray and Cha, 2017). Hence, the primary diagnosis of brain tumours is often this type of morphological imaging. Furthermore, detailed characterisations of the tumour, such as grading, can be challenging when using this type of imaging (Scott *et al.*, 2002). Indeed, several different disease processes disrupt the integrity of the tight junctions, that can lead to contrast enhancement on Gd-T1w. Hence, finding contrast enhancement is unspecific and sometimes can be misleading in clinical decision making (Falk Delgado *et al.*, 2019).

#### 1.4.1.2 T2-weighted-Fluid-Attenuated Inversion Recovery (T2-FLAIR)

The initial T2- weighted sequence enables a generic evaluation of tissue. Critical clinical information about various process in the tumour's environment is also provided by T2-FLAIR imaging (Shukla *et al.*, 2017). T2-FLAIR is a useful sequence for showing peritumoral oedema (vasogenic or infiltrative), non-enhanced tumours, gliosis and WM injury (Smirniotopoulos, G James *et al.*, 2007).

#### 1.4.1.3 Diffusion Weighted Imaging (DWI)

In the evaluation of brain tumours, DWI is of significant value. For the assessment of tumour cellularity, peritumoral oedema, integrity of the WM tract and postoperative injury, DWI is used given its ability to probe the random motion of water molecules. Corresponding ADCs, which are the means of water diffusion in three different directions, are derived for each voxel and displayed as a calculated ADC map. The role of DWI in the pre-treatment of brain tumours is to provide the best characterisation of tumour cellularity based on the idea that water diffusivity in the extracellular compartment is inversely proportional to the volume in the intracellular space. Hence, lower ADC values can be used to suggest that tumour cellularity is represented by decreased water diffusivity (Villanueva-Meyer, Mabray and Cha, 2017). In fact, pre- and post-treatment brain tumours have lower ADC values, which is usually due to their high tumour cellularity (Kim and Kim, 2016). However, the relationship between ADC change and treatment induced apoptosis may be complex (David *et al.*, 2007). The heterogeneity of brain tumours can make ADC assessment unreliable. Furthermore, although there is a preliminary study showing a correlation between ADC change and tumour response, there has not been a definite study demonstrating the ability of diffusion MRI to predict tumour response. Hence, it is critical that diffusion MRI predictions of tumour response are further validated (Moffat *et al.*, 2005).

### 1.4.2 Novel MR imaging techniques in GBM

#### 1.4.2.1 MR Perfusion imaging

There are several MR perfusion techniques currently employed, namely, DCE, Dynamic Susceptibility Contrast (DSC) and Arterial Spin Labelling (ASL). DCE consists of repeated images with a T1-weighted sequence that provides

information about endothelial permeability (Weber, Zoubaa and Schlieter, 2006). Higher permeability suggests a higher grade and tumour progression or recurrence (Villanueva-Meyer, Mabray and Cha, 2017). DSC is based on T2* susceptibility effects of a gadolinium contrast agent. Relative Cerebral Blood Volume (rCBV) is the most robust quantitative variable derived from DSC imaging. With the DSC imaging modality, higher blood volume suggests a higher grade or progressive tumour. ASL is a non-invasive imaging technique that quantitatively measures CBF, without injection of an exogenous contrast media (Ferré *et al.*, 2013). ASL acquires two images: first, a label image where an inversion pulse is used to magnetically label the inflowing blood; second, a control image, where in-flowing blood is not inverted. The subtraction of these two images yields a signal, the magnitude of which is weighted by blood flow (Villanueva-Meyer, Mabray and Cha, 2017). In fact, this signal is detected in only a few of the original images. Consequently, many repetitions of labelled-controlled paired images must be acquired and averaged to ensure an adequate signal-to-noise ratio (SNR). Further, on clinical MRI, ASL is becoming available and its use is increasingly easy. It is important to recognise that, the quality of ASL images may be limited by a low SNR and by several types of artifacts (Ferré *et al.*, 2013).

#### 1.4.2.2 Magnetic Resonance Spectroscopy (MRS)

Major metabolites can be measured by MRS in a defined region of tumours and the surrounding brain tissue. The MRS technique has enough sensitivity to detect compounds present in the millimoles per litre range (Waldman *et al.*, 2009). It is obtained using single voxel techniques from a targeted Region of Interest (ROI). It also covers a broad area and can better evaluate different biochemical differences. A multivoxel technique can be used. The most recognizable peaks on long echo $^{1}H$ MRS include: N-AcetylAspartate (NAA), Creatine (Cr), Choline (Cho) and Myo-insitol (MI)(Villanueva-Meyer, Mabray and Cha, 2017). A common pattern in brain tumours is a reduction in NAA. Because it is found in axons as it is transported from the site of synthesis in the neuronal mitochondria, NAA is also found in both WM and GM and is considered to be a highly specific neuronal marker. Malignant tumours, such as brain tumours, cause destruction of neurons and a loss of NAA. Further, NAA levels might reflect neuronal dysfunction rather than actual neuronal loss (Hayat, 2011). Hence, the reduced levels of NAA that have been detected in malignant tumours are ascribed to the breaking of neuronal

integrity. Furthermore, in malignant tumours , increased levels of Cho have been detected and ascribed to an increased cellular membrane turnover (Brindle *et al.*, 2017). For quantification of the metabolic abnormalities in tumours, the Cho:NAA ratio and the Cho:Cr ratio are the most useful indices (Laprie *et al.*, 2005). Conventional MRIs are usually used to evaluate changes in tumoral metabolites to assess stability and progression of the disease after therapy (Weber, Giesel and Stieltjes, 2008). In fact, MRS can anticipate changes in metabolic tumour changes before dimensional changes. Decreased Cho levels after radiotherapy are suggestive of partial remission while increased or stable Cho level are suggestive of disease progression (Nelson *et al.*, 2002)(Lupo and Nelson, 2014)(Graves *et al.*, 2001)(Heesters *et al.*, 1993). Radiotherapy treatment aims to target regions of highest metabolic and cellular activity (gross tumour volume) with a maximised dose of radiation, while limiting the dose received to perilesional tissue which might include normal brain tissues or tumour infiltration (clinical target volume)(Robertson, 2006)(Nelson *et al.*, 2002). MRS, in this setting, can add an important information, complementing that gained from MRI, regarding about the areas of tumour activity in radiotherapy treatment planning to MRI (Nelson *et al.*, 2002). Some authors have tested that MRS has the ability to detect areas of tumour infiltration beyond contrast enhancement or within oedema (Arnold *et al.*, 1990)(Ricci *et al.*, 2000). Consequently, MRS is a promising non-invasive technique which provides both information not only about tumour metabolites but also insight into the physiology of malignant transformation in the brain tumours. Hence, in clinical applications, MRS has been heavily investigated for both cancer diagnosis and monitoring treatment response (Laino *et al.*, 2020).

#### 1.4.2.3 Diffusion Tensor Imaging (DTI)

Tissue microstructure can be assessed using DTI by measuring the diffusion of water molecules in three-dimensional space (Le Bihan *et al.*, 2001)(Chan *et al.*, 2009). The ability of water molecules to diffuse in the brain structure is affected by the WM tract structure and the biochemical and biophysical properties of the myelin in these WM tracts. While water molecules freely diffuse in all directions in an unstructured space, in a well-structured space molecules diffuse preferentially in one direction. Fractional Anisotropy (FA) is usually used to indicate whether the water molecules in a particular region are free to diffuse equally in all directions (spherical diffusion) or preferentially in one direction

(elliptical diffusion). The value of FA ranges between 0 and 1. Little structure or spherical diffusion is indicated by lower FA values, while high FA values indicate highly-structured or elliptical diffusion (Greene-Schloesser *et al.*, 2012).

A clinical study used DTI to assess WM injury in both adult and paediatric patients treated with fWBI (Nagesh *et al.*, 2008). A recent study applied DTI to patients with high-grade glioma (n=19), low-grade glioma (n=3) and benign tumours (n=3). These tumours were scanned before, during and after fWBI, showing progressive DTI changes in the genu and splenium of the corpus callosum (Nagesh *et al.*, 2008). During the first 3 months post-radiotherapy treatment, demyelination was observed, particularly in areas treated with high doses. Six months later, demyelination had also spread to lower radiation treatment regions. This present progressive finding of the demyelination of the axonal structures over several months presents an opportunity during which intervention therapies can be implemented to treat and stop further deterioration of WM structures and also therapy to minimise neurocognitive dysfunction (Nagesh *et al.*, 2008).

Overall, DTI is a promising non-invasive imaging tool that can be used to detect early microstructural changes in WM integrity before progressive injury such as necrosis (Nagesh *et al.*, 2008). Such microanatomical changes in normal-appearing WM measures properties which are likely to be due to the interaction between radiation and oligodendrocytes, astrocytes and neurons. Before and after irradiation, DTI imaging and cognitive impairment tests are required to ascertain any correlation between these microstructural changes and late delayed cognitive impairment. Further, cognitive impairment can occur without change to axons, myelin sheath loss or demyelination and changes in the number of oligodendrocytes, one year following fWBI (Shi *et al.*, 2009). This finding suggests the need for more important sensitive imaging techniques such as DTI, which might detect the neurobiological changes that lead to changed neuronal function following fWBI (Lerner *et al.*, 2014).

### 1.4.3 Biomarkers

The National Institutes of Health Biomarkers Definitions Working Group defined a biomarker as “a characteristic that is objectively measured and evaluated as an indicator of normal biological processes, pathogenic processes, or pharmacologic

responses to a therapeutic intervention" (Puntmann, 2009). To study the effects of radiation injury in patients and to improve radiation therapy protocols, non-invasive and sensitive biomarkers of irradiation injury are still needed to monitor brain damage. In fact, limited information on tumour characterization and prognosis is provided by conventional structural imaging. Owing to, advances in neurosurgical techniques, radiotherapy planning and novel drug treatment of the brain tumour, patients are living longer but also suffering more from cognitive impairments. Hence, there is an increasing need for reproducible, non-invasive quantitative imaging biomarkers of irradiation injury (Waldman *et al.*, 2009) to ensure biomarkers are clinically acceptable. Indeed, to assist in the diagnosis of brain tumours, neuro-oncologists are seeking for non-invasive imaging biomarkers, given the limitations associated with histopathological diagnosis.

## 1.5 Conclusion

In cancer patients, greater understanding of the mechanisms underlying cognitive dysfunction will be critical in the design of an optimal MRI sequence and in optimizing individual therapies for preventing later neurotoxicity such as dementia and WM necrosis. In clinical trials for high-grade glioma patients, neurocognitive function and quality of life are new important endpoints, especially for GBM patients who have a very short life expectancy. As a result, the search continues for imaging biomarkers to identify patients who are, and who are not, likely to develop cognitive impairment after radiotherapy treatment. To date, no clinically relevant biomarkers have been identified that could be used as an early determinant of tumour response. In the future, this may help with the early identification of patients likely to suffer from reduced cognitive function. MRI biomarkers that can be used to identify patients who will suffer from WM integrity damage might be very helpful to also predict patients who will suffer from negative radiotherapy effects, allowing the early commencement of intervention. Our understanding of the microstructural mechanism of the development and progression of tissue injury due to radiation therapy will greatly improve by applying these non-invasive imaging techniques to radiation oncology. Finally, this improvement will allow the best planning for radiation-therapy treatment by oncologists that, in turn, will lead to improve their patients' quality of life.

## 1.6 References

Abayomi, O. K. (1996) 'Pathogenesis of irradiation-induced cognitive dysfunction', *Acta Oncologica*, 35(6), pp. 659–663. doi: 10.3109/02841869609083995.

Abayomi, O. K. (2002) 'Pathogenesis of cognitive decline following therapeutic irradiation for head and neck tumors', *Acta Oncologica*, 41(4), pp. 346–351. doi: 10.1080/028418602760169389.

Abayomi, O. K. (2009) 'Pathogenesis of Irradiation-Induced Cognitive Dysfunction'. doi: 10.3109/02841869609083995.

Acharya, M. M. *et al.* (2016) 'Elimination of microglia improves cognitive function following cranial irradiation', *Scientific Reports*, 6(April), pp. 1–11. doi: 10.1038/srep31545.

Acres, W. M. (1941) 'Banbury church', *Notes and Queries*, 180(4), p. 70. doi: 10.1093/nq/180.4.70-a.

Allhenn, D., Shetab Boushehri, M. A. and Lamprecht, A. (2012) 'Drug delivery strategies for the treatment of malignant gliomas', *International Journal of Pharmaceutics*. Elsevier B.V., 436(1–2), pp. 299–310. doi: 10.1016/j.ijpharm.2012.06.025.

Arfanakis, K. *et al.* (2002) 'Diffusion tensor MR imaging in diffuse axonal injury', *American Journal of Neuroradiology*, 23(5), pp. 794–802.

Armstrong, C. L. *et al.* (2000) 'Radiotherapeutic effects on brain function: double dissociation of memory systems.', *Neuropsychiatry, neuropsychology, and behavioral neurology*, 13(2), p. 101.

Armstrong, C. L. *et al.* (2004) 'A critical review of the clinical effects of therapeutic irradiation damage to the brain: The roots of controversy', *Neuropsychology Review*, 14(1), pp. 65–86. doi: 10.1023/B:NERV.0000026649.68781.8e.

Armstrong, G. T. *et al.* (2013) 'Evaluation of memory impairment in aging adult

survivors of childhood acute lymphoblastic leukemia treated with cranial radiotherapy', *Journal of the National Cancer Institute*, 105(12), pp. 899–907. doi: 10.1093/jnci/djt089.

Arnold, D. L. *et al.* (1990) 'Proton and phosphorus magnetic resonance spectroscopy of human astrocytomas in vivo. Preliminary observations on tumor grading', *NMR in Biomedicine*, 3(4), pp. 184–189. doi: 10.1002/nbm.1940030407.

Arnold, K. M. *et al.* (2018) 'The Impact of Radiation on the Tumor Microenvironment: Effect of Dose and Fractionation Schedules', *Cancer Growth and Metastasis*, 11, p. 117906441876163. doi: 10.1177/1179064418761639.

Assaf, Y. and Pasternak, O. (2008) 'Diffusion tensor imaging (DTI)-based white matter mapping in brain research: A review', *Journal of Molecular Neuroscience*, 34(1), pp. 51–61. doi: 10.1007/s12031-007-0029-0.

Barani, I. J., Benedict, S. H. and Lin, P. S. (2007) 'Neural Stem Cells: Implications for the Conventional Radiotherapy of Central Nervous System Malignancies', *International Journal of Radiation Oncology Biology Physics*, 68(2), pp. 324–333. doi: 10.1016/j.ijrobp.2007.01.033.

Barazzuol, L. *et al.* (2015) 'Radiosensitization of glioblastoma cells using a histone deacetylase inhibitor (SAHA) comparing carbon ions with X-rays', *International journal of radiation biology*, 91(1), pp. 90–98.

Barnett, G. C. *et al.* (2009) 'UKPMC Funders Group Normal tissue reactions to radiotherapy ':, *Oncology*, 9(2), pp. 134–142. doi: 10.1038/nrc2587.Normal.

Basser, P. J. and Pierpaoli, C. (1996) 'Microstructural and physiological features of tissues elucidated by quantitative-diffusion-tensor MRI', *Journal of Magnetic Resonance - Series B*, 111(3), pp. 209–219. doi: 10.1006/jmrb.1996.0086.

Basser, P. J. and Pierpaoli, C. (1998) 'A simplified method to measure the diffusion tensor from seven MR images', *Magnetic Resonance in Medicine*, 39(6), pp. 928–934.

Le Bihan, D. *et al.* (2001) 'Diffusion tensor imaging: Concepts and applications', *Journal of Magnetic Resonance Imaging*. doi: 10.1002/jmri.1076.

Bleehen, N. M. and Stenning S P (1991) 'A Medical Research Council trial of two radiotherapy doses in the treatment of grades 3 and 4 astrocytoma Stenning on behalf of the Medical Research Council Brain Tumour Working Party*', *Br. J. Cancer*, 64, pp. 769–774.

Block, M. L., Zecca, L. and Hong, J.-S. (2007) 'Microglia-mediated neurotoxicity: uncovering the molecular mechanisms.', *Nature reviews. Neuroscience*, 8(1), pp. 57–69. doi: 10.1038/nrn2038.

Bosma, I. *et al.* (2007) 'The course of neurocognitive functioning in high-grade glioma patients1', *Neuro-Oncology*, 9(1), pp. 53–62. doi: 10.1215/15228517-2006-012.

Brada, M. (2006) 'Radiotherapy in malignant glioma', *Annals of Oncology*, 17(suppl_10), pp. x183–x185. doi: 10.1093/annonc/mdl257.

Briere, T. M. *et al.* (2017) 'Sparing of normal tissues with volumetric arc radiation therapy for glioblastoma: Single institution clinical experience', *Radiation Oncology*. Radiation Oncology, 12(1), pp. 3–11. doi: 10.1186/s13014-017-0810-3.

Brindle, K. M. *et al.* (2017) 'Brain tumor imaging', *Journal of Clinical Oncology*, 35(21), pp. 2432–2438. doi: 10.1200/JCO.2017.72.7636.

Brown, P. D. *et al.* (2003) 'Effects of radiotherapy on cognitive function in patients with low-grade glioma measured by the Folstein mini-mental state examination', *Journal of Clinical Oncology*, 21(13), pp. 2519–2524. doi: 10.1200/JCO.2003.04.172.

Brown, P. D. *et al.* (2004) 'Importance of baseline mini-mental state examination as a prognostic factor for patients with low-grade glioma', *International Journal of Radiation Oncology Biology Physics*, 59(1), pp. 117–125. doi: 10.1016/j.ijrobp.2003.10.040.

Brown, P. D. *et al.* (2006) 'Detrimental effects of tumor progression on cognitive function of patients with high-grade glioma', *Journal of Clinical Oncology*, 24(34), pp. 5427–5433. doi: 10.1200/JCO.2006.08.5605.

Burns, T. C. *et al.* (2016) 'Radiation-induced brain injury: low-hanging fruit for neuroregeneration', *Neurosurgical Focus*, 40(5), p. E3. doi: 10.3171/2016.2.focus161.

Butler, J. M., Rapp, S. R. and Shaw, E. G. (2006) 'Managing the cognitive effects of brain tumor radiation therapy', *Current Treatment Options in Oncology*, 7(6), pp. 517–523. doi: 10.1007/s11864-006-0026-5.

Calvo, W. *et al.* (1988) 'Time- and dose-related changes in the white matter of the rat brain after single doses of X rays', *British Journal of Radiology*, 61(731), pp. 1043–1052. doi: 10.1259/0007-1285-61-731-1043.

Cameron, H. A. *et al.* (1993) 'Differentiation of newly born neurons and glia in the dentate gyrus of the adult rat.', *Neuroscience*, 56(2), pp. 337–44. Available at: http://www.ncbi.nlm.nih.gov/pubmed/8247264.

Cao, Y. *et al.* (2009) 'Dynamic contrast-enhanced magnetic resonance imaging as a biomarker for prediction of radiation-induced neurocognitive dysfunction', *Clinical Cancer Research*, 15(5), pp. 1747–1754. doi: 10.1158/1078-0432.CCR-08-1420.

Chakraborti, A. *et al.* (2012) 'Cranial Irradiation Alters Dendritic Spine Density and Morphology in the Hippocampus', 7(7), pp. 1–9. doi: 10.1371/journal.pone.0040844.

Chan, K. C. *et al.* (2009) 'MRI of Late Microstructural and Metabolic Alterations in Radiation-Induced Brain Injuries', 1020, pp. 1013–1020. doi: 10.1002/jmri.21736.

Chan, M. D. *et al.* (2012) 'Radiation-induced brain injury: A review', *Frontiers in Oncology*, 2(July), pp. 1–18. doi: 10.3389/fonc.2012.00073.

Chang, C. H. *et al.* (1983) 'Comparison of postoperative radiotherapy and

combined postoperative radiotherapy and chemotherapy in the multidisciplinary management of malignant gliomas. A joint radiation therapy oncology group and eastern cooperative oncology group study', *Cancer*, 52(6), pp. 997–1007. doi: 10.1002/1097-0142(19830915)52:6<997::AID-CNCR2820520612>3.0.CO;2-2.

Chang, E. L. *et al*. (2007) 'Evaluation of Peritumoral Edema in the Delineation of Radiotherapy Clinical Target Volumes for Glioblastoma', *International Journal of Radiation Oncology Biology Physics*, 68(1), pp. 144–150. doi: 10.1016/j.ijrobp.2006.12.009.

Chapman, C. H. *et al*. (2016) 'Diffusion tensor imaging predicts cognitive function change following partial brain radiotherapy for low-grade and benign tumors', *Radiotherapy and Oncology*. Elsevier Ireland Ltd, 120(2), pp. 234–240. doi: 10.1016/j.radonc.2016.06.021.

Chiang, C. S., McBride, W. H. and Withers, H. R. (1993) 'Radiation-induced astrocytic and microglial responses in mouse brain', *Radiotherapy and Oncology*, 29(1), pp. 60–68. doi: 10.1016/0167-8140(93)90174-7.

Choi, S. Y. C. *et al*. (2014) 'Lessons from patient-derived xenografts for better in vitro modeling of human cancer', *Advanced Drug Delivery Reviews*. The Authors, 79, pp. 222–237. doi: 10.1016/j.addr.2014.09.009.

Connor, M. *et al*. (2016) 'Dose-dependent white matter damage after brain radiotherapy', *Radiotherapy and Oncology*. Elsevier Ireland Ltd, 121(2), pp. 209–216. doi: 10.1016/j.radonc.2016.10.003.

Constine, L. S. *et al*. (1988) 'Adverse effects of brain irradiation correlated with MR and CT imaging', *International Journal of Radiation Oncology, Biology, Physics*, 15(2), pp. 319–330. doi: 10.1016/S0360-3016(98)90011-6.

Correa, D. D. (2010) 'Neurocognitive Function in Brain Tumors', (March), pp. 232–239. doi: 10.1007/s11910-010-0108-4.

Crawley, J. N. (2008) 'Behavioral Phenotyping Strategies for Mutant Mice', *Neuron*, 57(6), pp. 809–818. doi: 10.1016/j.neuron.2008.03.001.

Crompton, M. R. and Layton, D. D. (1958) ‘DELAYED RADIONECROSIS OF THE BRAIN FOLLOWING THERAPEUTIC X-RADIATION OF THE PITUITARY IRRADIATION of the brain has been carried out for many years as a therapeutic measure in patients with neoplasms . It was Fischer and Holfelder in 1930 who first describ’.

Crossen, B. J. R. *et al*. (2019) ‘Neurobehavioral Sequelae of Cranial Irradiation in Adults : A Review of Radiation-Induced Encephalopathy’, 12(3), pp. 627–642.

Crossen R.Jhon, Garwood Dan,Glatstein and Neuwelt A Edward. (1994) ‘Neurobehavioral sequelae of cranial irradiation in adults: A review of radiation-induced encephalopathy’, *Journal of Clinical Oncology*, 12(3), pp. 627–642. Available at: http://ovidsp.ovid.com/ovidweb.cgi?T=JS&PAGE=reference&D=emed3&NEWS=N&AN=1994087595.

Danoff, B. F. *et al*. (1982) ‘Assessment of the long-term effects of primary radiation. Therapy for brain tumors in children’, *Cancer*, 49(8), pp. 1580–1586. doi: 10.1002/1097-0142(19820415)49:8<1580::AID-CNCR2820490810>3.0.CO;2-7.

David, F. *et al*. (2007) ‘MRI-measured water mobility increases in response to chemotherapy via multiple cell-death mechanisms David’, *NMR in Biomedicine*, 20(3), pp. 304–325. doi: 10.1002/nbm.

DeAngelis, L. M. (2001) ‘Brain Tumors’, *The New England Journal of Medicine*, 344(2), pp. 114–123. doi: 10.1227/01.NEU.0000311254.63848.72.

Dietrich, J. *et al*. (2008) ‘Clinical Patterns and Biological Correlates of Cognitive Dysfunction Associated with Cancer Therapy’, *The Oncologist*, 13(12), pp. 1285–1295. doi: 10.1634/theoncologist.2008-0130.

Douglas H. Smith, D. F. M. and W. H. S. (2003) ‘Diffuse axonal injury in adults’, *Trauma*, 5(4), pp. 227–234. doi: 10.1191/1460408603ta289oa.

Douw, L. *et al*. (2009) ‘Cognitive and radiological effects of radiotherapy in patients with low-grade glioma: long-term follow-up’, *The Lancet Neurology*, 8(9), pp. 810–818. doi: 10.1016/S1474-4422(09)70204-2.

Elkabes, S., DiCicco-Bloom, E. M. and Black, I. B. (1996) 'Brain microglia/macrophages express neurotrophins that selectively regulate microglial proliferation and function.', *The Journal of neuroscience : the official journal of the Society for Neuroscience*, 16(8), pp. 2508–21. Available at: http://www.ncbi.nlm.nih.gov/pubmed/8786427.

Falk Delgado, Anna *et al.* (2019) 'Diagnostic value of alternative techniques to gadolinium-based contrast agents in MR neuroimaging—a comprehensive overview', *Insights into Imaging*. Insights into Imaging, 10(1), pp. 1–15. doi: 10.1186/s13244-019-0771-1.

Ferré, J. C. *et al.* (2013) 'Arterial spin labeling (ASL) perfusion: Techniques and clinical use', *Diagnostic and Interventional Imaging*. Elsevier Masson SAS, 94(12), pp. 1211–1223. doi: 10.1016/j.diii.2013.06.010.

Fike, J. R., Rosi, S. and Limoli, C. L. (2009) 'Neural Precursor Cells and Central Nervous System Radiation Sensitivity', *Seminars in Radiation Oncology*. Elsevier Inc., 19(2), pp. 122–132. doi: 10.1016/j.semradonc.2008.12.003.

Graves, E. E. *et al.* (2001) 'Serial proton MR spectroscopic imaging of recurrent malignant gliomas after gamma knife radiosurgery', *American Journal of Neuroradiology*, 22(4), pp. 613–624.

Greene-schloesser, D. *et al.* (2012) 'Radiation-induced brain injury : a review', 2(July), pp. 1–18. doi: 10.3389/fonc.2012.00073.

Greene-Schloesser, D. *et al.* (2012) 'Radiation-induced brain injury: A review', *Front Oncol*, 2(73), pp. 1–18.

Greene-Schloesser, D., Moore, E. and Robbins, M. E. (2013) 'Molecular pathways: radiation-induced cognitive impairment', *Clinical Cancer Research*, 19(9), pp. 2294–2300.

Greene-schloesser, D. and Robbins, M. E. (2012) 'Radiation-induced cognitive impairment- from bench to bedside', pp. 37–44.

Hahn, C. A. *et al.* (2009) 'Dose-Dependent Effects of Radiation Therapy on Cerebral Blood Flow, Metabolism, and Neurocognitive Dysfunction', *International Journal of Radiation Oncology Biology Physics*, 73(4), pp. 1082–1087. doi: 10.1016/j.ijrobp.2008.05.061.

Hansson, E. (1988) 'Astroglia from defined brain regions as studied with primary cultures', *Progress in Neurobiology*, 30(5), pp. 369–397. doi: 10.1016/0301-0082(88)90008-1.

Hayat, M. A. (2011) *Tumors of the Central Nervous System: Volume 1*. Dordrecht; New York: Springer. Available at: http://uq.summon.serialssolutions.com/2.0.0/link/0/eLvHCXMwY2AwNtIz0EUrE4yBSSctDdj2SAU2UVMtkoGNiFRgXZWWaAaqspIsUYY_eBDllZsQA1NqniiDtJtriLOHbmlhPHRUIz4JWC8CmyZmBsZiDCzAnnKqBIOCiYVJinmiQZIxuKIF1pwmxonGlsapScA2M7CqNZVkEMFmAgCYWiq-.

Heesters, M. A. A. M. *et al.* (1993) 'Localized proton spectroscopy of inoperable brain gliomas. Response to radiation therapy', *Journal of Neuro-Oncology*, 17(1), pp. 27–35. doi: 10.1007/BF01054271.

Hodges, H. *et al.* (1998) 'Late behavioural and neuropathological effects of local brain irradiation in the rat', *Behavioural Brain Research*, 91(1–2), pp. 99–114. doi: 10.1016/S0166-4328(97)00108-3.

Hopewell, J. W. *et al.* (1986) 'Vascular irradiation damage : Its cellular basis and likely consequences', *British Journal of Cancer*, 53(SUPPL. 7), pp. 181–191.

Hopewell, J. W. (1998) 'Radiation injury to the central nervous system', *Medical and Pediatric Oncology*, 30(SUPPL. 1), pp. 1–9. doi: 10.1002/(sici)1096-911x(1998)30:1+<1::aid-mpo1>3.3.co;2-p.

Hospital, W. G. *et al.* (1996) 'Neuropsychometric evaluation of long-term survivors of adult brain tumours : relationship with tumour and treatment parameters', 8140(96).

Hubenak, J. R. *et al.* (2014) 'Mechanisms of injury to normal tissue after

radiotherapy: A review', *Plastic and Reconstructive Surgery*, 133(1), pp. 1–12. doi: 10.1097/01.prs.0000440818.23647.0b.

Hurria, A. *et al.* (2006) 'Cognitive Function of Older Patients Receiving Adjuvant Chemotherapy for Breast Cancer : A Pilot Prospective Longitudinal Study', pp. 925–931. doi: 10.1111/j.1532-5415.2006.00732.x.

Torres, I.J. *et al.* (2003) 'A longitudinal neuropsychological study of partial brain radiation in adults with brain tumors.', *Neurology*, 60(7), pp. 1113–1118. Available at: http://ovidsp.ovid.com/ovidweb.cgi?T=JS&PAGE=reference&D=psyc4&NEWS=N&AN=2003-03421-009%5Cnhttp://ovidsp.ovid.com/ovidweb.cgi?T=JS&PAGE=reference&D=emed9&NEWS=N&AN=36418770.

Ishii, A. *et al.* (2009) 'Human myelin proteome and comparative analysis with mouse myelin', *Proceedings of the National Academy of Sciences*, 106(34), pp. 14605–14610. doi: 10.1073/pnas.0905936106.

Izquierdo, I. and Medina, J. H. (1997) 'Memory formation: The sequence of biochemical events in the hippocampus and its connection to activity in other brain structures', *Neurobiology of Learning and Memory*, 68(3), pp. 285–316. doi: 10.1006/nlme.1997.3799.

Jacob, J. *et al.* (2018) 'Cognitive impairment and morphological changes after radiation therapy in brain tumors: A review', *Radiotherapy and Oncology*. Elsevier B.V., 128(2), pp. 221–228. doi: 10.1016/j.radonc.2018.05.027.

Jain, R., Scarpace, L. and Rock, J. P. (2007) 'FIRST-PASS PERFUSION COMPUTED TOMOGRAPHY: INITIAL EXPERIENCE IN DIFFERENTIATING RECURRENT BRAIN TUMORS FROM RADIATION EFFECTS AND RADIATION NECROSIS', 61(4), pp. 133–134. doi: 10.1227/01.NEU.0000280100.67726.25.

Jamilloux, Y. *et al.* (2013) 'Inflammasome activation restricts Legionella pneumophila replication in primary microglial cells through flagellin detection', *Glia*, 61(4), pp. 539–549. doi: 10.1002/glia.22454.

Jiang, Y. H. *et al.* (2010) 'Altered ultrasonic vocalization and impaired learning and memory in Angelman syndrome mouse model with a large maternal deletion from Ube3a to Gabrb3', *PLoS ONE*, 5(8). doi: 10.1371/journal.pone.0012278.

Johnson, B. E. *et al.* (1985) 'Neurologic, neuropsychologic, and computed cranial tomography scan abnormalities in 2- to 10-year survivors of small-cell lung cancer', *Journal of Clinical Oncology*, 3(12), pp. 1659–1667. doi: 10.1200/JCO.1985.3.12.1659.

Kazda, T. *et al.* (2014) 'Why and how to spare the hippocampus during brain radiotherapy : the developing role of hippocampal avoidance in cranial radiotherapy', pp. 1–10.

Kim, M. and Kim, H. S. (2016) 'Emerging techniques in brain tumor imaging: What radiologists need to know', *Korean Journal of Radiology*, 17(5), pp. 598–619. doi: 10.3348/kjr.2016.17.5.598.

Kimura, M. *et al.* (2013) 'Glioblastoma multiforme: Relationship to subventricular zone and recurrence', *Neuroradiology Journal*, 26(5), pp. 542–547. doi: 10.1177/197140091302600507.

Kinnunen, K. M. *et al.* (2011a) 'White matter damage and cognitive impairment after traumatic brain injury', *Brain*, 134(2), pp. 449–463. doi: 10.1093/brain/awq347.

Kinnunen, K. M. *et al.* (2011b) 'White matter damage and cognitive impairment after traumatic brain injury', *Brain*, 134(2), pp. 449–463. doi: 10.1093/brain/awq347.

Koontz, B. F., Verhaegen, F. and Ruysscher, D. D. E. (2017) 'SMALL ANIMAL IGRT SPECIAL FEATURE : REVIEW ARTICLE Tumour and normal tissue radiobiology in mouse models : how close are mice to mini-humans ?', (May 2016).

Kusumawidjaja, G. *et al.* (2016) 'Dose-escalated intensity-modulated radiotherapy and irradiation of subventricular zones in relation to tumor control outcomes of patients with glioblastoma multiforme', *OncoTargets and Therapy*,

9, pp. 1115–1122. doi: 10.2147/OTT.S96509.

Laack, N. N. *et al.* (2005) 'Cognitive function after radiotherapy for supratentorial low-grade glioma: A North Central Cancer Treatment Group prospective study', *International Journal of Radiation Oncology Biology Physics*, 63(4), pp. 1175–1183. doi: 10.1016/j.ijrobp.2005.04.016.

Laino, M. E. *et al.* (2020) 'Magnetic resonance spectroscopic imaging in gliomas: Clinical diagnosis and radiotherapy planning', *BJR|Open*, (January), p. 20190026. doi: 10.1259/bjro.20190026.

Laprie, A. *et al.* (2005) 'Longitudinal multivoxel MR spectroscopy study of pediatric diffuse brainstem gliomas treated with radiotherapy', *International Journal of Radiation Oncology Biology Physics*, 62(1), pp. 20–31. doi: 10.1016/j.ijrobp.2004.09.027.

Leach, J. K. *et al.* (2001) 'Ionizing Radiation-induced , Mitochondria-dependent Generation of Reactive Oxygen / Nitrogen 1', pp. 3894–3901.

Lee, M. C. *et al.* (2005) 'Dynamic susceptibility contrast perfusion imaging of radiation effects in normal-appearing brain tissue: Changes in the first-pass and recirculation phases', *Journal of Magnetic Resonance Imaging*, 21(6), pp. 683–693. doi: 10.1002/jmri.20298.

Lee, W. H. *et al.* (2010) 'Irradiation induces regionally specific alterations in pro-inflammatory environments in rat brain', *International Journal of Radiation Biology*, 86(2), pp. 132–144. doi: 10.3109/09553000903419346.

Lenzi, R. *et al.* (2004) 'The Cognitive Sequelae of Standard-Dose Adjuvant Results of a Prospective , Randomized , Longitudinal Trial', (April), pp. 2292–2299. doi: 10.1002/cncr.20272.

Lerner, A. *et al.* (2014) 'Clinical Applications of Diffusion Tensor Imaging', *World Neurosurgery*, 82(1–2), pp. 96–109. doi: 10.1016/j.wneu.2013.07.083.

Li, W. *et al.* (2009) 'Memory and learning behavior in mice is temporally associated

with diet-induced alterations in gut bacteria', *Physiology and Behavior*. Elsevier Inc., 96(4–5), pp. 557–567. doi: 10.1016/j.physbeh.2008.12.004.

Liao, H. *et al.* (2017) 'Mesenchymal stem cells attenuate radiation-induced brain injury by inhibiting microglia pyroptosis', *BioMed Research International*, 2017. doi: 10.1155/2017/1948985.

Lin, R. *et al.* (2015) 'Neurobiology of Disease Neurogenesis is enhanced by stroke in multiple new stem cell niches along the ventricular system at sites of high BBB permeability', *Neurobiology of Disease*. The Authors, 74, pp. 229–239. doi: 10.1016/j.nbd.2014.11.016.

Linkermann, A. *et al.* (2014) 'Nri3743', 14.

Lupo, J. M. and Nelson, S. J. (2014) 'Methods for Planning and Monitoring Radiation Therapy in Patients With', *Seminars in Radiation Oncology*, 24(4), pp. 248–258. doi: 10.1016/j.semradonc.2014.06.008.

Van Der Maazen, R. W. M. *et al.* (1993) 'Repair capacity of adult rat glial progenitor cells determined by an in vitro clonogenic assay after in vitro or in vivo fractionated irradiation', *International Journal of Radiation Biology*, 63(5), pp. 661–666. doi: 10.1080/09553009314450861.

Vigliani.M.C, Duyckaerts.C, Hauw.J.J, Poisson.M, Magdelenat.H. . and Delattre. J.Y . (1999) 'Dementia following treatment of brain tumors with radiotherapy administered alone or in combination with nitrosourea-based chemotherapy: A clinical and pathological study', *Journal of Neuro-Oncology*, 41(2), pp. 137–149. Available at: http://www.embase.com/search/results?subaction=viewrecord&from=export&id=L29161009%5Cnhttp://dx.doi.org/10.1023/A:1006183730847%5Cnhttp://sfx.library.uu.nl/utrecht?sid=EMBASE&issn=0167594X&id=doi:10.1023/A:1006183730847&atitle=Dementia+following+treatment.

Makale, M. T. *et al.* (2016) 'Mechanisms of radiotherapy-associated cognitive disability in patients with brain tumours', *Nature Reviews Neurology*. Nature Publishing Group, 13(1), pp. 52–64. doi: 10.1038/nrneurol.2016.185.

Marsh, J. C. *et al.* (2010) 'Cognitive Sparing during the Administration of Whole

Brain Radiotherapy and Prophylactic Cranial Irradiation: Current Concepts and Approaches', *Journal of Oncology*, 2010, pp. 1–16. doi: 10.1155/2010/198208.

Marsh, J. C. *et al.* (2012) 'Feasibility of cognitive sparing approaches in children with intracranial tumors requiring partial brain radiotherapy: A dosimetric study using tomotherapy', *journal of Cancer Therapeutics and Research*, 1(1), p. 1. doi: 10.7243/2049-7962-1-1.

Martin C. Raff, Robert H. Miller and Mark Noble (1983) 'A glial progenitor cell that develops in vitro into an astrocyte or an oligodendrocyte depending on culture medium', *Nature*, 303(5916), pp. 390–396. Available at: https://www.nature.com/articles/303390a0.pdf.

McTyre, E., Scott, J. and Chinnaiyan, P. (2013) 'Whole brain radiotherapy for brain metastasis', *Surgical Neurology International*, 4(SUPPL4). doi: 10.4103/2152-7806.111301.

Meyers, C. A. *et al.* (2004) 'Neurocognitive function and progression in patients with brain metastases treated with whole-brain radiation and motexafin gadolinium: Results of a randomized phase III trial', *Journal of Clinical Oncology*, 22(1), pp. 157–165. doi: 10.1200/JCO.2004.05.128.

Meyers, C. A. and Brown, P. D. (2006) 'Role and relevance of neurocognitive assessment in clinical trials of patients with CNS tumors', *Journal of Clinical Oncology*, 24(8), pp. 1305–1309. doi: 10.1200/JCO.2005.04.6086.

Miao, E. A. *et al.* (2006) 'Cytoplasmic flagellin activates caspase-1 and secretion of interleukin 1ß via Ipaf', *Nature Immunology*, 7(6), pp. 569–575. doi: 10.1038/ni1344.

Miszczyk, J. *et al.* (2018) 'Do protons and X-rays induce cell-killing in human peripheral blood lymphocytes by different mechanisms?', *Clinical and Translational Radiation Oncology*, 9, pp. 23–29. doi: 10.1016/j.ctro.2018.01.004.

MJB, T. *et al.* (1994) 'Cognitive functions and quality of life in patients with low-grade gliomas: The impact of radiotherapy', *Annals of neurology*, 36(1), pp. 48–54. Available at:

http://ovidsp.ovid.com/ovidweb.cgi?T=JS&PAGE=reference&D=emed6&NEWS=N&AN=24205823.

Moffat, B. A. *et al.* (2005) 'Functional diffusion map: A noninvasive MRI biomarker for early stratification of clinical brain tumor response', *Proceedings of the National Academy of Sciences of the United States of America*, 102(15), pp. 5524–5529. doi: 10.1073/pnas.0501532102.

Monje, M. L. *et al.* (2007) 'Impaired human hippocampal neurogenesis after treatment for central nervous system malignancies', *Annals of Neurology*, 62(5), pp. 515–520. doi: 10.1002/ana.21214.

Moretti, R. *et al.* (2005) 'Neuropsychological evaluation of late-onset post-radiotherapy encephalopathy: A comparison with vascular dementia', *Journal of the Neurological Sciences*, 229–230, pp. 195–200. doi: 10.1016/j.jns.2004.11.027.

Morris, R. G. M. (1981) 'Spatial localization does not require the presence of local cues', *Learning and Motivation*, 12(2), pp. 239–260. doi: 10.1016/0023-9690(81)90020-5.

Nagesh, V. *et al.* (2008) 'Radiation-Induced Changes in Normal-Appearing White Matter in Patients With Cerebral Tumors: A Diffusion Tensor Imaging Study', *International Journal of Radiation Oncology Biology Physics*, 70(4), pp. 1002–1010. doi: 10.1016/j.ijrobp.2007.08.020.

Nazemi-Gelyan, H. *et al.* (2015) 'Evaluation of organs at risk's dose in external radiotherapy of brain tumors', *Iranian Journal of Cancer Prevention*, 8(1), pp. 47–52.

Nelson, S. J. *et al.* (2002) 'In vivo molecular imaging for planning radiation therapy of gliomas: An application of 1H MRSI', *Journal of Magnetic Resonance Imaging*, 16(4), pp. 464–476. doi: 10.1002/jmri.10183.

Ngen, E. J. *et al.* (2016) 'A preclinical murine model for the early detection of radiation-induced brain injury using magnetic resonance imaging and behavioral tests for learning and memory: with applications for the evaluation of possible

stem cell imaging agents and therapies', *Journal of Neuro-Oncology*, 128(2), pp. 225–233.

Okamoto, T. *et al*. (2007) 'Cerebral blood flow in patients with diffuse axonal injury - Examination of the easy Z-score imaging system utility', *European Journal of Neurology*, 14(5), pp. 540–547. doi: 10.1111/j.1468-1331.2007.01742.x.

Padovani, L. *et al*. (2012) 'Neurocognitive function after radiotherapy for paediatric brain tumours', *Nature Reviews Neurology*. Nature Publishing Group, 8(10), pp. 578–588. doi: 10.1038/nrneurol.2012.182.

Panagiotakos, G. *et al*. (2007) 'Long-term impact of radiation on the stem cell and oligodendrocyte precursors in the brain', *PLoS ONE*, 2(7). doi: 10.1371/journal.pone.0000588.

Parent, J. M. *et al*. (1999) 'Inhibition of dentate granule cell neurogenesis with brain irradiation does not prevent seizure-induced mossy fiber synaptic reorganization in the rat', *Journal of Neuroscience*, 19(11), pp. 4508–4519. doi: 10.1523/jneurosci.19-11-04508.1999.

Peiffer, A. M. *et al*. (2014) 'Radiation-induced cognitive impairment and altered diffusion tensor imaging in a juvenile rat model of cranial radiotherapy', *International Journal of Radiation Biology*, 90(9), pp. 799–806. doi: 10.3109/09553002.2014.938278.

Peißner, W. *et al*. (1999) 'Ionizing radiation-induced apoptosis of proliferating stem cells in the dentate gyrus of the adult rat hippocampus', *Molecular Brain Research*, 71(1), pp. 61–68. doi: 10.1016/S0169-328X(99)00170-9.

Pocock, J. M. and Liddle, A. C. (2001) 'Microglial signalling cascades in neurodegenerative disease', *Progress in Brain Research*, 132, pp. 555–565. doi: 10.1016/S0079-6123(01)32103-9.

Puntmann, V. O. (2009) 'How-to guide on biomarkers: Biomarker definitions, validation and applications with examples from cardiovascular disease', *Postgraduate Medical Journal*, 85(1008), pp. 538–545. doi:

10.1136/pgmj.2008.073759.

Purdy, J. A. (2008) 'Dose to normal tissues outside the radiation therapy patient's treated volume: A review of different radiation therapy techniques', *Health Physics*, 95(5), pp. 666–676. doi: 10.1097/01.HP.0000326342.47348.06.

Raber, J. *et al.* (2004) 'Radiation-Induced Cognitive Impairments are Associated with Changes in Indicators of Hippocampal Neurogenesis', *Radiation Research*, 162(1), pp. 39–47.

Reddick, W. E. *et al.* (2006) 'Smaller white-matter volumes are associated with larger deficits in attention and learning among long-term survivors of acute lymphoblastic leukemia', *Cancer*, 106(4), pp. 941–949. doi: 10.1002/cncr.21679.

Reinhold, H. S. *et al.* (1990) 'Development of blood vessel-related radiation damage in the fimbria of the central nervous system', *International Journal of Radiation Oncology, Biology, Physics*, 18(1), pp. 37–42. doi: 10.1016/0360-3016(90)90264-K.

Ricci, P. E. *et al.* (2000) 'Effect of voxel position on single-voxel MR spectroscopy findings', *American Journal of Neuroradiology*, 21(2), pp. 367–374.

Robbins, M. *et al.* (2012) 'Imaging Radiation-Induced Normal Tissue Injury', *Radiation Research*, 177(4), pp. 449–466. doi: 10.1016/j.surg.2006.10.010.Use.

Robertson, P. L. (2006) 'Advances in Treatment of Pediatric Brain Tumors', *NeuroRx*, 3(2), pp. 276–291. doi: 10.1016/j.nurx.2006.01.001.

Roman, D. D. and Sperduto, P. W. (1995) 'Neuropsychological effects of cranial radiation: current knowledge and future directions', *International Journal of Radiation Oncology, Biology, Physics*, 31(4), pp. 983–998. doi: 10.1016/0360-3016(94)00550-8.

Saad, S. and Wang, T. J. C. (2015) 'Neurocognitive deficits after radiation therapy for brain malignancies', *American Journal of Clinical Oncology: Cancer Clinical Trials*, 38(6), pp. 634–640. doi: 10.1097/COC.0000000000000158.

Sawada, M., Matsumoto, M. and Sawamoto, K. (2014) 'Vascular regulation of adult neurogenesis under physiological and pathological conditions', 8(March), pp. 1–7. doi: 10.3389/fnins.2014.00053.

Schindler, M. K. *et al.* (2008) 'Aging-Dependent Changes in the Radiation Response of the Adult Rat Brain', *International Journal of Radiation Oncology Biology Physics*, 70(3), pp. 826–834. doi: 10.1016/j.ijrobp.2007.10.054.

Schultheiss, T. E. *et al.* (1995) 'Radiation response of the central nervous system', *International Journal of Radiation Oncology, Biology, Physics*, 31(5), pp. 1093–1112. doi: 10.1016/0360-3016(94)00655-5.

Schultheiss, T. E. and Stephens, L. C. (2009) 'Permanent radiation myelopathy', *The British Journal of Radiology*, 65(777), pp. 737–753. doi: 10.1259/0007-1285-65-777-737.

Scott, J. N. *et al.* (1999) 'Which Glioblastoma Multiforme Patient Will Become a Long-Term Survivor ? A Population-Based Study', pp. 183–188.

Scott, J. N. *et al.* (2002) 'How often are nonenhancing supratentorial gliomas malignant? A population study', *Neurology*, 59(6), pp. 947–949. doi: 10.1212/WNL.59.6.947.

Segal, M. (2010) 'Dendritic spines , synaptic plasticity and neuronal survival : activity shapes dendritic spines to enhance neuronal viability', 31(April), pp. 2178–2184. doi: 10.1111/j.1460-9568.2010.07270.x.

Sherman, J. C. *et al.* (2016) 'Neurocognitive effects of proton radiation therapy in adults with low-grade glioma', *Journal of Neuro-Oncology*. Springer US, 126(1), pp. 157–164. doi: 10.1007/s11060-015-1952-5.

Shi, L. *et al.* (2009) 'Maintenance of white matter integrity in a rat model of radiation-induced cognitive impairment', *Journal of the Neurological Sciences*. Elsevier B.V., 285(1–2), pp. 178–184. doi: 10.1016/j.jns.2009.06.031.

Shukla, G. *et al.* (2017) 'Advanced magnetic resonance imaging in glioblastoma: A

review', *Chinese Clinical Oncology*, 6(4), pp. 1–12. doi: 10.21037/cco.2017.06.28.

Smirniotopoulos G. James, Murphy M. Frances, Rushing F.Elizabeth, R. H. J. and S. W. J. (2007) 'Patterns of Contrast Enhancement in the Brain and Meninges', *Radiographics*, 27(6), pp. 525–552.

Snyder, J. S., Kee, N. and Wojtowicz, J. M. (2001) 'Effects of adult neurogenesis on synaptic plasticity in the rat dentate gyrus', *Journal of Neurophysiology*, 85(6), pp. 2423–2431. doi: 10.1152/jn.2001.85.6.2423.

Squire, L. R., Amaral, D. G. and Press, G. A. (1990) 'Magnetic resonance imaging of the hippocampal formation and mammillary nuclei distinguish medial temporal lobe and diencephalic amnesia', *Journal of Neuroscience*, 10(9), pp. 3106–3117. doi: 10.1523/jneurosci.10-09-03106.1990.

Stollg, G. and Jander, S. (1999) 'The role of microglia and macrophages in the pathophysiology of the CNS', *Progress in Neurobiology*, 58(3), pp. 233–247. doi: 10.1016/S0301-0082(98)00083-5.

Sundgren, P. C. *et al.* (2009) 'Metabolic alterations: A biomarker for radiation induced normal brain injury-an MR spectroscopy study', *Journal of Magnetic Resonance Imaging*, 29(2), pp. 291–297. doi: 10.1002/jmri.21657.

Sundgren, P. C. and Cao, Y. (2009) 'Brain Irradiation: Effects on Normal Brain Parenchyma and Radiation Injury', *Neuroimaging Clinics of North America*. Elsevier Ltd, 19(4), pp. 657–668. doi: 10.1016/j.nic.2009.08.014.

Surma-aho, O. and Jääskeläinen, J. (2001) 'Adverse long-term effects of brain radiotherapy in adult low-grade glioma patients', *Neurology*, 57(11), p. 2151.

Szerlip, N. *et al.* (2011) 'Factors impacting volumetric white matter changes following whole brain radiation therapy', *Journal of Neuro-Oncology*, 103(1), pp. 111–119. doi: 10.1007/s11060-010-0358-7.

Tada, E. *et al.* (2000) 'X-irradiation causes a prolonged reduction in cell proliferation in the dentate gyrus of adult rats', *Neuroscience*, 99(1), pp. 33–41.

doi: 10.1016/S0306-4522(00)00151-2.

Taphoorn, M. J. and Klein, M. (2004) 'Cognitive deficits in adult patients with brain tumours', *The Lancet Neurology*, 3(3), pp. 159–168. doi: 10.1016/S1474-4422(04)00680-5.

Tofilon, P. J. and Fike, J. R. (2000) 'The radioresponse of the central nervous system: a dynamic process.', *Radiation research*, 153(4), pp. 357–70. doi: 10.1667/0033-7587(2000)153[0357:TROTCN]2.0.CO;2.

Twijnstra, A. *et al.* (1987) 'Neurotoxicity of prophylactic cranial irradiation in patients with small cell carcinoma of the lung', *European Journal of Cancer and Clinical Oncology*, 23(7), pp. 983–986. doi: 10.1016/0277-5379(87)90345-2.

Villanueva-Meyer, J. E., Mabray, M. C. and Cha, S. (2017) 'Current clinical brain tumor imaging', *Clinical Neurosurgery*, 81(3), pp. 397–415. doi: 10.1093/neuros/nyx103.

Volpe, B. T. and Hirst, W. (1983) 'The Characterization of an Amnesic Syndrome Following Hypoxic Ischemic Injury', *Archives of Neurology*, 40(7), pp. 436–440. doi: 10.1001/archneur.1983.04050070066017.

Vleeschouwer, S. De (2017) 'Mouse Models of Glioblama', in *Glioblastoma*. 1St edn. Australia, pp. 131–137. doi: 10.1016/B978-0-12-410529-4.00078-4.

Waldman, A. D. *et al.* (2009) 'Quantitative imaging biomarkers in neuro-oncology', *Nature Reviews Clinical Oncology*. Nature Publishing Group, 6(8), pp. 445–454. doi: 10.1038/nrclinonc.2009.92.

Walker, M. D., Strike, T. A. and Sheline, G. E. (1979) 'An analysis of dose-effect relationship in the radiotherapy of malignant gliomas', *International Journal of Radiation Oncology, Biology, Physics*, 5(10), pp. 1725–1731. doi: 10.1016/0360-3016(79)90553-4.

Weber, M. A., Giesel, F. L. and Stieltjes, B. (2008) 'MRI for identification of progression in brain tumors: From morphology to function', *Expert Review of*

*Neurotherapeutics*, 8(10), pp. 1507–1525. doi: 10.1586/14737175.8.10.1507.

Weber, M. A., Zoubaa, S. and Schlieter, M. (2006) 'Erratum: Diagnostic performance of spectroscopic and perfusion MRI for distinction of brain tumors (Neurology (2006) 66, (1899-1906))', *Neurology*, 67(5), p. 920. doi: 10.1212/01.wnl.0000239682.19745.e7.

Wilson, J. X. (1997) 'Antioxidant defense of the brain: a role for astrocytes.', *Canadian journal of physiology and pharmacology*, 75(10–11), pp. 1149–63. Available at: http://www.ncbi.nlm.nih.gov/pubmed/9431439.

Yang, L. *et al.* (2017) 'Pathophysiological Responses in Rat and Mouse Models of Radiation-Induced Brain Injury', *Molecular Neurobiology*, 54(2), pp. 1022–1032. doi: 10.1007/s12035-015-9628-x.

Yazlovitskaya, E. M. *et al.* (2006) 'Lithium treatment prevents neurocognitive deficit resulting from cranial irradiation', *Cancer Research*, 66(23), pp. 11179–11186. doi: 10.1158/0008-5472.CAN-06-2740.

Zhou, H. *et al.* (2011) 'Encephalopathy in a Young Rat Model : Cognitive Dysfunction and Histologic Findings', *AJNR Am J Neuroradiol*, 32, pp. 1795–1800. doi: 10.3174/ajnr.A2643.

# Chapter2

# Chapter-2 Theoretical aspects of Magnetic Resonance Imaging

In this chapter we introduce the fundamental concepts of Nuclear Magnetic Resonance and their application to MRI. We explain the principles of MRI and describe several MRI techniques such as T1, T2, Spin-Echo (SE), and Stimulated-Echo (STE) sequences and their application to DWI. Information has come from multiple sources, such as (Malcolm H. Levitt, 2008),(Van Hecke, Emsell and Sunaert, 2015),(Kȍchli, Weishaupt and Marincek, 2006) and (Chris Guy, 2005).

## 2.1 History of MRI

Nuclear Magnetic Resonance (NMR) has been used as a tool in analytic chemistry, biochemistry and the study of atomic interactions since it was discovered by Isidor Rabi in 1938 (I. I. RABI, J. R. ZACHARIAS, 1938). He subsequently won a Nobel Prize for this work in 1944. Felix Bloch and Edward Mills Purcell shared a Nobel Prize in physics in 1952 for their research showing that spin resonance can be detected among nuclear spins in bulk matter (Hendee and Morgan, 1984). In 1971, the physician Raymond Damadian reported anomalous long NMR relaxation times in excised mouse tumours.

Damadian's experiment was expanded later that year by Lauterbur, who imposed small magnetic field gradients on an NMR spectrum (Mansfield, 1976). Following this discovery, many research groups started developing techniques and systems for spatial imaging. In 1974, the first cross-sectional NMR image of a living mouse was published by Lauterbur (Lauterbur, 1974). Two years later at the University of Nottingham in England, the first NMR image of a human body part was acquired by Peter Mansfield (Hinshaw, Bottomley and Holland, 1977). In 1978, Mansfield and his team developed a mathematical technique to accelerate NMR imaging scan times, which also improved the NMR image quality (Mansfield *et al.*, 1978). In 2004, Paul Lauterbur and Peter Mansfield shared a Nobel Prize awarded for their work in the transformation of NMR from a spectroscopic laboratory tool into a clinical imaging technology(Schwarzschild, 2003). In particular, the work by Mansfield showed how fast imaging could be achieved by MRI. Subsequent developments have tremendously improved MRI and made it applicable for routine clinical practice (Schaeffter, 2005).

## 2.2 Principles of Nuclear Magnetic Resonance

To understand MRI, it is necessary to understand the properties of atoms. Atoms are comprised of three subatomic particles: the proton, the neutron, and the electron. Electrons are negatively charged ($e=1.6021773x10^{-19}$ C), while protons are positively charged and neutrons are electrically neutral. Protons and neutrons create the nucleus of an atom, while electrons orbit around their collective centre (Figure 2.1) (Hendrick, 2008). The diameter of the nucleus is much smaller than the diameter of the atom, typically between 20,000 and 140,000 times smaller.

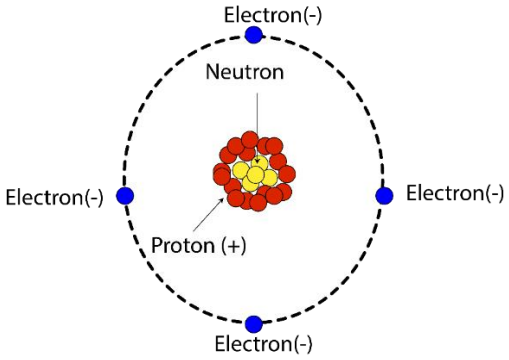


**Figure 2.1: Subatomic particles: electron (-), proton (+) and neutron (neutral).**

The principles of MRI rely on the spin properties of specific nuclei in biological tissues, which are known as MR active nuclei (Table 2.1). The magnetic property depends on the spin associated with the nucleus. Generally, MRI uses the signal from hydrogen nuclei which, in-vivo, are mainly present in the form of water and lipid molecules. The hydrogen nucleus has a spin quantum number I=1/2, giving two spin states of +1/2 and -1/2. This spin generates a magnetic field, thus, hydrogen protons have magnetic moments. Other, nuclei can experience the phenomenon of NMR if they have a non-zero spin angular momentum and magnetic moment (μ). However, nuclei with an even number of protons and neutrons, such as $^{12}C$, result in a zero-spin nuclear spin quantum number $I$=0 and are NMR inactive.

**Table 2.1: Common NMR active nuclei and their nuclear spin (I) and gyromagnetic ratio ($\gamma$).**

| Isotope | Nuclear spin($I$) | Gyromagnetic ratio ($\gamma$) ($rads^{-1}T^{-1}$) |
|---|---|---|
| $^{1}H$ | 1/2 | 267.522 |
| $^{13}C$ | 1/2 | 67.283 |
| $^{19}F$ | 1/2 | 251.815 |
| $^{23}Na$ | 3/2 | 70.808 |
| $^{31}P$ | 1/2 | 108.394 |

## 2.2.1 Spin precession

Both NMR and MRI depend on the interaction between the nuclear magnetic moment ($\mu$) and the applied static magnetic field $B_0$ (Chris Guy, 2005). This interaction of the magnetic moment ($\mu$) of the hydrogen proton with $B_0$ causes precession around the magnetic field (Figure 2.2).

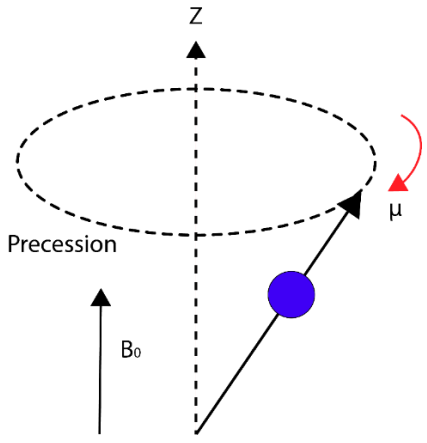


**Figure 2.2: The precession of a proton in a strong magnetic field. ($\mu$) is the spinning magnetic moment and $B_0$ is the external magnetic field.**

The precession frequency depends linearly on the strength of the magnetic field, which is represented by Equation :

**Equation 2.1**

$$\omega_o = \gamma B_o$$

Where $\omega_o$ is the Larmor frequency, γ is the gyromagnetic ratio (hydrogen =267.522 **rads$^{-1}$T$^{-1}$**, which equals 42.58 MHz/T) and $B_0$ is the external magnetic field in Tesla (T).

### 2.2.2 Alignment of spins in $B_0$

In the absence of an external magnetic field, the nuclear magnetic moments are oriented randomly, resulting in zero net magnetisation (Figure 2.3). The spin state is either parallel or anti-parallel to the external magnetic field. The spins at a low energy level are parallel to the main magnetic field (spin-up), while spins at a high energy level are anti-parallel (spin-down). At equilibrium, there are more spins with low energy (parallel) than spins with high energy (anti-parallel).

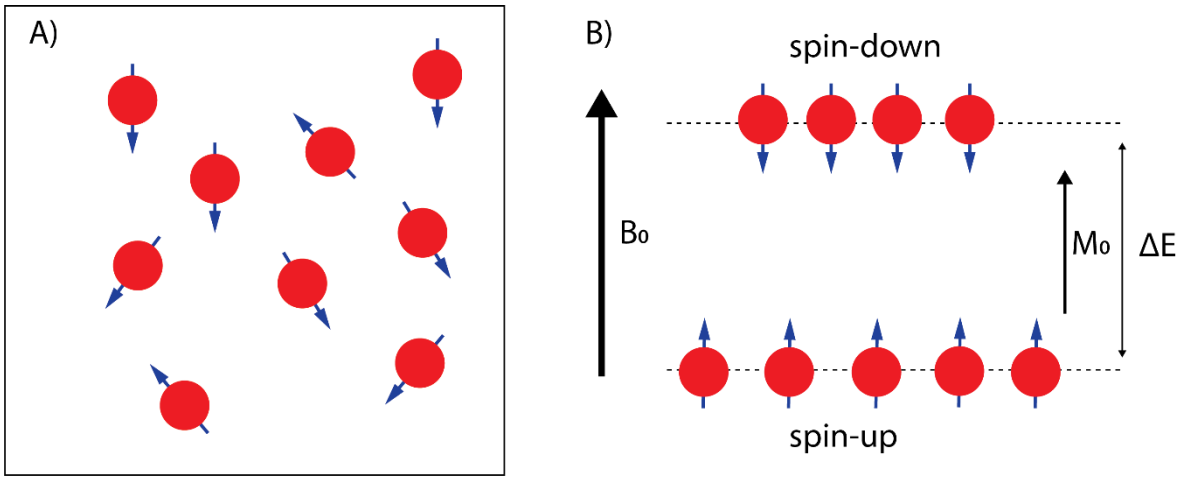


**Figure 2.3: Alignment of NMR spins in the case of *I* = ½. (A) Spins are randomly aligned due to the absence of an external magnetic field, however, each spin precesses about its axis. (B) When an external magnetic field is present, more spins align parallel than anti-parallel to the field, creating a net magnetization, $M_0$.**

The population of spin states is dictated by the Boltzmann distribution (Figure 2.4),

**Equation 2.2**

$$N_{\uparrow}/N_{\downarrow} = e^{-\Delta E/KT}$$

Where $N_{\uparrow}/N_{\downarrow}$ are the populations at different energy levels, K= Boltzmann constant is equal 1.3805 x $10^{-23}$ $JK^{-1}$, and T is the temperature in degrees kelvin.

ΔE is the separation between two energy levels,

The population difference, ΔN between the parallel and anti-parallel states can be determined by this equation.

**Equation 2.3**

$$\Delta N = N_{\uparrow} - N_{\downarrow} = N\left[\frac{1}{1 + e\frac{-h\,\omega_0}{kT}} - \frac{1}{1 + e\frac{h\omega_0}{kT}}\right]$$

Where *h* is Planck's constant, which is equal to 6.62X $10^{-34}$ Js

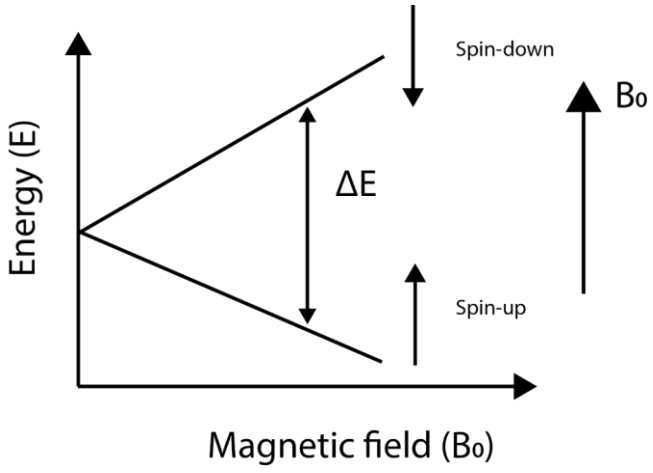


**Figure 2.4: Zeeman splitting shows energy differences between parallel (spin-up) and anti-parallel states (spin-down), with increasing magnetic field $B_0$.**

The energy difference between the spin-up and spin-down states also depends on the magnetic field strength. In other words, the differences in population between the spins increase with increasing magnetic field strength. Thus, as the magnetic field increases, more and more spins align parallel to $B_0$.

The alignment of spins along the direction of the static magnetic field, known as the longitudinal direction or z-axis, results in a net magnetisation ($M_0$) along that direction (Figure 2.5).

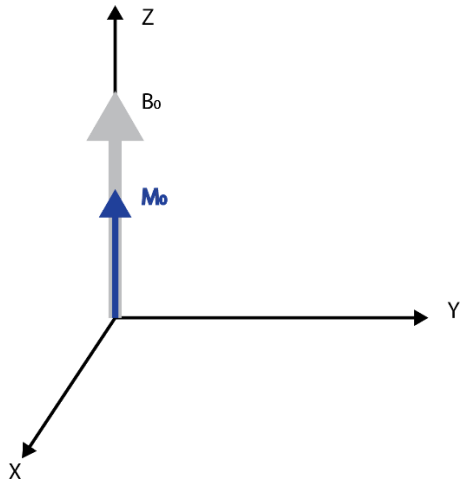


**Figure 2.5: Alignment of $M_0$ with the external magnetic field $B_0$.**

### 2.2.3 Radiofrequency (RF) Excitation

The main result of a Radiofrequency (RF) pulse is that spins are disturbed from their equilibrium state, becoming out of alignment with $B_0$. The disturbance occurs through the transference of energy from the RF pulse to the spin system generating a phase coherence. This phenomenon happens only when the RF pulse has the same frequency as the precessional frequency and is known as resonance (Figure 2.6) (Currie *et al.*, 2013). Consequently, RF pulses are set at or near the Larmor frequency $\omega_0$.

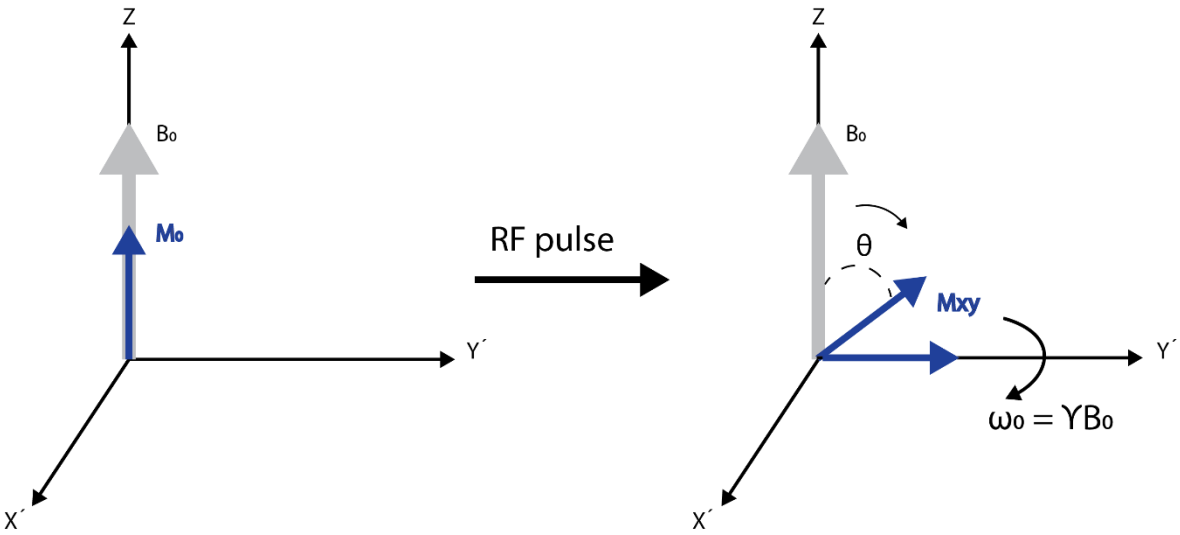


**Figure 2.6: Effect of RF pulse excitation on net magnetisation in laboratory frame.**

In the rotating reference frame, the effect of the RF pulse is to rotate the equilibrium net Magnetisation $M_0$ into the transverse plane (see Figure 2.6). The angle of the RF pulse that rotates the longitudinal magnetisation, $M_0$, is known as the flip angle θ.

### 2.2.4 Signal Generation

Following excitation by a RF pulse, the transverse magnetisation, $M_{xy}$, precesses at the Larmor frequency in the laboratory frame. When a conductive receiver coil is placed in proximity to the sample, a change in voltage is induced across it. This leads to the generation of an electrical current that can be detected as a signal (Figure 2.7) (Currie *et al.*, 2013). The physical principles of this signal generation are derived from Faraday's law of Electromagnetic Induction and are analogous to an electric generator.

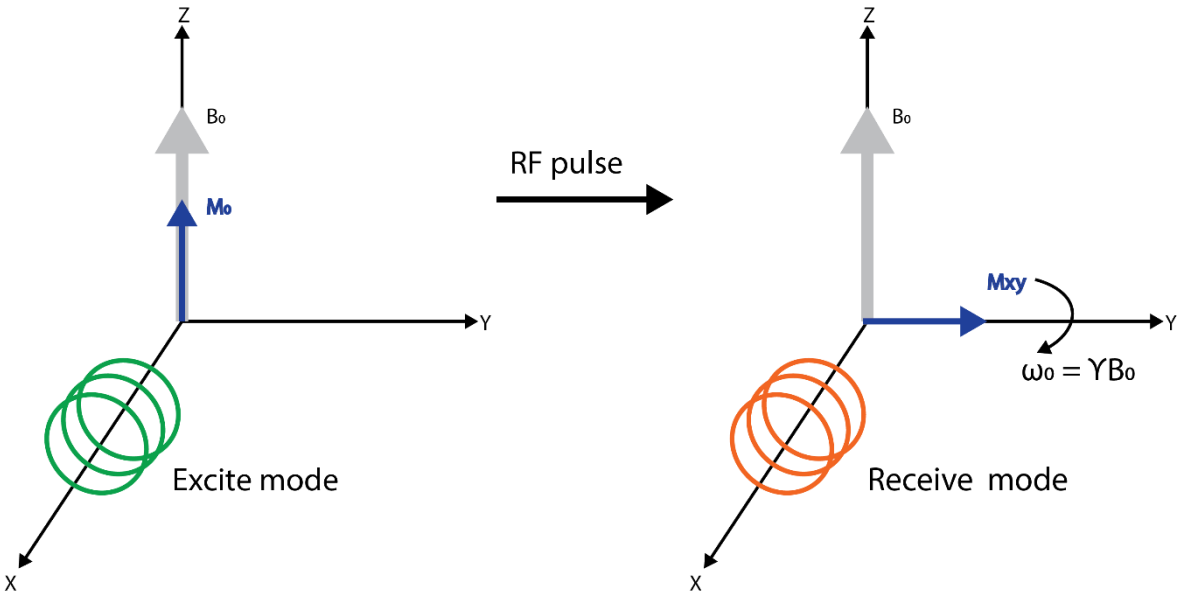


**Figure 2.7: In the laboratory frame, as the net magnetisation, $M_{xy}$, precesses in the xy plane, it induces a voltage in the RF coil.**

This basic pulsed NMR signal, called Free Induction Decay (FID), oscillates sinusoidally with a frequency ($\omega_o$-$\omega_1$). FID is at its greatest magnitude immediately after the RF pulse is switched off, and it decreases due to T2* relaxation (Figure 2.8) (Currie *et al.*, 2013).

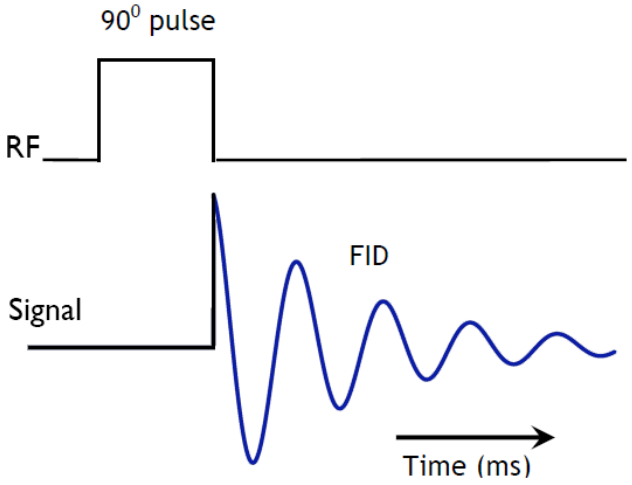


**Figure 2.8: Free Induction Decay (FID) after $90^0$ RF pulse.**

## 2.2.5 Relaxation process of the NMR signal

As soon as the RF pulse is switched off, the individual nuclear magnetic moments start to lose their phase coherence (T2 relaxation) and return to the equilibrium population of spin states (T1 relaxation). This process is called relaxation (Currie *et al.*, 2013)(Figure 2.9).

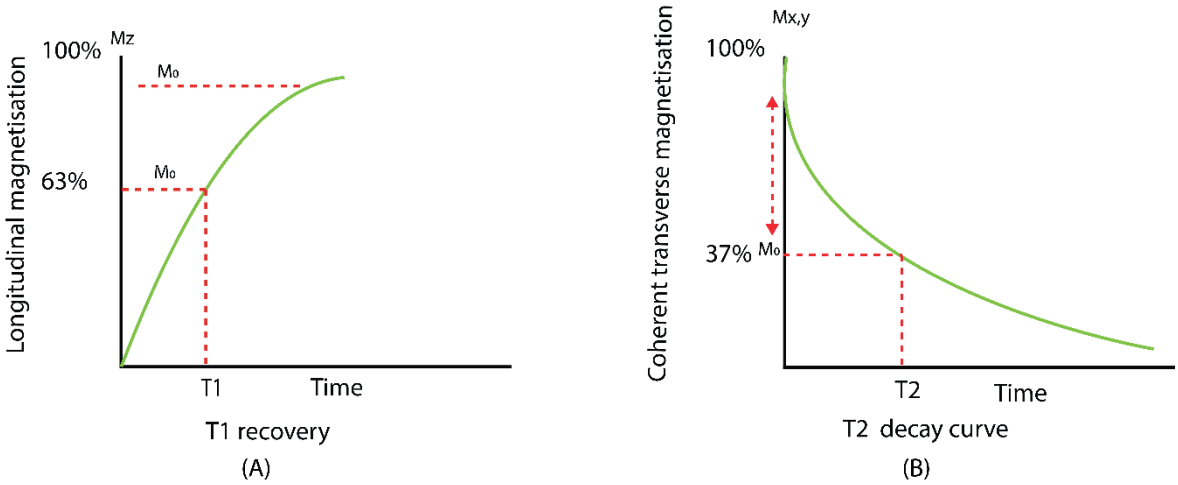


**Figure 2.9: (A) longitudinal recovery curve that represents the exponentially increasing longitudinal component of the net magnetisation. (B) T2 decay curve, which represents the decay of magnetisation in the transverse plane.**

### 2.2.5.1 Longitudinal relaxation (T1)

The process whereby the spin system begins to exchange energy with its surroundings to return to its equilibrium state is termed T1 relaxation. This process depends on the tumbling rate of the molecule in which the spins reside. A fluctuating local magnetic field, to which spins in neighbouring molecules are subjected, is generated due to the tumbling molecules. When the frequency component of this oscillating local magnetic field matches the Larmor frequency, it can drive transitions between energy levels. Following inversion, the exponential growth of longitudinal magnetisation due to T1 relaxation is described by:

**Equation 2.4**

$$M_z = M_0\,(1 - 2e^{(-\frac{t}{T1})})$$

Different molecules have different T1 relaxation times as a result of their different tumbling rates and the properties of the surrounding tissue. The energy exchange between spins and their surroundings is also known as spin-lattice relaxation or longitudinal relaxation (Currie *et al.*, 2013).

#### 2.2.5.2 Transverse relaxation (T2)

Following excitation, the individual nuclear magnetic moment starts to lose its phase coherence leading to loss of the transverse component of the net magnetisation to decay with time. This is known as transverse relaxation or spin-spin relaxation. The T2 relaxation time of the tissue is the exponential time constant of the decay. The amount of transverse magnetisation, $M_{xy}$, present at time t, is given by the following equation.

**Equation 2.5**

$$\boldsymbol{M_{x,y} = M_0\, e^{\left(-\frac{t}{T2}\right)}}$$

#### 2.2.5.3 T2* relaxation (field inhomogeneity)

In addition to spin-spin interaction, inhomogeneity of the $B_0$ magnetic field also contributes to the decay of the $M_{xy}$ component with relaxation time constant (T2' relaxation). The combined effects of both spin-spin interaction and field inhomogeneity increase the rate of signal loss and the net decay is described by T2* relaxation, which is always shorter than T2.

**Equation 2.6**

$$\boldsymbol{\frac{1}{T2^*} = \frac{1}{T2} + \frac{1}{T2'}}$$

The magnetic field inhomogeneities may be the result of the differences in the magnetic susceptibility of different tissue components when placed in a magnetic field.

## 2.2.6 Spin Echo (SE)

The loss of phase coherence can be recovered in some circumstances. SE is recognised as one of the most basic methods for recovering phase coherence. For excitation, the SE sequence uses a slice selective $90^0_x$ RF pulse. Following the excitation pulse, transverse magnetisation decays with T2*. Dephasing of spins occurs due to the faster precessing of some spins than others, owing to static magnetic field inhomogeneities, which are always present. A second $180^0_y$ RF pulse is applied to refocus the spins (Weishaupt and Marincek, 2008). The spin rephasing process, creates a spin echo signal at the Echo Time TE (TE), which is the time from the middle of the $90^0$ RF excitation pulse to the appearance of the centre of the echo, while Repetition Time (TR) indicates the time between repetitions of the $90^0$ excitation pulses (Figure 2.10).

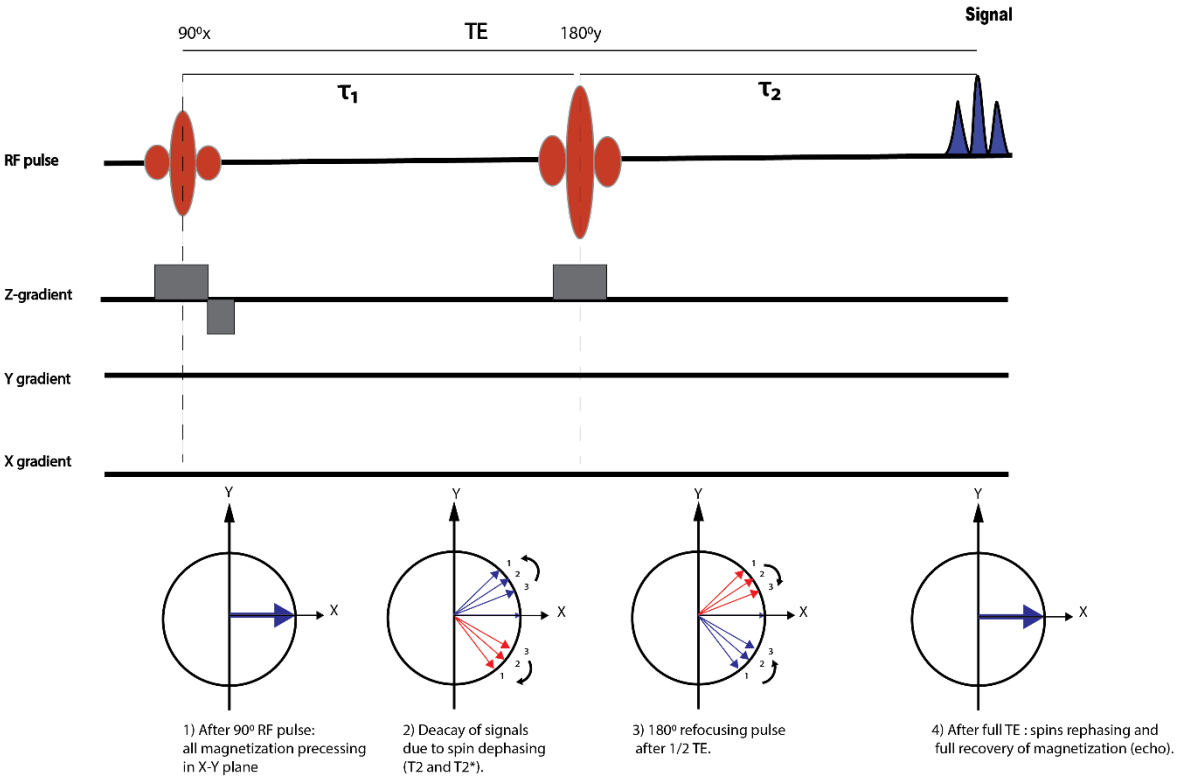


**Figure 2.10: Spin Echo (SE) pulse sequence diagram and the excitation ($90^0$) and refocused ($180^0$) RF pulses. Spins showing in the rotating frame.**

### 2.2.7 Stimulated echo imaging

A limitation of the spin-echo sequence is that these signal experiences T2 relaxation, which, in biological tissue, is considerably faster than T1 relaxation (Demberg *et al.*, 2019). Hence, at longer echo-times the spin-echo will lose most of its signal. An alternative is the STE sequence which uses three RF pulses, where the signal decays with the longer T1 relaxation time (Derek K. Jones, 2011). As a result, there is no need for a $180^0$ RF pulse, thereby eliminating a variety of problems associated with a conventional SE imaging (e.g. Specific Absorption Rate (SAR) level). Three $90^0$ RF pulses are the basic pulse sequence that give rise to a stimulated echo signal that was first described by Hahn in 1950 (Hahn, 1950) and later used for NMR diffusion measurements (Experiments, 2004)(Method and Diffusion, 2003). The stimulated echo pulse sequence is shown in Figure2.11. The first $90^0_{-x}$ RF pulse will tip the net magnetization along the -y-axis, giving the spins a phase coherence. However, inhomogeneities of the magnetic field result in a dephasing of this transverse magnetization. The second $90^0_x$ RF pulse has the effect of rotating the y components of the magnetization along the z-axis. This magnetization is stored in the longitudinal direction and experiences T1 relaxation. The stored magnetization along the z-axis will return to the transverse plane after the application of the third $90^0_{-x}$ RF pulse. A STE then forms.

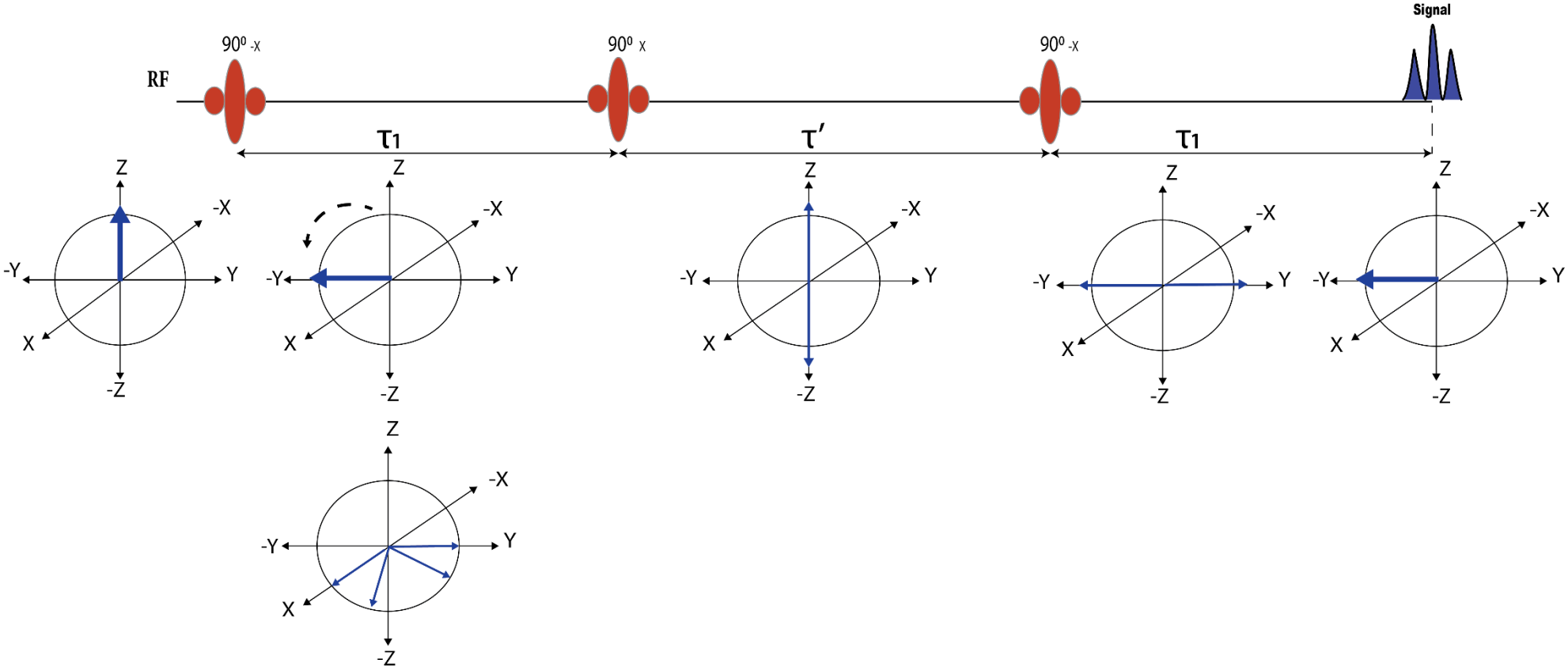


**Figure2.11: The formation of Stimulated Echo by three $90^0$ RF pulses. After the second $90^0$ RF pulse, we consider that the Z component is not precessing, but growing, due to T1 relaxation. The stored longitudinal components are flipped back into the transverse plane by the third $90^0$ RF pulse, leading to rephasing and stimulated echo formation.**

## 2.3 MRI system

### 2.3.1 Main magnet

A main static magnetic field, $B_0$, is required for MRI experiments. The magnetic field should be homogenous and stable over time. Large magnetic fields lead to a large net magnetisation that, in turn, lead to a larger MRI signal. Superconducting coils are used to produce the main magnetic field. When a superconducting material is cooled substantially, resistance to the flow of the electrical current can be reduced to a negligible level. This allows a high electrical current to produce a high magnetic field strength with little heat dispersion. This principle is employed in the generation of superconducting magnets. The main magnet coil typically used in MRI systems is made of a superconducting metal, with alloy coils being cooled using liquid helium (~4 K or -269 $^0$C ) (Jacobs, Ibrahim and Ouwerkerk, 2007). A strong magnetic field ($B_0$) is generated by the main magnet coils to which the patient is exposed. Tesla (T) is the unit of the strength of the magnetic field which is 20,000 times greater than Earth's magnetic field (Currie *et al.*, 2013).

### 2.3.2 Shim coils

Because of the magnetic susceptibility of the sample, the main magnetic field inside the bore of the magnet is altered. Shim coils are an additional set of coils that are used to improve the homogeneity of the magnetic field over the sample. By adjusting the current sent through these shim coils, the homogeneity of the magnetic field is optimised.

### 2.3.3 Gradient system

A MR system uses a set of gradient coils to define the direction of the magnetic field gradients. Three orthogonal directions (X, Y and Z) are represented by gradient coils (Figure 2.12), which lie concentrically within the main magnet. Gradient coils are not supercooled and are operated at close to room temperature. Gradient coils generate magnetic fields that are superimposed onto the main $B_0$ field (Currie *et al.*, 2013). The magnetic field of theses gradients can be defined according to the following equation:

**Equation 2.7**

$$G_x = \frac{\partial B_z}{\partial x}\,, \qquad G_y = \frac{\partial B_z}{\partial y}\,, \qquad G_z = \frac{\partial B_z}{\partial z}$$

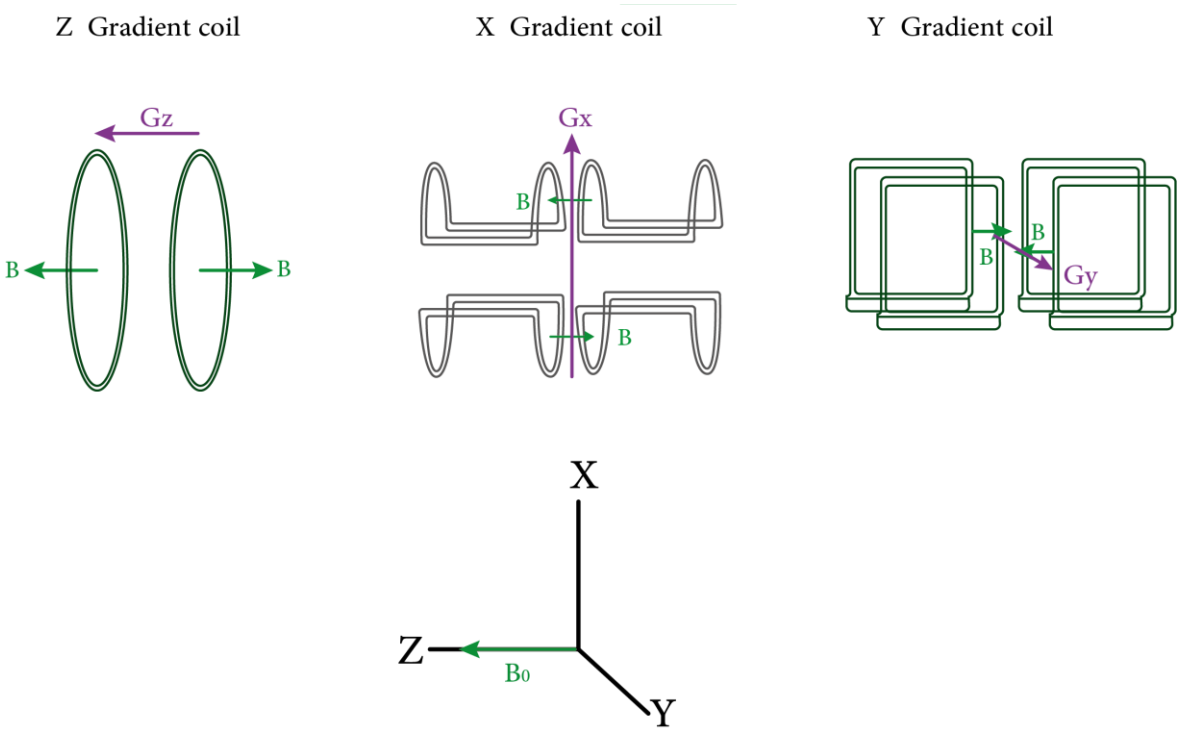


**Figure 2.12: Coil arrangements used to create magnetic field gradients in the X, Y and Z directions.**

Important parameters for gradient specification are the amplitude, slew rate and rise time. The amplitude of the gradient is also known as gradient strength and is defined as Tesla per metre or Gauss per centimetre, with 10 mT/m= 1 G/cm. The gradient system of the 7T Bruker MRI system used in this thesis had a maximum strength of 400 mT/m. The time that the gradient needs to reach its maximum strength is called the rise time and is measured in milliseconds. The slew rate of the gradient is defined as the ratio of the gradient strength divided by the rise time. It is measured in Tesla per metre per second (Jacobs, Ibrahim and Ouwerkerk, 2007).

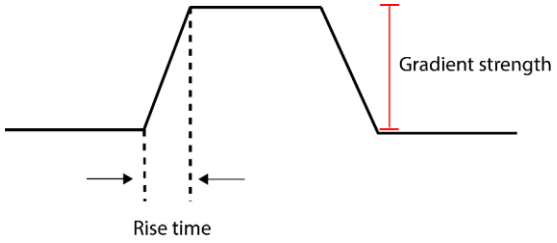


**Figure 2.13: Gradient rise time.**

### 2.3.4 RF coils

RF coils are usually designed as either volume coils (e.g. birdcage coil) or surface coils. Modern coils have parallel-transmit or phased-array receive configurations. There are two purposes for the use of RF coils: to transmit the RF energy to the tissue of interest and to receive the RF signal (Jacobs, Ibrahim and Ouwerkerk, 2007). RF coils are placed concentric to each other and to the gradient coil system There are several types of RF coils, some of them being used either as a transmitter or receiver while others are a combination of both transmitters and receivers (Jacobs, Ibrahim and Ouwerkerk, 2007) (Figure 2.14). For the work presented in this thesis, a 72 mm inner diameter birdcage coil was used for transmitting and a 4-channel phased array mouse brain surface coil for receiving.

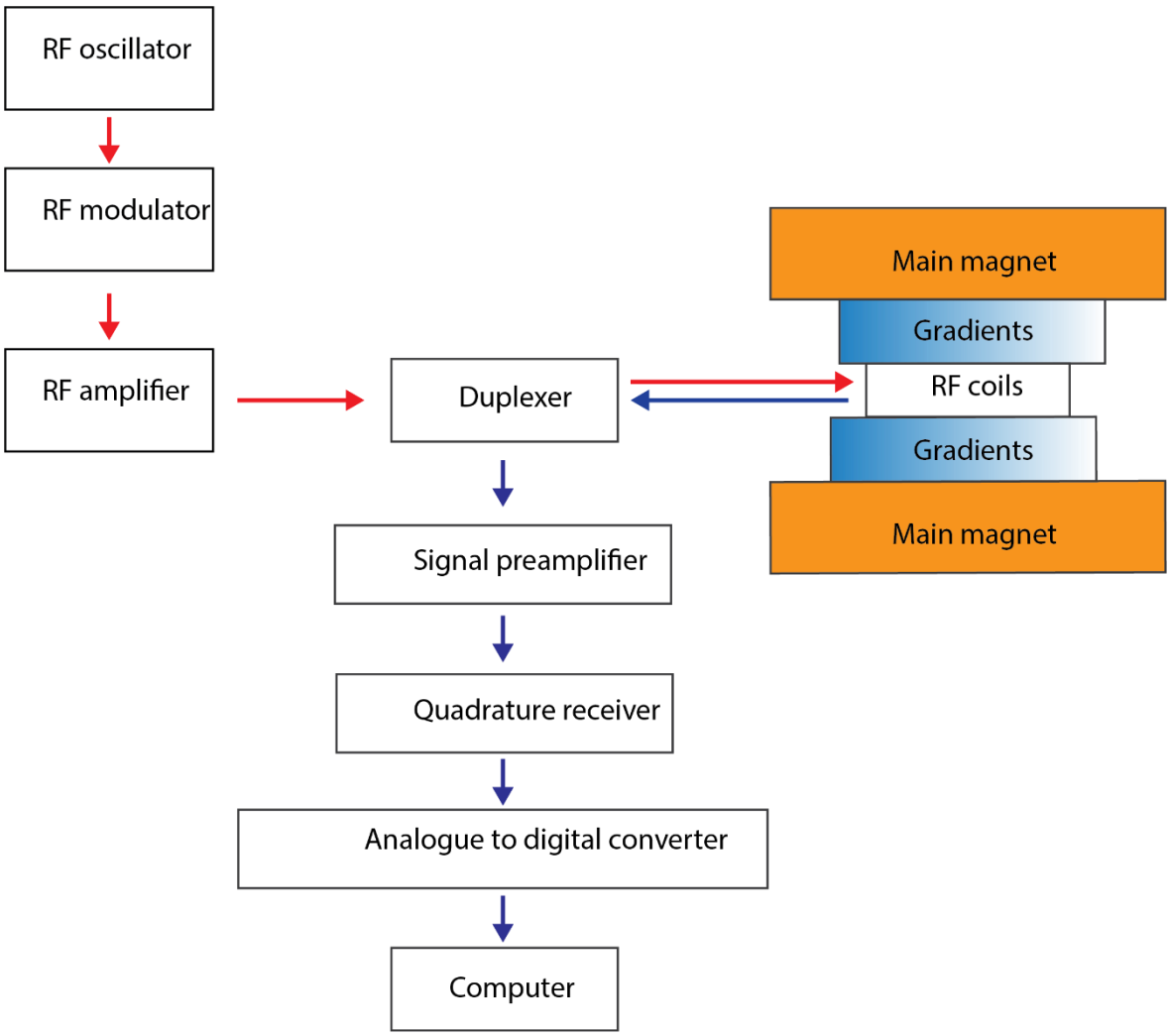


**Figure 2.14: Schematic diagram of electronics involved in formation of an MR image. Transmitter and receiver sections are indicated by red and blue colours, respectively.**

#### 2.3.4.1 RF oscillator

A RF oscillator produces an oscillating voltage at a well-defined frequency. The base frequency of the RF oscillator on our 7T Bruker MRI system was 300 MHz, with a potential range from 200 MHz to 400 MHz.

#### 2.3.4.2 RF modulator

Modulation of the amplitude of the RF pulses over time is the main purpose of the RF modulator. Different shaped RF pulses are used to selectively excite the spins inside a slice, leading to better defined slice profiles.

#### 2.3.4.3 RF amplifier

The RF amplifier amplifies the shaped RF pulse, in order to produce a large amplitude RF pulse for transmission to the RF coil. Our 7T Bruker system used a 1000 W RF amplifier.

#### 2.3.4.4 Duplexer

A Duplexer performs two main tasks. First, it directs the high power (amplifier) RF pulse to the RF coil. Next, the duplexer directs the weak MR signal to the receiver section. The duplexer protects the sensitive electronic components in the receiver section from the high-power RF pulse generated in the transmitter. Finally, the entire produced signal is sent to the receiver section.

#### 2.3.4.5 Signal amplifier

The weak RF signal that is generated by the nuclear spins of the sample is directed to the preamplifier to scale it to a conventional voltage level. Hence, the preamplifier is always kept close to the main magnet to reduce any signal loss.

#### 2.3.4.6 Quadrature receiver and analogue to digital converter

The raw MR signal is converted from its high frequency (e.g. 300 MHz) to a lower frequency (kHz) to allow analogue-to-digital conversion. The conversion happens by comparing the raw MR signal with a reference signal from the RF oscillator. The analogue-to-digital converter then converts the signal into digital form where it

can be processed by the computer. Our 7T Bruker system converts the analogue MRI signal into a 16-bit digital signal.

#### 2.3.4.7 Computer

An operator console is connected to the computer system to enable operator input, scan choice and pulse sequence selection. To control gradients, RF transmitter and receiver functions, the computer is connected to a real-time operating system. Image reconstruction is also handled by the computer.

## 2.4 MR Imaging

#### 2.4.1.1 Slice selection

Localisation of the RF excitation pulse is the initial step in MRI. It is accomplished by using a frequency selective pulse in conjunction with a slice selection gradient ($G_{ss}$). The slice orientation is determined by the combination gradient directions (X, Y and Z) used, while the slice thickness and position are determined by both gradient amplitude and specific RF pulse characteristics (Brian M. Dale, Mark A. Brown and Richard C. Semelka, 2015). After slice selection, all spins will precess with the same frequency (Larmor frequency). If a field gradient is applied perpendicular to the z-axis and the slice selection uses the z-gradient, spins will experience a magnetic field at the given position, Z.

**Equation 2.8**

$$\boldsymbol{B = B_0 \ + G_z \, Z}$$

With the gradient applied, the Larmor frequency becomes dependent on the spin's position along the z-axis

**Equation 2.9**

$$\boldsymbol{\omega = \ \gamma(B_0 + G_z \, Z)}$$

The frequency selective RF pulse will, therefore, excite a slice containing nuclei with the same bandwidth frequencies. By adjusting the magnitude of the field gradient, Gz, and the bandwidth of the RF pulse, Δω, the thickness of the slice can be changed (Chris Guy, 2554).

**Equation 2.10**

$$\Delta Z = \frac{\Delta \omega}{\gamma G_z}$$

#### 2.4.1.2 Frequency encoding (Readout)

After the RF pulse is switched off, a spatial encoding gradient is applied along the frequency encoding direction. This magnetic field gradient leads the magnetisation at different positions to precess at different frequencies depending on their position, thus labelling their spatial position along the frequency encoding direction (Brian M. Dale, Mark A. Brown and Richard C. Semelka, 2015).

#### 2.4.1.3 Phase encoding

The phase encoding direction is visualised, in addition to the readout direction, in a two dimensional (2D) image (Brian M. Dale, Mark A. Brown and Richard C. Semelka, 2015). When the phase encoding gradient is applied, some spins will precess faster than others. This creates phase differences into magnetisation, depending on the spins' position within the gradient, due to the linearly varying magnetic field gradient along the phase encoding direction. For each excitation acquisition, the acquired data forms a single line of the raw matrix in the K-space, as the phase encoding step is performed (Currie *et al.*, 2013).

## 2.5 Image reconstruction

### 2.5.1 k-space

The data obtained from the read and phase gradients are spatially encoded in K-space and stored in a matrix format. k-space is a two-dimensional array ($K_x$, $K_y$). Kx is the horizontal axis and corresponds to the time points in the readout direction, while Ky, the vertical axis, corresponds to the phase encoding direction. The highest signal is in the centre of k-space, and it is filled with the low-frequency component of the bulk image (Weishaupt and Marincek, 2008). A low signal is obtained at the edge of k-space, which corresponds to the high frequency components that contain the fine details of the image (Jacobs, Ibrahim and Ouwerkerk, 2007)(Figure 2.15).

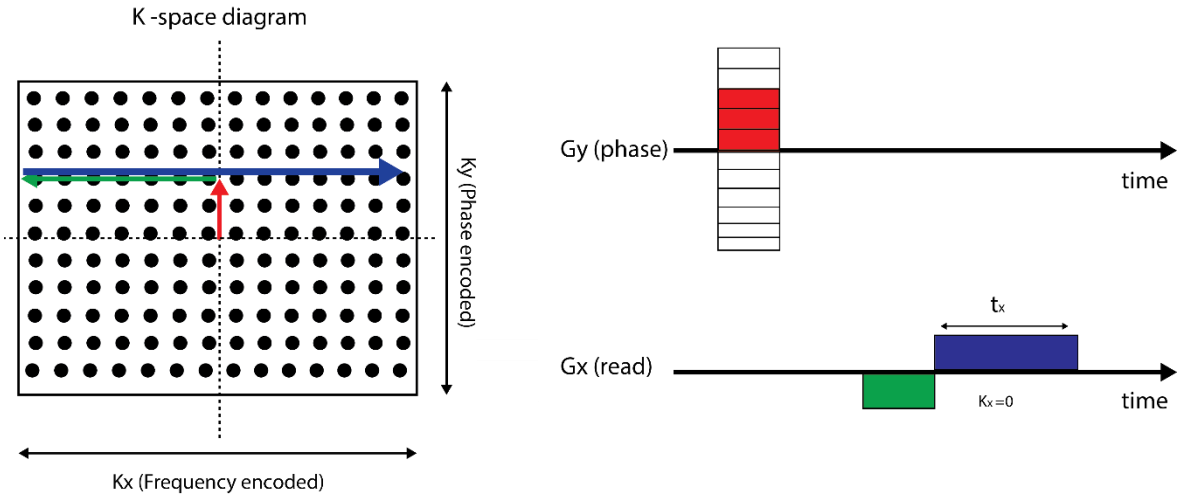


**Figure 2.15: Echoes are stored in K-space following analogue-to-digital conversion. The x and y direction gradients are responsible for the frequency (read) and phase encoding, respectively.**

## 2.6 MRI diffusion

### 2.6.1 Physics of diffusion

Robert Brown, in 1828, was the first person who described the random movement of particles within a fluid. This is known as diffusion or Brownian motion (Brown, 1828).

The physical law that describes the phenomenon of diffusion is called Fick's law. It is related to the diffusive flux between different concentrations and is expressed by the formula below:

**Equation 2.11**

$$\boldsymbol{J = -D\nabla C}$$

Where *J* is the vector or the net flux, C is the concentration and D is the diffusion coefficient. According to Fick's law, in any region, molecules with different levels of concentration tend to move from high to low concentration levels (Figure 2.16).

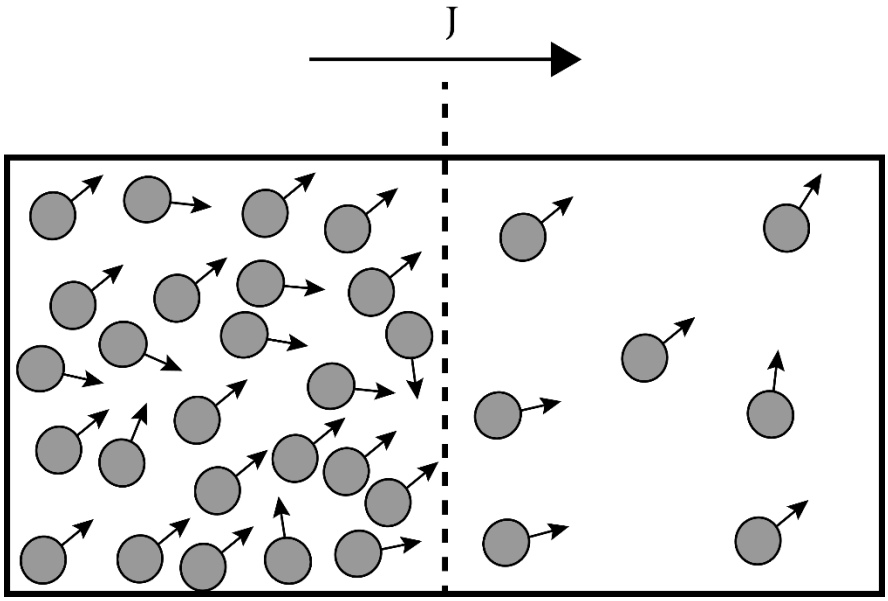


**Figure 2.16: Different regions with different molecular concentrations and molecules moving from high to low concentrations, leading to flux.**

Later, Albert Einstein's law characterised the relationship between the mean squared displacements of ensemble and its self-diffusion coefficient D (Einstein, 1905), which is characterised by the formula:

**Equation 2.12**

$$X^2 = 6D\Delta$$

Where $X^2$ is the mean square of the particle's displacement during the time of diffusion Δ and D is the diffusion coefficient (Figure 2.17).

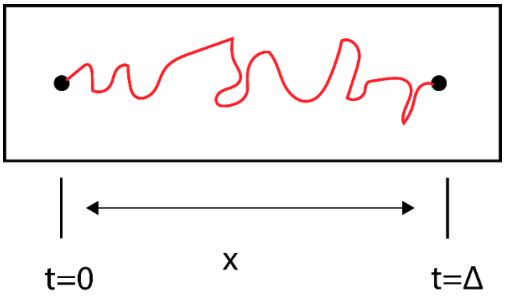


**Figure 2.17: Free diffusion displacement moving from two points.**

Because the tissue microstructure is affected by the diffusion of water molecules, when the square mean displacement is plotted as a function of time, t, deviation from Einstein's law is observed (Figure 2.18).

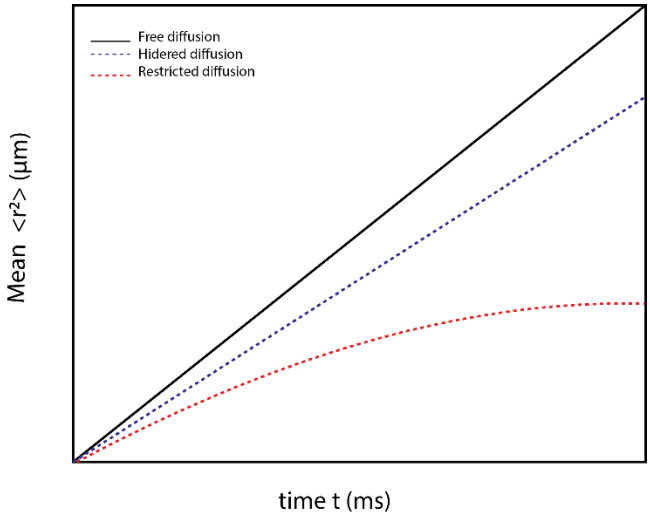


**Figure 2.18: Mean square displacement of water molecules for free, hindered and restricted diffusion.**

## 2.6.2 Basic principles of Diffusion MRI

Diffusion-Weighted MRI (DW-MRI) is a special technique that is particularly sensitive to the microscopic motion of water molecules. Based on their water diffusion properties, DW-MRI allows for non-invasive characterisation of the biological tissue (Chenevert *et al.*, 2002). A standard method of measuring diffusion was developed by Stejskal and Tanner in 1965 known as Pulse Gradient Spin Echo (PGSE) (Stejskal and Tanner, 1965). DW-MRI experiments involved the adaptation of the standard T2 weighted image sequence by adding a symmetrical pair of diffusion bipolar sensitizing gradients around the $180^0$ refocusing pulse. This is the basic approach for many DWI sequences used today (Figure 2.19) (Koh and Collins, 2007).

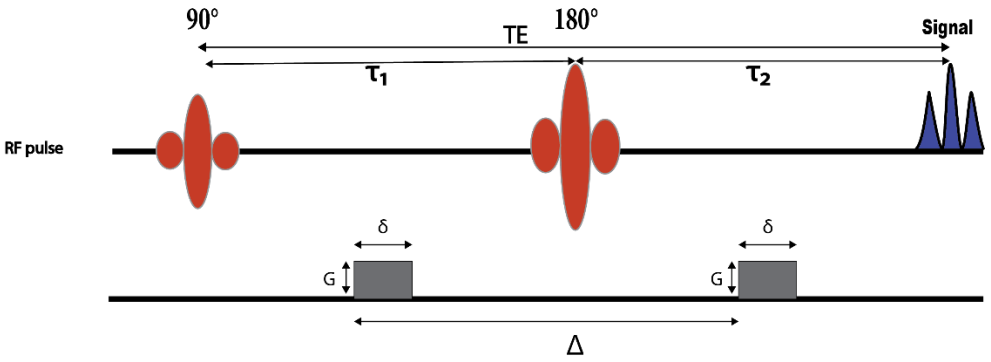


**Figure 2.19: Schematic representation of a PGSE sequence where Δ is the time between the onsets of the two gradients (observation time), G is the gradient strength and δ is the pulse gradient duration.**

Typically, a PGSE sequence is applied using $90^0$ and $180^0$ RF pulses, denoted as $90_x$ and $180_y$. Molecules, both static and moving, acquire phase shift information, due to the presence of the first gradient. However, for static spins that information will be rephased by the second pair of the diffusion gradients, leading to non-significant changes in the measured signal intensity. Moving molecules acquire phase shift information from the first diffusion gradient and their signals are not completely rephased by the second gradient. This leads to signal loss. Consequently, the attenuation of the measured signal intensity at DWI is sensitive to the motion of water molecules (Koh and Collins, 2007). The reduction in signal,

due to diffusion of spins while the gradients are applied, is calculated as follows in the equation.

**Equation 2.13**

$$S = S_0 \, e^{-(\gamma^2 \, G^2 \, \delta^2 \left(\Delta - \frac{\delta}{3}\right) D}$$

Which can be written in terms of the *b* value as:

**Equation 2.14**

$$S = S_0 \, e^{-bD}$$

**Equation 2.15**

$$b = \gamma^2 \, G^2 \, \delta^2 \, (\Delta - \delta/3)$$

Where **S** is the signal, $S_0$ is the signal when zero gradient is applied, **δ** is the gradient duration, **Δ** is the time between gradients, **G** is the gradient strength and **D** is the diffusion constant. The ***b*** value (factor) controls the three parameters (**G,** **δ** and **Δ**) that control the amount of diffusive attenuation of the signal.

### 2.6.3 Apparent Diffusion Coefficient

The apparent Diffusion Coefficient (ADC) can be generated by the measurement of diffusion coefficient in three orthogonal directions (Dx, Dy, Dz).

**Equation 2.16**

$$ADC = \frac{D_x + D_y + D_z}{3}$$

ADC calculations requires at least two *b* values. In a clinical setting, for example, usually the two *b* values are used (0 and 1000 s/mm$^2$). Diffusion can be measured as the slope of a linear regression after performing a linear fit between $\ln(S/S_0)$ and *b* (Figure 2.20) (Le Bihan *et al.*, 1986).

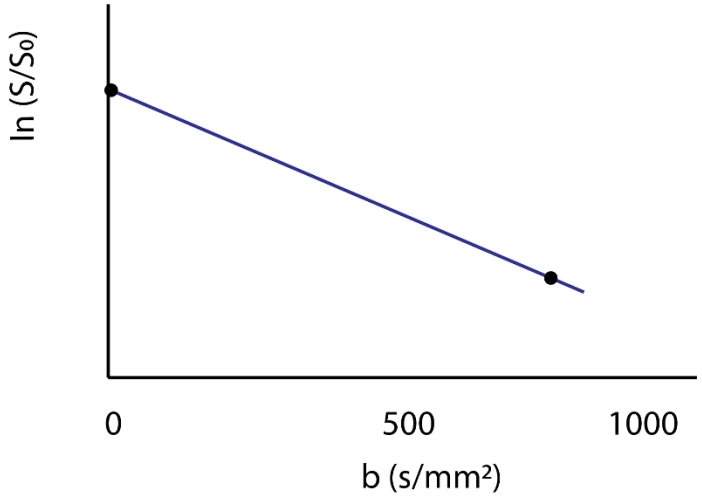


**Figure 2.20: Single exponential decay curve of water signal in MR. Diffusion coefficient is represented by the slope of the line.**

## 2.7 Diffusion Weighted Imaging (DWI)

### 2.7.1 Spin- Echo DWI

Spin-echo DWI is the most common method to sensitise an MRI signal to molecular diffusion. It comprises a spin echo pulses ($90^0$ and $180^0$ RF pulse) with field gradient pulses before and after the refocusing $180^0$ RF pulse. As illustrated in Figure 2.19, the first $90^0$ RF tipped the net magnetisation into the transverse plane and, due to the variation of the frequency along the gradient, the first gradient dephases the spins, encoding the phase according to the initial spatial position. The $180^0$ RF rotates the magnetisation around the y-axis and is rephased by the second gradient (Hecke, Emsell and Sunaert, 2016) to produce the echo or signal. The decay of the signal results in the T2 relaxation process. This dephases the nuclear spins again, leading to a decrease in the net transverse magnetization. Thus, only a limited range of observation times (20-80 ms) can be used before all of the signal is lost.

### 2.7.2 Stimulated Echo Acquisition Mode

To achieve DWI contrast with a Stimulated Echo Acquisition Mode (STEAM) pulse sequence, three $90^0$ RF excitation pulses must be used with two diffusion encoding gradients. The first diffusion-encoding gradient must be placed between the first and second $90^0$ RF pulses, while the second diffusion encoding gradient must be

placed after the third $90^0$ RF pulse (Figure 2.21), (Bammer, 2003). Therefore, between the second and third $90^0$ RF pulses, a mixing time occurs and becomes part of the diffusion time. Importantly, following the second $90^0$ RF pulse, the magnetization is stored in the longitudinal direction and experiences T1 relaxation. Application of the third $90^0$ RF pulse will return the stored magnetization along the z-axis to the transverse plane and at time TE ($\tau_1+\tau_2$) the STE forms. A disadvantage of STEAM is that half of the signal is immediately lost. To study slow diffusion rates, or to compensate for the unavailability of large diffusion gradients, the longer diffusion time of sequences, such as STEAM, is useful. In fact, for tissues with a short T2, or when a spin echo cannot be used, STE is primarily used (McMahon, 2014).

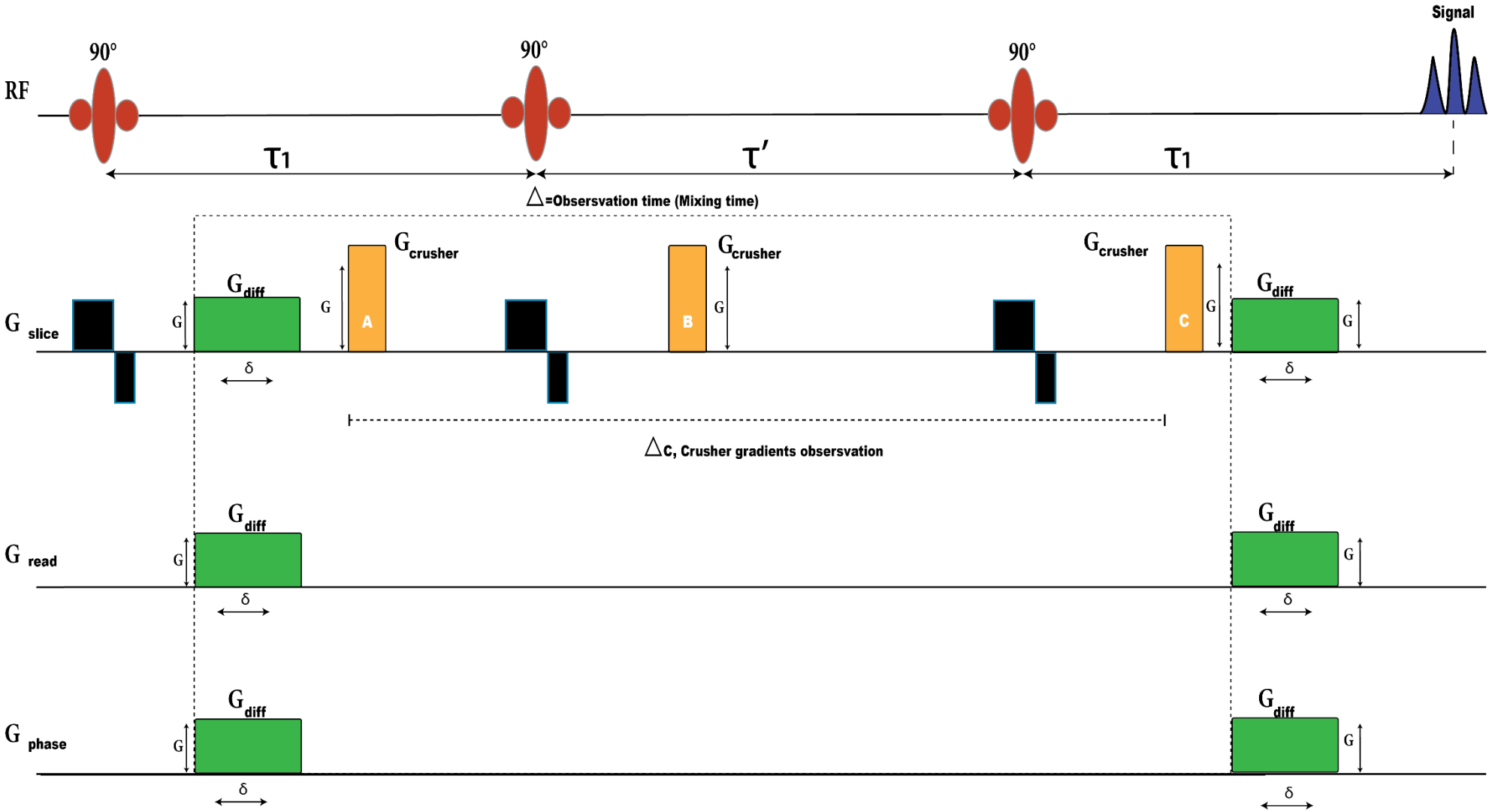


**Figure 2.21: STEAM pulse sequence.**

### 2.7.3 Multiple *b* value DWI

Usually two *b* values are used in DWI examinations, based on the theory that the relationship between the MR signal and *b* factor is mono-exponential (Liu and Xiao, 2013). However, if multiple high *b* values are used in DWI, bi-exponential decay curve better describes signal decay (Niendorf *et al.*, 1996) (Mulkern *et al.*, 1999). In a bi-exponential model, there are two diffusion compartments: fast and slow. Researchers assume that fast diffusion represents the extracellular space components, while slower diffusion represents the intracellular spaces (Bui *et al.*, 1999) (Buckley *et al.*, 1999). When the *b* value increases, there is a noticeable progressive change between brain regions and an overall drop in ADC (Bashat *et al.*, 2005)(Burdette *et al.*, 2001)(Yoshiura *et al.*, 2001)(DeLano *et al.*, 2000). In fact, this drop in ADC can be better explained by the biexponential model and cannot be adequately interpreted by monoexponential diffusion in tissue (Bashat *et al.*, 2005)(DeLano *et al.*, 2000)(Yoshiura *et al.*, 2001)(Clark and Le Bihan, 2000). It is more difficult to detect true diffusive motion at very low *b* value ($b$<100 s/mm$^2$), where the measurement can be affected by local blood flow, this is termed the intra voxel incoherent motion (IVIM) effect (Yacoub *et al.*, 2008). In fact, diffusion weighting is directional , hence, the attenuation depends on the diffusion and flow parameters along the applied direction (Miller *et al.*, 2007). Consequently, there is an argument that the signal at higher *b* values represents a true diffusion effect rather than a vascular effect with significant onset delay (Le Bihan *et al.*, 2006).

### 2.7.4Diffusion Tensor Imaging (DTI) and anisotropic diffusion

The displacement of water molecules can be modelled as a sphere and described by a single isotropic diffusion coefficient, when the water molecules move randomly in all directions (Le Bihan *et al.*, 2001). Diffusion is a three-dimensional process; the molecular mobility may not be same in all directions, which is known as anisotropy. This anisotropic diffusion may be due to the physical arrangement of the medium (e.g. liquid crystal) or due to the impedance of diffusion in some directions, a result of the presence of some obstacles (Derek K. Jones, 2011). Hence, diffusion can be more prevalent in one particular direction than others.

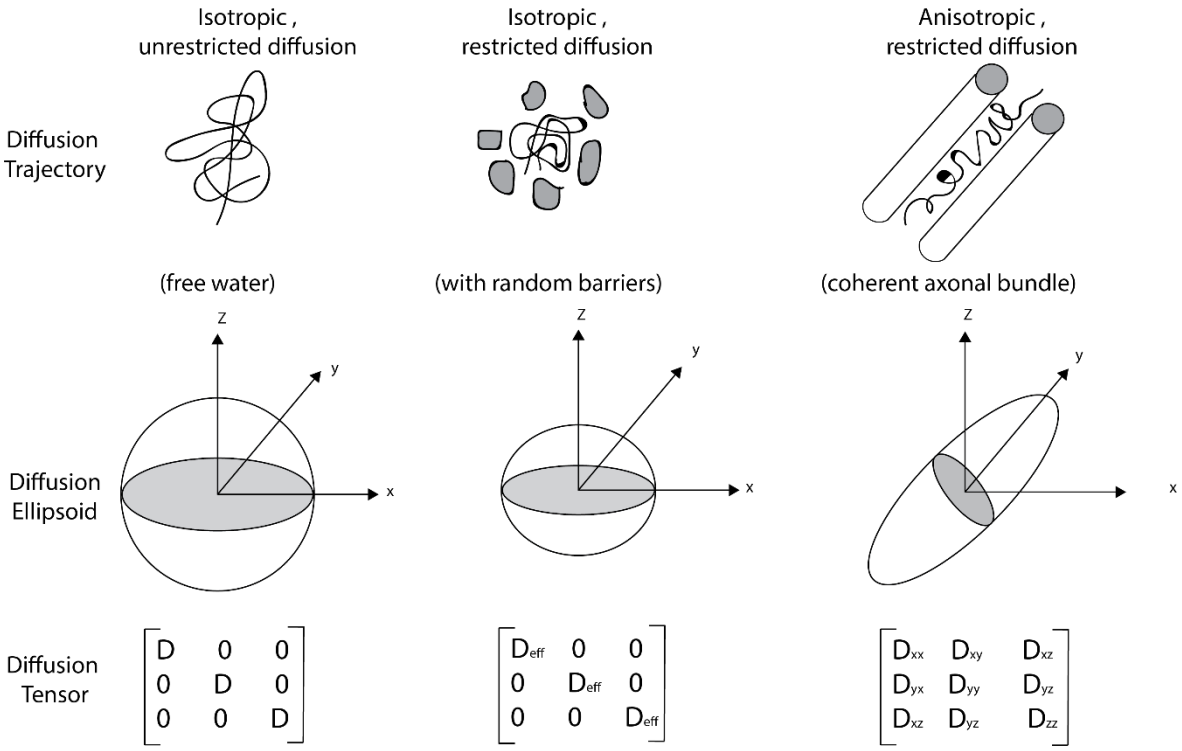


**Figure 2.22: Difference in diffusivity in unrestricted isotropic diffusion, isotropic restricted diffusion and anisotropic restricted diffusion.**

To measure the scale of the ADC in isotropic diffusion, the diffusion gradient can be applied in any direction, hence, the ADC measured will be identical no matter which direction is chosen. However, in an anisotropic medium, the measurement of the diffusion will depend on the direction of the diffusion. At least three orthogonal directions are needed to calculate ADC correctly, owing to the difference in diffusion in each direction. Scalar ADC does not provide a complete description of the diffusion where the medium is anisotropic. In biological tissues, such as WM, which is an ordered microstructure, the molecular mobility and, hence, diffusion will be anisotropic. This, in turn, means that the amount of diffusion will be different in each direction. Therefore, anisotropic diffusion cannot be represented by one diffusion constant. To completely characterise it, a diffusion tensor (D) is used. This is a 3 X 3 matrix of numbers which describes diffusion in three directions (Figure 2.22).

A minimum of six separate measurement of diffusion are needed to measure D, plus one measurement without the diffusion gradient. The reason six, rather than nine, are required is that the matrix shown in Figure 2.22 is symmetrical ($\mathbf{D_{xy}=D_{yx}}$). To obtain these six measurements, gradients should be applied in six directions.

### 2.7.4.1 Extracting information from the tensor

The diffusion tensor is that shown in Figure 2.22 can be represented by a three-dimensional ellipsoid. To better understand how to extract the most information from the tensor, consider a two-dimensional tensor (as in Figure 2.23), where the two axes are in line with the x and y axes and have the lengths Dxx and Dyy. In the ellipsoid is rotated off the x and y axes lengths are not represented by Dxx and Dyy. The lengths of the ellipsoid are known as eigenvalues (λ), and the axes are called eigenvectors (**ε**). The eigenvalues ($\lambda_1$, $\lambda_2$, $\lambda_3$) and eigenvectors ($\boldsymbol{\varepsilon}_1$, $\boldsymbol{\varepsilon}_2$, $\boldsymbol{\varepsilon}_3$) of the diffusion tensor are used to calculate descriptions of anisotropy and determine principle directions of diffusivity.

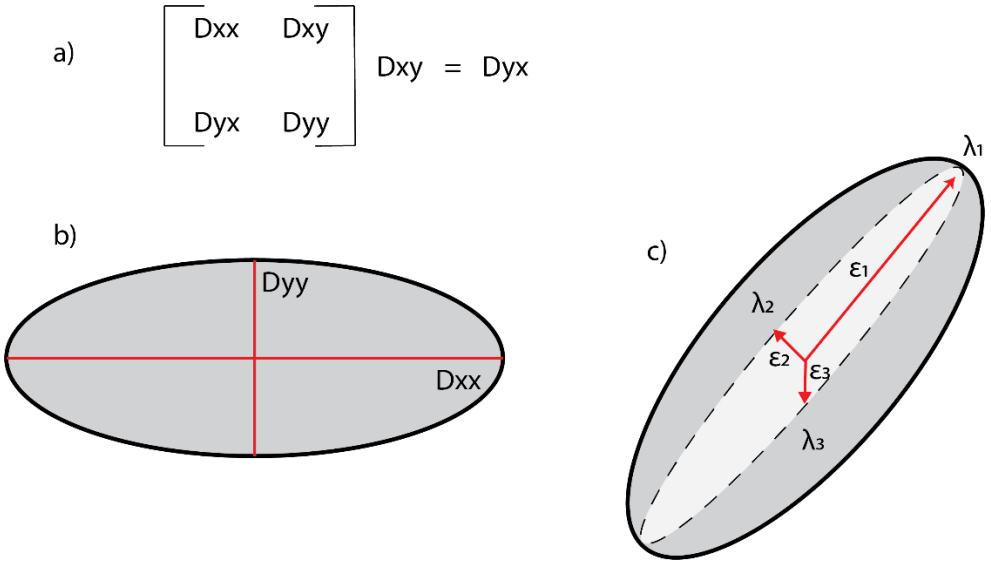


**Figure 2.23: (a) and (b) A two-dimensional tensor and its representation as an ellipse (c).**

### 2.7.4.2 Axial Diffusivity

Axial (longitudinal or parallel) diffusivity is the diffusivity along the principal axis of the diffusion ellipsoid and is represented by $\lambda_1$.

### 2.7.4.3 Radial Diffusivity

Radial (transverse or perpendicular) $\lambda_2$, $\lambda_3$ is the measure used to express the diffusivity perpendicular to the principal direction of diffusion. Radial diffusivity

is the mean of the second and third eigenvalues and is, by definition, perpendicular to the axial diffusivity.

**Equation 2.17**

$$\lambda_{radial} = \frac{\lambda_2 + \lambda_3}{2}$$

#### 2.7.4.4 Mean Diffusivity

This is the average of the apparent diffusion coefficient in all directions. Hence, complementary information is provided for fractional anisotropy (Johansen-Berg and Behrens, 2014). The overall mean squared displacement of molecules (average ellipsoid size) is simply measured using the following expression:

**Equation 2.18**

$$MD = \frac{\lambda_1 + \lambda_2 + \lambda_3}{3} = \frac{D_{xx} + D_{yy} + D_{zz}}{3}$$

#### 2.7.4.5 Fractional Anisotropy (FA)

Diffusion in different directions is described by diffusion anisotropy and measured by FA. In DTI, WM is characterised by higher directionality of diffusion and higher FA, while the combination of low FA and MD is suggestive of GM. FA in Cerebrospinal fluid (CSF) approaches zero. FA is a scalar index of the amount of anisotropy that ranges from 0 (completely isotropic diffusion) to 1 (completely anisotropic diffusion). When the diffusion is isotropic, the diffusion ellipsoid is a sphere and FA=0. However, with diffusion anisotropy the eigen values become more unequal and 0≥ FA ≤1. FA is calculated using the following formula:

**Equation 2.19**

$$FA = \sqrt{\frac{3}{2}} \sqrt{\frac{(\boldsymbol{\lambda_1} - \boldsymbol{MD})^2 + (\boldsymbol{\lambda_2} - \boldsymbol{MD})^2 + (\boldsymbol{\lambda_3} - \boldsymbol{MD})^2}{\boldsymbol{\lambda_1} + \boldsymbol{\lambda_2} + \boldsymbol{\lambda_3}}}$$

Furthermore, in areas with a complex fibre architecture, FA measurements are strongly affected (Pierpaoli and Basser, 1996). For example, FA values are lower in some areas due to the absence of single dominant diffusion direction and the

diffusion profile of the different fibre configurations average out (Hecke, Emsell and Sunaert, 2016).

## 2.8 Classification of Radiation

In general, there are two categories of radiation: ionising and non-ionising. Ionising radiation involves the ejection of one or more orbital electrons from the atom, leaving behind a positively charged ion. Ionising radiation energy is strong enough to overcome the binding energy of an electron and to knock it out of its orbit. Examples of ionising radiation are Alpha (α) rays, Beta (ß) rays, Gamma (γ) rays and protons. Ultrasound and microwaves are examples of non-ionizing radiation, which have no ability to knock an electron from its orbit around an atom to ionise it (Todd Pawlicki, 2005). Ionising radiation is divided into two types: direct ionising radiation and indirect ionising radiation. Ionising radiation that imparts energy to matter directly, through many small electrostatic interactions along the track of the radiation, is called direct ionising radiation. Alpha (α) is a direct ionising radiation which ionises matter directly upon interaction. However, indirect ionising radiation first transfers energy to charged particles in the matter through which they pass. The charged particles then deliver the energy to the matter. Examples of indirect ionising radiation are electromagnetic radiation (X-rays and Gamma (γ) rays) and neutrons, both of which transfer their energy to electrons and protons inside matter first, and the electros and protons then transfer that energy to matter (Grupen, 2010).

## 2.9 Types of Ionising Radiation

There are different types of ionising radiation, such as that emitted by unstable nuclei called radioactive nuclei or radioactive material through a process known as radioactivity.

### 2.9.1 X-Rays

X-Rays are emitted as a result of electrons moving from a higher-energy level to a lower-energy level in an atom. Due to the electronic transition inside the atom, X-rays are emitted, which are termed characteristic X-rays. When the fast-moving electron is slowing down in an electrostatic field, this also results in the emission of electromagnetic radiation or X-rays, termed continuous X-rays or

Bremsstrahlung radiation. The energy of an X-ray is usually given in terms of the generating voltage in practical applications in medicine. The energy range of X-rays, in terms of the generating voltage, are: 0.1-20 kV Low-energy or soft X-rays, 20-120 kV diagnostic–range X-rays, 120-300 kV Orthvoltage X-rays, 300 kV-1 MV intermediate-energy X-rays and 1 MV and above Megavoltage X-rays(Grupen, 2010)(Smith, 2002).

X-rays are the type of ionising radiation used in this study to irradiate mice. A Small Animal Radiation Research Platform (SARRP) will be used to deliver high energy x-ray beams to different animal models systems, such as mice with the G7 glioblastoma model and the brain tissue of the healthy mice. The SARRP system provides new research opportunities that more realistically bridge laboratory research and clinical translation.

### 2.9.2 Gamma (γ) Rays

Gamma (γ) rays are electromagnetic radiation produced in an annihilation process between matter and antimatter or emitted from the nucleus of an atom. Gamma rays can cause serious damage to the nucleus of cells and internal body organs, as they may easily pass through the skin and other organic substances (Garcia-Sanchez *et al.*, 2018).

### 2.9.3 (β) Rays

Beta rays are a type of ionising radiation, which originate from the nucleus of the atom. Beta rays are subdivided into two types: $ß^-$ and $ß^+$. $ß^-$ has the same charge and mass as that possessed by an electron, while ß+, like a positron, has the same mass as possessed by an electron but with an opposite charge (Grupen, 2010). Their penetration is much greater than Alpha particles. They can be stopped by a few centimetres of wood or a thin sheet of metal. Like Alpha particles, they can cause serious damage to the human body (Garcia-Sanchez *et al.*, 2018).

### 2.9.4 Alpha rays (α)

Found most commonly in a nuclear reaction or radioactive disintegration, Alpha (α) particles' capacity for penetration is low and they cannot pass through the

thickness of multiple sheets. However, they can be very harmful if their emitter enters the body (Garcia-Sanchez *et al.*, 2018).

This chapter has described the basic hardware and theory of MRI. In addition, it has given a detailed description of Diffusion MRI, SE- and STE- DTI. In the next chapters, these methods are applied to investigate the effects of radiation therapy on the brain tissue of the healthy and treatment of glioblastoma.

## 2.10 References:


Bammer, R. (2003) 'Basic principles of diffusion-weighted imaging', *European Journal of Radiology*, 45(3), pp. 169–184. doi: 10.1016/S0720-048X(02)00303-0.

Bashat, D. Ben *et al.* (2005) 'Normal white matter development from infancy to adulthood: Comparing diffusion tensor and high b value diffusion weighted MR images', *Journal of Magnetic Resonance Imaging*, 21(5), pp. 503–511. doi: 10.1002/jmri.20281.

Le Bihan, D. *et al.* (1986) 'MR imaging of intravoxel incoherent motions: Application to diffusion and perfusion in neurologic disorders', *Radiology*, 161(2), pp. 401–407. doi: 10.1148/radiology.161.2.3763909.

Le Bihan, D. *et al.* (2001) 'Diffusion tensor imaging: Concepts and applications', *Journal of Magnetic Resonance Imaging*. doi: 10.1002/jmri.1076.

Le Bihan, D. *et al.* (2006) 'Direct and fast detection of neuronal activation in the human brain with diffusion MRI', *Proceedings of the National Academy of Sciences of the United States of America*, 103(21), pp. 8263–8268. doi: 10.1073/pnas.0600644103.

Brian M. Dale, P. M. M., Mark A. Brown, P. and Richard C. Semelka, M. (2015) *MRI Basic Principles and Applications*. 5th edn. John Wiley & Sons, Ltd Registered.

Brown, R. (1828) ' XXVII. A brief account of microscopical observations made in the months of June, July and August 1827, on the particles contained in the pollen of plants; and on the general existence of active molecules in organic and inorganic bodies ', *The Philosophical Magazine*, 4(21), pp. 161–173. doi: 10.1080/14786442808674769.

Buckley, D. L. *et al.* (1999) 'The effect of ouabain on water diffusion in the rat hippocampal slice measured by high resolution NMR imaging', *Magnetic Resonance in Medicine*, 41(1), pp. 137–142. doi: 10.1002/(SICI)1522-2594(199901)41:1<137::AID-MRM19>3.0.CO;2-Y.

Bui, J. D. *et al.* (1999) 'Nuclear magnetic resonance imaging measurements of water diffusion in the perfused hippocampal slice during N-methyl-D-aspartate-induced excitotoxicity', *Neuroscience*, 93(2), pp. 487–490. doi: 10.1016/S0306-4522(99)00191-8.

Burdette, J. H. *et al.* (2001) 'High b-value diffusion-weighted MRI of normal brain', *Journal of Computer Assisted Tomography*, 25(4), pp. 515–519. doi: 10.1097/00004728-200107000-00002.

Chenevert, T. L. *et al.* (2002) 'Diffusion MRI: A new strategy for assessment of cancer therapeutic efficacy', *Molecular Imaging*, 1(4), pp. 336–343. doi: 10.1162/153535002321093945.

Chris Guy, D. ffytche (2005) *An Introduction to The Principles of Medical Imaging*. London: Imperial College Press,.

Chris Guy, D. ffytche (2554) *An Introduction to The Principles of Medical Imaging*. Imperial College Press,.
Clark, C. A. and Le Bihan, D. (2000) 'Water diffusion compartmentation and anisotropy at high b values in the human brain', *Magnetic Resonance in Medicine*, 44(6), pp. 852–859. doi: 10.1002/1522-2594(200012)44:6<852::AID-MRM5>3.0.CO;2-A.

Currie, S. *et al.* (2013) 'Understanding MRI: Basic MR physics for physicians', *Postgraduate Medical Journal*, 89(1050), pp. 209–223. doi: 10.1136/postgradmedj-2012-131342.

DeLano, M. C. *et al.* (2000) 'High-b-value diffusion-weighted MR imaging of adult brain: Image contrast and apparent diffusion coefficient map features', *American Journal of Neuroradiology*, 21(10), pp. 1830–1836.

Demberg, K. *et al.* (2019) 'Stimulated echo double diffusion encoded imaging of closed pores: Influence and removal of unbalanced terms', *Physical Review E*.

American Physical Society, 100(4), p. 42408. doi: 10.1103/PhysRevE.100.042408.
Derek K. Jones, P. (ed.) (2011) *Diffusion MRI theory, methods, and appliations*. doi: 10.1017/CBO9781107415324.004.

Einstein, A. (1905) 'Uber die von der molekularkinetischen Theorie der Warme geforderte Bewegung von in ruhenden Flussigkeiten suspendierten Teilchen (On the Motion of Small Particles Suspended in a Stationary Liquid, as Required by the Molecular Kinetic Theory of Heat)', *Ann. d. Phys.*, (17), pp. 549–560.

Experiments, R. S. (2004) 'Effects of Diffusion in Nuclear Magnetic', 2057(December 1960). doi: 10.1063/1.1731821.

Garcia-Sanchez, A. J. *et al.* (2018) 'Ionizing radiation measurement solution in a hospital environment', *Sensors (Switzerland)*, 18(2). doi: 10.3390/s18020510.

Grupen, C. (2010) *Introduction to Radiation Protection: Practical Knowledge for Handling Radioactive Sources (Google eBook)*. Available at: http://books.google.com/books?id=hdj9eLVGBkQC&pgis=1.

Hahn, E. L. (1950) 'Spin echoes', *Physical Review*, 80(4), pp. 580–594. doi: 10.1103/PhysRev.80.580.

Van Hecke, W., Emsell, L. and Sunaert, S. (2015) *Diffusion Tensor Imaging: A Practical Handbook*. Springer.

Hecke, W. Van, Emsell, L. and Sunaert, S. (2016) *Diffusion Tensor Imaging*. Edited by W. V. H. L. E. • S. Sunaert.

Hendee, W. R. and Morgan, C. J. (1984) 'Magnetic resonance imaging. Part I - physical principles', *Western Journal of Medicine*, 141(4), pp. 491–500.

Hendrick, R. E. (2008) 'Fundamentals of Magnetic Resonance Imaging'.
Hinshaw, W. S., Bottomley, P. A. and Holland, G. N. (1977) 'Radiographic thin-section image of the human wrist by nuclear magnetic resonance', *Nature*, 270(5639), pp. 722–723. doi: 10.1038/270722a0.

I. I. RABI, J. R. ZACHARIAS, S. M. & P. K. (1938) 'A new method of measuring Nuclear Magnetic Moment', *Physical review*, 32(1), pp. 318–318.

Jacobs, M. A., Ibrahim, T. S. and Ouwerkerk, R. (2007) 'Brief Overview and Emerging Applications', *Radiographics : a review publication of the Radiological Society of North America, Inc*, 27(4), pp. 1213–1230.

Johansen-Berg, H. and Behrens, T. E. J. (2014) *Diffusion MRI: from quantitative measurement to in vivo neuroanatomy*. Academic Press. Available at: http://uq.summon.serialssolutions.com/2.0.0/link/0/eLvHCXMwY2BQAFZBpkmplkmWZikWyWZGiYYWwDrDNCUpKc0QmJ7AO1wRMYpUmrsJMTCl5okySLu5hjh76JYWxkOHMOKTQPtFLYCNZ0MxBt5E0NLvvBLwFrEUAGH3Gws.

Köchli, V. D., Weishaupt, D. and Marincek, B. (2006) *How does MRI work?: an introduction to the physics and function of magnetic resonance imaging*. New York: Springer Berlin Heidelberg. doi: 10.1007/978-3-540-37845-7.

Koh, D. M. and Collins, D. J. (2007) 'Diffusion-weighted MRI in the body: Applications and challenges in oncology', *American Journal of Roentgenology*, 188(6), pp. 1622–1635. doi: 10.2214/AJR.06.1403.

Lauterbur, P. C. (1974) 'Magnetic Resonance Zeugmatography', *Pure and Applied Chemistry*, 40(1–2), pp. 149–157. doi: 10.1351/pac197440010149.

Liu, Z. and Xiao, X. (2013) 'The use of multi b values diffusion-weighted imaging in patients with acute stroke', *Neuroradiology*, 55(3), pp. 371–376. doi: 10.1007/s00234-012-1129-2.

Malcolm H. Levitt (2008) *Spin dynamics: Basics of Nuclear Magnetic Resonance, Second Edition*. 2nd edn, *Medical Physics*. 2nd edn. John Wiley & Sons Ltd. doi: 10.1118/1.3273534.

Mansfield, P. (1976) 'Proton spin imaging by nuclear magnetic resonance', *Contemporary Physics*, 17(6), pp. 553–576. doi: 10.1080/00107517608219056.

Mansfield, P. *et al.* (1978) 'Human whole body line-scan imaging by NMR', *The British Journal of Radiology*. The British Institute of Radiology, 51(611), pp. 921–922. doi: 10.1259/0007-1285-51-611-921.

McMahon, K. (2014) *Fast Imaging Techniques MRES7005*. Available at: http://mrt.cai.uq.edu.au/login/index.php.

Method, S. and Diffusion, R. (2003) 'Use of the Stimulated Echo in NMR Diffusion Studies', 2523(September). doi: 10.1063/1.1673336.

Miller, K. L. *et al.* (2007) 'Evidence for a vascular contribution to diffusion FMRI at high b value', *Proceedings of the National Academy of Sciences of the United States of America*, 104(52), pp. 20967–20972. doi: 10.1073/pnas.0707257105.

Mulkern, R. V *et al.* (1999) 'Multi-component Apparent Diffusion Coefficients in Human Brain', *NMR in Biomedicine*, 12, pp. 51–62.

Niendorf, T. *et al.* (1996) 'Biexponential diffusion attenuation in various states of brain tissue: Implications for diffusion-weighted imaging', *Magnetic Resonance in Medicine*, 36(6), pp. 847–857. doi: 10.1002/mrm.1910360607.

Pierpaoli, C. and Basser, P. J. (1996) 'Toward a quantitative assessment of diffusion anisotropy', *Magnetic Resonance in Medicine*, 36(6), pp. 893–906. doi: 10.1002/mrm.1910360612.

Schaeffter, T. (2005) 'Imaging modalities: Principles and information content', *Progress in Drug Research*, 62, pp. 15–81. doi: 10.1007/3-7643-7426-8_2.

Schwarzschild, B. (2003) 'Lauterbur and Mansfield Awarded Nobel Medicine Prize for Magnetic Resonance Imaging', *Physics Today*, 56(12), pp. 24–27. doi: 10.1063/1.1650215.

Smith, P. H. S. (2002) *An introduction to medical physics*, *The International Journal of Applied Radiation and Isotopes*. doi: 10.1016/0020-708x(76)90176-9.

Stejskal, E. O. and Tanner, J. E. (1965) 'Spin diffusion measurements: Spin echoes in the presence of a time-dependent field gradient', *The Journal of Chemical Physics*, 42(1), pp. 288–292. doi: 10.1063/1.1695690.

Todd Pawlicki, D. J. S. and G. S. (2005) *Hendee's Radiation Therapy Physics*. 4th edn. John Wiley & Sons.

Weishaupt, D. and Marincek, B. (2008) *How Does MRI Work ? An Introduction to the Physics and Function of Magnetic Resonance Imaging*. Second Edi. Available at: papers3://publication/uuid/F2EC282D-FF52-4C88-8720-3E66239857DE.

Yacoub, E. *et al.* (2008) 'Decreases in ADC observed in tissue areas during activation in the cat visual cortex at 9.4 T using high diffusion sensitization', *Magnetic Resonance Imaging*, 26(7), pp. 889–896. doi: 10.1016/j.mri.2008.01.046.
Yoshiura, T. *et al.* (2001) 'Highly diffusion-sensitized MRI of brain: Dissociation of gray and white matter', *Magnetic Resonance in Medicine*, 45(5), pp. 734–740. doi: 10.1002/mrm.1100.

# Chapter 3

# Chapter-3 MRI ability to probe the early stage effects of ionising radiation treatment on the invasiveness of an infiltrative rodent GBM model

## 3.1 Introduction:

GBM is the most aggressive and incurable primary brain tumour which leads to severe neurological, psychological and cognitive symptoms (Birch *et al.*, 2018). It is comprised of a heterogeneous population of cells. Despite the current advances in both radiotherapy and chemotherapy (Grossman and Batara, 2004), GBM-related morbidity and mortality remain very high. The standard of GBM care consists of maximal surgical resection followed by radiotherapy and chemotherapy. Despite that, such a treatment strategy does not target the diffuse infiltrative nature of the tumour (de Gooijer *et al.*, 2018). Unfortunately, the radical resection of the primary tumour mass is not curative, due to its high degree of invasiveness. In the surrounding brain, the infiltrating tumour cells invariably remain, leading to disease progression or recurrence, either distant from the primary brain tumour or locally (Wainwright *et al.*, 2012). Consequently, the extensive infiltration of the tumour surrounding parenchyma is recognised as one of the clinical hallmarks of GBM (Claes, Idema and Wesseling, 2007). In fact, the hallmark features of aggressive invasion into the surrounding tissue are shared by all GBM subtypes. Consequently, the major obstacles for curative therapy are the invasive glioblastoma cells that escape surgery and focal therapies (Vollmann-Zwerenz *et al.*, 2020) and also the resistance of these invasive cells to both radio- and chemo-therapeutic approaches (de Gooijer *et al.*, 2018). As a result, any curative therapy for this fatal disease should include treatment strategies which interfere with GBM invasiveness. It is critical that the mechanisms of GBM invasion should be investigated and understood (de Gooijer *et al.*, 2018).

GBMs are comprised of heterogenous brain tumours characterised by increased cellularity, mitosis, cellular pleomorphism, necrosis and endothelial proliferation. Microvascular proliferation and necrosis are also essential diagnostic features of GBMs, and tumour growth is heavily dependent on angiogenesis (Fischer *et al.*, 2006). In addition to the heterogeneity of histological features, this is accompanied by regional variations in vascular development and maturity, blood flow, and vascular density, which result in variations in the vascular

microenvironment. These, in turn, leads to different treatment responses. For example, areas with hypoperfusion and hypoxia are associated with poor radiotherapy response and poor chemotherapy delivery (Winkler *et al.*, 2004). GBM cell invasion occurs along pre-existing structures such as WM, blood vessels and the subarachnoid space (Cuddapah *et al.*, 2014), which might be coordinated by specialised cells that may lead to collective invasion (Vitorino, 2009)(Hartmann and Klein, 2006). Furthermore, by remodelling their own cytoskeleton and the extracellular matrix (Cuddapah *et al.*, 2014), GBM cells can cross tissue barriers and then invade as individual cells (Claes, Idema and Wesseling, 2007) or collectively (Friedl and Wolf, 2003)(Wolf and Friedl, 2006). Consequently, there is an urgent clinical need to investigate in more detail the mechanisms that lead to invasion. To date, current standard treatment therapies are unable to target the infiltrative tumour cells and there are no available effective anti-invasive treatment strategies (Vollmann-Zwerenz *et al.*, 2020).

In addition, angiogenesis, which is the growth of new capillaries from the pre-existing blood supply, is essential for tumour growth. GBMs are highly vascularised tumours and this enables rapid tumour growth. In fact, angiogenesis is a complex process involving proliferation, migration and differentiation of vascular endothelial cells under stimulation of specific signals. Angiogenesis is controlled by the balance between its promoting and inhibiting factors. Various angiogenic genes and factors which stimulate glioma angiogenesis have been identified which stimulate glioma angiogenesis. As a result, attention has been directed to anti-angiogenesis therapy in which glioma proliferation is inhibited by inhibiting the formation of new tumour vessels using angiogenesis inhibitor factors and drugs (Vollmann-Zwerenz *et al.*, 2020).

Radiotherapy is given as standard care to all GBM patients to provide targeted ablation of tumour cells and increase the chance of survival. Whilst it remains an effective treatment, radiotherapy can confer unwanted phenotypes on tumour cells that remain after therapy. For instance, recent studies, including one from our own laboratory carried out by Birch *et al.*, have shown that radiotherapy can promote infiltration of the normal brain tissue by GBM cells (Birch *et al.*, 2018). As infiltration by GBM cells contributes to both the profound cognitive and neurological symptoms experienced by patients and to disease recurrence,

achieving better understanding of these processes is crucial to improve patient outcomes in the future.

Because most of these invariably highly invasive and aggressive phenotypes, there is a recurrence of GBM cells within the radiation treatment field, particularly at the resection margins, where the highest radiation doses are applied (Minniti *et al.*, 2010). This means that radiation stimulates the infiltrative behaviour of GBM cells (D'Alessandro *et al.*, 2019). Unfortunately, little is known about the negative effects of these recurrent GBM cells and their role in triggering invasion. Hence, new strategies to supress GBM cell migration induced by radiation are urgently needed. In this chapter, we describe how we sought to determine the impact of radiation-induced changes in promoting GBM recurrent cells in an animal model. If the effects of radiation therapy could be replicated in a brain micro-environment in an animal model, this would be a significant advance.

## 3.2 Aim

The aim of this preliminary study was to use MRI (T2-weighted imaging) to probe early stage effects of IR treatment on the invasiveness of an infiltrative rodent GBM model. The T2 weighted MRI was used to define the tumour margins and the tumour volume. The diffuse, infiltrative border of GBM lesions makes delineation of the tumour border difficult to determine precisely, due to lack of knowledge about the exact molecular mechanisms underlying infiltration of GBM cells. Hence, this growth pattern is a major factor in therapeutic failure. Further, radiological visualization of the invasive front of the diffuse GBM is difficult. Consequently, we aimed to measure brain volume at two time points post-irradiation for both irradiated and controlled brains, looking for any effect on the infiltrative nature of the tumour. Histology was used for validating the infiltration in parallel with MRI.

## 3.3 Methods

### 3.3.1 Experimental design

Female CD1 nude mice were injected with a G7 tumour cell line and allowed to grow for 10 to 11 weeks. This reduces delineation errors and increases infiltrative margins. MRI was acquired at week 12 post-injection to confirm the presence of tumours which were irradiated with 6 Gy fractionated dose (3x2 Gy) to the whole brain. Mice were also scanned with MRI at weeks 13 and 14 post-injection and culled for histology at week 14 to validate the infiltration. MRI was acquired at early time points to avoid losing too many animals due to tumour enlargement. We injected the G7 tumour model into CD1 female mice (n=32) which were separated into two cohorts with different time end-points, with each cohort further separated into IR and non-IR groups. Cohort numbers were lower than expected before the experiment started (n=19) due to the inherent cohort attrition rate of the model, with animals succumbing to tumour burden before the start date of the experiment. As a result of the rapid spread of the G7 cancer cells, thirteen mice (n=13) were lost before the study started. Group one was culled 7 days post-IR (IR (n=6) and non-IR (n=5)) (Figure 3.1), whereas group two was culled 14 days post-IR (IR (n=5) and non-IR (n=3)) (Figure 3.2). At the time of these experiments, there was no available estimate of the G7 model attrition rate. However, subsequent experiments carried out by another researcher in our group were able to use our attrition rate data, which led them to double the number of experimental mice used from n=32 to n=64 (Birch *et al.*, 2018).

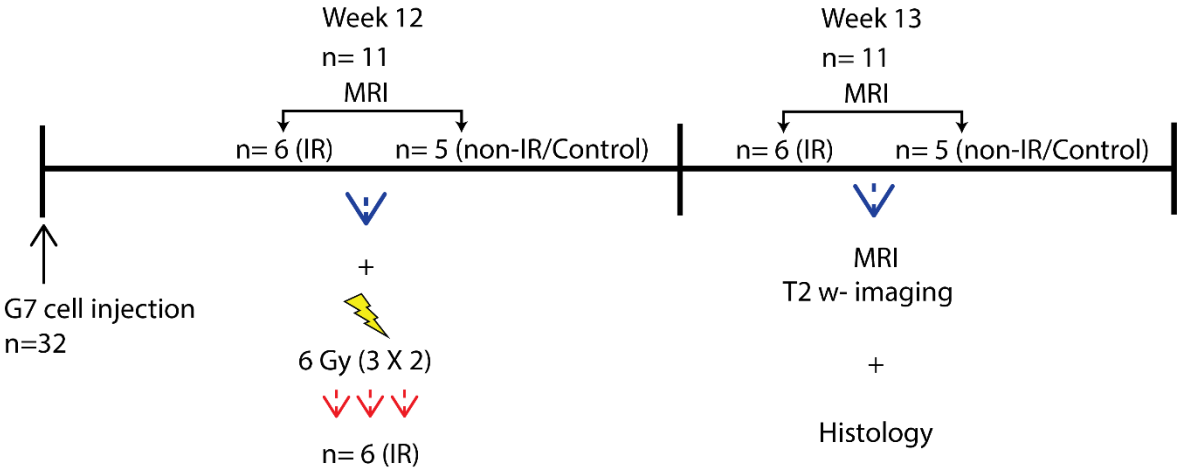


**Figure 3.1: Experimental design of study one.**

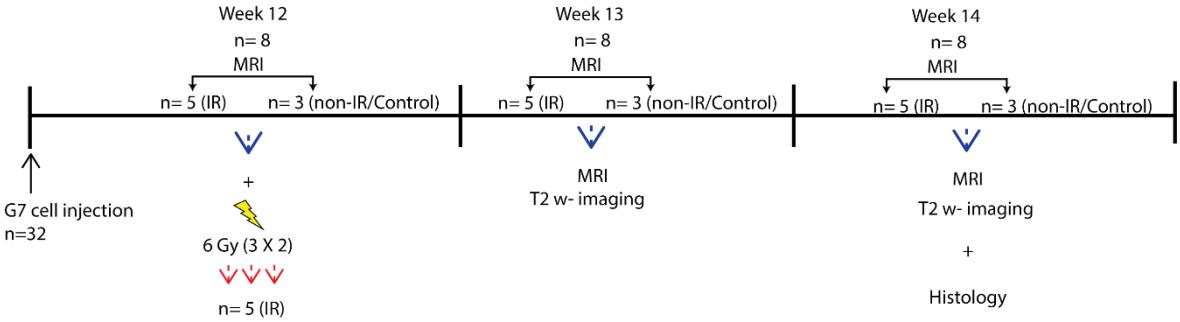


**Figure 3.2: Experimental design of two design.**

## 3.3.2 G7 tumour model

Despite the multi-modalities of treatment, GBM is still a highly aggressive brain tumour with very poor prognosis (Norden, Drappatz and Wen, 2010). Consequently, there is an urgent need for appropriate rodent models for preclinical studies, due to the recent failure of targeted therapy for these tumours (Jacobs *et al.*, 2011). The most commonly used rodent models of GBM are U87, U251, GL261, C6, 9L and CNS-1. These models have the potential to recapitulate the human brain neoplasm at the genetic, pathophysiology, imaging, and therapeutic levels (Jacobs *et al.*, 2011). The U87 GBM model, for example, shows highly cellularity with atypia such as mitotic figures and irregular nucleoid, and profuse neovascularization (Candolfi *et al.*, 2008). However, the U87 model is

dissimilar to GBM as it shows a non-diffusely infiltrative growth pattern, with a well-demarcated tumour mass which is surrounded by reactive astrocytes (de Vries, Beijnen and van Tellingen, 2009). In this study, we used the G7 model of GBM was used and obtained from Colin Watts (Cambridge) which was derived from anonymised patient resection specimens (Fael Al-Mayhani *et al.*, 2009)(Ahmed *et al.*, 2015). The G7 tumour model is characterised by the formation of a bulk tumour mass after injection and, over time, cells leave the invasive tumour edge cells. In fact, the G7 tumour is characterised by its high degree of invasiveness at the tumour margins (Mannino *et al.*, 2014). Further, as the G7 cells are human in origin, it is simple to discriminate between the replicating tumour cells and the non-proliferating cells of the mouse brain (Birch *et al.*, 2018).

## 3.3.3 Intracranial tumour model methods

G7 cells were cultured in stem-like conditions (Advanced DMEM:F12, containing 20uM EGF/FGF, 1% B27, 0.5%N2, heparin, 1% L-Glut) on matrigel coated plates. 1 x $10^5$ cells were injected intracranially into the SVZ of n=32 female CD1 nude mice (Ahmed *et al.*, 2015)(Gomez-Roman *et al.*, 2017), using stereotactic equipment. The SVZ in the adult mouse brain is known to be a major source of neuronal stem cell progenitors and its functions as a supportive niche promoting self-renewal and inhibiting differentiation (David T. Scadden, 2006)(Shen *et al.*, 2004)(Goffart *et al.*, 2015). Tumours were allowed to develop for 12 weeks with the presence of tumour confirmed by MRI before the irradiation.

### 3.3.3.1 Protocol for the intracranial model

The surgery involved in intracranial injection of G7 cells was undertaken by an expert biologist, guided by the following protocol. The table below details some of the equipment used during surgery.

**Table 3.1: Table shows all items that were used during intracranial surgery and their roles.**

| **Items** | **Use** |
|---|---|
| 70% Etahnol | For sterilising mouse skin before incision |
| **Lacrilube** | Eye ointment |

| | |
|---|---|
| **vetergesic** | Pain relief |
| **Forceps** | For repairing wound |
| **isofluane** | Gas anaesthesia |
| **10ul Hamilton syringe** | For injecting tumour cells |
| **1ml microfine insulin needles** | For applying skin glue |

1. **Harvest cells**
    a. Accutase for 2-4 min.
    b. Centrifuge: 1200 rpm for 5 min.
    c. wash cells in PBS
    d. Centrifuge: 1200 rpm for 5 min.
    e. Resuspend cells in PBS and count (we typically inject 1x10^5 cells per mouse)
    f. Centrifuge: 1200 rpm for 5 min.
    g. Resuspend cells in PBS – 1x10^5 cells per 5ul PBS (total volume PBS/cells to be injected into mouse brain = 5ul)
    h. Put cell resuspension on ice, resuspend by pipetting before each injection.

2. **Prepare mouse and drill skull**
    a. Anaesthetise mouse.
    b. Place mouse in stereotaxic frame (hook teeth onto bar, place mouse on top of gauze to keep warm) (see Figure 3.3 )
    c. Apply lacrilube to eyes (to prevent drying out)
    d. Pre-operation acute analgesic (Vetergesic (10-20 µg/kg (200ul/20g) to be given subcutaneously – dilute 100ul vetergesic in 900ul saline
    e. Ensure mouse is sufficiently asleep via pedal response
    f. Wipe skull with 70% ethanol.
    g. Make a small incision (approx. 1cm) through skin along the middle of skull along its length (from just behind the eyes).
    h. Use a sterile cotton bud to remove periosteum membrane that is covering the skull, to ensure skull doesn't get too dry, dampen with saline.
    i. Locate the Bregma (the junction point of the sagittal and coronal sutures of the skull).
    j. Ensure mouse is sufficiently asleep via pedal response
    k. Use a burr to drill a hole in the skull at (Drill bit: Harvard Apparatus (Cat# 72-4958))
        i. 3mm towards the tail
        ii. 2mm to right if the mouse's nose is away from you
        iii. Avoid blood vessels


**Figure 3.3: Image shows intracranial surgery for intracranial injection of GBM cells in CD1 nude mice.**

3. **Load Syringe and inject cells**
    a. Move the plunger holder to the maximum position
        i. Set rate to 2ul/min, vol as required (5ul), config ul/min
        ii. Make sure diameter is appropriate for the syringe type being used
    b. Mix cells with pipette.
    c. Load the syringe to 10ul with cells and ensure that there are no bubbles within the syringe.
    d. Return the cells to ice.
    e. Place the syringe in the holder. Ensuring that the plunger hits in the plunger holder and the top of the syringe is also supported in its holder.
    f. Move the syringe above the burr hole using x, y and z of the stereotaxic frame. Ensure that the x y and z are locked in place.
    g. Move the syringe (using x, y, and z) so that the tip of the needle is touching the durra (see below).
    h. Press the z on the digital read out of x y z to ensure it is reading zero
    i. Insert the needle 3mm (turn z slowly clockwise until the z co-ordinate reads -3.0).
    j. Press Run on the Nanomite and a number of cells in 5ul at 2ul/min will be injected.
    k. Leave needle in for a further 5min to ensure no reflux of the cells. **(screw z anticlockwise to remove needle**)

4. **After-care of the mouse**
    a. Gently push the skin on the skull together using forceps and apply the glue to the wound. Ensure that the edges of the wound meet but don't cross. Wait for it to dry (should be 1-3mins).
    b. Observe mouse until recovered (keep mouse warm)
    c. Post-operation chronic analgesia - Rimadyl (carprofen) 2mls diluted in 1litre drinking water for 1-2days.

d. Mouse should be observed daily for any signs of distress or neurological symptoms.

### 3.3.4 Irradiation

Radiation treatment was delivered using the XStrahl SARRP with a 6 Gy fraction dose (3 X 2Gy). Animals were anaesthetised with 2% to 2.5% isoflurane delivered in a 70/30 mixture of $N_2O/O_2$. Brain irradiation was performed using parallel opposed beams and a 10 x 10 mm collimator to ensure adequate tumour coverage in all animals. The cone beam was acquired using the following parameters: 220 Kv, 13 mA and 20 seconds. All mice received an absorbed dose of 6 Gy (3 x 2Gy) (Figure 3.4). Irradiation was delivered to the mice three days a week (Monday, Wednesday, and Friday).


**Figure 3.4: Image shows example of G7 tumour mouse irradiation setup on the XStrahl SARRP acquired by Muriplan software.**

The CT-scan image using SARRP before irradiation allowed tissue segmentation and selection of an isocentre (approximately 5 mm below cell injection drill hole). Figure 3.5 shows that dose distributions were uniform across the brain area.

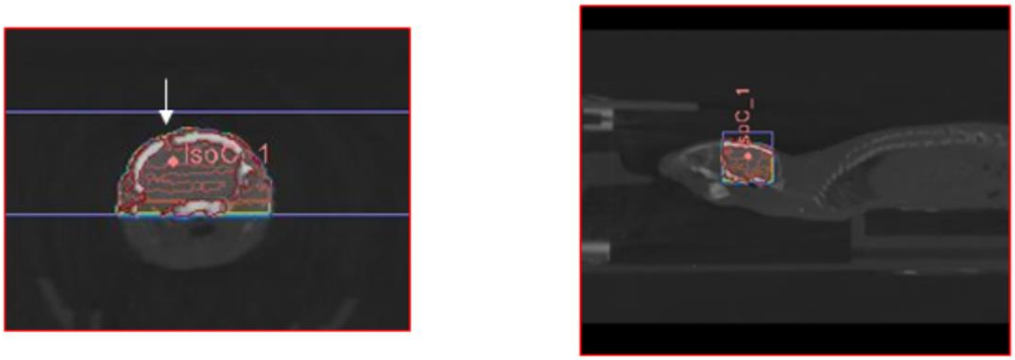


(a) (b)

**Figure 3.5: (a) CT imaging of mice prior to irradiation to allow tissue segmentation and positioning of isocentre below surgery drill hole (white arrow). (b) The irradiated area is encompassed by the blue lines.**

Rutherford et al., 2019, from our lab, show in his research that SARRP is capable of delivering accurate doses to small volumes, thus in providing confidence and clinical relevance to preclinical studies. Furthermore, SARRP can provide relatively complex plan types and also deliver accurate doses while sparing OARs , thus enabling the study of long term efficacy and toxicity (Rutherford *et al.*, 2019)

## 3.4 MRI

MRI was acquired before IR, at 7 days (groups 1 and 2) and at 14 days (group 2) post-IR. T2 weighted imaging was acquired on a 7T Bruker Biospec scanner using the following parameters: RARE sequence (Rapid Acquisition with Relaxation Enhancement), TR/TE = 4300/10ms, Field of View (FOV) =2cm, slice thickness = 0.5mm, matrix 176X176 and number of slices = 14.

## 3.5 Post Processing:

MRI data were exported in the DICOM format for post-processing and analysed using an in-house Matlab code. On each T2-weighted slice, tumour-related abnormal regions were manually selected. The number of voxels within abnormal regions were multiplied by the voxel volume to evaluate tumour volume (Figure 3.6).

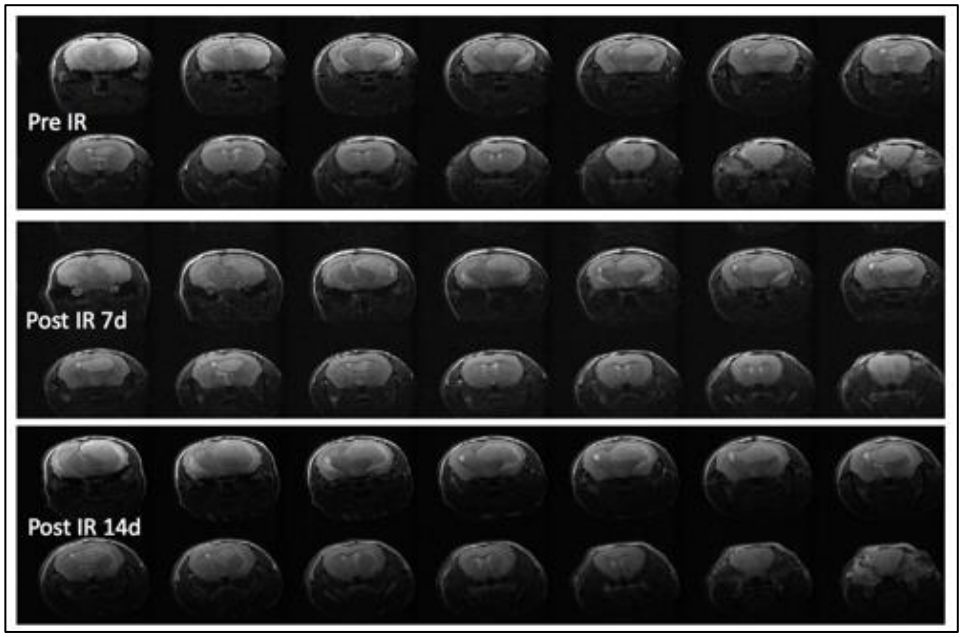


**Figure 3.6: Example of a G7 glioblastoma tumour with different T2 weighted image slices at all-time points (pre-IR, post-IR 7 days and post-IR 14 days) from all groups. All T2 weighted image slices (n=14 slices) were manually selected to calculate tumour volume for each mouse.**

Another reason for using our own Matlab code for processing was to generate all T2 weighted images for all slices, from which the tumour region was manually selected from all visible slices (Figure 3.7). The T2 weighted slices which did not show visible tumour were discarded. Using our own Matlab code, all volumes from invisible slices with a value of zero were calculated. For each mouse, the tumour was manually selected twice (by myself and by another researcher) and the data were averaged.

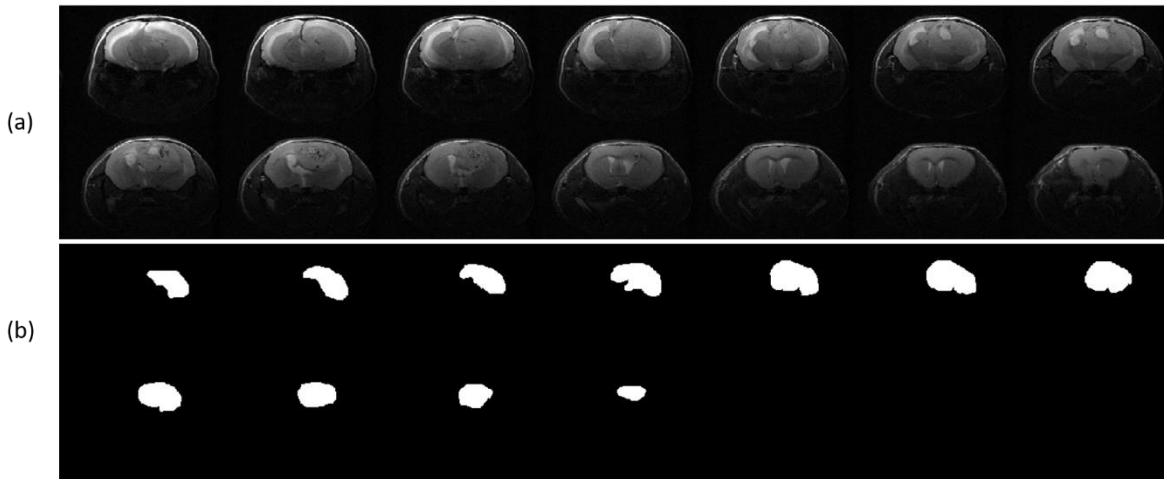


**Figure 3.7: Image (a) shows example of G7 tumour growth on one mouse for all 14 T2 weighted image slices at day 14 post-irradiation, while image (b) shows manual selection of the tumour from the 11 T2 weighted slices where the tumour was visible.**

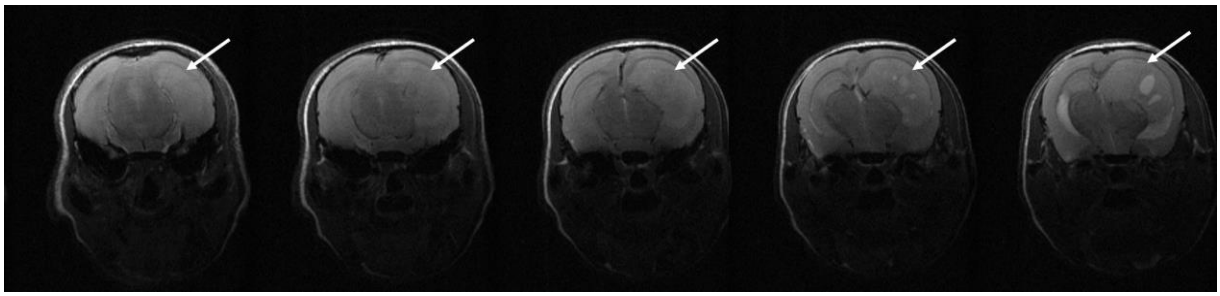

**Figure 3.8: Image shows an example of the first five slices acquired for a G7 tumour for one mouse (white arrows). As shown above, the G7 tumour was clear in the first slices. That made the selection easier than for the last slice, where the tumour starts to become invisible. Because a mouse brain is very small, image zoomed to make them easier to see.**

## 3.6 Results

In our study, we assessed the ability of MRI to investigate the behaviour of G7 tumour cell invasion after radiotherapy treatment. Figure 3.9 shows tumour volume change at 7 days for the IR treated and non-IR treated groups. No significant difference between groups was found at this stage. This was confirmed by the second brain volume measurement at the same time point post-IR in the second cohort (see Figure 3.10). Between day 0 and day 7, large tumour growth was observed in both the IR and non-IR groups, but with no significant difference.

However, between day 7 and day 14, the IR treated group showed significantly greater tumour growth than the non-IR treated group, potentially through increased infiltration (Figure 3.10).These results suggest that the IR effects on tumour invasiveness can be analysed using T2 weighted imaging.

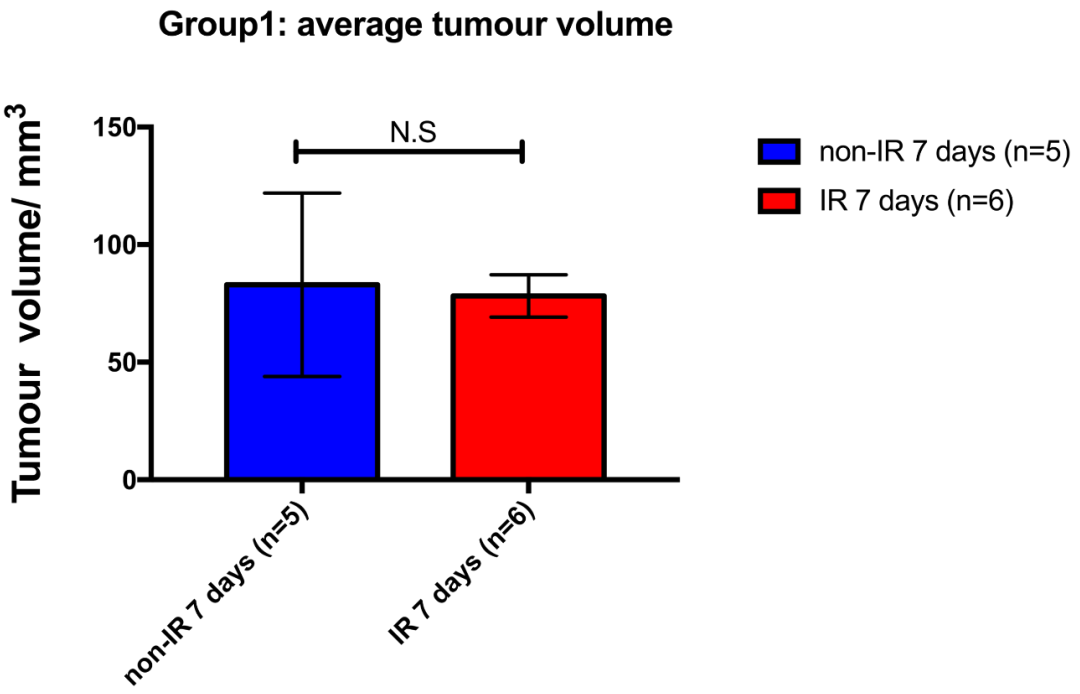


**Figure 3.9: Image shows average tumour growth for group one study (IR and non-IR groups) at day 7. No significant differences were found between groups at this time point (p. value=0.77). All data represent mean ± S.E.M. Statistical analysis: two-tailed, unpaired t-test. N.S=not significant.**

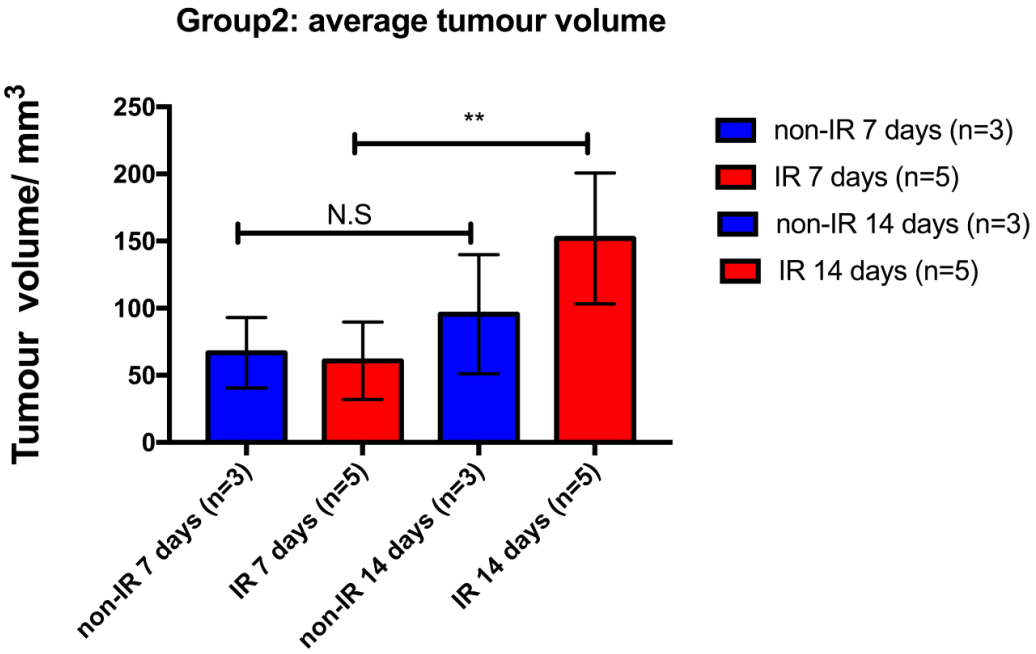


**Figure 3.10: Image shows tumour growth for the two groups in study 2 (IR and non-IR) at two time points post-irradiation (7 and 14 days). No significant differences in tumour growth was found between non-IR groups (between days 7 and 14). However, significance was reached between irradiated groups (p-value=0.007). All data represent mean ± S.E.M. Statistical analysis, two-tailed, unpaired t-test. **= significant. **p<0.05.**

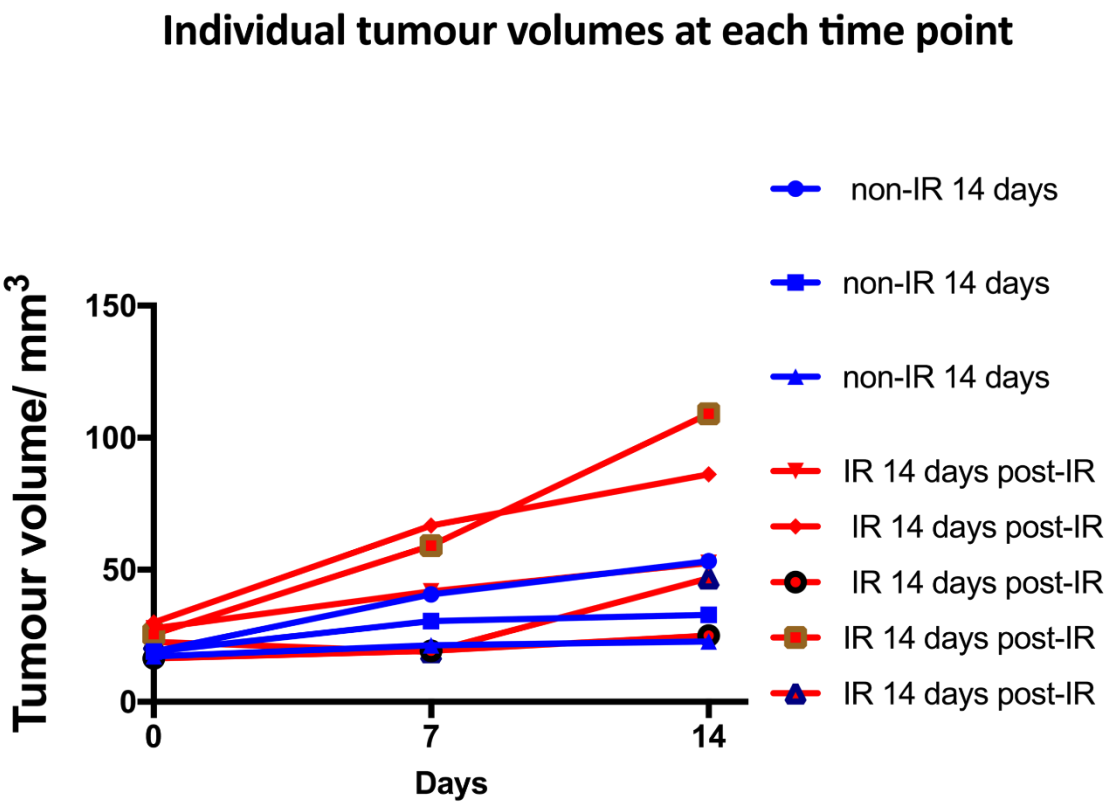


**Figure 3.11: Image shows individual plots volume growth for IR and non-IR groups in study two, starting from day zero (week 12) and days 7 and 14 respectively.**

### 3.6.1 Histology

Histopathological analysis was conducted by a post-doctoral researcher (Dr Joanna Birch). Tumours were sub-dissected and freshly-frozen specimens sent for PK analysis (Vertex). Formalin-fixed, paraffin-embedded sections were stained for Ki67 and then scanned using a Hamamatsu Nanozoomer Slide scanning machine with Leica SlidePath Slide imaging software. Algorithms were optimised for each stain individually and automated, quantitative analysis undertaken. The defining of contralateral regions was performed blind.

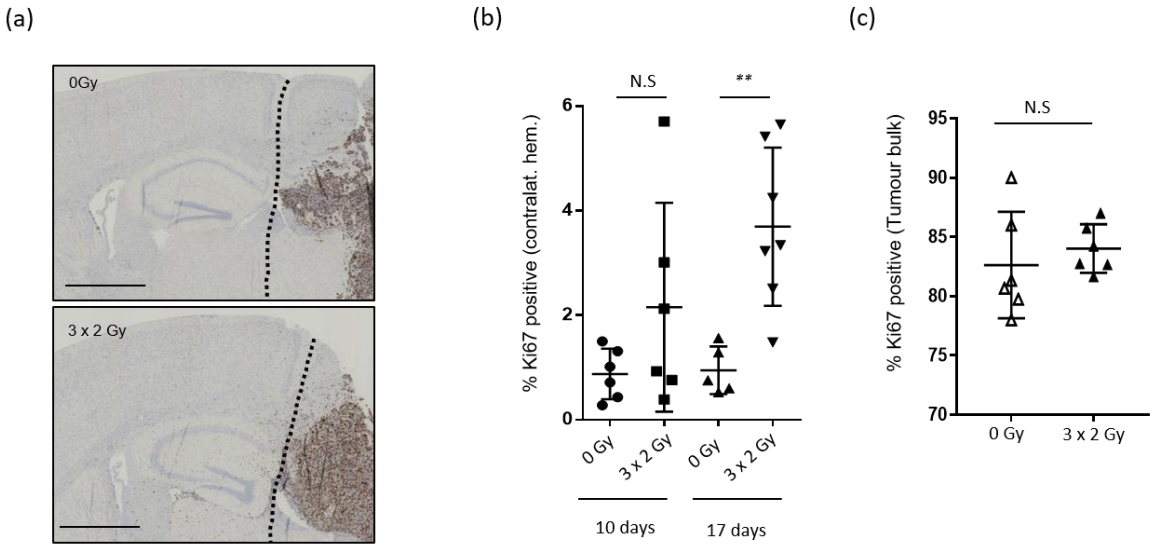


**Figure 3.12: (a) Brain sections from control and irradiated mice bearing G7 intracranial tumours were stained via IHC for Ki67 to indicate presence of cycling GBM tumour cells (GBM positive cells). (b) In the contralateral hemisphere of mice culled 7 or 14 days after initiation of treatment was quantified using automated image analysis. (c) % Ki67 positive cells in the tumour bulk were quantified using automated analysis in specimens from mice culled 10 days after initiation of treatment; n = 6 in both cohorts. The percentage of Ki67 positive cells Scale bar: 1mm. Statistical analysis: two tailed, unpaired t test. N.S. = not significant, ** $p < 0.005$.**

## 3.7 Discussion:

Despite the state-of-the-art treatment that involves surgical resection, chemotherapy and radiation, GBM is still an incurable disease. As a highly invasive and aggressive phenotype, GBM invariably recurs, with the majority of these recurrences being within the radiation treatment field (Duan *et al.*, 2019). This phenomenon has been confirmed by many different reports, thus demonstrating

that different radiation protocols stimulate cell migration in GBM (Mao *et al.*, 2018)(Trog *et al.*, 2006). Unfortunately, little information is known about the negative effect of ionising radiation on these pathways and its role in migration and invasion (Reyes *et al.*, 2013)(Kwiatkowska *et al.*, 2011). To improve the outcomes for patients with recurrent GBM, preclinical modelling approaches are required to understand the underlying mechanism of the invasion. The model herein focused specifically on the role of radiation on the tumour cells. Irradiation of mouse brains 12 weeks post-tumour cell injection showed an invasive tumour growth pattern, which was confirmed with both MRI and histology. T2 weighted MRI scans showed an increase in tumour volume for both groups after 7 and 14 days, with a significant increase between day 7 and 14 for the IR group, despite the small number of animals that could be included in the study (Figure 3.13). This suggests that ionising radiation induced an extrinsic effect on the tumour, leading to an increase in tumour volume. Staining with Ki67, which is a marker of proliferating cells, was used to indicate the presence of cycling GBM tumour cells. Ki67 positive cells were quantified in the contralateral hemisphere of mice culled 7 and 14 days after the initiation of treatment. Quantification of Ki67 staining in the tumour bulk was included to show that ionising radiation not only caused a general increase in proliferation but that is also why there was an increase in the contralateral hemisphere. Unlike Ki67 staining, MRI cannot be used as a sensitive biomarker for measuring individual invasive GBM cells in the contralateral hemisphere. Histological assessment of tumour cell infiltration may be limited by inherent variability in tumour position and growth post-surgery.

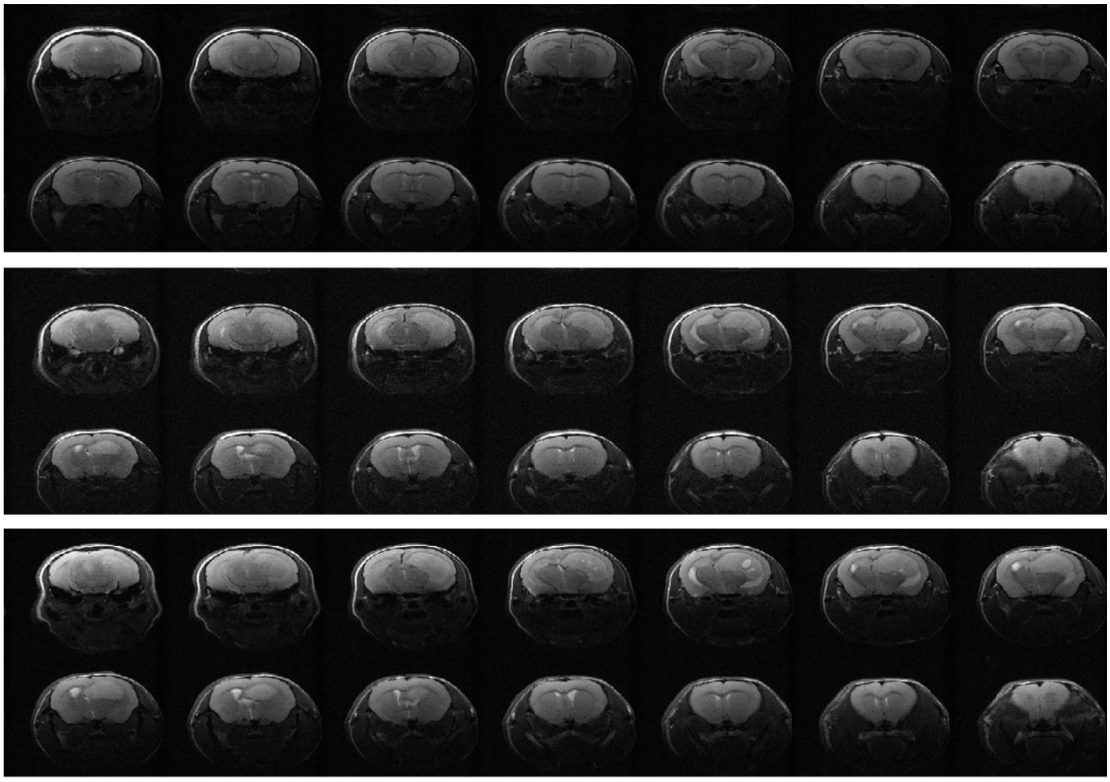


**Figure 3.13: Image shows invasive tumour growth patterns on different days for the same mouse. (a) at day 12 pre-irradiation and (b) and (c) at days 13 and 14 post-irradiation, respectively.**

## 3.8 Conclusion:

GBM is recognised as one of the most aggressive primary brain tumours in adults and the least responsive to treatment. The adverse clinical features of GBM are partly attributed to the infiltrative nature of the disease. This is due to the number of biological and morphological changes which GBM undergo that allow them to migrate through the perivascular spaces and white matter tracts of the brain (Birch *et al.*, 2018). For many years, the ability of radiation to promote GBM cell invasion has remained controversial. Our data is consistent with that of previous studies, showing compelling evidence that ionising radiation, despite increasing the survival rate of GBM patients, may also play a negative role by promoting the invasiveness and infiltration of GBM tumour cells. Gaining a better understanding of these processes will help to identify potential novel avenues of treatment to contain infiltration during therapy and improve potential outcomes in the future.

## 3.9 Limitation of the work

Loosing too many mice (n=13) before the experiment started was the main issue. This was due to the enlargement and fast growing of the G7 tumour model. This issue was avoided in the second part of this experiment, that was carried out by another researcher in our group, by doubling the number of injected mice to *n*=64.

## 3.10 References:

Ahmed, S. U. *et al.* (2015) 'Selective inhibition of parallel DNA damage response pathways optimizes radiosensitization of glioblastoma stem-like cells', *Cancer Research*, 75(20), pp. 4416–4428. doi: 10.1158/0008-5472.CAN-14-3790.

Birch, J. L. *et al.* (2018) 'A novel small-molecule inhibitor of MRCK prevents radiation-driven invasion in glioblastoma', *Cancer Research*, 78(22), pp. 6509–6522. doi: 10.1158/0008-5472.CAN-18-1697.

Candolfi, Marianela *et al.* (2008) 'Intracranial glioblastoma models in preclinical neuro-oncology: neuropathological characterization and tumor progression', 85(2), pp. 133–148.

Claes, A., Idema, A. J. and Wesseling, P. (2007) 'Diffuse glioma growth: A guerilla war', *Acta Neuropathologica*, 114(5), pp. 443–458. doi: 10.1007/s00401-007-0293-7.

Cuddapah, V. A. *et al.* (2014) 'A neurocentric perspective on glioma invasion', *Nature Reviews Neuroscience*. Nature Publishing Group, 15(7), pp. 455–465. doi: 10.1038/nrn3765.

D'Alessandro, G. *et al.* (2019) 'Radiation increases functional KCa3.1 expression and invasiveness in glioblastoma', *Cancers*, 11(3), pp. 1–14. doi: 10.3390/cancers11030279.

David T. Scadden (2006) 'The stem-cell niche as an entity of action', *Nature*, 441, pp. 1075–1079.

Duan, C. *et al.* (2019) 'Late Effects of Radiation Prime the Brain Microenvironment for Accelerated Tumor Growth', *International Journal of Radiation Oncology Biology Physics*. Elsevier Inc, 103(1), pp. 190–194. doi: 10.1016/j.ijrobp.2018.08.033.

Fael Al-Mayhani, T. M. *et al.* (2009) 'An efficient method for derivation and propagation of glioblastoma cell lines that conserves the molecular profile of their original tumours', *Journal of Neuroscience Methods*, 176(2), pp. 192–199. doi:

10.1016/j.jneumeth.2008.07.022.

Fischer, I. *et al.* (2006) 'Angiogenesis in Gliomas: Biology and Molecular Pathophysiology', *Brain Pathology*, 15(4), pp. 297–310. doi: 10.1111/j.1750-3639.2005.tb00115.x.

Friedl, P. and Wolf, K. (2003) 'Tumour-cell invasion and migration: Diversity and escape mechanisms', *Nature Reviews Cancer*, 3(5), pp. 362–374. doi: 10.1038/nrc1075.

Goffart, N. *et al.* (2015) 'Adult mouse subventricular zones stimulate glioblastoma stem cells specific invasion through CXCL12/CXCR4 signaling', *Neuro-Oncology*, 17(1), pp. 81–94. doi: 10.1093/neuonc/nou144.

Gomez-Roman, N. *et al.* (2017) 'A novel 3D human glioblastoma cell culture system for modeling drug and radiation responses', *Neuro-Oncology*, 19(2), pp. 229–241. doi: 10.1093/neuonc/now164.

de Gooijer, M. C. *et al.* (2018) 'An Experimenter's Guide to Glioblastoma Invasion Pathways', *Trends in Molecular Medicine*. Elsevier Ltd, 24(9), pp. 763–780. doi: 10.1016/j.molmed.2018.07.003.

Grossman, S. A. and Batara, J. F. (2004) 'Current management of glioblastoma multiforme', in *Seminars in oncology*. Elsevier, pp. 635–644.

Hartmann, C. H. and Klein, C. A. (2006) 'Gene expression profiling of single cells on large-scale oligonucleotide arrays', *Nucleic Acids Research*, 34(21). doi: 10.1093/nar/gkl740.

Jacobs, V. L. *et al.* (2011) 'Current review of in vivo GBM rodent models: Emphasis on the CNS-1 tumour model', *ASN Neuro*, 3(3), pp. 171–181. doi: 10.1042/AN20110014.

Kwiatkowska, A. *et al.* (2011) 'Downregulation of Akt and FAK phosphorylation reduces invasion of glioblastoma cells by impairment of MT1-MMP shuttling to lamellipodia and downregulates MMPs expression', *Biochimica et Biophysica Acta*

- *Molecular Cell Research*. Elsevier B.V., 1813(5), pp. 655–667. doi: 10.1016/j.bbamcr.2011.01.020.

Mannino, M. *et al.* (2014) 'Differential sensitivity of Glioma stem cells to Aurora kinase A inhibitors: Implications for stem cell mitosis and centrosome dynamics', *Stem Cell Research*. The Authors., 13(1), pp. 135–143. doi: 10.1016/j.scr.2014.05.001.

Mao, L. *et al.* (2018) 'Enhancement of invadopodia activity in glioma cells by sublethal doses of irradiation and temozolomide', *Journal of Neurosurgery*, 129(3), pp. 598–610. doi: 10.3171/2017.5.JNS17845.

Minniti, G. *et al.* (2010) 'Patterns of failure and comparison of different target volume delineations in patients with glioblastoma treated with conformal radiotherapy plus concomitant and adjuvant temozolomide', *Radiotherapy and Oncology*. Elsevier Ireland Ltd, 97(3), pp. 377–381. doi: 10.1016/j.radonc.2010.08.020.

Norden, A. D., Drappatz, J. and Wen, P. Y. (2010) 'Malignant gliomas in adults', *Blue Books of Neurology*, 36, pp. 99–120. doi: 10.1016/B978-0-7506-7516-1.00005-0.

Reyes, S. B. *et al.* (2013) 'αvβ8 integrin interacts with RhoGDI1 to regulate Rac1 and Cdc42 activation and drive glioblastoma cell invasion', *Molecular Biology of the Cell*, 24(4), pp. 474–482. doi: 10.1091/mbc.E12-07-0521.

Rutherford, A. *et al.* (2019) 'Evaluation of four different small animal radiation plans on tumour and normal tissue dosimetry in a glioblastoma mouse model', *British Journal of Radiology*, 92(1095). doi: 10.1259/bjr.20180469.

Shen, Q. *et al.* (2004) 'Endothelial cells stimulate self-renewal and expand neurogenesis of neural stem cells', *Science*, 304(5675), pp. 1338–1340. doi: 10.1126/science.1095505.

Trog, D. *et al.* (2006) 'Pro-invasive gene regulating effect of irradiation and combined temozolomide-radiation treatment on surviving human malignant

glioma cells', *European Journal of Pharmacology*, 542(1–3), pp. 8–15. doi: 10.1016/j.ejphar.2006.05.026.

Vitorino, P. M. (2009) 'Modular Control of Endothelial Sheet Cohesion and Collective Cell Migration', *Stanford University Thesis*, 1, pp. 3268–3281. doi: 10.1101/gad.1725808.tracheal.

Vollmann-Zwerenz, A. *et al*. (2020) 'Tumor cell invasion in glioblastoma', *International Journal of Molecular Sciences*, 21(6), pp. 1–21. doi: 10.3390/ijms21061932.

de Vries, N. A., Beijnen, J. H. and van Tellingen, O. (2009) 'High-grade glioma mouse models and their applicability for preclinical testing', *Cancer Treatment Reviews*. Elsevier Ltd, 35(8), pp. 714–723. doi: 10.1016/j.ctrv.2009.08.011.

Wainwright, D. A. *et al*. (2012) 'Recent developments on immunotherapy for brain cancer', *Expert Opinion on Emerging Drugs*, 17(2), pp. 181–202. doi: 10.1517/14728214.2012.679929.

Winkler, F. *et al*. (2004) 'Kinetics of vascular normalization by VEGFR2 blockade governs brain tumor response to radiation', *Cancer Cell*, 6(6), pp. 553–563. doi: 10.1016/j.ccr.2004.10.011.

Wolf, K. and Friedl, P. (2006) 'Molecular mechanisms of cancer cell invasion and plasticity.', *The British journal of dermatology*, 154 Suppl, pp. 11–15. doi: 10.1111/j.1365-2133.2006.07231.x.

# Chapter 4

# Chapter-4 T2 relaxometry and multiple *b*-value diffusion imaging for detection of acute radiation effects on the brain tissue: preliminary experiments

## 4.1 Introduction

Over the last few decades, the technological development in radiation therapy has led to a progressive increase in survival rates for cancer patients (Robbins *et al.*, 2012). As a result, radiation therapy is recognised as one of the major treatment options for cancer patients. However, in the course of radiation therapy used to treat cancer, normal tissues are exposed to radiation. Consequently, patients may experience symptoms associated with damage to normal tissues for a few weeks, months or even years after a course of radiotherapy (Marsh *et al.*, 2010)(Chan *et al.*, 2012). These symptoms may be the result of cell death or wound-healing within irradiated tissue and may be accelerated by exposure to further injury or trauma (Stone *et al.*, 2003).

Immediately after exposure to brain radiation, the pathological process of radiation injury begins. However, clinical and histological features take days, months or years after treatment to become apparent. Based on the time of clinical expression, the commonly classified radiation-induced brain injuries are acute, early-delayed and late-delayed injury (Stone *et al.*, 2003). In fact, the most frequent complications in long term survivors after radiotherapy are cognitive dysfunction and leukoencephalopathy (Crossen *et al.*, 1994). The symptoms of these complications include headaches, drowsiness, vomiting and fever (Keime-Guibert, Napolitano and Delattre, 1998)(Soussain *et al.*, 2009). Hence, the total safe dose which can be targeted at a tumour is limited by the risk of acute and late radiation injury to normal tissues, which has unavoidably been involved in the treatment volume (Greene-schloesser *et al.*, 2012). Thus, understanding the aetiology of radiation-induced acute brain tissue injury and developing a potential strategy for the management of this effect is becoming more important than ever.

In our laboratory, previous pilot experiments were conducted by Dr. Vallatos, to detect clinically relevant structural and functional changes in mouse brains, 24-

and 48-hours post-irradiation. These techniques included whole brain T1 and T2 relaxometry mapping to define anatomical microstructure (Sean C.L. Deoni, 2012), contrast enhanced (CE)-MRI to detect changes in integrity of the BBB (Leten *et al.*, 2014), diffusion weighted (DW)-MRI for oedema (Charles-Edwards and De Souza, 2006), DTI for WM changes including subacute demyelination and late WM necrosis (Wang *et al.*, 2009), ASL to detect acute and late microvascular changes, and MRS to interrogate neuronal markers, neurotransmitters and indicators of mitochondrial injury (Waldman *et al.*, 2009). In the pilot experiments of Dr. Vallatos, most of these techniques did not show any significant changes between IR and non-IR brain hemispheres 24- and 48-hours post-IR (IR=20 Gy). However, there was indication of a difference in quantitative T2 measurements, namely, an increase in the "standard deviation of the fit" parameter obtained using the Bruker Paravision software (Paravision 5.0). This indicated that the signal decay in the IR hemisphere was multi-exponential, rather than the mono-exponential decay found in the non-IR hemisphere.

Multi-exponential decay is characteristic of two or more distinctive relaxation rates within a single voxel. In biological systems the origins of multi-exponential decay are complex and not completely understood, but they can be related to variations in the local chemical composition, rate of molecular tumbling and rate of exchange between different environments/compartments (Bakker and Vriend, 1984). Recently, multi-exponential relaxation analysis has been used to probe the presence of tumour cells in rat glioblastoma (Dortch *et al.*, 2009). In addition, to maximise the information gained from the animals used for the quantitative T2 weighted study, we performed scoping experiments using multiple *b*-value diffusion MRI. Note, this was not a study, as different experimental parameters were tested on different animals.

## 4.2 Aim

Our aim was to investigate the potential of MRI modalities to act as imaging biomarkers to detect radiation-induced damage in the brains of mice. First, we aimed to reproduce previous results obtained by our group. These indicated that quantitative T2 mapping could detect acute effects of radiation. The mice were scanned pre- and only 24 hours post-irradiation, with a 20 Gy single dose to the right brain hemisphere. Second, to obtain more information from these animals,

we intended to investigate multiple *b*-value DWI as a potential imaging biomarker. Note, these multiple *b*-value experiments were scoping experiments and not a designed study.

## 4.3 Methods

### 4.3.1 Animal preparation

All studies were performed in compliance with relevant procedures of The University of Glasgow and approved by the Home Office Local Ethical Review Panel. Nude mice (*n*=6) were irradiated with a single, well-collimated X-ray beam (20 Gy, 2 x 9 $mm^2$) in the right brain hemisphere (Figure 4.1). During the radiation and MRI experiments, animals were anaesthetised with 2-2.5% isoflurane delivered in a 70/30 mixture of $N_2O/O_2$.

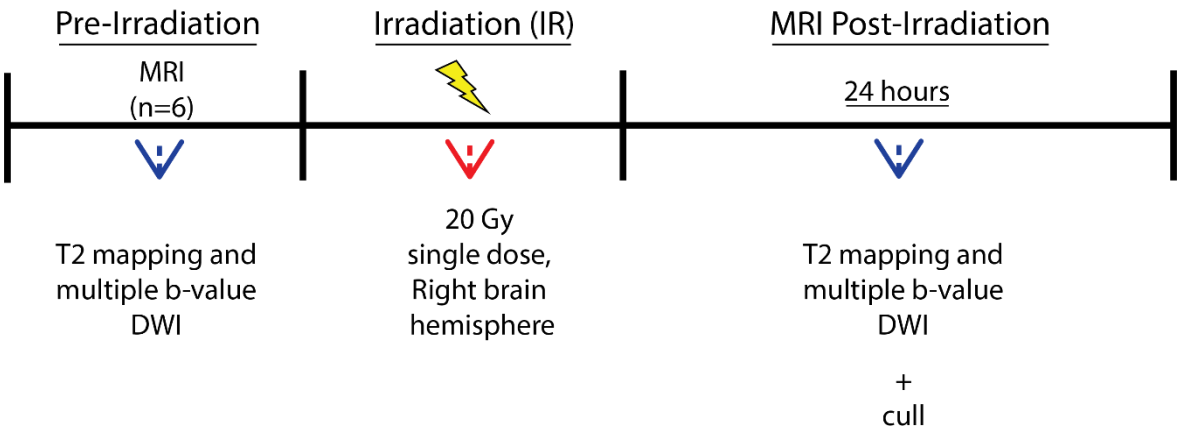


**Figure 4.1: Timeline and design of the experiment.**

### 4.3.2 Irradiation protocols using Small Animal Radiation Research Platform (SARRP)

#### 4.3.2.1 X-ray source

Both for imaging and irradiation SARRP uses a common X-ray source (X-ray tube). A small focal point is desirable for imaging, using between 50-225 kVp (peak voltage) applied across the X-ray tube. For the irradiation of laboratory animals

(i.e. mice), anatomical structures were targeted using the Muriplan software. To allow a greater dose output, a larger focal point is used.

#### 4.3.2.2 Collimation system

A collimator system is used for achieving rigid alignment in the X-ray field. The collimator plays a vital role in adjusting the X-ray field to irradiate only the target area and minimise the dose to other tissues, thus mimicking a clinical situation. Using a beam collimator for the radiation, we can use the CT image to precisely localise the radiation beam in the brain.

#### 4.3.2.3 Imaging system

To ensure that the mouse is in the correct position, a CT image is used. The SARRP imaging system can acquire images in about ~1 minute, meaning that the user can easily verify that the animal is in the correct position. The real benefit of these images is seen when applying a fractionated dose, which requires the mouse to be in the same position for every irradiation visit. Cone-beam CT is achieved by rotating the horizontal animal between the stationary X-ray source and a flat-panel detector (Wong *et al.*, 2008).

#### 4.3.2.4 Animal irradiation studies

The SARRP system, has been designed to allow targeted irradiation studies on small animals. It has been used with beam sizes as small as 0.5 mm and is guided by a radiation on board cone beam CT (CBCT) (Matinfar *et al.*, 2009), which provides a quick and efficient beam size with minimal scatter of radiation to the surrounding tissues. As in clinical irradiation therapy, treatment planning is needed (Gutierrez, Descamps and Vanhove, 2015), hence the SARRP has an integrated CT X-ray scanner.

#### 4.3.2.5 Radiation Therapy Treatment Planning

In planning our radiation therapy, CT scans were acquired and used as described above. For CT image acquisition, animals were moved to the SARRP using the multimodality bed to maintain a fixed mouse head position. The acquired images are used to plan irradiation with the Muriplan treatment planning system. This

software allows for very quick dose planning, organ contouring, fusion images, calculating the irradiation dose and also draws a dose volume histogram. Irradiation planning targets only the particular volume inside the animal, defining the amount of irradiation dose at that point. Based on the target volume and adjacent organs for irradiation, the dose distribution is calculated. Consequently, each treatment plan is different in order to accurately target the irradiation area (Figure 4.2).

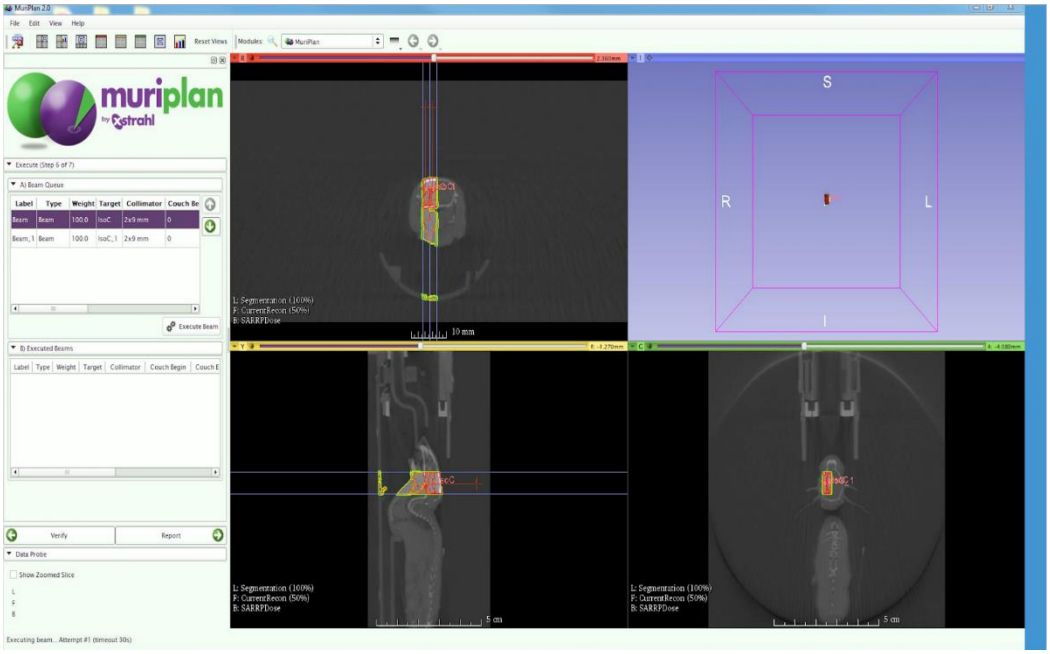


**Figure 4.2: Muriplan Treatment System and 3D representation image on a one mouse treatment plan after irradiation dose countering and dose volume histogram for the right mouse brain hemisphere.**

Mice were immobilised in a fixation device. Under guidance of CT X-ray image, two single-fraction exposures of the mouse right brain hemisphere were performed, which targeted a region of interest of 10 x 10 $mm^2$. The cone beam was applied with the following parameters: 220 kVp, 13 mA and 409 seconds. One mouse brain hemisphere received an absorbed dose of 20 Gy (Figure 4.3).

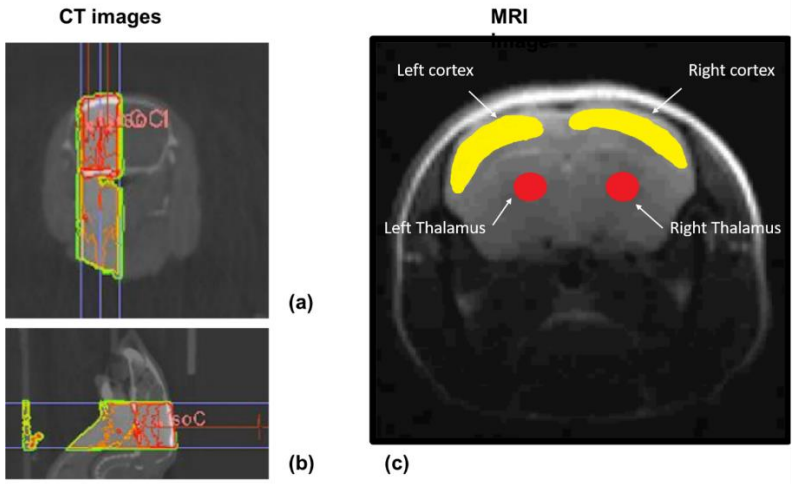


**Figure 4.3: CT X-ray image with 20Gy (IR) dose highlighted on the right brain hemisphere (a) and (b) and MRI image (c).**

## 4.3.3 MRI

MRI was acquired using a horizontal bore 7 T small animal scanner (Bruker Biospec) at pre- and ~ 24-hour post-irradiation (IR) using a high-power gradient coil [400 mT/m] and a 4-channel mouse phased array coil. The animal was transferred to the MRI scanner, secured within the cradle by plastic tape and with tooth and ear bars to restrict head movement, with the four-channel phased array coil positioned on the mouse's head. A closed circuit thermal jacket was used during the experiment to maintain body temperature at 37+/- $0.5^0$ C. A rectal thermocouple was used for assessing body temperature during the experiments.

### 4.3.3.1 MRI Sequences background:

T2 mapping: T2 weighted imaging was performed using the Multiple Slice Multiple Echo sequence (MSME). A multiple echo time data set is acquired and, for each voxel, the signal decay with echo time is fitted to the following Equation 4.1:

**Equation 4.1**

$$S = S_0 \, exp^{(\frac{-t}{T2})}$$

Where: $S_0$ and T2 are the fitting parameters. If this fitting is repeated for all voxels, then several parameter maps can be generated: signal intensity $S_0$, transverse relaxation time T2 and standard deviation of the fit. Note: the transverse relaxation time T2 value is a physical parameter with units of time.

However, application of Equation 4.1 visibly resulted in a poor fit to the data, as it does not consider the positive baseline created by taking the magnitude of the image noise. Hence, Equation 4.2 was used

**Equation 4.2**

$$S = S_0 \, exp^{(\frac{-t}{T2})} + C$$

Where C is a baseline offset. This resulted in significantly better fits (Figure 4.6). In addition, we could use the standard deviation of the fit as a proxy for how mono-exponential the signal decay is.

Multiple *b*-value DWI: DWI permits the non-invasive measurement of water molecule diffusion, which is influenced by tissue configuration at a microscopic level. DWI techniques appear to be useful, particularly in brain abnormality monitoring. In MRI, diffusion can be measured in-vivo by encoding the MR signal to motion see Chapter-2, 2.7.3. When the diffusion gradients are applied, characterised by the parameter *b*, it leads to spin dephasing and signal attenuation dependent upon the diffusion coefficient of the water molecules, as below

**Equation 4.3**

$$S = S_0 \, exp^{-bD}$$

Where S is the measured signal intensity, $S_0$ is the signal without diffusion weighting gradients applied (i.e. b=0) and D is the diffusion coefficient.

From the above Equation 4.3, it is clear that the reduction in signal decays exponentially, according to the *b* factor or value. The *b* value is expressed by the following expression:

**Equation 4.4**

$$b = \gamma^2 \, G^2 \delta^2 \, (\Delta - 1/3)$$

Where: $\gamma$ is the gyromagnetic ratio, G is the gradient strength for encoding diffusion, $\delta$ is the duration for the gradient pulse and Δ is the observation time, which is the time between the leading edges of the pair of gradient pulses.

### 4.3.4 Data collection

T2 weighted images were acquired at multiple echo times using a "multiple slice multiple echo" (MSME), (TE = 7.7ms, TR = 3000, number of echo per images=30 and matrix size 96x96), Field of view (FOV = 1.7 cm), slice thickness = 1.00 mm, number of slices = 3, scan time = 7 min, and number of averages = 4. Scans were performed at two time points (pre- and post-IR) using C57 BL/6 mice in-vivo.

Multiple *b*-value DWIs were acquired with different *b*-values (e.g. *b* = 200, 700, 1200, 1700 and 2200) and directions, as well (30 directions). Spin-Echo–DWIs (SE-DWI) were collected with the following parameters Δ = 12ms, 20, 25 and 100 ms, and $\delta$= 5 and 6 ms, whereas Stimulated Echo Acquisition Mode-DWIs (STEAM-DWI) were acquired with the following parameters Δ = 30ms, 150 and 200 ms and $\delta$= 5. Scan time was 8 min. In these scoping experiments, we tried different imaging parameters on different mice.

## 4.4 Data analysis

For each mouse, the cortex and thalamus in the T2 weighted images were segmented using the tools provided in the Bruker Paravision software. The average values in these regions of interest for the individual cortices and thalamus were then measured. Both the average value and its standard deviation were recorded for each region of interest for each mouse using both the Bruker Paravision system and Matlab. Six mice which were analysed pre-IR, with one mouse being excluded from post-IR analysis due to artefacts in the acquired images.

## 4.5 Results

### 4.5.1 Acute IR effect on T2- analysed with Paravision

T2 mapping data when analysed using Bruker Paravision software (Paravision 5.0) indicated no significant change in actual T2 values (Figure 4.4), but showed an indication of effects due to the differences between standard deviation of the fit with the Paravision software between pre- and post-IR. This indicated a potential indicating a multi-exponential signal decay.

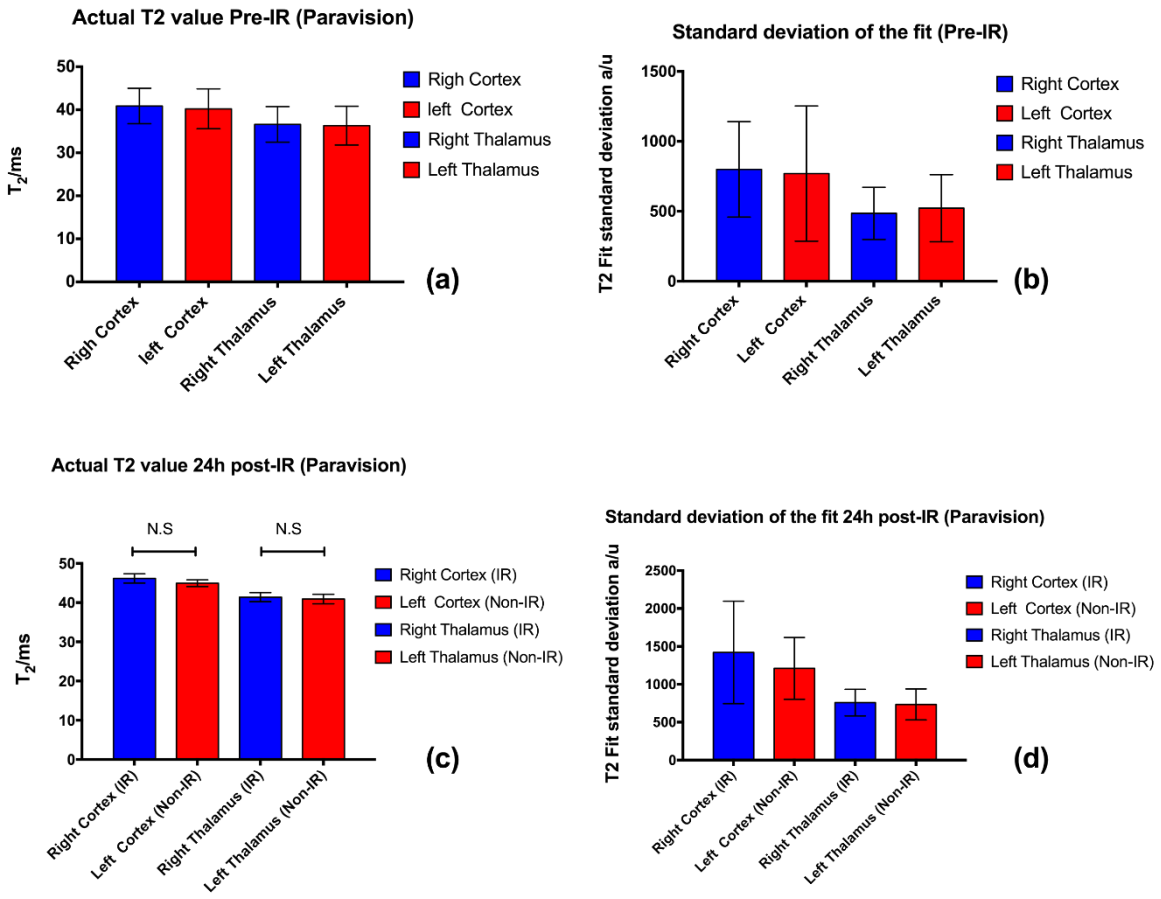


**Figure 4.4: The mean of T2 weighted value (a and c) and standard deviation of the fit (b and d) acquired with Paravision pre- and 24 hours post-IR. Data are presented as the mean ± standard deviation (SD). All statistical analyses analyse were carried out using GraphPad Prism software version 7.0. Statistical analysis: two-tailed, unpaired t test. N.S=not significant, significantly different (P<0.05).**

### 4.5.2 Acute IR effect on T2- analysed with Matlab

The same T2 mapping analysed in the section above, when analysed using in-house Matlab code, also indicated no significant change in actual T2 values (Figure 4.5). However, the Matlab software used $R^2$ to determine the goodness of fit, the value of which, unlike the Paravision parameter ("standard deviation of the fit"), is independent of the signal magnitude.

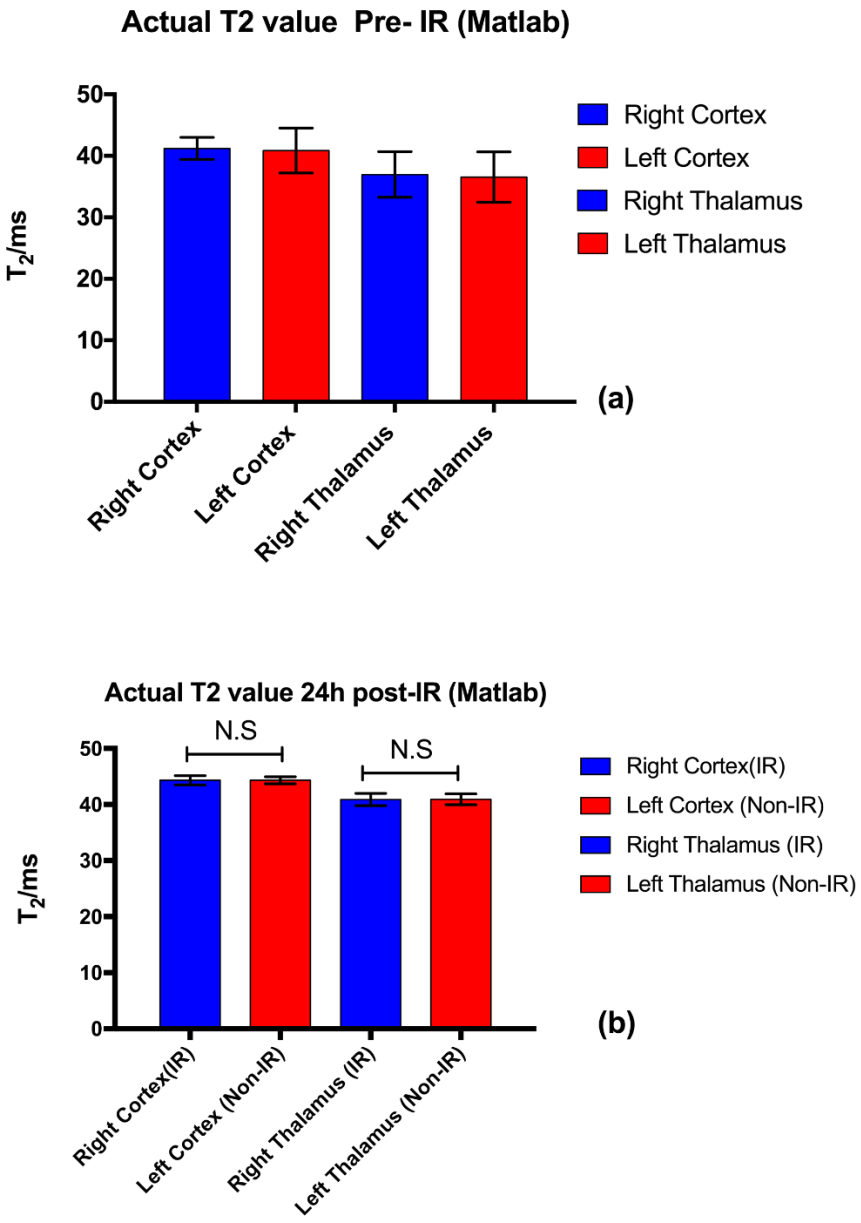


**Figure 4.5: Mean of T2 value (a and b) acquired with Matlab pre-and 24h post-IR. All statistical analyses were carried out using GraphPad Prism software version 7.0. Statistical analysis: two-tailed, unpaired t-test. N.S.=not significant, significantly different (P=0.05). Data are presented as the mean ± standard deviation (SD).**

An example of the signal decay from the T2 mapping data is shown in Figure 4.6, along with Matlab fit. For four regions of interest (right cortex, right thalamus, left thalamus, left cortex) the R-square value was 0.99, which is an almost perfect fit, hence, it shows mono-exponential decay.

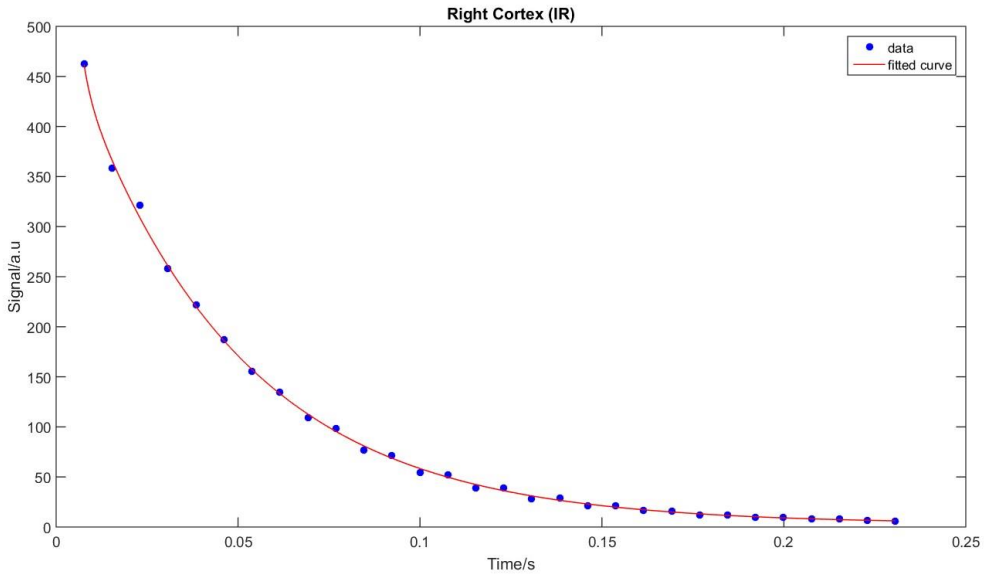


**Figure 4.6: Plot shows example data from a T2 mapping experiment, for the right cortex (IR) 24h post-irradiation. The red curve is the fit to Equation 4.2, using in-house Matlab code.**

### 4.5.3 Acute IR effect on multiple *b*-value DWI

DWI was performed at multiple *b*-values using a Spin Echo (SE-DWI) sequence. Figure 4.7 shows characteristic decays fitted with SE-DWI with Δ=12ms and showed no deviation from normal Gaussian behaviour. However, we found evidence of deviation from normal Gaussian behaviour using multiple *b*-value STE-DWI with Δ= 200 ms, (Figure 4.8) suggesting that diffusion with a long observation time might be informative.

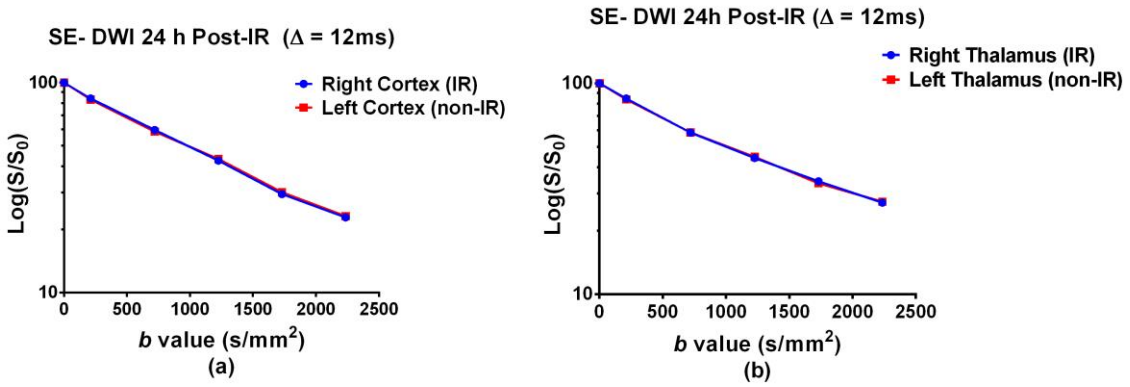


**Figure 4.7:SE-DWI with 12 ms observation time for both right and left cortex and right and left thalamus pre-and 24h post-IR for *n*=1.**

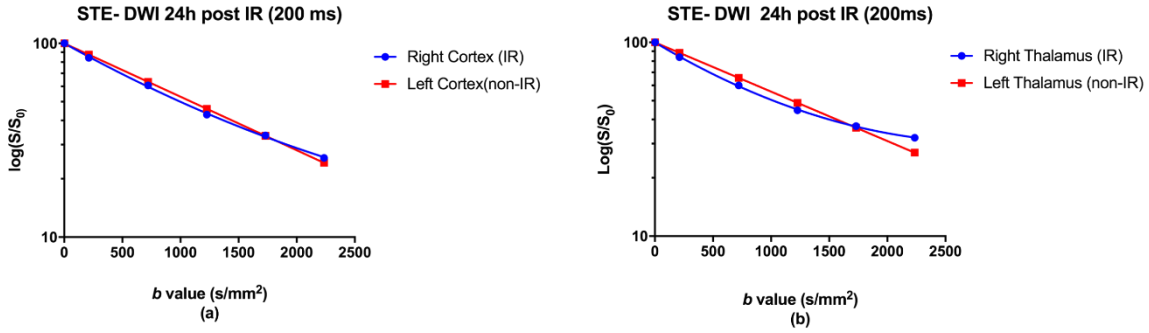


**Figure 4.8: STE-DWI with 200ms observation time for both right and left cortex and right and left thalamus pre-and 24h post-IR for *n*=1.**

## 4.6 Discussion

### 4.6.1 T2 mapping

An earlier pilot study performed by Dr. Vallatos in our lab, investigated whether or not T2 mapping could be used to detect structural and functional changes in mouse brains, 24- and 48-hours post-irradiation. This pilot showed no significant changes in the actual T2 values, but did show a significant difference in the Paravision parameter "standard deviation of the fit", between the right and the left hemispheres for the six mice (Figure 4.9 c). The irradiated hemispheres (right) systematically exhibited higher "standard deviation of the fit", suggesting that the irradiated hemisphere had stronger multi-exponential relaxation behaviour.

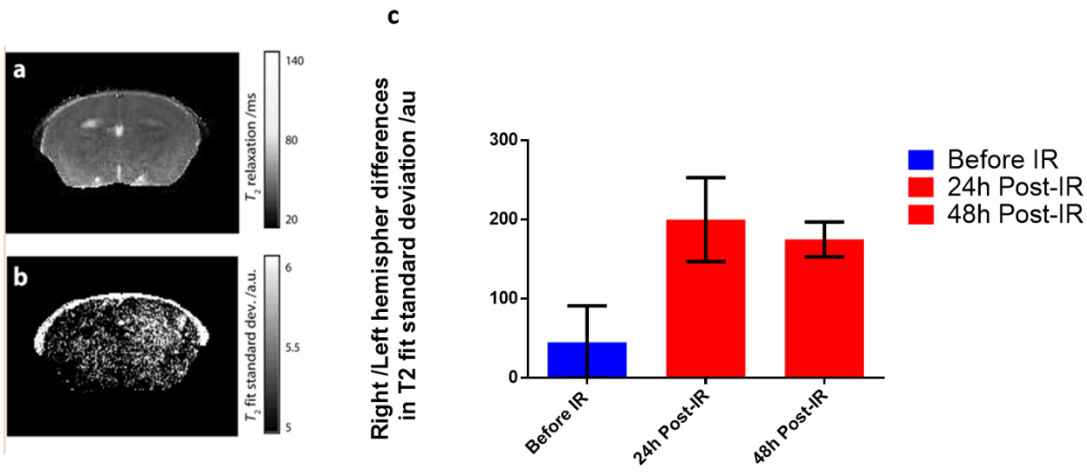


**Figure 4.9: (a) T2 relaxation map and (b) map of the fit standard deviation of the fit for the same data. (c) Difference between right (IR) and left hemisphere fit standard deviation of the fit before and after radiation with 20Gy. The error bars correspond to the standard deviation of the *n*=6 mice.**

In this first study, our aim was to try to reproduce the results of Vallatos. In addition to T2 mapping, it was also decided to investigate multiple *b*-values DWI, as potential imaging biomarkers for post-irradiation microstructural changes. Consistent with the study carried out previously by Dr. Vallatos, this pilot study did not show any significant differences in actual T2 values measured between IR and non-IR brain hemispheres 24 hours post IR. However, unlike Dr. Vallatos, we found no significant difference in the Paravision "standard deviation of the fit", between IR and non-IR brain hemispheres 24 hours post-IR, see Figure 4.4 .

To investigate the lack of agreement with Dr. Vallatos' previous results, we went back and reanalysed our T2 mapping data using an inhouse Matlab program. This Matlab program analysed the goodness of fit via an R-squared parameter, whereas Paravision used a "standard deviation of the fit" parameter. The R-square of the fit indicated no significant differences between IR and non-IR hemisphere, as seen in Figure 4.6.Indeed, for both the IR and non-IR hemispheres the R-square was greater than 0.99, suggesting that there was virtually no multi-exponential behaviour.

Upon further investigation, it was found that the "standard deviation of the fit" parameter used in the Paravision software, depends on the magnitude of the MRI signal. Returning to the experimental data of Dr. Vallatos, we noticed that the head position of the mouse was systematically angled (Figure 4.10). As a consequence, the right hemisphere was systematically closer to the receiver surface coil, resulting in a higher signal, hence a higher value of "standard deviation of the fit". Hence, the difference in standard deviation to the fit between IR and non-IR, found by Dr. Vallatos, was not due to the effect of radiation, but due only to the head position of the animal. In this regard the R-squared measure is far superior, as its value is independent of signal magnitude. Using the R-square measure we found no significant difference between IR and non-IR, indeed, all signal decays were near perfect mono-exponential.

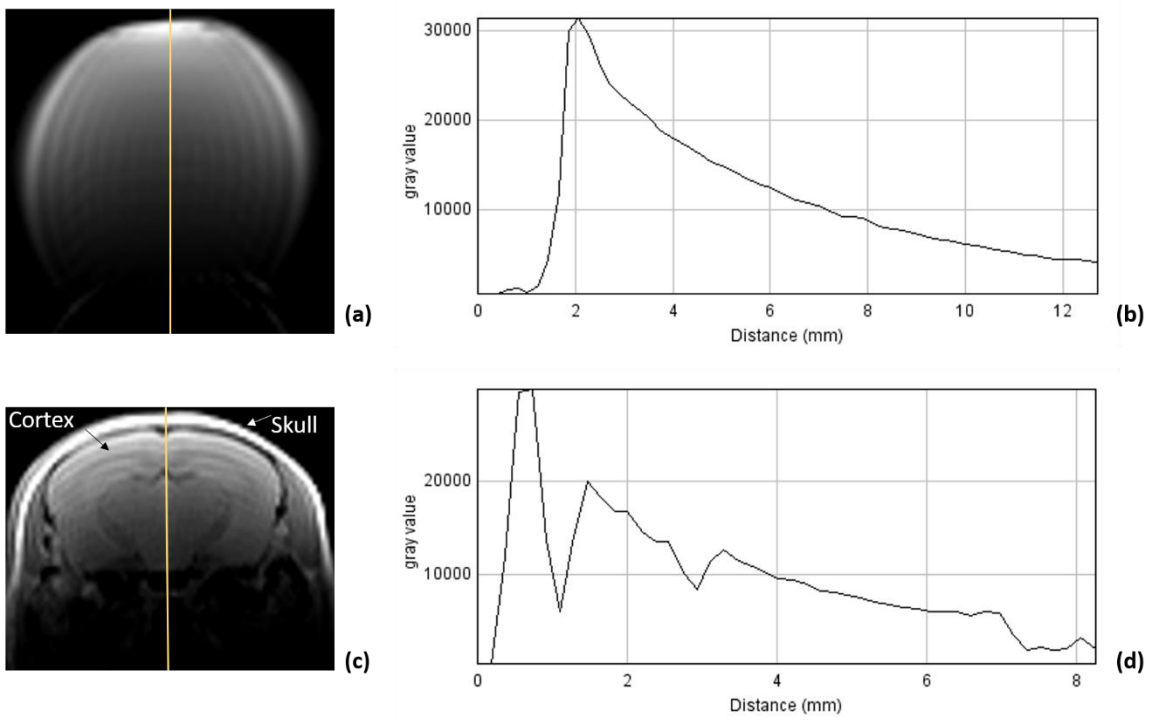


**Figure 4.10: Example images showing signal decay with distance from the receiver coil, illustration (a) T2 weighted image of water phantom, (b) profile from the yellow line, showing the signal decay with distance from RF receiver coil. (c) T2 weighted image of mouse in-vivo, (d) profile from the yellow line showing the signal decay with distance from RF receiver coil.**

### 4.6.2 Multiple *b*-value

To make the fullest use of the animals used in the T2 mapping study, we also performed some additional scoping experiments with multiple *b*-value DWI. In diffusion, *b*-value is a composite measure of imaging parameters and represents the degree of diffusion weighting in the image. Previous studies have shown the diffusion signal decay at high *b*-values, is not well described by a single Gaussian diffusion coefficient. This means that the traditional DWI, does not capture the full extent of information contained in the diffusion encoded signal (Aggarwal, Smith and Calabresi, 2020).

Hence, Diffusion Kurtosis Imaging (DKI) that has been recently proposed to acquire more information about the heterogenous micro-environment of brain tissue (Hui *et al.*, 2008). Furthermore, DKI has recently been shown to be a sensitive biomarker for microstructures in health and disease (Henriques, Jespersen and Shemesh, 2020). Such non-Gaussian diffusion imaging has shown clinical value in traumatic brain injury (Karlsen *et al.*, 2019)(Grossman *et al.*, 2012),glioma (Jiang *et al.*, 2015), neurodegenerative disease , and the spinal cord (Raz *et al.*, 2013).

Consequently, we considered that deviation from Gaussian diffusion could be used as an indication of brain microstructural changes after irradiation. The pilot data from the multiple *b*-value DWI did show a deviation from Gaussian behaviour, in the right brain hemisphere. However, this result was observed in only one of the scoping experiments performed on one animal.

## 4.7 Conclusion

The aim of this study was to assess the ability of quantitative T2 mapping to detect microstructural changes resulting of from ionising radiation-induced early brain injury. Consistent with an earlier study by Dr. Vallatos, T2 data analysed with both Paravision and Matlab software indicated no significant differences between in T2 values for the IR and non-IR brain hemisphere. However, unlike Dr. Vallatos, we found no significant differences in the Paravision "standard deviation of fit" parameter. Upon investigation, we found that the "standard deviation of the fit" parameter was a poor measure, as it depended on the magnitude of the MRI signal. Instead, our in- house Matlab code was used for determining the goodness of the fit, using an $R^2$ of the fit, which is independent of the signal magnitude. In addition, we performed some scoping experiments using multiple *b*-value DWI. In one experiment, using STE acquisition with a long observation time (200ms), we found an indication of non-Gaussian diffusion in the irradiated hemisphere. In the next chapter, we investigate this further and more systematically in a larger group of mice.

## 4.9 References


Aggarwal, M., Smith, M. D. and Calabresi, P. A. (2020) 'Diffusion-time dependence of diffusional kurtosis in the mouse brain', *Magnetic Resonance in Medicine*, (January), pp. 1–15. doi: 10.1002/mrm.28189.

Bakker, C. J. G. and Vriend, J. (1984) 'Multi-Exponential water proton spin-lattice relaxation in biological tissues and its implications for quantitative NMR imaging', *Physics in Medicine and Biology*, 29(5), pp. 509–518. Available at: papers3://publication/uuid/57165B7A-154F-42CA-8AF6-7F78ADC8720B.

Chan, M. D. *et al.* (2012) 'Radiation-induced brain injury: A review', *Frontiers in Oncology*, 2(July), pp. 1–18. doi: 10.3389/fonc.2012.00073.

Charles-Edwards, E. M. and De Souza, N. M. (2006) 'Diffusion-weighted magnetic resonance imaging and its application to cancer', *Cancer Imaging*, 6(1), pp. 135–143. doi: 10.1102/1470-7330.2006.0021.

Crossen R.Jhon, Garwood Dan, G. E. and N. A. E. (1994) 'Neurobehavioral sequelae of cranial irradiation in adults: A review of radiation-induced encephalopathy', *Journal of Clinical Oncology*, 12(3), pp. 627–642. Available at: http://ovidsp.ovid.com/ovidweb.cgi?T=JS&PAGE=reference&D=emed3&NEWS=N&AN=1994087595.

Dortch, R. D. *et al.* (2009) 'Evidence of multiexponential T2 in rat glioblastoma', *NMR in Biomedicine*, 22(6), pp. 609–618. doi: 10.1002/nbm.1374.

Greene-schloesser, D. *et al.* (2012) 'Radiation-induced brain injury : a review', 2(July), pp. 1–18. doi: 10.3389/fonc.2012.00073.

Grossman, E. J. *et al.* (2012) 'Thalamus and cognitive impairment in mild traumatic brain injury: A diffusional kurtosis imaging study', *Journal of Neurotrauma*, 29(13), pp. 2318–2327. doi: 10.1089/neu.2011.1763.

Gutierrez, S., Descamps, B. and Vanhove, C. (2015) 'MRI-Only Based Radiotherapy Treatment Planning for the Rat Brain on a Small Animal Radiation Research Platform (SARRP)', *Plos One*, 10(12), p. e0143821.

Henriques, R. N., Jespersen, S. N. and Shemesh, N. (2020) 'Correlation tensor magnetic resonance imaging', *NeuroImage*, 211(January). doi: 10.1016/j.neuroimage.2020.116605.

Hui, E. S. *et al.* (2008) 'Towards better MR characterization of neural tissues using directional diffusion kurtosis analysis', *Neuroimage*, 42(1), pp. 122–134.

Jiang, R. *et al.* (2015) 'Diffusion kurtosis imaging can efficiently assess the glioma grade and cellular proliferation', *Oncotarget*, 6(39), pp. 42380–42393. doi: 10.18632/oncotarget.5675.

Karlsen, R. H. *et al.* (2019) 'Diffusion kurtosis imaging in mild traumatic brain injury and postconcussional syndrome', *Journal of Neuroscience Research*, 97(5), pp. 568–581. doi: 10.1002/jnr.24383.

Keime-Guibert, F., Napolitano, M. and Delattre, J. Y. (1998) 'Neurological complications of radiotherapy and chemotherapy', *Journal of Neurology*, 245(11), pp. 695–708. doi: 10.1007/s004150050271.

Leten, C. *et al.* (2014) 'In vivo and ex vivo assessment of the blood brain barrier integrity in different glioblastoma animal models', *Journal of neuro-oncology*, 119(2), pp. 297–306. doi: 10.1007/s11060-014-1514-2.

Marsh, J. C. *et al.* (2010) 'Cognitive Sparing during the Administration of Whole Brain Radiotherapy and Prophylactic Cranial Irradiation: Current Concepts and Approaches', *Journal of Oncology*, 2010, pp. 1–16. doi: 10.1155/2010/198208.

Matinfar, M. *et al.* (2009) 'Image-guided small animal radiation research platform: Calibration of treatment beam alignment', *Physics in Medicine and Biology*, 54(4), pp. 891–905. doi: 10.1088/0031-9155/54/4/005.

Raz, E. *et al.* (2013) 'A better characterization of spinal cord damage in multiple sclerosis: A diffusional kurtosis imaging study', *American Journal of Neuroradiology*, 34(9), pp. 1846–1852. doi: 10.3174/ajnr.A3512.

Robbins, M. *et al.* (2012) 'Imaging Radiation-Induced Normal Tissue Injury',

*Radiation Research*, 177(4), pp. 449–466. doi: 10.1016/j.surg.2006.10.010.Use.

Sean C.L. Deoni (2012) 'Quantitative Relaxometry of the Brain Sean', *Journal of Rehabilitation*, 78(3), pp. 20–26. doi: 10.1097/RMR.0b013e31821e56d8.Quantitative.

Soussain, C. *et al.* (2009) 'CNS complications of radiotherapy and chemotherapy', *The Lancet*. Elsevier Ltd, 374(9701), pp. 1639–1651. doi: 10.1016/S0140-6736(09)61299-X.

Stone, H. B. *et al.* (2003) 'Effects of radiation on normal tissue: consequences and mechanisms', *The lancet oncology*, 4(9), pp. 529–536.

Waldman, A. D. *et al.* (2009) 'Quantitative imaging biomarkers in neuro-oncology', *Nature Reviews Clinical Oncology*. Nature Publishing Group, 6(8), pp. 445–454. doi: 10.1038/nrclinonc.2009.92.

Wang, S. *et al.* (2009) 'Longitudinal diffusion tensor magnetic resonance imaging study of radiation-induced white matter damage in a rat model', *Cancer Research*, 69(3), pp. 1190–1198. doi: 10.1158/0008-5472.CAN-08-2661.

Wong, J. *et al.* (2008) 'High-Resolution, Small Animal Radiation Research Platform With X-Ray Tomographic Guidance Capabilities', *International Journal of Radiation Oncology Biology Physics*, 71(5), pp. 1591–1599. doi: 10.1016/j.ijrobp.2008.04.025.

# Chapter 5

# Chapter-5 Preliminary study using diffusion MRI to detect early delayed radiation-induce brain injury

## 5.1 Introduction:

DWI is sensitive to various factors, such as intra- and extra-cellular spaces and the degree of cellularity. For example, in glioblastoma patients with true recurrence, there is more intracellular space and a higher concentration of malignant cells at the site of recurrence, which means there is highly restricted diffusion due to less free random motion of water molecules (Walker *et al.*, 2014). With normal diffusion, the water molecules diffuse with a Gaussian distribution of displacements, however, when water diffuses within more complex structures it can lead to non-Gaussian displacement distributions (Derek K. Jones, 2011). In this chapter we describe how we investigated such non-Gaussian diffusions, initially using DWI with three gradient directions (X, Y and Z) but with multiple *b*-values. This allowed the full signal decay with *b*-values to be analysed. Note, this can be extended to performing measurements using the gradient in multiple directions, a technique called Diffusion Kurtosis Imaging (DKI). Micro-structural changes or the effect of the rate of exchange across, such as intracellular and extra-cellular barriers, can be identified using DKI (Andrew B Rosenkrantz *et al.*, 2015). A more accurate model of diffusion for quantifying the deviation from a Gaussian distribution can be provided by DKI (Jiang *et al.*, 2015) (Figure 5.1). Furthermore, DKI can detect changes in GM and fibre crossing (Cauter *et al.*, 2012)(Raab *et al.*, 2010). It has shown utility in detecting ischemia and infarction (Hui *et al.*, 2012), traumatic brain injury (Grossman *et al.*, 2012), neoplasm (Cauter *et al.*, 2012)(Raab *et al.*, 2010)(Tietze *et al.*, 2015), demyelination diseases (Yoshida *et al.*, 2013). Hence, DKI may be more suitable for the detection of microstructural changes in tissues and cells than DWI and DTI (Jiang *et al.*, 2015). Additionally, an advantage of DKI over FA is that, it can be used to evaluate both GM and WM, because DK does not rely on spatially oriented tissue structures (Hori *et al.*, 2012). Furthermore, non-monoexponential decays are experimentally observed in both GM and WM when high *b* values are used (Wu and Cheung, 2010)(Niendorf *et al.*, 1996)(Assaf and Cohen, 1998). Historically, at *b*- values greater than 1000 s/mm$^2$, the ability of clinical MRI scanners abilities to obtain

images are limited, owing to limited SNR and increased anatomic distortions and larger induced eddy current (Andrew B. Rosenkrantz *et al.*, 2015).

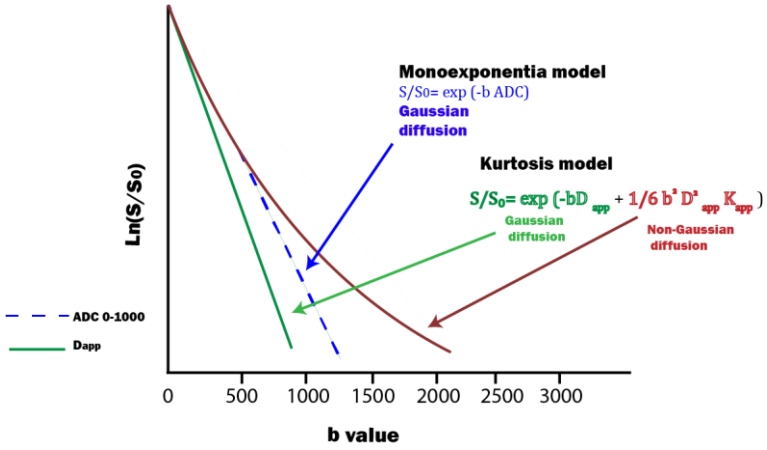


**Figure 5.1: Schematic diagram showing comparison of diffusion signal intensity decay plots for monoexponential model, reflecting solely Gaussian diffusion and kurtosis model, reflecting both components of Gaussian and non-Gaussian diffusion. (Modified from** (Andrew B. Rosenkrantz *et al.*, 2015)**)**

DKI technique uses a diffusion sensitizing pulse sequence and the signal intensity data are fitted to the functional form (Equation 5.1) (Jensen *et al.*, 2005)(Jensen and Helpern, 2010).

$$S = S_0 \exp(-bD_{app} + \frac{1}{6}\ b^2\ D_{app}^2\ K_{app}\ )$$

**Equation 5.1**

Where $S_0$ is the signal intensity without diffusion gradients ($b$=0), where $D_{app}$ is the ADC, and $K_{app}$ is the apparent diffusional kurtosis. The $b$ value is given by $b=\gamma^2\delta^2G^2(\Delta-\delta/3)$. Where G is the gradient strength, γ is the nuclear spin gyromagnetic ratio and Δ is the observation time, the time between the leading edges of the two diffusion gradients.

## 5.2 Aim:

In this chapter we describe how we used DWI-MRI with multiple *b*-values to investigate the effect of ionising radiation on healthy mouse brain tissues, using

histology sections to relate any MRI changes to micro-structural changes following irradiation.

## 5.3 Materials and methods

### 5.3.1 Mouse experiments

Female CD1 nude mice (*n*=8) were irradiated in the right brain hemisphere with a 20 Gy single dose. Two single fraction exposures of mouse brains were performed in the right brain's hemispheres. All mice were scanned pre-irradiation and at 24 hours, 10, 17, 60 and 80 days post-irradiation (Figure 5.2). Mice were monitored for the duration of the experiment and were euthanised on the last day post-MRI scan (day 80).

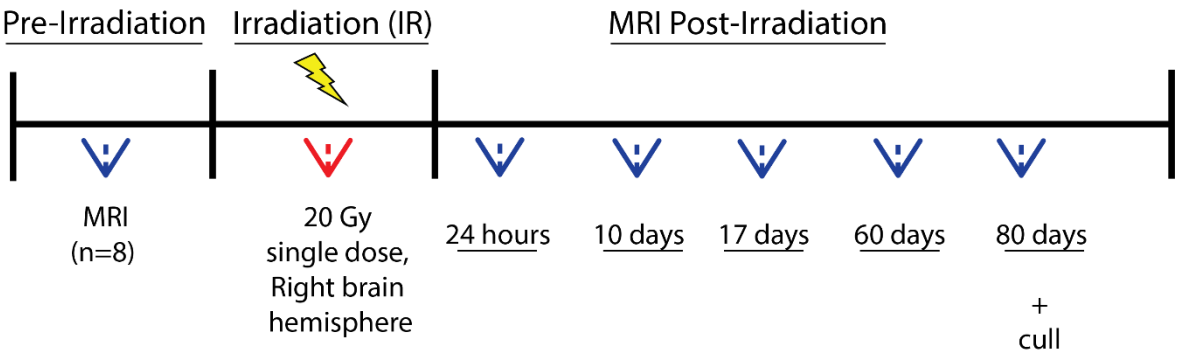


**Figure 5.2: Experimental design and timeline.**

### 5.3.2 MRI

The MRI was acquired with a Bruker Biospec 7 T small animal scanner using a high-power gradient coil [400 mT/m] and a 4-channel mouse-phased array coil. The animal was transferred to the MRI scanner, secured within the cradle using plastic tape and with tooth and ear bars to restrict head movement. The four-channel phased array coil was then positioned on the mouse's head. A closed-circuit thermal jacket was used during the experiment to maintain body temperature at 37± $0.5^0$ C. Multiple *b*-value Spin Echo Diffusion Weighted Images (SE-DWI) were collected in three diffusion directions (X, Y, Z) with different *b*-values (*b*=109,221,345,464,636,916 and 1245) and for different observation times , Δ= 20, 50 and 80 ms. Using δ=5 ms, number of slices = 1, slice thickness = 1.5 mm,

TR = 4000 ms and number of averages = 1. Stimulated Diffusion Weighted Images (STE-DWI) were collected in three diffusion directions (X, Y, Z) with different *b*-values (*b*=109,221,345,464,636,916 and 1245), $\Delta = 200$, and 400 ms, small delta $\delta$=5 ms, number of slices = 1, slice thickness = 1.5 mm, TR = 4000 ms and number of averages = 2. Two different MRI acquisitions were used to probe molecular diffusion. For a short range of structures, SE-DWI was used see section 2.2.6 and for a long range of structures STE-DWI was used se section 2.7.2 in Chapter-2.

### 5.3.3 Segmentation

For each mouse, the cortex, thalamus and fimbria in the SE-DWI and STE-DWI were segmented using the tools provided in the Bruker Paravision 5.0 software. WM plays a key role in cognition by linking cortical territories, whereas the cortex (GM) plays a vital role in memory and cognition in the frontal and temporal lobes and the hippocampal regions (Makale *et al.*, 2017). In the WM, fimbria is the most sensitive region to X-ray (Yang *et al.*, 2017) (Tsuruda *et al.*, 1987). In addition, changes in brain WM are time dependent (Kurita *et al.*, 2001) and the thalamus was selected as there is strong evidence it contributes directly to cognitive functions as a diverse as attention, memory, perception, motor planning, language processing, motivation and decision making (Moustafa *et al.*, 2017). The average signal in these ROIs for the individual cortices, thalamus and fimbria were then measured and normalised to the initial signal at all different time points in all gradient directions (X, Y and Z). The average signals from all regions of interest were plotted with GraphPad Prism tools for all gradient directions (X, Y and Z) at all-time points.

### 5.3.4 Histology:

After the MRI experiment, the mouse brains were transcardially perfused with 4% paraformaldehyde (PFA). The brains were then removed and cut into 6-micron sections through to the level of the fimbria and the hippocampus and stained with hematoxyline and eosin (H&E) for general morphological examination, GFAP and Luxol fast blue (LFB).

## 5.4 Results

Using two MRI sequences (SE-DWI and STE-DWI) and different observation times, we investigated the acute and early delayed effects of ionizing radiation on healthy mouse brain tissues. Unlike the result that was described in Chapter-4, where a deviation from Gaussian distribution behaviour was found 24 hours post-irradiation (*n*=1), see section 4.5.3. However, using a large group size in this study we found no ROI's showed any significant difference between irradiated and non-irradiated brain hemispheres (*n*=8) (Figure 5.3).

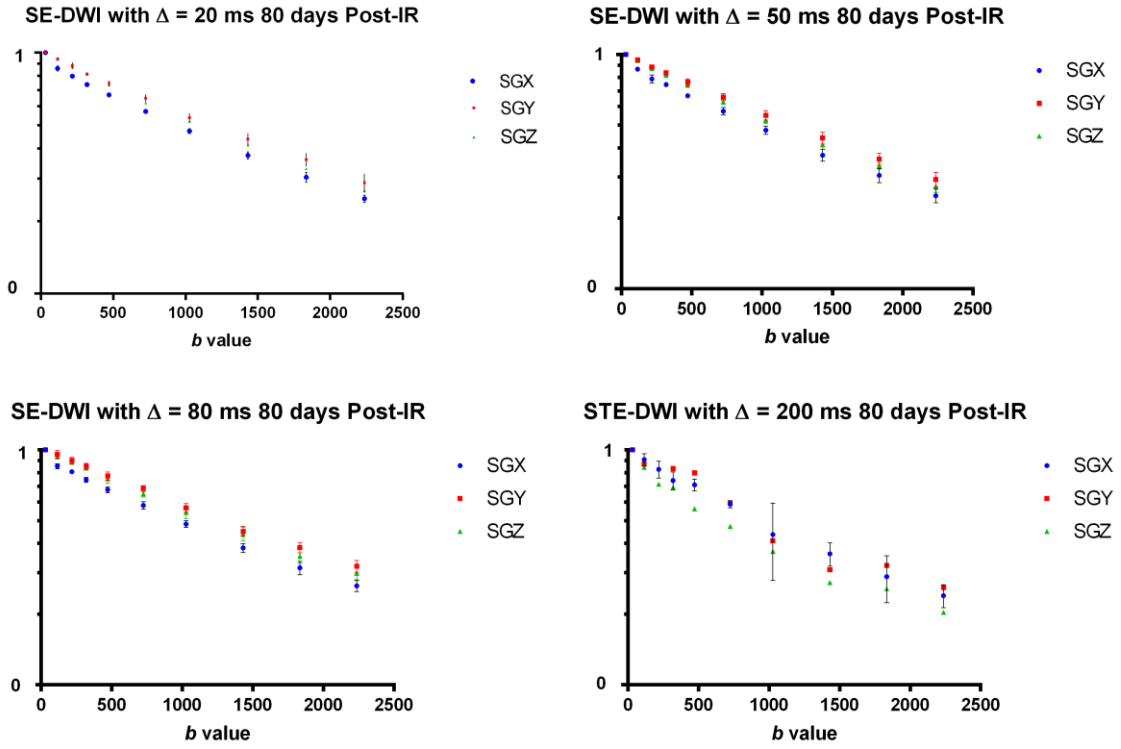


**Figure 5.3: Average DWI signal decay (n=8) from right cortex for all gradient directions (X, Y and Z).**

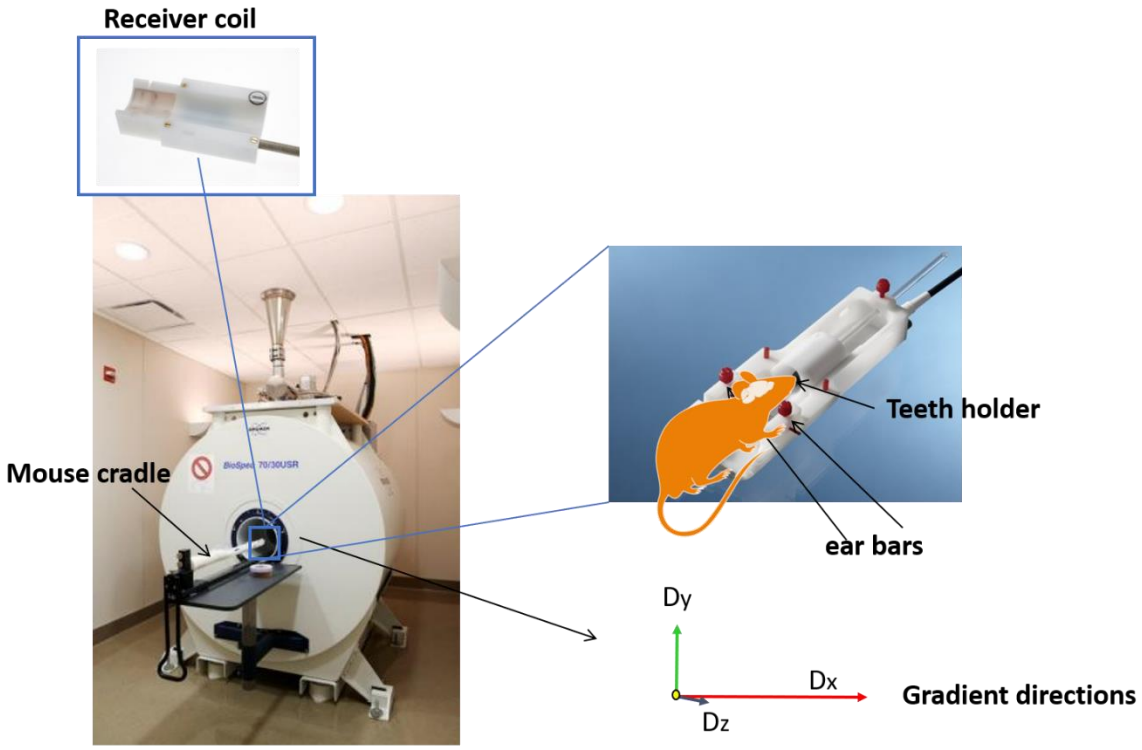


**Figure 5.4: Image show preclinical 7T MRI and gradient frame of references. The gradient direction are determined by three physical gradient coils (X, Y, Z), with the direction marked on the gradient insert.**

## 5.5 MRI Findings:

Figure 5.5 and Figure 5.6 illustrate the different images acquired using the SE-DWI sequence with different *b*-values and in all gradient directions. There are no noticeable differences between irradiated and non-irradiated brain hemispheres. However, using the STE-DWI sequence with 200 ms observation time, visual effects can be seen on the right brain hemisphere, particularly in the X direction, but not in the Y and Z directions. On inspection of the individual SE-DWI images (Figure 5.5) , there was no noticeable changes along any gradient directions, whereas with STE-DWI with long observation time (Figure 5.6), there was a noticeable drop in the signal in the fimbria with the gradient in the X direction. Figure 5.7 show a representative DTI colour map image, which illustrates the principle diffusion direction in a mouse brain. The black spot shown in Figure 5.6 using the X-gradient, appears to correspond to fimbria, where the principle diffusion direction is along the X-axis. Figure 5.8 shows the measurement of diffusion coefficient for all directions, X, Y and Z, and shows no significant differences difference between

ROI's for all gradient directions (X,Y and Z), however, looking to the standard deviation error between right and left fimbria there was an indication of an effect (Figure 5.8 (a)).

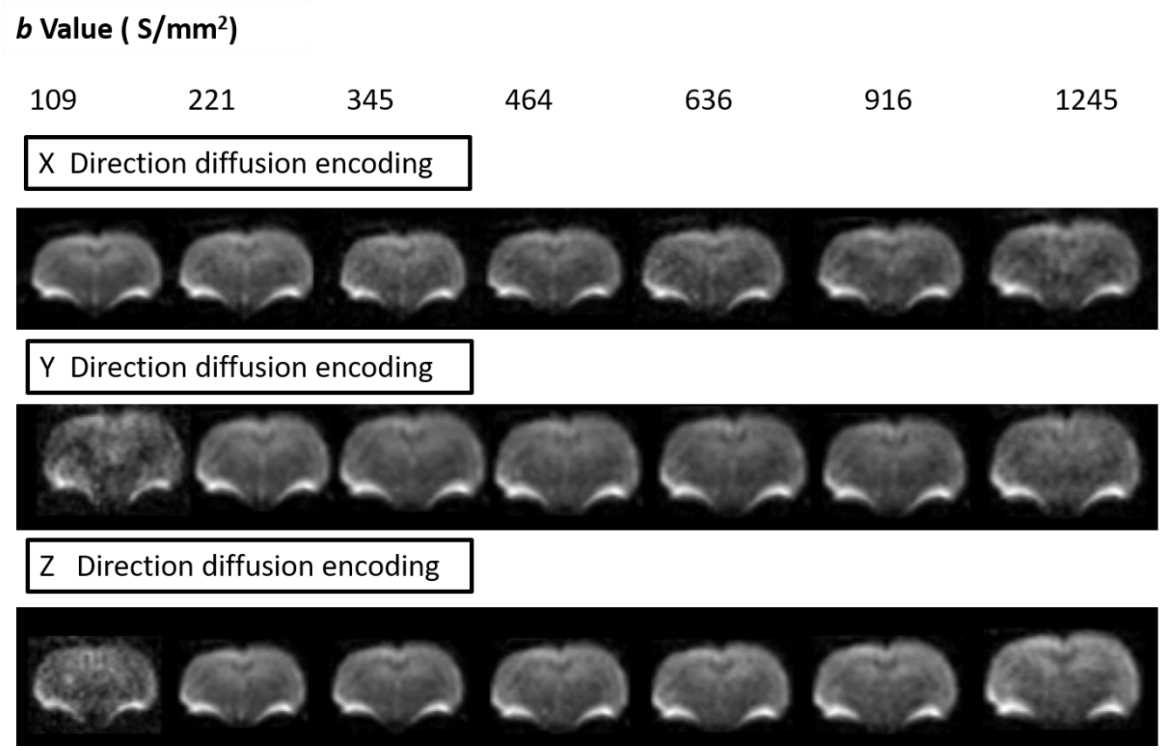


**Figure 5.5: Images acquired, at day 60 post-IR, from different *b*-values using the SE-DWI sequence with 50 ms observation time.**

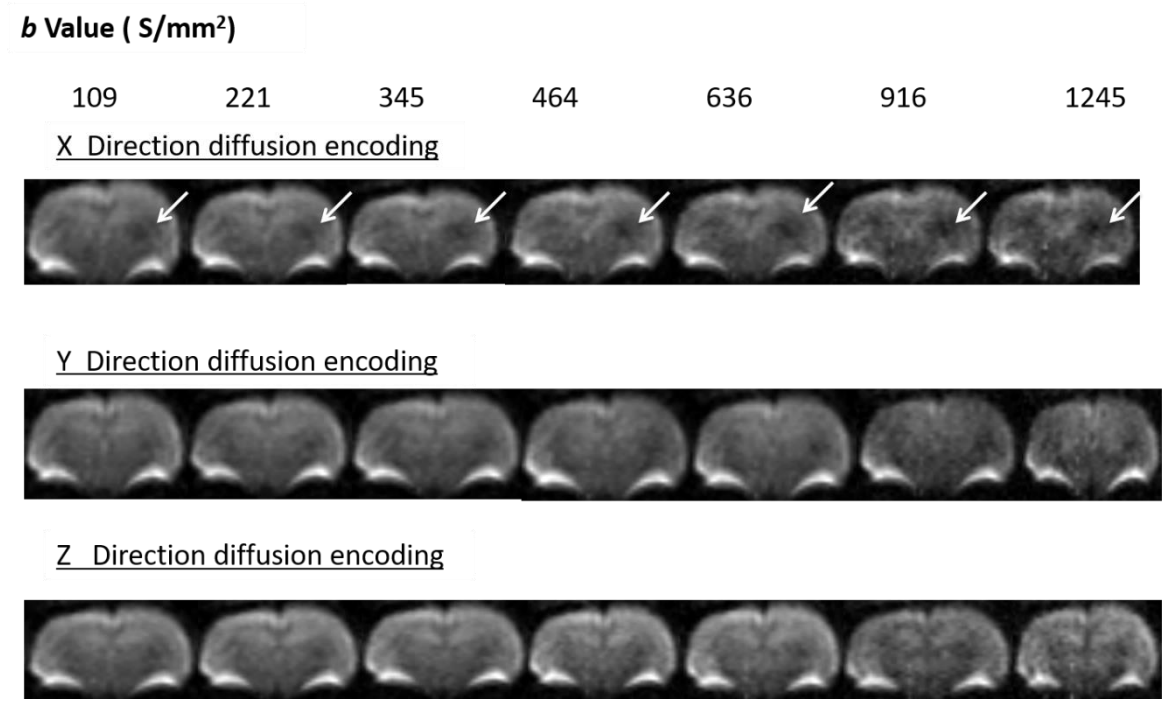


**Figure 5.6: Images acquired, at day 60 post-IR, from different *b*-values using the STE-DWI sequence with 200 ms observation time. White arrows indicate the visual effects of irradiation in the fimbria in the X direction encoding diffusion with different *b*-values.**

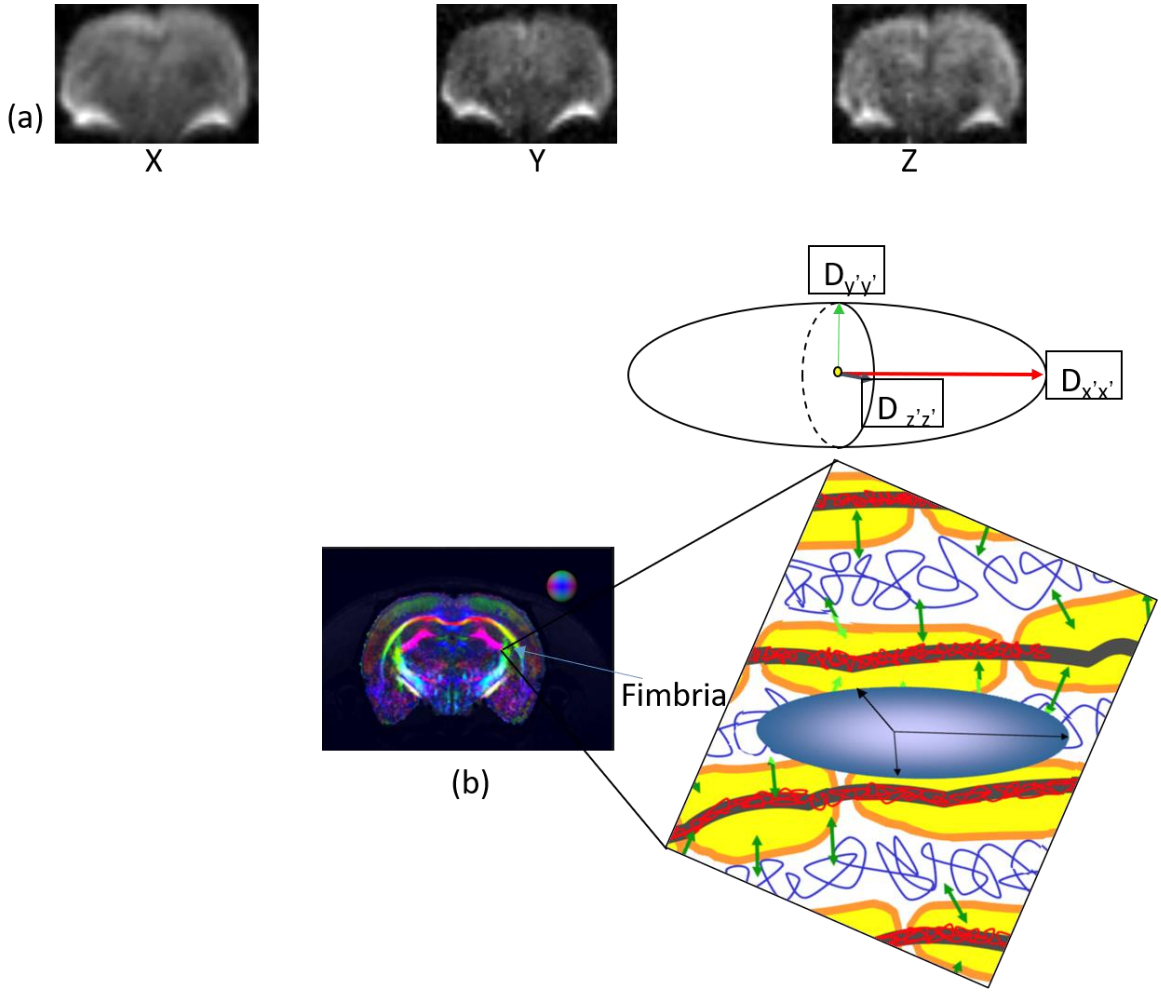


**Figure 5.7: Image shows (a) diffusion weighted images with X , Y, Z diffusion gradient applied (b) A representative DTI colour map of a mouse brain , indicating the principle diffusion direction (Red-x axis, Green- y axis, Blue-z axis) shows schematic diagram of water diffusion within the fimbria.**

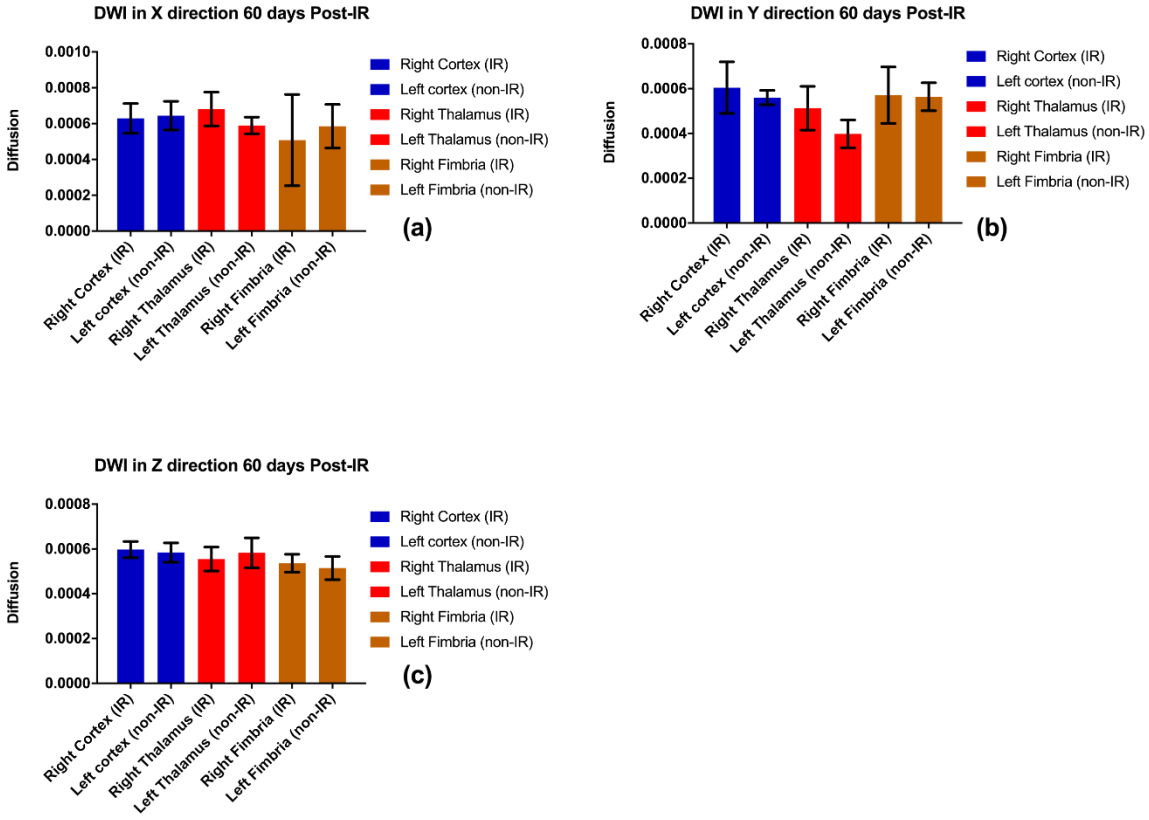


**Figure 5.8: Images (a) to (c) were acquired at day 60 post-IR using STE-DWI with 200 ms observation time. They show measured diffusion coefficients in all gradient directions (*n*=5) for different regions of interest. Graphs (a), (b) and (c) show the average diffusion for X, Y and Z directions for right and left cortex, right and left thalamus and right and left fimbria. Data presented as the mean ± standard deviation (SD), all statistical analysis analyse were carried out using GraphPad Prism software version 7.0. Statistical analysis: two tailed, unpaired t test. N.S=not significant, significantly different (P<0.05).**

## 5.6 Histopathology:

Histopathological analysis was done by a post-doctoral researcher Dr. Apostolos Zarros. Below, we present the results of the assessment of H&E, cresyl violet, GFAP and LFB staining in CNS structures of relevance such as the hippocampus, fimbria, external capsule, thalamus and selected cortical regions. To highlight the important features of the tissue as well as to enhance the tissue contrast, H&E staining was used. Haematoxylin stains cell nuclei giving them a bluish colour while eosin stains the extracellular matrix and cytoplasm giving it a pink colour (Alturkistani, Tashkandi and Mohammedsaleh, 2015). GFAP is frequently used as a reliable marker of tumours with glial origin and astrocytes (Duffy, Huang and Rapport, 1982)(Rutka *et al.*, 1997). Furthermore, GFAP is a standard for visualization of reactive astrocytes (Schmidt-Kastner *et al.*, 1993). The myelin sheath surrounds the axons of nerve cells and is vulnerable to radiation injury. Demyelination was determined by LFB staining, which is the stain commonly stain used to detect demyelination in the CNS (Chen *et al.*, 2013).

H&E staining revealed no significant changes between the examined regions, with the exception of a mild histological disorganization and demyelination that was evident in selected sections of the irradiated fimbria (compared with the respective non-irradiated ones)(Figure 5.9).

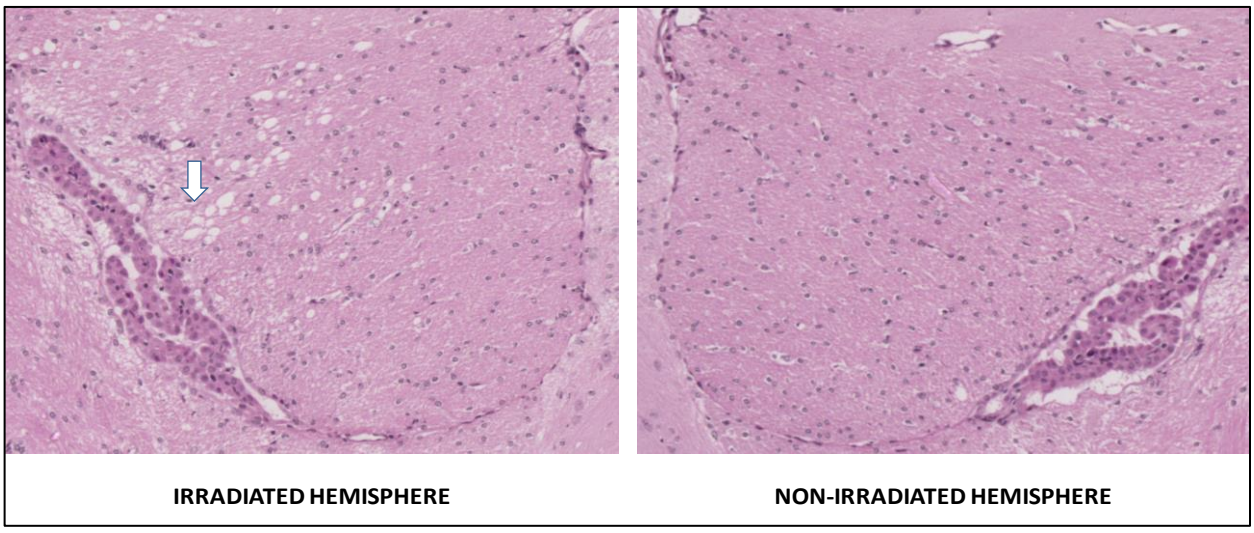


**Figure 5.9: Representative sections of the fimbria of hippocampus from an irradiated mouse brain stained with H&E in both ipsilateral and contralateral hemispheres. The arrow indicates spongiform changes are more prominent and tissues appear more disorganised.**

Both the caudoputamen region of the striatum and the amygdala nuclei exhibited significant overexpression of GFAP in the irradiated hemispheres compared with the respective non-irradiated anatomical regions (n=4/4) (Figure 5.10).

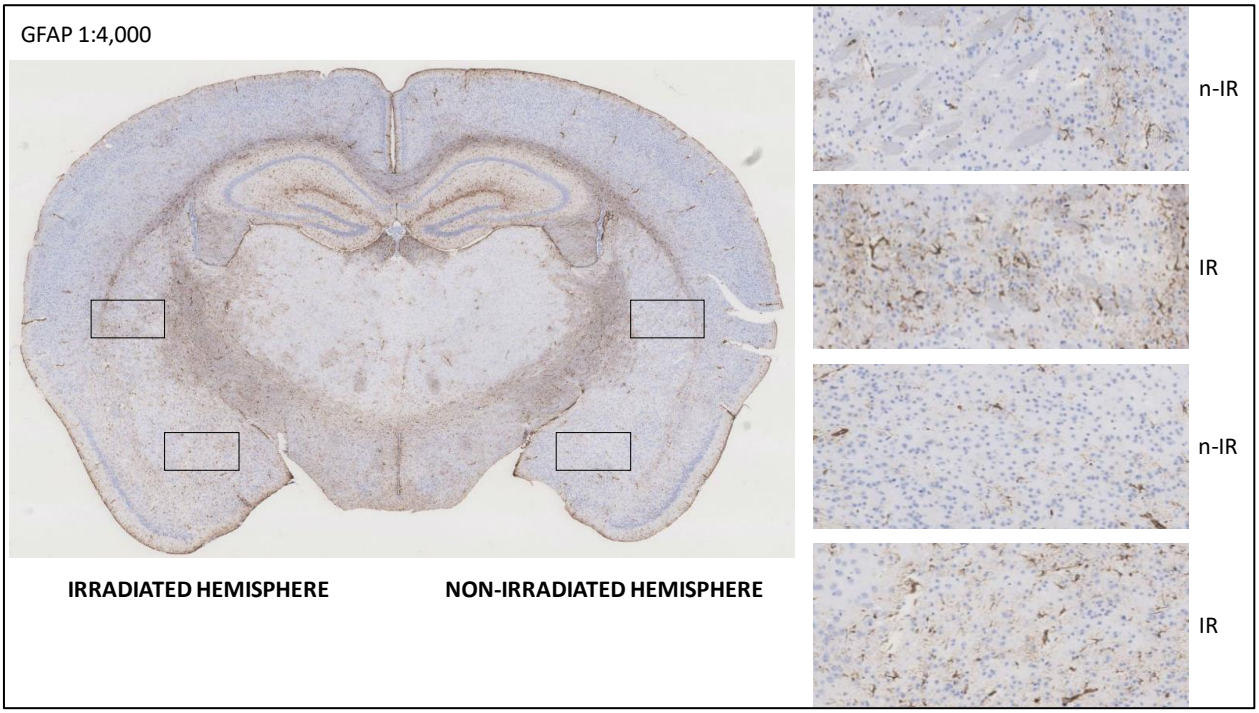


**Figure 5.10: Image shows more GFAP stain in the caudoputamen region of the striatum and the amygdala.**

A similar effect was evident in the posterior parietal association areas of the cortex of the irradiated hemisphere, compared with the non-irradiated equivalent (Figure 5.11 (a)). Neither the cellularity (assessed with cresyl violet), nor the GFAP-positive cells displayed any significant differences in the Cornu Ammonis (CA3) region of the hippocampus when a comparison was attempted between irradiated and non-irradiated regions (Figure 5.11 (b)). The CA3 region has a specific role in memory process, susceptibility to seizures, and neurodegeneration (Cherubini and Miles, 2015).

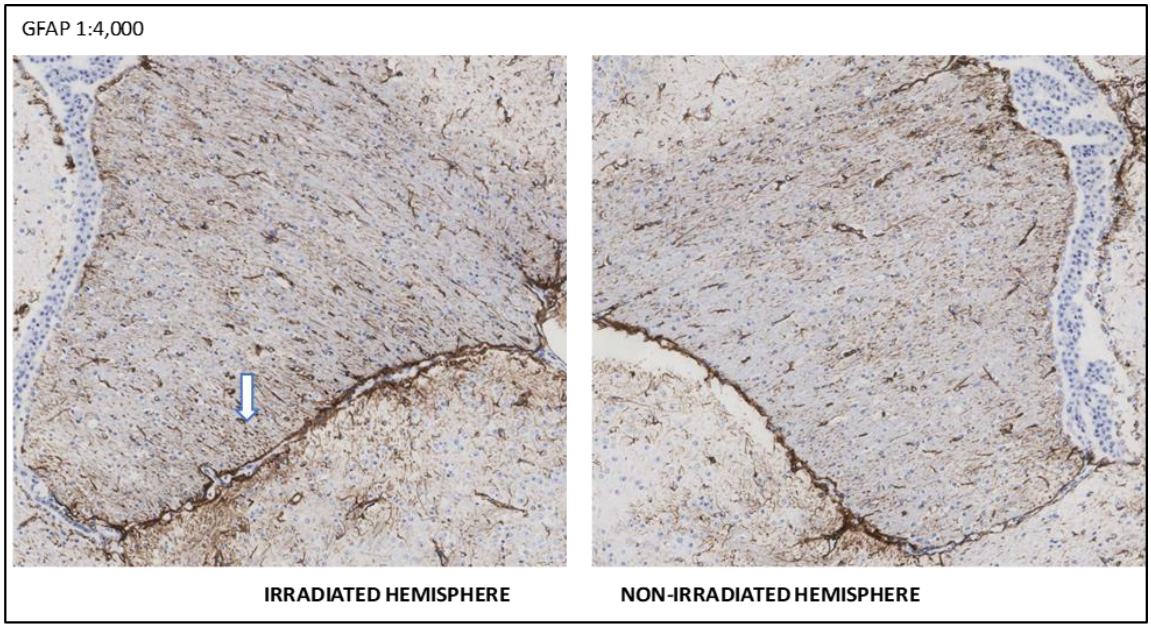


(a)

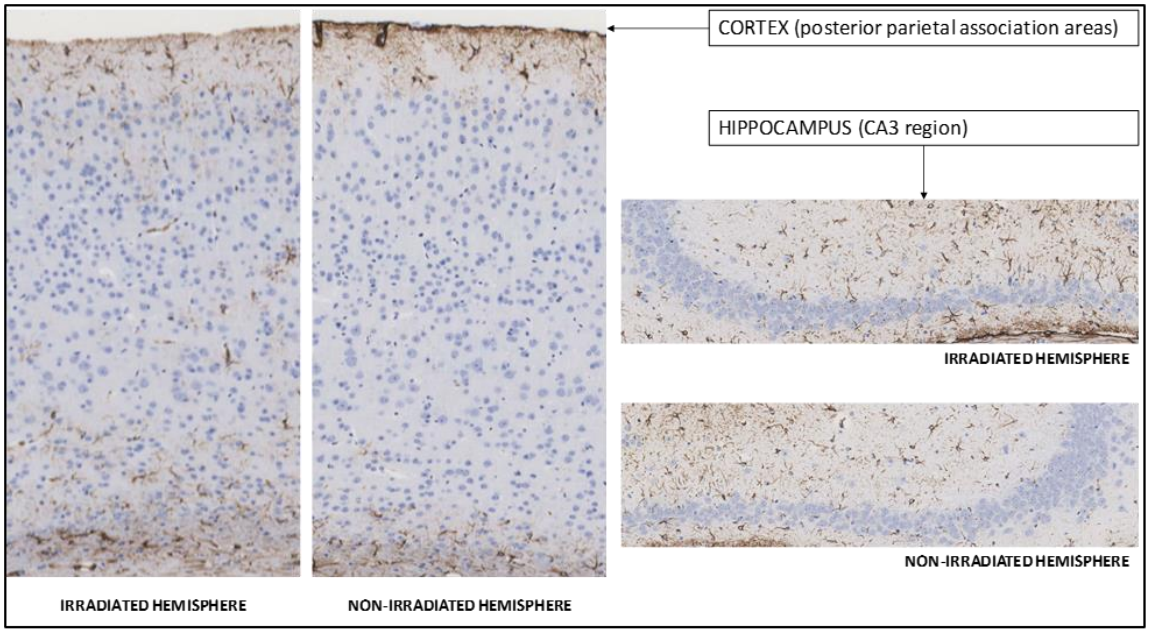


(b)

**Figure 5.11: (a) Staining with GFAP (1:4,000) reveals a higher abundance of reactive astrocytes in the fimbria of the irradiated hemisphere, particularly in areas close to the thalamus (indicated by arrow). (b) GFAP in the CA3 region of the hippocampus.**

Staining with LFB suggested some mild WM injury in the corpus callosum that was not evident in all examined samples (n=2/4). When combined with GFAP, it indicated that glial reactivity is an event occurring across the WM track in both hemispheres, spreading from there into the cortical regions (Figure 5.12).

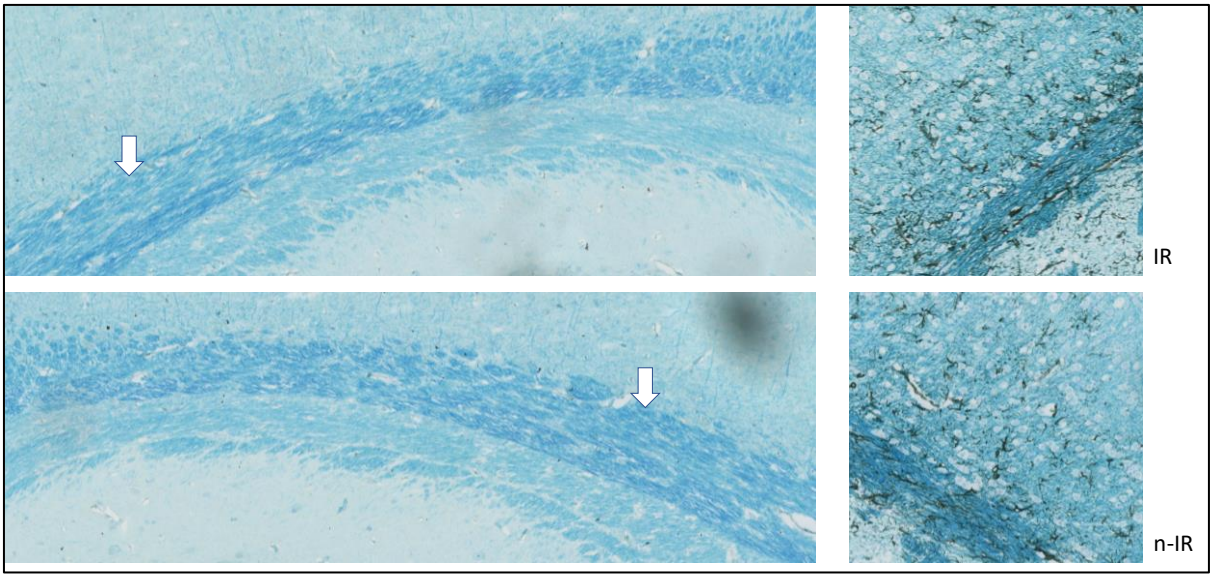


**Figure 5.12: Staining with LFB in the corpus callosum showing mild WM injury.**

## 5.7 Discussion

In chapter 4, in addition to the main study, we also performed an investigative pilot experiments using multiple *b*-value DWI, to evaluated its potential to detect microstructural changes 24 hours post-irradiation. In along observation time multiple *b*-value experiment, only performed on one animal, where we piloted the acquisition of multiple *b*-values, a deviation from Gaussian behaviour was observed in the irradiated brain hemisphere see Figure 4.8,Chapter-4. Mesoscopic organisation of the tissue can potentially be characterised by long diffusion time signals (Novikov *et al.*, 2014), providing markers for axonal varicosities (Fieremans *et al.*, 2016), undulations (Nilsson *et al.*, 2012), and WM fiber dispersion (Fieremans *et al.*, 2016).

In this current chapter, we aimed to reproduce this result using a larger group size to test significance. Contrary to the pilot experiment, this study did not show any

significant deviation from Gaussian diffusion in the irradiated hemisphere with increasing *b*-value, in either the X, Y or Z directions (see Figure 5.3).

However, at day 60, a greatly increased standard deviation of diffusion coefficient was seen in the irradiated fimbria, but only using long observation times (200ms) and with the diffusion gradient aligned along the x-axis (see Figure 5.8 (C)). On inspection of the individual images (see Figure 5.6), for long observation times (200ms) there was a noticeable drop in the STE-DWI signal in the fimbria with the gradient in the X direction, but not with the gradient in the Y or Z direction. However, this effect was not present at shorter observation times (20, 50 and 80ms). Initially we believed that there was a high probability this was the result of artefacts during imaging. Hence, we investigated if this effect was an artefact. First, we swapped between read and phase encoding directions, which would not only change a potential artefact but shift it into a different direction. However, the same effect was still seen in the region of the fimbria (Figure 5.13, a. b). We also investigated changing the imaging module, acquiring STE-DWI using both an EPI readout and a Spin-Echo readout. However, the same effect was still seen in the region of the fimbria with whether using EPI or Spin-Echo imaging (Figure 5.13, c. d). Hence, we concluded this was a real effect and not an imaging artefact. Consequently, we found some acute effect of radiation in the fimbria in the right brain hemisphere with a gradient direction of X, which is the principal direction of fibre tracks in the structure.

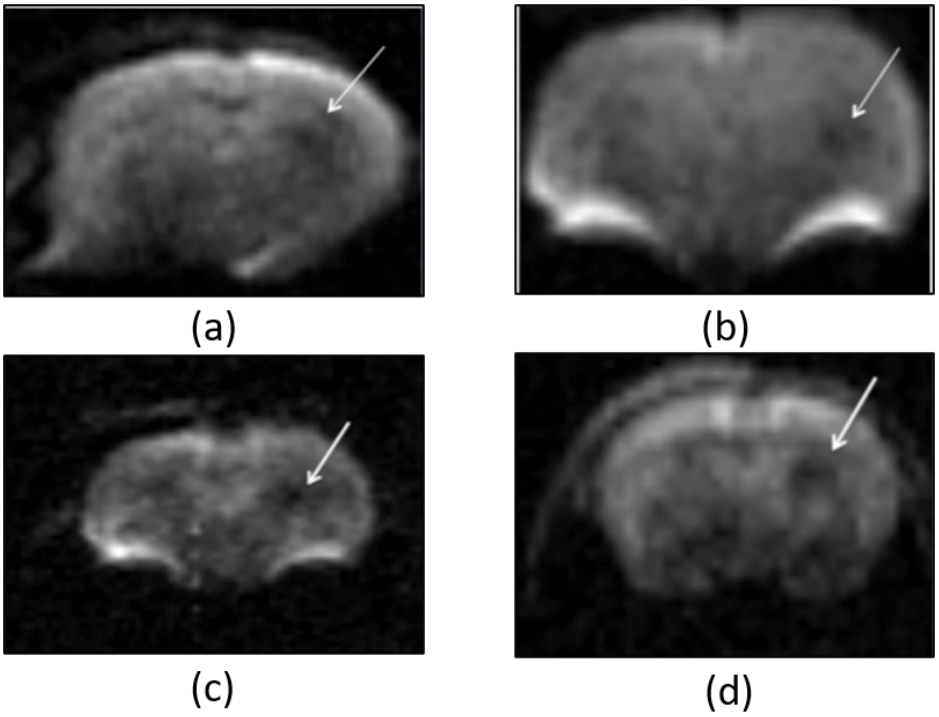


**Figure 5.13: (a) STE-DWI acquired from left to right (L-R) phase encoding direction with 200 ms observation time, (b) STE-DWI acquired from anterior to posterior (A-P) phase encoding direction with 200 ms observation time, (c) image acquired with EPI-STE-DWI and (d) image acquired with SE-DWI.**

These MRI findings were examined in parallel with neuropathological observations of the brain tissue of the irradiated mice 80 days post-irradiation. H&E staining showed a mildly disorganised pattern that was found in the selected section of the irradiated fimbria. These findings were consistent with earlier reports suggesting that the fimbria hippocampi are sensitive to radiation-induced injury (Reinhold *et al.*, 1990). Staining with GFAP showed significant expression at different irradiated regions such as the region of the caudoputamen in the striatum and amygdala. GFAP over-expression gives an indication of reactive astrocytes in the fimbria of the irradiated hemisphere. LFB results suggest there was a mild demyelination in the corpus callosum, however, this result was found in only 2 of four mice (n=2/4). Although our MRI results showed no significant differences between diffusion measurements in all gradient directions (X, Y and Z), the provided histopathological changes of radiation-induced brain injury supported the use of DTI as a biomarker to non-invasively monitor radiation-induced brain injury, especially with longer diffusion time STE-sequence.

## 5.8 Future Experiments

In this chapter we described how STE-DWI with a long observation time showed some sensitivity to radiation-induced changes in the region of the fimbria, but only when using a gradient in the x direction (along the line of fibres). In the next chapter, to better investigate the effect of radiation damage on WM, where fibre direction is important, we will employ, stimulated echo, diffusion tensor imaging (STE-DTI) with long observation times. These experiments will provide DTI metrics such as FA, mean diffusivity (MD) and radial diffusivity (RD), longitudinally with histology.

However, before applying this STE-DTI sequence in-vivo, in the next two chapters we consider its accuracy using water phantoms. In other words, diffusion was increased in this direction, which in turn resulted in a high likelihood of restriction due to microstructural changes due to irradiation. Consequently, DTI experiment will design for exploring this effect further in terms of the mechanism of diffusion or its biological specificity using DTI metrices such as FA, mean diffusivity (MD) and radial diffusivity (RD), longitudinally with histology.

## 5.9 References:


Alturkistani, H. A., Tashkandi, F. M. and Mohammedsaleh, Z. M. (2015) 'Histological Stains: A Literature Review and Case Study', *Global journal of health science*, 8(3), pp. 72–79. doi: 10.5539/gjhs.v8n3p72.

Assaf, Y. and Cohen, Y. (1998) 'Non-Mono-Exponential Attenuation of Water and N-Acetyl Aspartate Signals Due to Diffusion in Brain Tissue', *Journal of Magnetic Resonance*, 131(1), pp. 69–85. doi: 10.1006/jmre.1997.1313.

Cauter, S. Van *et al.* (2012) 'Gliomas : Diffusion Kurtosis MR', *Radiology*, 263(2), pp. 492–501.

Chen, Y. *et al.* (2013) 'Cerebral white matter injury and damage to myelin sheath following whole-brain ischemia', *Brain Research*. Elsevier, 1495, pp. 11–17. doi: 10.1016/j.brainres.2012.12.006.

Cherubini, E. and Miles, R. (2015) 'The CA3 region of the hippocampus: How is it? What is it for? How does it do it?', *Frontiers in Cellular Neuroscience*, 9(FEB), pp. 9–11. doi: 10.3389/fncel.2015.00019.

Derek K. Jones, P. (ed.) (2011) *Diffusion MRI theory, methods, and appliations*. doi: 10.1017/CBO9781107415324.004.

Duffy, P. E., Huang, Y. Y. and Rapport, M. M. (1982) 'The relationship of glial fibrillary acidic protein to the shape, motility, and differentiation of human astrocytoma cells', *Experimental Cell Research*, 139(1), pp. 145–157. doi: 10.1016/0014-4827(82)90328-7.

Fieremans, E. *et al.* (2016) 'In vivo observation and biophysical interpretation of time-dependent diffusion in human white matter', *NeuroImage*. Elsevier Inc., 129, pp. 414–427. doi: 10.1016/j.neuroimage.2016.01.018.

Grossman, E. J. *et al.* (2012) 'Thalamus and cognitive impairment in mild traumatic brain injury: A diffusional kurtosis imaging study', *Journal of Neurotrauma*, 29(13), pp. 2318–2327. doi: 10.1089/neu.2011.1763.

Hori, M. *et al.* (2012) 'Visualizing non-Gaussian diffusion: Clinical application of q-space imaging and diffusional kurtosis imaging of the brain and spine', *Magnetic Resonance in Medical Sciences*, 11(4), pp. 221–233. doi: 10.2463/mrms.11.221.

Hui, E. S. *et al.* (2012) 'Stroke assessment with diffusional kurtosis imaging', *Stroke*, 43(11), pp. 2968–2973. doi: 10.1161/STROKEAHA.112.657742.

Jensen, J. H. *et al.* (2005) 'Diffusional kurtosis imaging: The quantification of non-Gaussian water diffusion by means of magnetic resonance imaging', *Magnetic Resonance in Medicine*, 53(6), pp. 1432–1440. doi: 10.1002/mrm.20508.

Jensen, J. H. and Helpern, J. A. (2010) 'MRI quantification of non-Gaussian water diffusion by kurtosis analysis', *NMR in Biomedicine*, 23(7), pp. 698–710. doi: 10.1002/nbm.1518.

Jiang, R. *et al.* (2015) 'Diffusion kurtosis imaging can efficiently assess the glioma grade and cellular proliferation', *Oncotarget*, 6(39), pp. 42380–42393. doi: 10.18632/oncotarget.5675.

Kurita, H. *et al.* (2001) 'Radiation-induced apoptosis of oligodendrocytes in the adult rat brain', *Neurological Research*, 23(8), pp. 869–874. doi: 10.1179/016164101101199324.

Makale, M. T. *et al.* (2017) 'Brain irradiation and long-term cognitive disability: Current concepts', *Nature Reviews Neurology*, 13(1), pp. 52–64. doi: 10.1038/nrneurol.2016.185.

Moustafa, A. A. *et al.* (2017) 'The thalamus as a relay station and gatekeeper: Relevance to brain disorders', *Reviews in the Neurosciences*, 28(2), pp. 203–218. doi: 10.1515/revneuro-2016-0067.

Niendorf, T. *et al.* (1996) 'Biexponential diffusion attenuation in various states of brain tissue: Implications for diffusion-weighted imaging', *Magnetic Resonance in Medicine*, 36(6), pp. 847–857. doi: 10.1002/mrm.1910360607.

Nilsson, M. *et al.* (2012) 'The importance of axonal undulation in diffusion MR

measurements: A Monte Carlo simulation study', *NMR in Biomedicine*, 25(5), pp. 795–805. doi: 10.1002/nbm.1795.

Novikov, D. S. *et al.* (2014) 'Revealing mesoscopic structural universality with diffusion', *Proceedings of the National Academy of Sciences of the United States of America*, 111(14), pp. 5088–5093. doi: 10.1073/pnas.1316944111.

Raab, P. *et al.* (2010) 'Cerebral gliomas: diffusional kurtosis imaging analysis of microstructural differences', *Radiology*, 254(3).

Reinhold, H. S. *et al.* (1990) 'Development of blood vessel-related radiation damage in the fimbria of the central nervous system', *International Journal of Radiation Oncology, Biology, Physics*, 18(1), pp. 37–42. doi: 10.1016/0360-3016(90)90264-K.

Rosenkrantz, Andrew B *et al.* (2015) 'Body diffusion kurtosis imaging: basic principles, applications, and considerations for clinical practice', *Journal of Magnetic Resonance Imaging*, 42(5), pp. 1190–1202.

Rosenkrantz, Andrew B. *et al.* (2015) 'Body diffusion kurtosis imaging: Basic principles, applications, and considerations for clinical practice', *Journal of Magnetic Resonance Imaging*, 42(5), pp. 1190–1202. doi: 10.1002/jmri.24985.

Rutka, J. T. *et al.* (1997) 'Role of glial filaments in cells and tumors of glial origin: A review', *Journal of Neurosurgery*, 87(3), pp. 420–430. doi: 10.3171/jns.1997.87.3.0420.

Schmidt-Kastner, R. *et al.* (1993) 'Immunohistochemical staining for glial fibrillary acidic protein (GFAP) after deafferentation or ischemic infarction in rat visual system: Features of reactive and damaged astrocytes', *International Journal of Developmental Neuroscience*, 11(2), pp. 157–174. doi: 10.1016/0736-5748(93)90076-P.

Tietze, A. *et al.* (2015) 'Mean diffusional kurtosis in patients with glioma: Initial results with a fast imaging method in a clinical setting', *American Journal of Neuroradiology*, 36(8), pp. 1472–1478. doi: 10.3174/ajnr.A4311.

Tsuruda, J. S. *et al.* (1987) 'Radiation effects on cerebral white matter: MR evaluation', *American Journal of Roentgenology*, 149(1), pp. 165–171. doi: 10.2214/ajr.149.1.165.

Walker, A. J. *et al.* (2014) 'Postradiation imaging changes in the CNS: how can we differentiate between treatment effect and disease progression?', *Future Oncology*, 10(7), pp. 1277–1297.

Wu, E. X. and Cheung, M. M. (2010) 'MR diffusion kurtosis imaging for neural tissue characterization', *NMR in Biomedicine*, 23(7), pp. 836–848. doi: 10.1002/nbm.1506.

Yang, L. *et al.* (2017) 'Pathophysiological Responses in Rat and Mouse Models of Radiation-Induced Brain Injury', *Molecular Neurobiology*, 54(2), pp. 1022–1032. doi: 10.1007/s12035-015-9628-x.

Yoshida, M. *et al.* (2013) 'Diffusional kurtosis imaging of normal-appearing white matter in multiple sclerosis: Preliminary clinical experience', *Japanese Journal of Radiology*, 31(1), pp. 50–55. doi: 10.1007/s11604-012-0147-7.

# Chapter 6

# Chapter-6 Efficient gradient calibration based on diffusion MRI

## 6.1 Introduction

Pre-clinical, high field MRI systems are widely used to provide high resolution MRI images of animal models of human disease, which are used for in-vivo characterisation of tissue structure and anatomical volumes (O'Callaghan *et al.*, 2014). Accurate gradient calibration is a prerequisite for quantitative MRI. Over- or under-estimations in geometric measurements can be the result of a mis-calibration of the three gradient coils (X, Y, Z). This, in turn, can affects the ability of MRI to detect and provide useful information (Jezzard, Barnett and Pierpaoli, 1998). MRI diffusion measurements depend on the square of the gradient amplitude see Equation 2.13,Chapter-2, hence, diffusion MRI is particularly sensitive to poor gradient calibration (Teh, Maguire and Schneider, 2017) and any errors in the gradient calibration are exaggerated (Nagy *et al.*, 2007). Consequently, careful gradient calibration of the MRI scanner is required, especially for the diffusion MRI measurements of diffusion coefficients (O'Callaghan *et al.*, 2014). For clinical MRI scanners, gradient calibration is performed using a phantom, which usually consists of a suitable container filled with water and a structural object. To reduce the long relaxation time of water (T1=T2= ~3s), a contrast agent is also added, e.g. CuSO4 or Gd-DTPA.

Imaging gradients are calibrated by linear scaling factors in each of the principal imaging axes (x, y and z), and global compression or expansion in the acquired images will be the result of any errors in their values. It is assumed that, an imaging gradient is spatially linear, however, gradient nonlinearity can introduce image distortions (O'Callaghan *et al.*, 2014). Gradient calibration is generally achieved annually during routine maintenance by the scanner manufacturers. Scaling factors and gradient linearity are assessed using a structural phantom. In each single slice of an MRI image of the phantom, distances between structures are measured and compared with a physical measurement of the same distance (e.g. using micro-callipers). This approach to calibration is highly susceptible to error owing to operator inconsistency, the small number of measurements taken and the slice thickness used. However, it is considered adequate for routine clinical MRI scans (e.g. T1W, T2W). It should be noted that other methods to

calibrate clinical MRI gradients have been proposed (Wang, Doddrell and Cowin, 2004)(Wu and Alexander, 2007)(Bammer *et al.*, 2003)(Gunter *et al.*, 2009). However, these may not translate well to pre-clinical MRI scanners due to hardware differences. For example, the maximum gradients strength in pre-clinical scanners (400-1000mT/m) is much greater than found in in clinical scanners (e.g. 200mT/m for 1.5T) (Foster-Gareau *et al.*, 2003). Pre-clinical scanners have a much smaller bore size and FOV and use high static magnetic fields (7-17 Tesla) compared with clinical MRI (1.5 -3 T). In fact, outside the small uniform region, large non-linearities can be observed in pre-clinical gradients sets due to the challenging design considerations (Doran *et al.*, 2005).

From the exploratory in vivo measurements made in Chapter-4, there was an indication that the gradients in our MRI scanner were not perfectly calibrated, with differences between X, Y and Z in vivo measurements In the previous chapter we achieved promising results with early detected IR effects in the fimbria in the X direction only. We needed to minimise measurement related errors to properly assess such results. To be sure, we decided to recalibrate our gradients. The Bruker company's standard method for calibrating gradients is the same as for a clinical scanner, namely, making length measurements on phantom of known dimensions (a lego brick in water). However, for diffusion MRI, Bruker recommends calibrating the gradients by performing diffusion MRI measurements (in the X, Y and Z directions). This is done using a simple water phantom, which has a known diffusion coefficient that is the same in all directions. This method for gradient calibration was described in detail in the Bruker manual for Diffusion Tensor Imaging.

## 6.2 Methods

Diffusion measurements were made using SE-DWI ($\Delta$=20ms), from which new gradient calibration and scaling factors were calculated. Following this re-calibration, further diffusion measurements were made using both SE-DWI and STE-DWI.

### 6.2.1 Phantom design

A diffusion calibration water phantom was constructed by filling a 20-mm outer diameter plastic container with doped water. To reduce the long relaxation times of pure water, it was doped with 1 g/l $CuSO_4$ x $2H_2O$. To avoid air bubbles the solution was first degassed via application of a vacuum, then inserted into the phantom using a syringe. In fact, removing air bubbles is very important to minimise magnetic susceptibility artefacts (de Souza, Costa and Castellano, 2017).

The temperature of the water phantom was measured using a glass alcohol thermometer. After 24 hours inside the magnet bore with the gradient system on continuously, the water temperature was stable at 24.5 $^{o}$C. Our sample temperature was carefully maintained because the diffusion coefficient of water is known to be temperature dependent. To prevent the diffusion measurements from being affected by convection of the water, temperature gradients across the sample were avoided by setting the room temperature and the gradient temperature water-cooling at the same level. In addition, a pulse sequence with a moderate duty cycle was used to avoid heating of the gradient and sample during the experiment.

### 6.2.2 MRI sequence and diffusion measurements

Gradient Calibration: the water phantom was well centred by ensuring its main axes were parallel to the gradient coordinate system (Figure 6.1). We first measured the diffusion coefficient of water independently in all 6 directions (±X, ±Y, ±Z) (Table 6.1) using an SE-DWI sequence with a 20 ms observation time (TR = 3800, number of slices = 1, slice thickness = 1.5 mm, Δ= 4 ms, number of averages = 6, and 8 *b* values per direction = 200, 400, 600, 800, 1000, 1200, 1400 and 1600 s/mm$^2$).

The diffusion coefficient of the water was determined from the initial slope of the signal attenuation, which assumes a Gaussian behaviour at low values of the gradient strength (Mitra and Halperin, 1995).

Phantom test of long observation time Diffusion MRI experiments: once the gradients were calibrated, a series of multiple *b*-value diffusion experiments were

performed using SE-DWI and STE-DWI, for a range of observation times (20ms, 50ms, 100ms and 200ms) using the same imaging parameters described above.

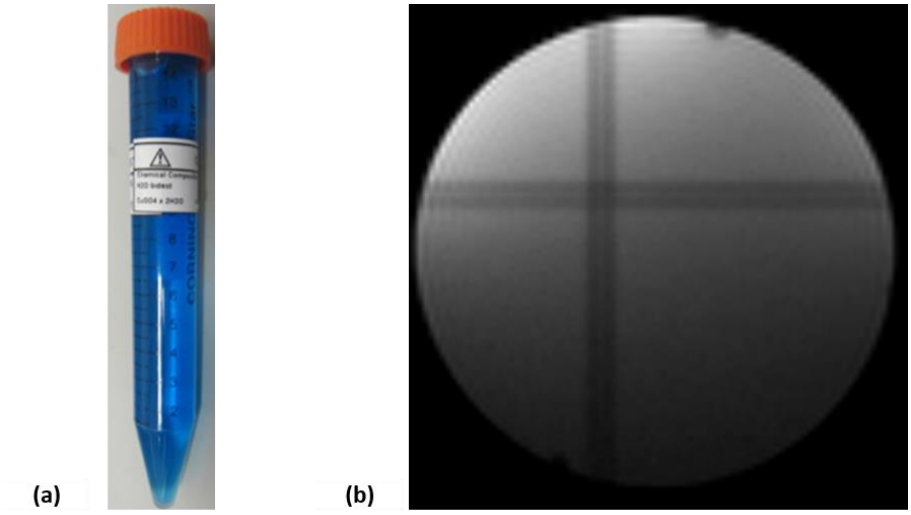


**Figure 6.1: Image illustrates water phantom (a) and its tripilot image (b).**

## 6.3 Results

## 6.4 Diffusion Coefficient acquisition

The diffusion coefficient was measured independently in all three gradients directions, with both + and – polarity. This result in six apparent diffusion coefficients ($D_x$,-$D_x$, Dy,-$D_y$, $D_z$ and -$D_z$) (Table 6.1).

**Table 6.1: Shows measured diffusion coefficient for all gradient directions ($mm^2/s$). (STD ± 0.0000004)**

| Directions | X | Y | Z | -X | -Y | -Z |
|---|---|---|---|---|---|---|
| Diffusion | 0.0024134 | 0.0024820 | 0.0024758 | 0.0024022 | 0.0024453 | 0.0024500 |

## 6.5 Scaling factors measurements and correction

The new relative gradient scaling values were then corrected according to the following equations based on the Bruker manual setup for diffusion gradient calibration:

**Equation 6.1**

$$Sx^{new} = SQRT\left\{\frac{\min(Dx,Dy,Dz)}{Dx}\right\} Sx^{old} = \sqrt{\frac{0.00241345}{0.00241345}}\, x\, 1 = 1$$

**Equation 6.2**

$$Sy^{new} = SQRT\left\{\frac{min(Dx,Dy,Dz)}{Dy}\right\} Sy^{old} = \sqrt{\frac{0.00241345}{0.00248207}}\, x\, 1 = 0.986079$$

**Equation 6.3**

$$Sz^{new} = SQRT\left\{\frac{\min(Dx,Dy,Dz)}{Dz}\right\} Sz^{old} = \sqrt{\frac{0.00241345}{0.00247581}}\, x\, 0.995411 = 0.982794$$

Where SQRT is the square root and $Sx^{new}$, $Sy^{new}$ and $Sz^{new}$ are the new scaling factors after new diffusion measurements in the x, y and z directions, while $Sx^{old}$, $Sy^{old}$, $Sz^{old}$ are the old scaling factors, previously on the system.

## 6.6 Correcting the gradient calibration constant (GCC)

From the literature, it is known that the diffusion coefficient of water is 2.03 x $10^{-9}$ $m^2/s$ at 20 $C^0$ and 2.30 x $10^{-9}$ $m^2/s$ at 25˚ C. In-between values can be linearly interpolated (Chenevert *et al.*, 2011).

The linear equation between these points is given in Equation 6.4.

**Equation 6.4**

$$D_{Literature} = (5.4\ x\ 10^{-11}\ x\ Temperature) + 9.5\ x\ 10^{-10}$$

From this Equation 6.4, we calculated the diffusion coefficient at the temperature of 24.5 $^oC$ as 2.27 x $10^{-9}$ $m^2/s$.

$$D_{Literature} = (5.4\ x\ 10^{-11}\ x\ 24.5) + 9.5\ x\ 10^{-10} = 2.27\ x\ 10^{-9}\ m^2/s$$

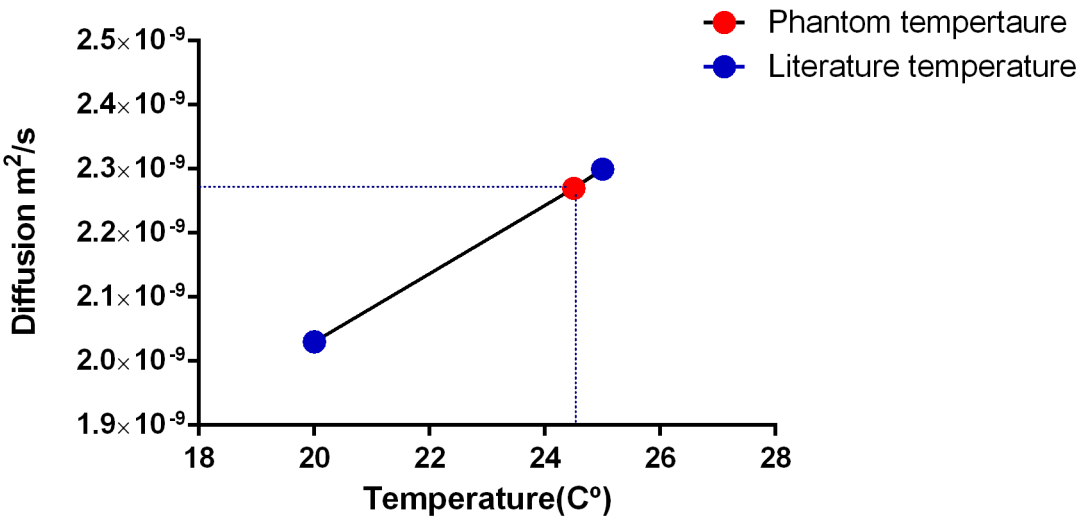


**Figure 6.2: Diffusion coefficient of water with increasing temperature with literature value of water diffusion shown (blue) and estimated water diffusion at phantom temperature 24.5˚ C (red).**

The gradient calibration constant (GCC) was corrected, as described in a Bruker technical manual using the following equation.

**Equation 6.5**

$$GCC^{new} = SQRT\left\{\frac{\min(Dx, Dy, Dz)}{D_{literature}}\right\} GCC^{old}$$

$$GCC^{new} = \sqrt{\frac{0.00241345}{2.27x\ 10^{-3}}}\ \text{x}\ 125127 = 129020\ Hz/cm$$

## 6.7 Applying New gradient scaling factor values

After we performed diffusion measurements using the water phantom and calculated the corrected scaling factor and GCC values, we replaced the old gradient parameters with the new parameters. This was done in the Pre-emphasis tool on Topspin (Set-Pre) and saved as the default (Figure 6.3).

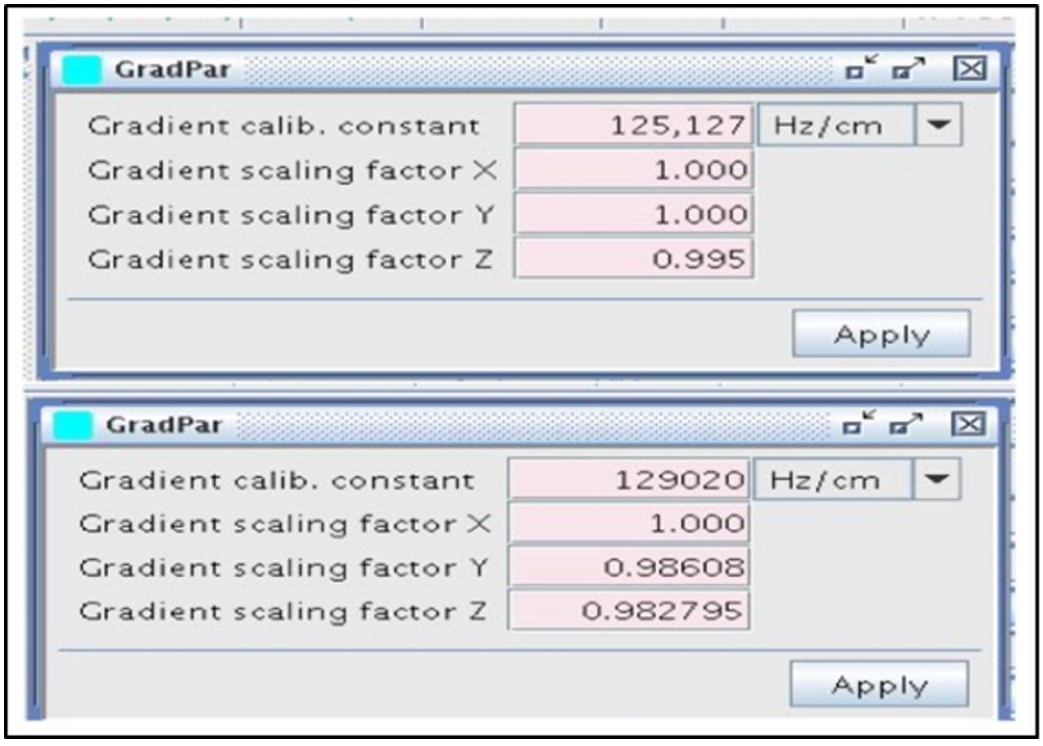


**Figure 6.3: Screen shot from ParaVision 5.0 software showing (a) the old gradient calibration constant and scaling values. (b) New values of calibration constant and scaling factor.**

## 6.8 Diffusion measurement varying observation time

After using the SE-DWI (20ms) data to calibrate the gradients, further data were then collected for the SE-DWI and STE-DWI sequences, using observation times of 20,50,100 and 200ms. The results (Figure 6.4) show that at short observation times for both SE-DWI and STE-DWI, all gradient directions had the same slope (i.e. same diffusion coefficient). However, for STE-DWI measurements at long observation times, only the read and phase gradient had the same slope. With the diffusion gradients along the slice gradient axis, there was substantial divergence with increasing *b*-value. The slope is underestimated with the diffusion gradients along the (+) slice direction and overestimated with diffusion gradients along the slice (-) slice direction.

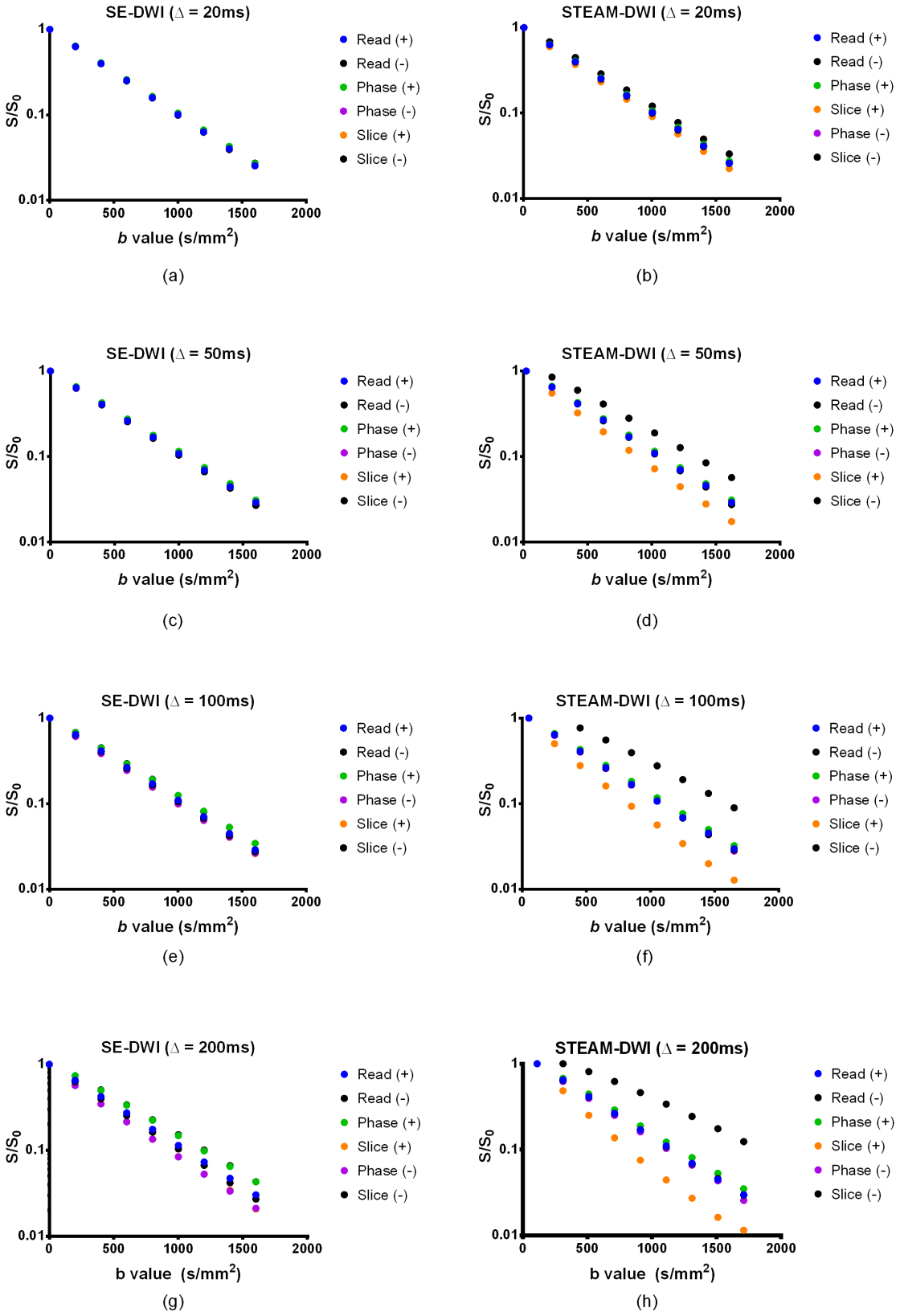


**Figure 6.4: After gradient calibration , multiple b-value measurements were performed using SE-DWI (left column) and STE-DWI (right column) for observation times of 20ms,50ms,100ms and 200ms. Measurements were also made in using different directions (read, -read, phase, -phase slice, - slice).**

## 6.9 Discussion

For an MRI system, calibration of the gradient coils is important, particularly for quantitative, comparative and longitudinal measurements, where precession and stability are paramount. On our Bruker preclinical scanner, it is standard for the service engineer to perform gradient calibrations using geometric measurements on a structural phantom. These calibrations are within the rather loose acceptance limits of the manufacturer but are acceptable for anatomical MRI (e.g. T2 scans). However, as we planned to perform in-vivo Diffusion Tensor Imaging experiments, for increased accuracy we used a calibration method based on measuring the diffusion coefficients of a water phantom for increased accuracy. This calibration was performed using a SE-DWI sequence with short observation times (20ms). The derived scaling factors and GCC were then applied to our MRI system.

Following the gradient calibration, we performed another series of further diffusion measurement, both with SE-DWI and STE-DWI, for a range of observation times and gradients (Figure 6.4). This highlighted a serious problem with the STE-DWI sequence, where measurements made at long observation times with a diffusion gradient applied in the + slice or – slice direction resulted in large errors. It is important to note that these errors cannot be corrected via gradient calibration, because both + and – slice gradients use the same gradient calibration constant and scaling factor.

## 6.10 Conclusion

At the end of Chapter 5, we described our intention to investigate the potential for long observation time STE-DWI to be a biomarker for radiation-induced brain damage. Therefore, this observed error (with + slice and – slice gradients, at long observation times) had important implications for our planned in-vivo experiments, particularly as the DTI sequence uses 30 directions, which are obtained from combinations of the read, phase and slice gradients. Hence, this error could have serious implications for long observation time STE-DWI

measurements such as MD and FA. Therefore, this issue is explored further in the next chapter with a view to minimise such errors.

## 6.11 References

Bammer, R. *et al.* (2003) 'Analysis and generalized correction of the effect of spatial gradient field distortions in diffusion-weighted imaging', *Magnetic Resonance in Medicine*, 50(3), pp. 560–569. doi: 10.1002/mrm.10545.

Chenevert, T. L. *et al.* (2011) 'Diffusion coefficient measurement using a temperature-controlled fluid for quality control in multicenter studies', *Journal of Magnetic Resonance Imaging*, 34(4), pp. 983–987. doi: 10.1002/jmri.22363.

Doran, S. J. *et al.* (2005) 'A complete distortion correction for MR images: I. Gradient warp correction', *Physics in Medicine and Biology*, 50(7), pp. 1343–1361. doi: 10.1088/0031-9155/50/7/001.

Eriko Yoshimaru et al., 2014 (2014) 'Design, manufacture, and analysis of customized phantoms for enhanced quality control in small animal MRI systems', *Physiology & behavior*, 176(1), pp. 139–148. doi: 10.1016/j.physbeh.2017.03.040.

Foster-Gareau, P. *et al.* (2003) 'Imaging single mammalian cells with a 1.5 T clinical MRI scanner', *Magnetic Resonance in Medicine*, 49(5), pp. 968–971. doi: 10.1002/mrm.10417.

Gunter, J. L. *et al.* (2009) 'Measurement of MRI scanner performance with the ADNI phantom', *Medical Physics*, 36(6), pp. 2193–2205. doi: 10.1118/1.3116776.

Jezzard, P., Barnett, A. S. and Pierpaoli, C. (1998) 'Characterization of and correction for eddy current artifacts in echo planar diffusion imaging', *Magnetic Resonance in Medicine*, 39(5), pp. 801–812. doi: 10.1002/mrm.1910390518.

Mitra, P. P. and Halperin, B. I. (1995) 'Effects of Finite Gradient-Pulse Widths in Pulsed-Field-Gradient Diffusion Measurements', *Journal of Magnetic Resonance, Series A*, pp. 94–101. doi: 10.1006/jmra.1995.1060.

Nagy, Z. *et al.* (2007) 'A method for improving the performance of gradient systems for diffusion-weighted MRI', *Magnetic Resonance in Medicine*, 58(4), pp. 763–768. doi: 10.1002/mrm.21379.

O'Callaghan, J. *et al.* (2014) 'Is your system calibrated? MRI gradient system calibration for pre-clinical, high-resolution imaging', *PLoS ONE*, 9(5), pp. 1–9. doi: 10.1371/journal.pone.0096568.

Seland, J. G. *et al.* (2000) 'Diffusion Measurements at Long Observation Times in the Presence of Spatially Variable Internal Magnetic Field Gradients', *Journal of Magnetic Resonance*, 146(1), pp. 14–19. doi: 10.1006/jmre.2000.2101.

de Souza, E. M., Costa, E. T. and Castellano, G. (2017) 'Phantoms for diffusion-weighted imaging and diffusion tensor imaging quality control: A review and new perspectives', *Research on Biomedical Engineering*, 33(2), pp. 156–165. doi: 10.1590/2446-4740.07816.

Sung, J.-J. *et al.* (2004) 'Diffusion tensor MRI as a diagnostic tool of upper motor neuron involvement in amyotrophic lateral sclerosis', *Journal of the Neurological Sciences*, 227(1), pp. 73–78. doi: 10.1016/j.jns.2004.08.014.

Teh, I., Maguire, M. L. and Schneider, J. E. (2017) 'Efficient gradient calibration based on diffusion MRI', *Magnetic Resonance in Medicine*, 77(1), pp. 170–179.

Uluğ, A. M. *et al.* (1999) 'Clinical use of diffusion-tensor imaging for diseases causing neuronal and axonal damage', *American Journal of Neuroradiology*, 20(6), pp. 1044–1048.

Wang, D., Doddrell, D. M. and Cowin, G. (2004) 'A novel phantom and method for comprehensive 3-dimensional measurement and correction of geometric distortion in magnetic resonance imaging', *Magnetic Resonance Imaging*, 22(4), pp. 529–542. doi: 10.1016/j.mri.2004.01.008.

Wu, Y. C. and Alexander, A. L. (2007) 'A method for calibrating diffusion gradients in diffusion tensor imaging', *Journal of Computer Assisted Tomography*, 31(6), pp. 984–993. doi: 10.1097/rct.0b013e31805152fa.

Zhong, J., Kennan, R. P. and Gore, J. C. (1991) 'Effects of susceptibility variations on NMR measurements of diffusion', *Journal of Magnetic Resonance (1969)*, 95(2), pp. 267–280. doi: 10.1016/0022-2364(91)90217-H.

# Chapter 7

# Chapter-7 Minimising observation time related errors on Stimulated echo diffusion acquisitions

## 7.1 Introduction

In performing the gradient calibration in the previous chapter, using diffusion MRI, an important error in STEAM-DWI measurements was discovered at long observation times. This error which occurred when measuring diffusion in the slice direction, could not be corrected by via gradient calibration. In diffusion MRI, systematic errors can arise from cross-terms unaccounted for in the *b*-value calculation. These can lead to errors in the *b*-value calculation, that can be extremely complex (Pierpaoli and Basser, 1996)(Marks *et al.*, 1996). Here we investigate what imaging parameters could affect this error and how it could be minimised. To achieve this, we used a simple water phantom doped with copper sulphate. Given their long-term stability and homogenous relaxation times, such phantoms are commonly used for quality control of MRI equipment (Kato *et al.*, 2005). In solution the paramagnetic copper ions reduces the long T2 value of pure water (3 seconds at 7Tesla) and reduce it down to values found in vivo.

## 7.2 Methods

To investigate the effect of the STEAM-DWI errors, described in Chapter-6,section 6.9, on STEAM-DTI measurements, a series of SE-DTI and STEAM-DTI experiments were performed. DTI measurements were made on a water phantom (0.5 mg $CuSO_4.5H_2O$/250 ml water) using standard DTI sequence templates (B_DIFUSSION, EPI- diffusion-tensor). This very low concentration of $CuSO_4$ has a negligible effect on the diffusion of water molecules.

A Spin Echo (SE-DTI) experiment was performed first without modifying any of the parameters with the geometry adjusted to the phantom. This used 5 $b_0$ imaging, 30 directions and $b$=1000 s/mm$^2$ (Figure 7.1). Without changing any other parameters of the sequence (Figure 7.2), the sequence was switched to the STEAM. Finally, a second STEAM experiment was performed, in which the diffusion gradient separation was increased from 20 ms (standard Bruker) to 200 ms (Figure

7.3). Here the averages were doubled from 1 to 2 for the last experiment to compensate for the additional loss of signal. The SNR is measured by comparing the level of the desired signal with the level of background noise (Welvaert and Rosseel, 2013). Before calculating the SNR, the same ROI's was taken from the water phantom and from the background noise of the image, outside any ghosting artefact. The mean of the signal was then divided by the mean of the noise to calculate the SNR.

## 7.3 Results

Figure 7.1 shows that for the SE-DTI (20ms) water phantom measurements, the data points for the 30 directions practically overlap. However, for the STEAM-DTI Figure 7.2 and Figure 7.3, at long observation times the data points become increasingly spread over a range of *b* values. Importantly, this spread was not in line with the expected signal decay for water, meaning that the wrong diffusion values were extracted.

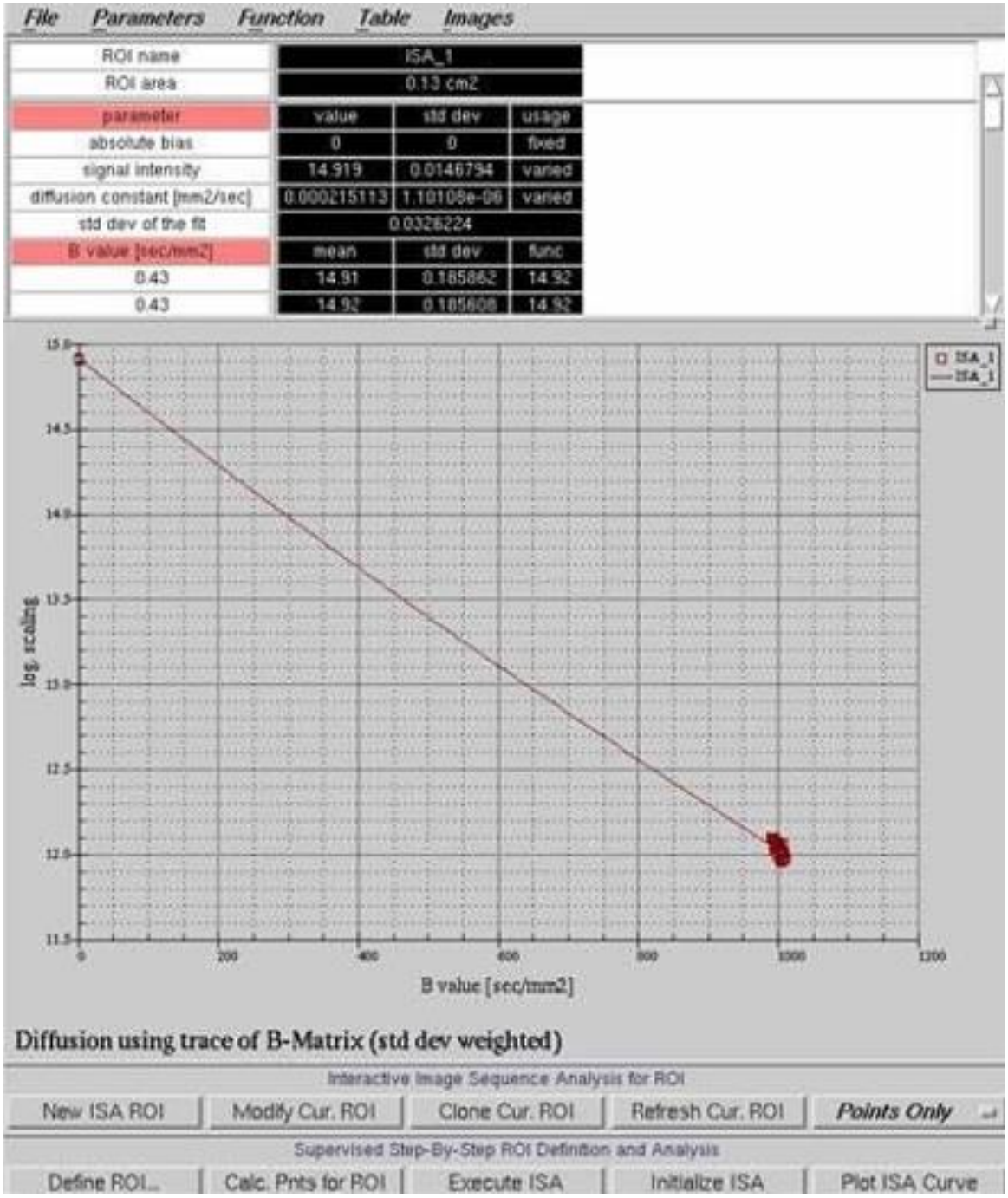


**Figure 7.1: Standard Bruker diffusion experiment (1 average, preset Bruker parameters) with gradient separation of 20ms.**

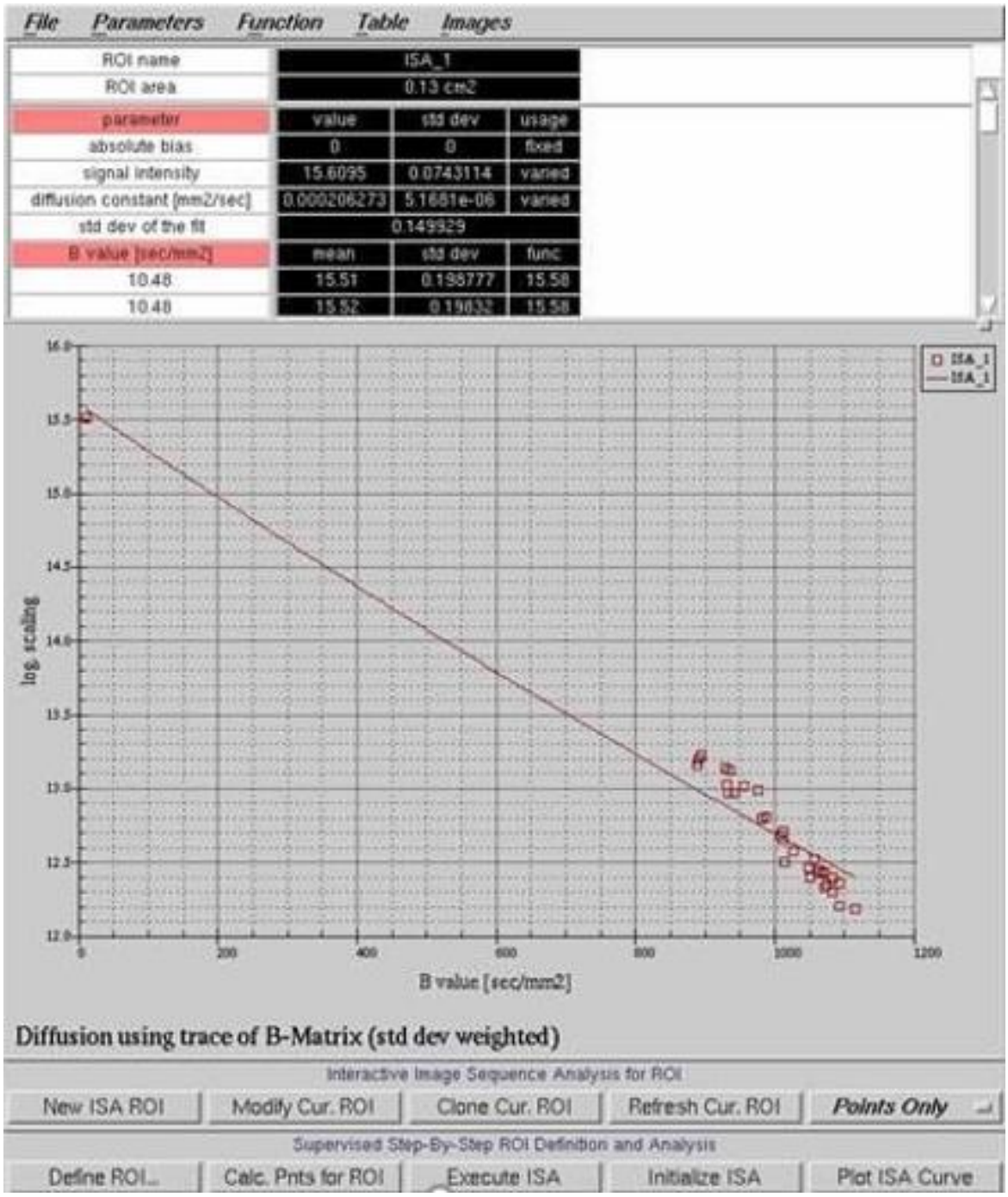


**Figure 7.2: Standard Bruker diffusion experiment (1 average, preset Bruker parameters) with gradient separation of 20ms but STE experiment.**

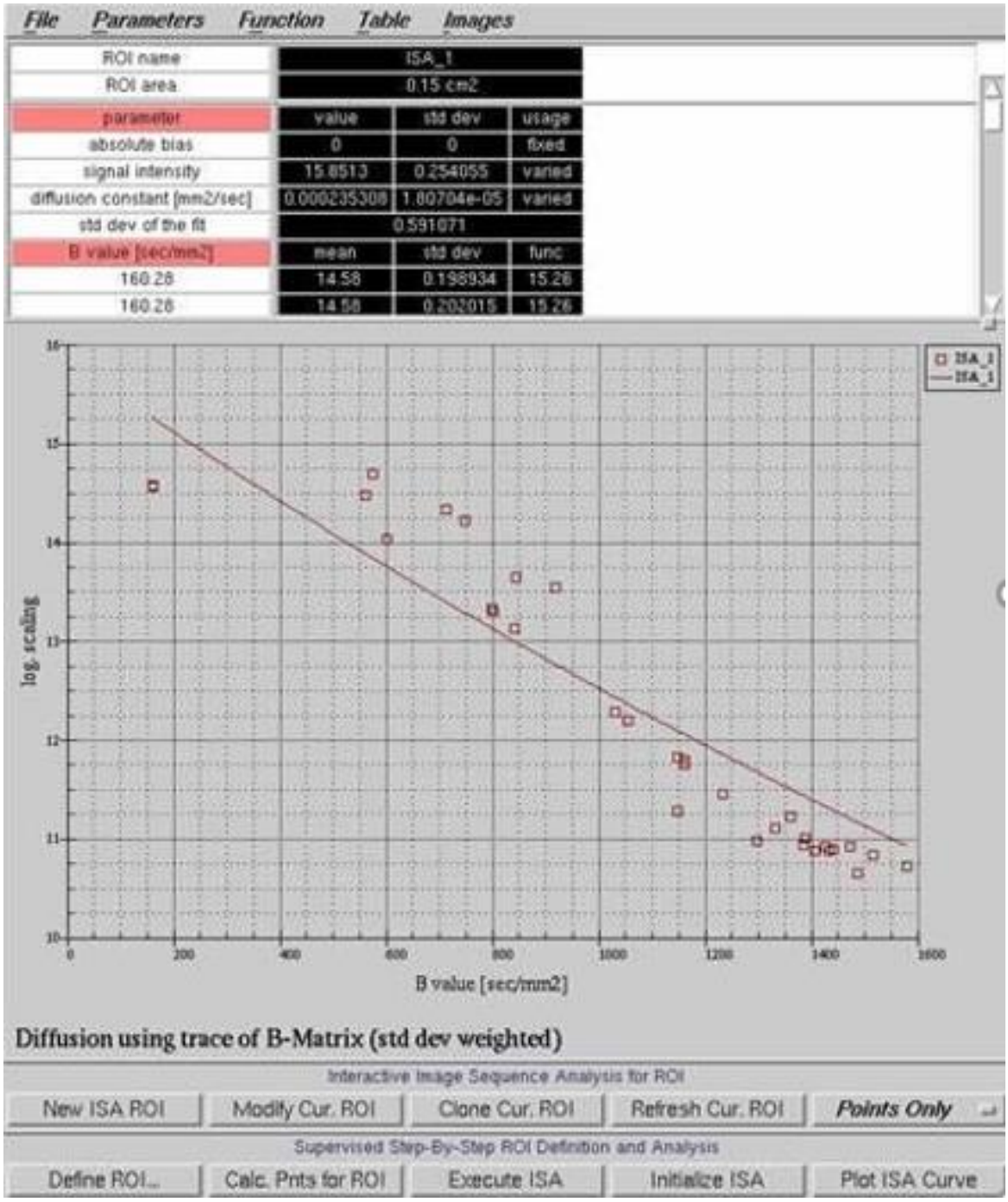


**Figure 7.3: Stimulated echo (STE) experiment with a diffusion gradient separation of 200ms (2 averages).**

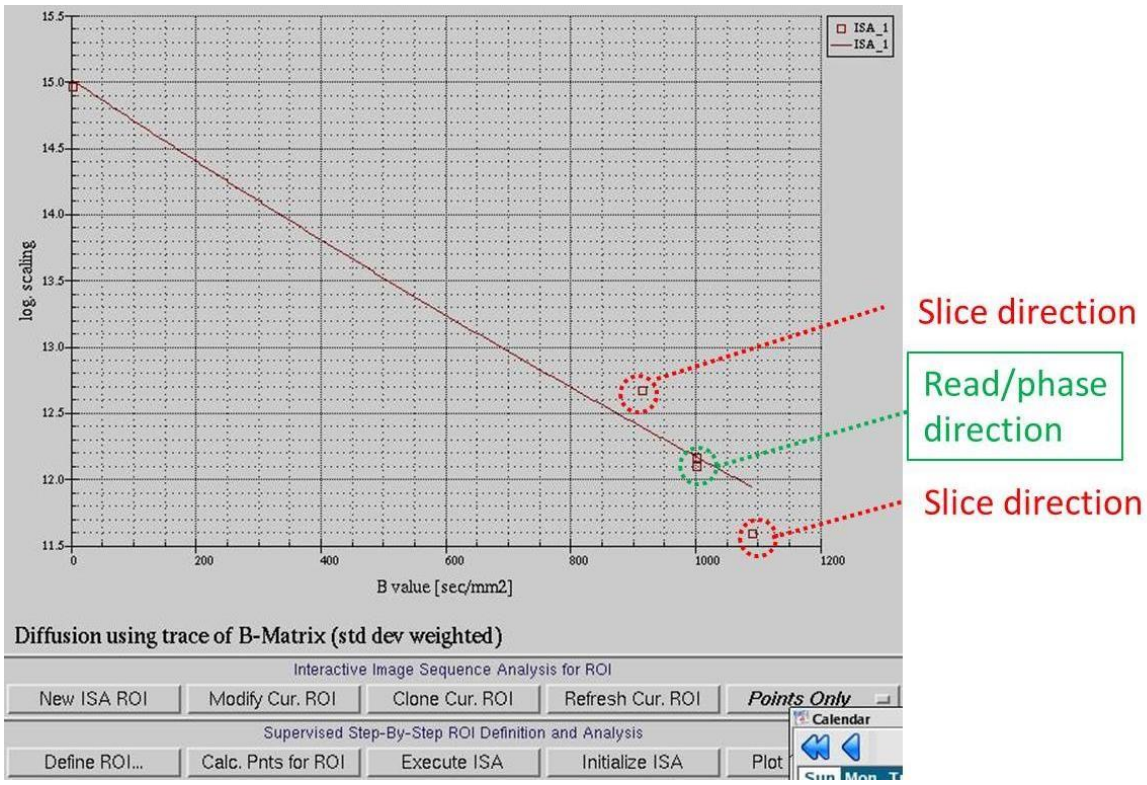


**Figure 7.4: Image shows slice direction (±) deviation when a long observation time (200ms) is used.**

Furthermore, when performing a DTI tensor reconstruction, we noticed changes in the FA values in the same ROI of the phantom: (FA= 0.0159) for Spin Echo; (FA=0.0389) for STEAM with 20 ms Diffusion gradient separation; and (FA=0.112) for STEAM with 200 ms Diffusion gradient separation. The expected value of fractional anisotropy of a water phantom is zero (Malyarenko, Ross and Chenevert, 2014).

It was suspected this could be related to how the "effective *b*- values" were being calculated in the MRI software (Bruker Paravision 5.0), which attempts to take into account the effect of other imaging gradients on the overall effective *b* value.

It was found that the larger the slice gradient component of the particular DTI direction, the stronger was the deviation with a long observation time (Figure 7.4). Further, the magnitude of the *b*-value evaluation error seems to vary linearly with the magnitude of the slice direction gradient used.

### 7.3.1 Pulse program and crusher gradients.

In STEAM-DWI gradient pulses, factors other than diffusion gradients contribute much greater diffusion weighting than in SE-DWI. That, in turn, leads to disrupt the measurement by introducing directional diffusion bias. Consequently, these contributions, particularly from crusher and slice gradients, should be taken into account to avoid the addition of unwanted diffusion weighting 'cross terms' in the B matrix (Basser, Mattiello and Lebihan, 1994). In SE-DWI, the contribution of crusher and slice gradients is usually negligible, because the observation time is very short (the length of the refocusing pulse is only a few milliseconds). However, in STEAM-DWI this effect is much more significant, because the selected crusher and slice gradients can be separated by the longer observation times. For example, experiments were performed with observation times ranging from 20ms to 400ms, hence, the contribution of these two gradients must be taken into account.

In this section, a simple modification to the STEAM-DTI sequence was made, which partially accounts for the unwanted directional bias caused by crusher and slice gradients. We propose a simple method to compensate for cross terms produced by imaging gradients in STEAM diffusion MRI and demonstrate the necessity for the compensation. In fact, in the STEAM sequence, crusher gradients are important not only for removing spurious spin echo coherences but also for not allowing these additional echoes to affect the true signal, thereby reducing image artefacts (Hutter *et al.*, 2018). Originally, in the Bruker DTI Pulse sequence, all three crusher gradient pulses A, B and C have the same values (40%) (Figure 7.5). For the pair of crusher gradients labelled "A" and "C" a 40% gradient combined with a long observation time is enough to entirely crush the signal. To overcome this issue, we changed these values from 40% to 4%.

However, in the Bruker STEAM-DTI pulse sequence programme, the value of the crusher pair "A" and "C" is also automatically applied to the single crusher "B". Unfortunately, reducing the value of crusher pair "B" to 4%, led to artefacts in the EPI image, as crusher B was also reduced to 4%. A low value of the 'B' crusher is insufficient to diphase spurious spin-coherences emanating from the second RF pulse. This additional signal then results in artefacts in the final image. Consequently, the STEAM-DTI pulse programme was modified to make the value

of crusher “B” fixed at 20% and independent of the value of crusher “A” and “C” (Table 7.1).

**Table 7.1: Table shows Crusher gradient values and all modification values for the original Bruker default STEAM- sequence.**

| **Crusher gradients** | **Original Bruker default sequence**<br><br>**A=B=C=40%** | **1st modification**<br><br>**A=B=C=4%** | **Last modification**<br><br>**A=C=4%,B=20%** |
|---|---|---|---|
| A | 40% | 4% | 4% |
| B | 40% | 4% | 20% |
| C | 40% | 4% | 4% |

The last modified pulse sequence was tested in both phantom (0.5 mg/250 ml CuSO4.5H2O) and in vivo using CD1 mice. The modified pulse sequence reduced the image artefact (see Figure 7.6 and Figure 7.7). In addition, the SNR in the cortex, improved from 12.9 with the original Bruker default STEAM-DTI sequence to 27.5 with the modified STEAM-DTI sequence.

However, the FA of the copper sulphate phantom was measured as FA=0.086 with STEAM-DTI ($\Delta$=200ms). For an isotropic water phantom, the FA should be zero because diffusion is the same all directions. Hence, in the next section we describe how other STEAM-DTI imaging parameters may lead to FA errors.

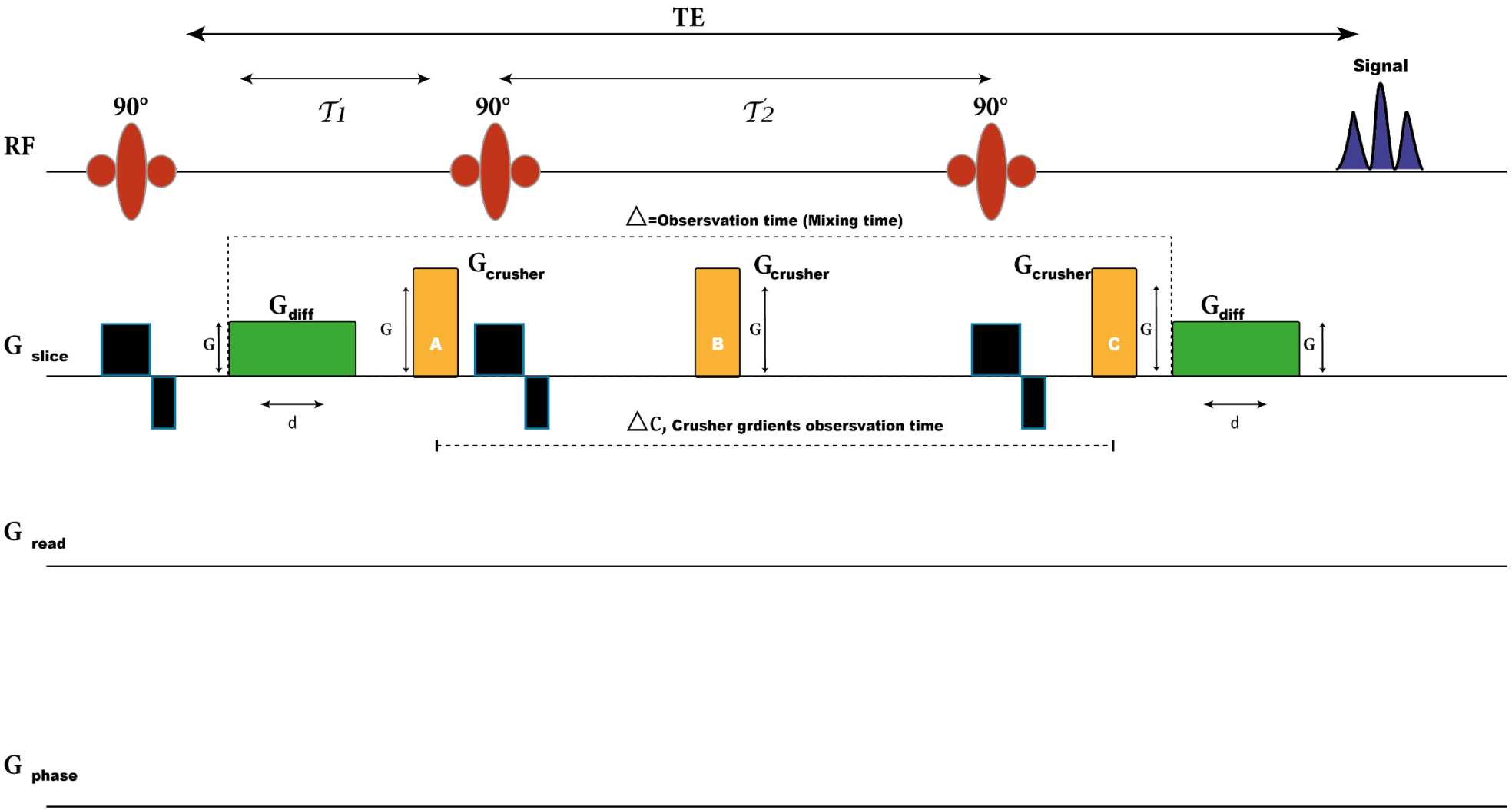


**Figure 7.5: Diagram of the Bruker default Stimulated Echo Acquisition Mode (STEAM) Pulse Sequence.**

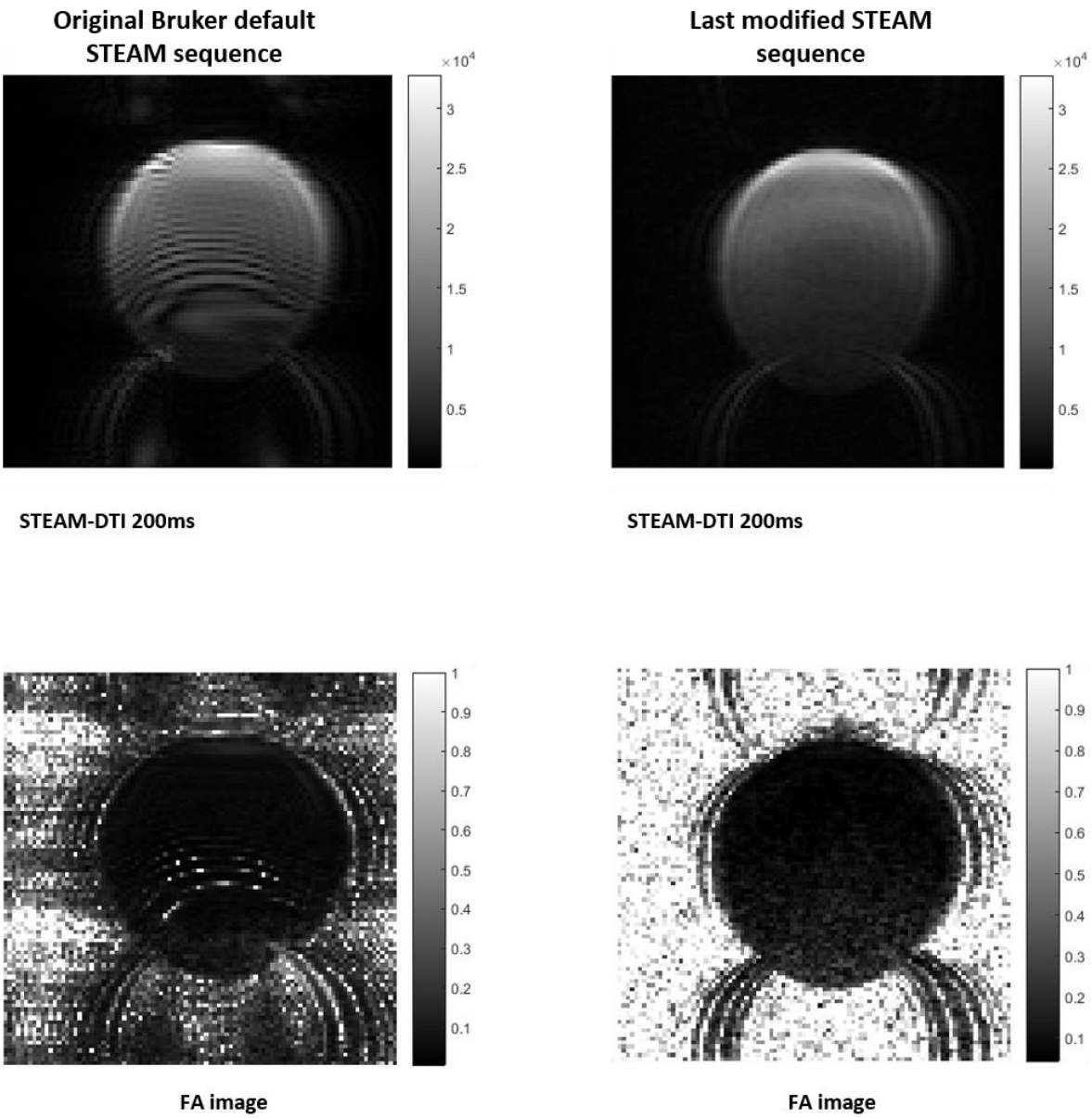


**Figure 7.6: STEAM-DTI, with 200 ms observation time, that was acquired with both the original Bruker default sequence and our last modified STEAM-DTI pulse sequence on an isotropic liquid phantom.**

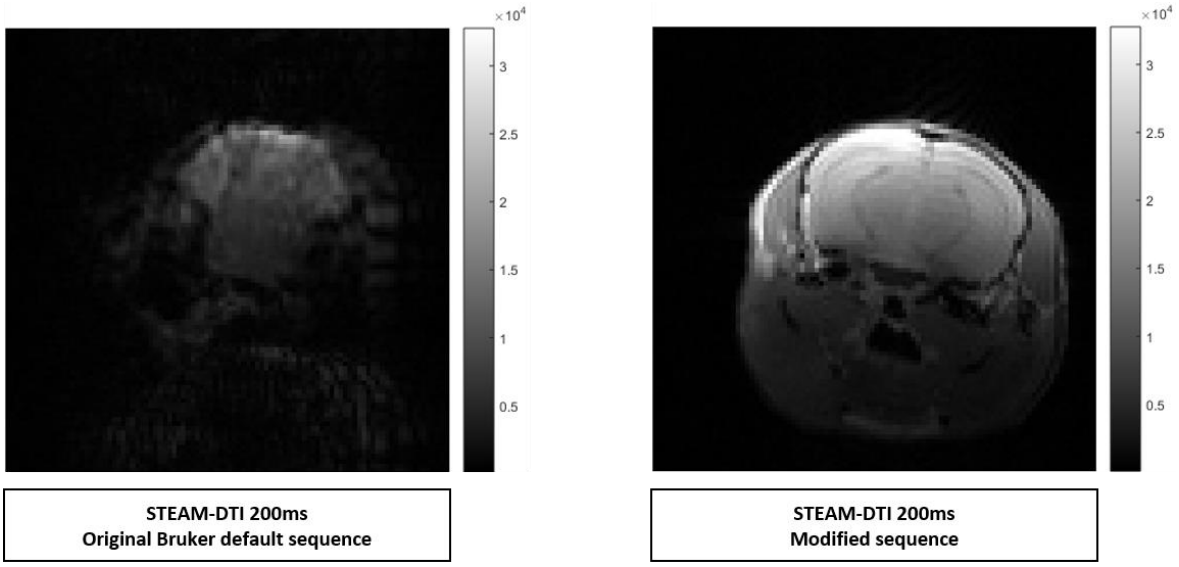


**Figure 7.7: STEAM-DTI with 200 ms observation time, acquired with both the original Bruker default sequence and our last modified STEAM-DTI pulse sequence on an in vivo CD1 mouse (*n*=1).**

## 7.4 Investigating the effect of MRI parameters on accuracy of STEAM-DTI

The effect of various MRI parameters were investigated with the aim of minimising STEAM-DTI errors. DTI experiments were performed on a water phantom (0.5 mg/250 ml $CuSO_4.5H_2O$), which had a T2 of 137ms. The effect of slice thickness, *b* value, observation time and RF pulse were systematically investigated.

### 7.4.1 Effect of different *b* value on FA measurements

In order to investigate the effect of observation time and *b*-value on FA measurements, a series of measurements were performed on a water phantom (1 g/l $CuSO_4$). For SE-DTI, the measured FA is close to the expected value of zero, however, it does deviate slightly from zero for lower *b*-values and long observation times (Figure 7.8(a)). For the STEAM-DTI measurements, the deviation from the expected FA=0, is very marked at lower *b*- values and longer observation times. With FA=0.14 for Δ=200 and *b*=300 (Figure 7.8 (b)).

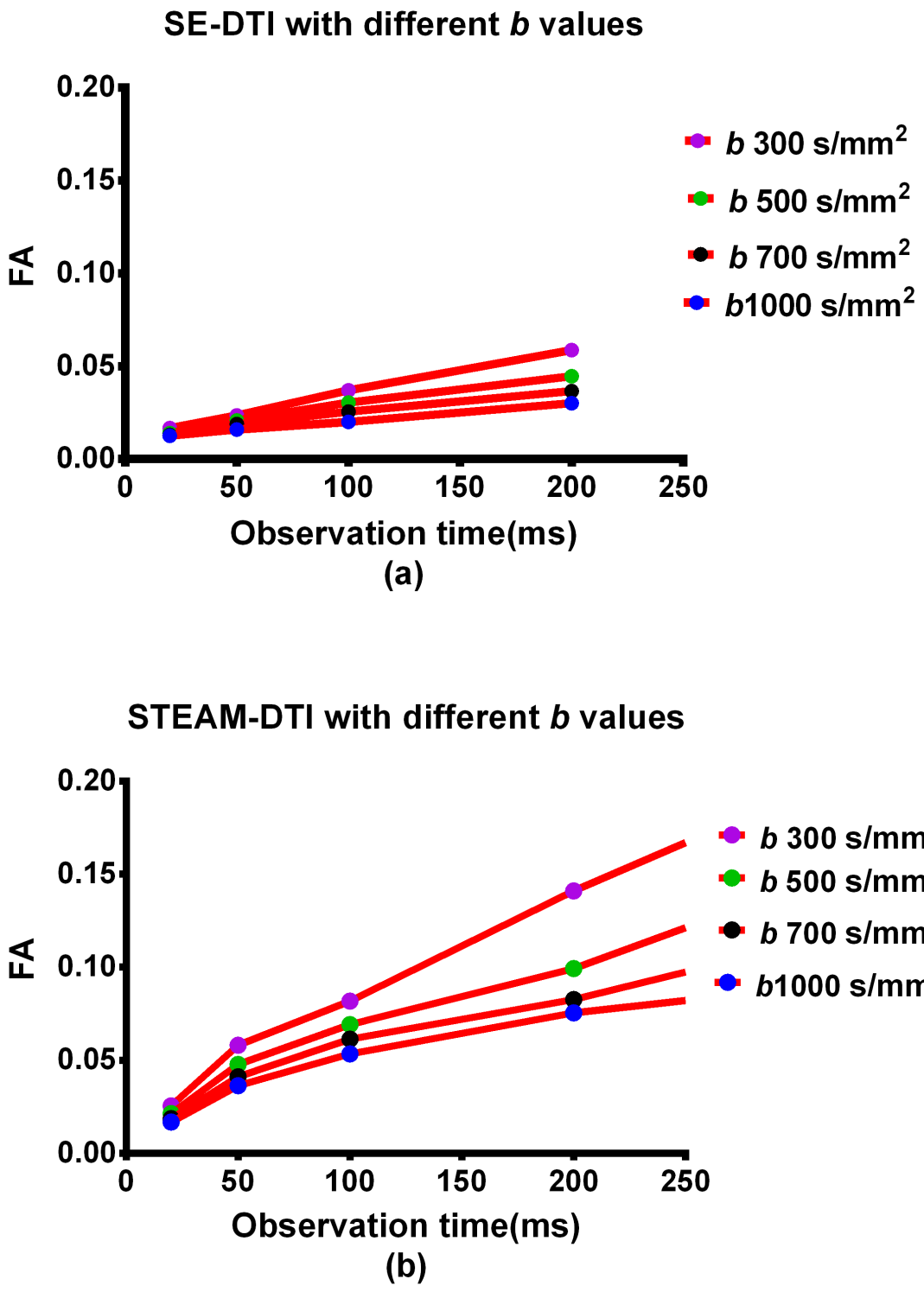


**Figure 7.8: FA value acquired with different *b* values and observation times with SE-DTI and STEAM-DTI acquisition modes.**

The range of 700-1000 s/mm$^2$ is the range used by the majority of DTI studies nowadays. That, in turn, leads to a 30-50% reduction in the signal, assuming that the mean diffusivity of normal WM is approximately 0.8 to 1x $10^{-3}$ mm$^2$/s (Tournier,

Mori and Leemans, 2011). As in our experiment, the measure of FA on the copper sulphate phantom was affected by the number and the strength of *b* values for both SE-DTI and STEAM-DTI. Moreover, the number and strength of *b* values influenced measures of (FA) value, particularly with STEAM, due to the long observation times (Figure 7.8 (b)). From the figure above, a larger *b* value for both DTI sequences led to higher measures of signal attenuation compared with a lower *b* value and greater errors for the same time. Hence, *b*=700 s/mm$^2$ seemed to be reasonable for our experiment, due to the long observation times we planned to use which, in turn, led to fewer errors and less signal loss. In addition, this *b*-value appeared to be optimal for the mean diffusivity of the WM that we estimated to be between 0.8 and 1x $10^{-3}$ mm$^2$/s.

### 7.4.2 Effect of slice thickness on FA measurements

STEAM-DTI was performed with *b*-values of 1000,700,500 and 300 s/mm$^2$. For all *b*- values, the slice thicknesses were 1, 2,3 and 4 mm and the gradient separation time (Δ) was 200ms. As shown in Figure 7.9, the FA value decreased in with thicker slices with different *b*-values (1000,700,500 and 300s/mm$^2$). However, a 4mm thicker slice would be very large by comparison with the size of a mouse brain. Consequently, we decided to use 1mm slices as a compromise. Different spoiler gradients with a Hermite pulse shape were also investigated with different slice thicknesses. A thicker slice was found to be more accurate for FA measurement than a thinner slice with a long observation time (Figure 7.10).

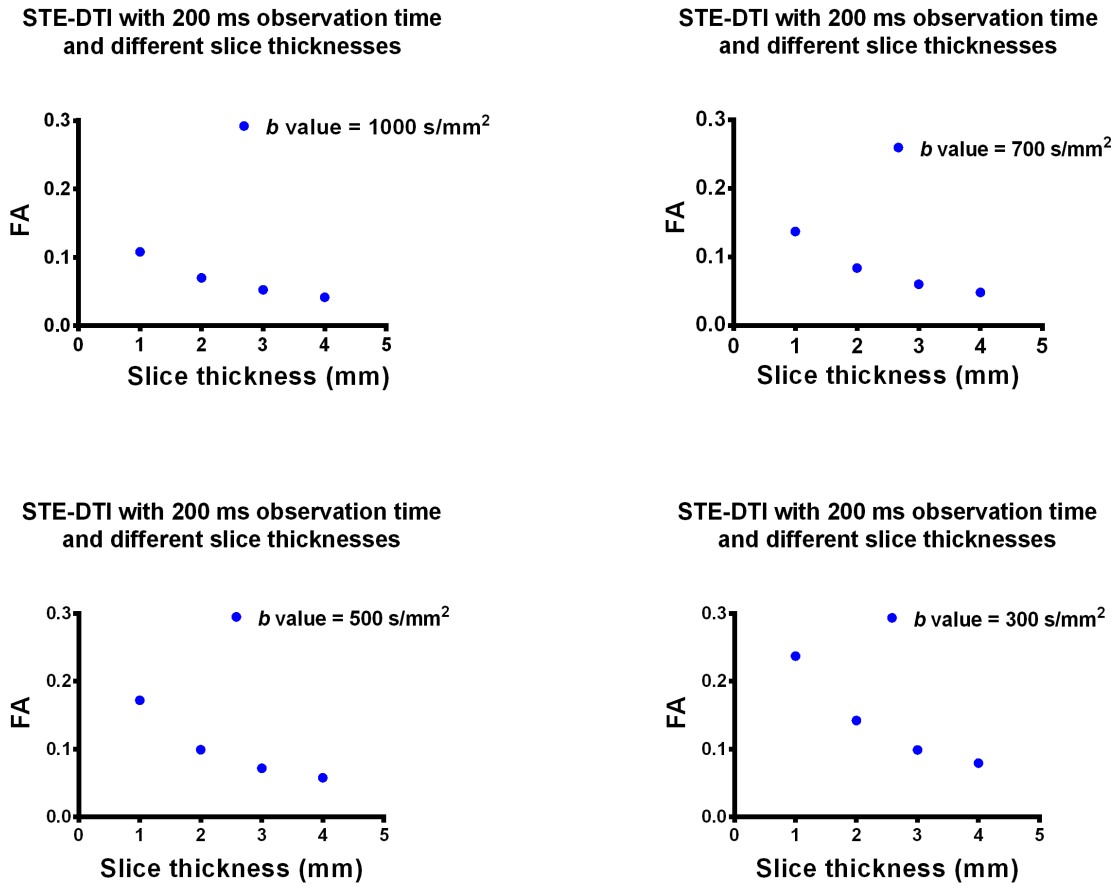


**Figure 7.9: Effect of slice thickness on FA value measurement with 200 ms observation time and different *b* values. FA values were closer to zero than we expected with thicker slices, each with different *b* values.**

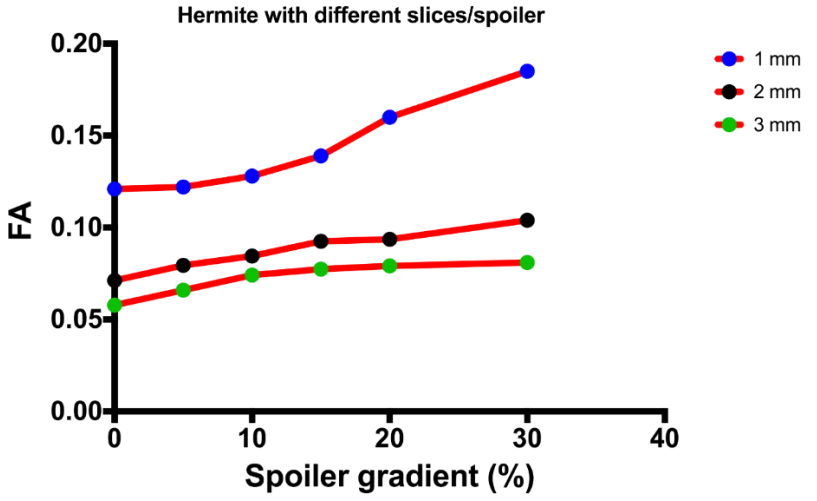


**Figure 7.10: Effect on FA value of different slice thickness and spoiler gradient.**

To acquire a signal in magnetic resonance, it is necessary to generate a component of the net magnetisation in the transverse plane (Pooley, 2005). This is achieved by applying a RF pulse at the Larmor frequency. In MR, it is often necessary to have very well-defined excitation profiles. This is achieved using amplitude and/or phase modulated RF pulses. Amplitude modulated pulses are often referred to as shaped pulses and, within the spectrometer, this is achieved using a modulator, where the output of a frequency synthesiser is modulated by a particular low frequency shape. The excitation bandwidth of the RF pulse will be a function of this shape and the length of the pulse. In fact, there are different radiofrequency pulse shapes such as Sinc, Gaussian, Hermite and Halfgause. A good compromise between the requirements of a simple pulse shape with low power requirements and good slice profile is represented by the hermite pulse shape.

Different pulse shapes and length were also investigated. The experimental results demonstrated that RF pulse shape had no significant effect on FA value measurements (Figure 7.11).

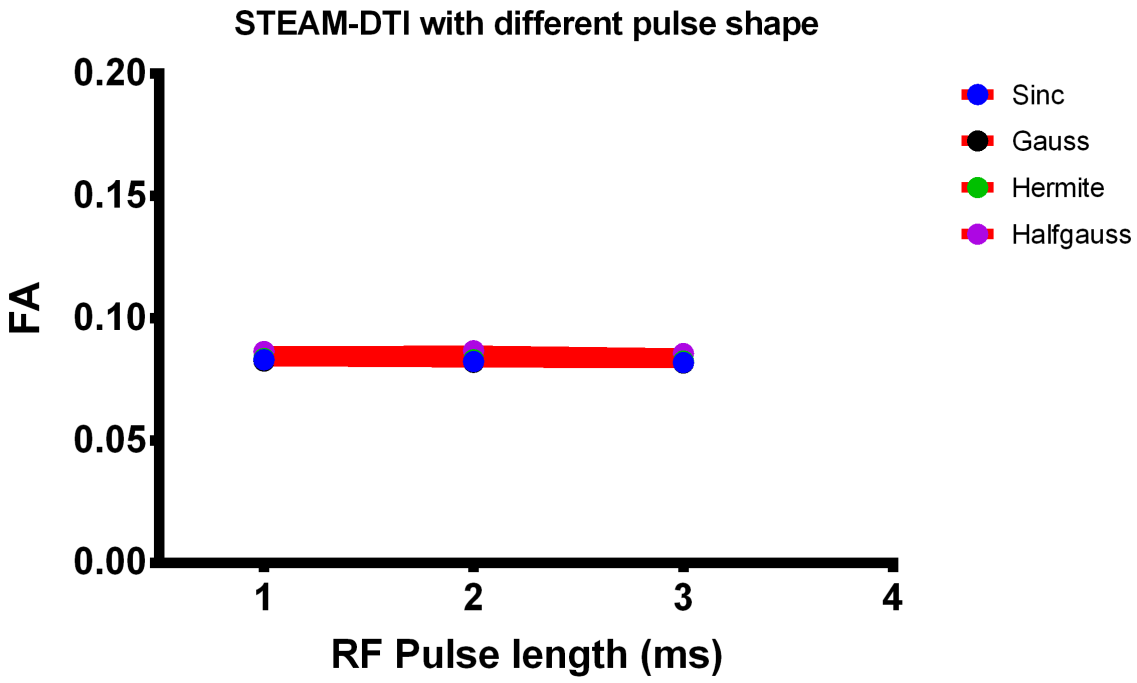


**Figure 7.11: FA value with different RF pulse shape and length.**

## 7.5 Discussion

In this study we optimised different imaging acquisition parameters of STEAM-DTI for a long observation time. We observed a strong dependence of FA value on different imaging parameters including long observation time, different slice thickness and *b* values. However, different pulse shape and length did not show any significant effect on FA measurement. After we noted this effect and investigated using previous measurements, we decided to use a slice thickness of 1 mm for the in vivo experiment and *b*=700mm$^2$/s to minimise errors. Although not optimal for accurate FA measurements, this decision had to take account of the size of the mouse brain (508.91 ± 23.42 mm$^3$)(Badea, Ali-Sharief and Johnson, 2007), and the need to acquire multiple slices across the brain. In addition, using a very thick slice (e.g. 4mm) would result in the averaging of the signal through the slice, resulting in 'blurred' anatomical images. The parameters of *b*-value, slice thickness and crusher gradients, in conjunction with STEAM, may provide a new way to probe the tissue structure using a long observation time. Although these acquisition parameters reduced the error, we considered it necessary to also correct *b* matrices.

## 7.6 B matrices correction

In diffusion MRI, the relationship between signal, *b*-value and diffusion coefficient is expressed as:

**Equation 7.1**

$$S = S_0 \, exp^{-bD}$$

Where: S= signal with diffusion gradients, $S_0$= signal without diffusion gradients; *b* is the *b*-value; D is the diffusion coefficient.

It is extremely difficult to theoretically correct the *b*-matrices for STEAM-DTI (Pierpaoli and Basser, 1996)(Marks *et al.*, 1996). Hence, we decided to correct the *b*-matrices by first performing STEAM-DTI measurements on a doped water phantom. These corrected *b*-matrices would then be applied to in vivo data. As

the diffusion coefficient of water is isotropic and known from previous literature, the correct *b*-matrices can be back calculated by rearranging Equation 7.1, as below:

**Equation 7.2**

$$\boldsymbol{b} = \left(\frac{\boldsymbol{-1}}{\boldsymbol{D}}\right) \mathbf{x}\ \boldsymbol{In}\left(\frac{\boldsymbol{S}}{\boldsymbol{S_0}}\right)$$

From Equation 7.2, we calculated the correct *b* value for diffusion with all the different observation times (20, 200 and 400ms). Figure 7.12 shows the diffusion value before and after correction. It is noticeable from the graph that the diffusion value is much better and more accurate after *b* value correction, particularly with longer observation times (STEAM-200 ms and STEAM-400 ms). Moreover, FA measured after correction, compared with non-correction, shows values close to zero; FA=0.028 with STEAM 200ms (Figure 7.13 (a)). Although it is not zero, it is much better than before the correction. Moreover, the mean diffusivity is more stable after correction than before (Figure 7.13 (b)). However, we need to consider this offset on our FA value (~0.02 for STEAM 200ms and 0.05 for STEAM 400). Thus, diffusion after correction was faster and better aligned and this, in turn, allowed a much better opportunity to probe any microstructural changes for in vivo experiments.

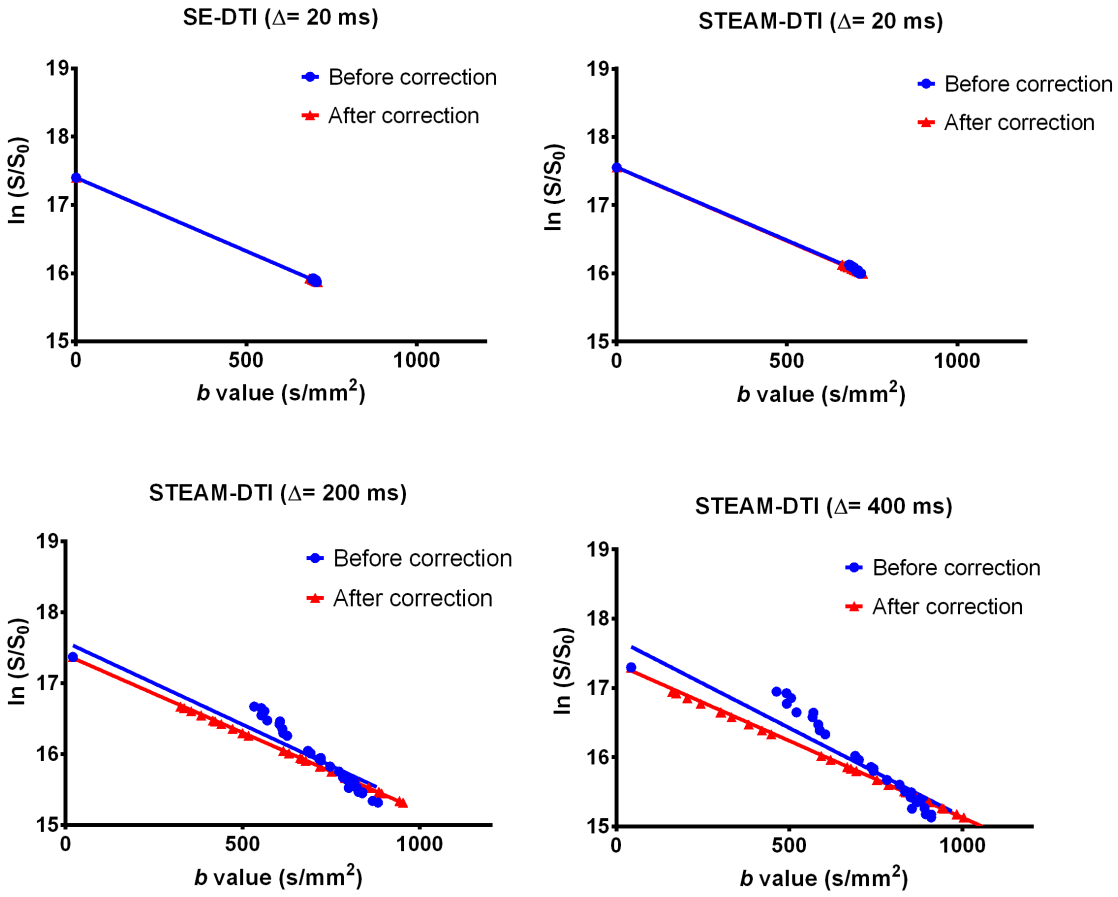


**Figure 7.12: Diffusion before and after *b* value correction.**

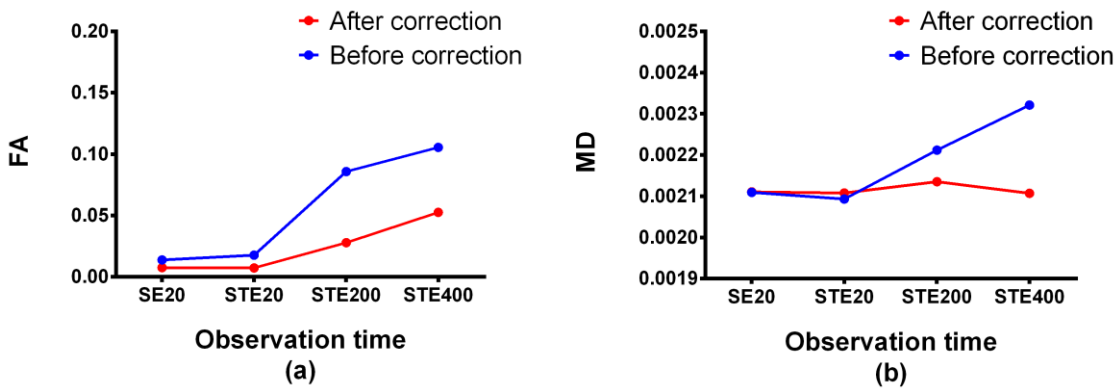


**Figure 7.13: FA (a) and mean diffusivity MD (b) before and after *b* value correction with different observation time.**

While the original sequence applied to the in vivo experiment (*n*=1) shows some artefacts, they appear to be eliminated using the modified sequence (Figure 7.7).

## 7.7 Conclusion

For MRI diffusion acquired where the observation time is long compared with the T2-relaxation time, it can be more advantageous to use STEAM rather than SE-DWI (Method and Diffusion, 2003)(Hanicke, 1991). This, in turn, has a potential positive effect for diffusion imaging where T2- relaxation time is short, particularly for 7T and higher magnetic field strengths. During the mixing time, the STEAM signal decays as the rate of T1 relaxation increases the diffusion time, whereas with SE-DWI T2 the decay occurs during the whole SE-DWI sequence. In fact, SE-DWI is preferable for many standard DWI applications and avoids the loss of the initial 50% signal. However, with STEAM-DWI, half of the echo is lost (Lundell, Alexander and Dyrby, 2014). STEAM-DWI is useful for measuring tissues with short T2-relaxation times, such as muscle or cartilage (Brihuega-Moreno, Heese and Hall, 2003), and is also useful for measuring diffusivity in water compartments with lower T2 relaxation like myelin water that has been reported with SE-DWI in pre-clinical settings (Andrews, Osborne and Does, 2006).

In general, as the field strength increases, T2 decreases (Michaeli *et al.*, 2002), and T1 increases, hence, early evidence suggests the benefits of STEAM-DWI for in vivo human brain tensor imaging at 7T (Heidemann *et al.*, 2010). Dyrby et al. (Dyrby *et al.*, 2014) suggest the need for longer observation times to ensure sensitivity for axon diameter, which is very useful for microstructural imaging such as the distribution of neuronal fibre $A_X$ caliber (Assaf *et al.*, 2015).

To detect any pre-clinical or clinical changes in diffusion, sources of technical bias must be separated from biological- and therapy-induced changes such as ionizing radiation and chemotherapy. Therefore, both gradient calibration and correction could play a vital role in general diffusion imaging, and these techniques may facilitate our longitudinal study design. The result from the copper sulphate and in vivo experiments clearly show the advantages of using the optimization strategy. In fact, the measurement of diffusion anisotropy in an isotropic copper

sulphate phantom acts as an indicator of precision because any errors in measurement of the anisotropy must be attributed to the estimation error of the tensor. It is important to stress that the parameters derived in these experiments were for a particular DTI experiment with a long observation time. The protocol and retrospective correction were shown to be effective.

## 7.8 References

Andrews, T. J., Osborne, M. T. and Does, M. D. (2006) 'Diffusion of Myelin Water', 385(April), pp. 381–385. doi: 10.1002/mrm.20945.

Assaf, Y. *et al.* (2015) 'HHS Public Access', 59(6), pp. 1347–1354. doi: 10.1002/mrm.21577.AxCaliber.

Badea, A., Ali-Sharief, A. A. and Johnson, G. A. (2007) 'Morphometric analysis of the C57BL/6J mouse brain', *NeuroImage*, 37(3), pp. 683–693. doi: 10.1016/j.neuroimage.2007.05.046.

Basser, P. J., Mattiello, J. and Lebihan, D. (1994) 'MR Diffusion Tensor Spectroscopy and Imaging', 66(October 1993).

Brihuega-Moreno, O., Heese, F. P. and Hall, L. D. (2003) 'Optimization of Diffusion Measurements Using Cramer-Rao Lower Bound Theory and Its Application to Articular Cartilage', *Magnetic Resonance in Medicine*, 50(5), pp. 1069–1076. doi: 10.1002/mrm.10628.

Dyrby, T. B. *et al.* (2014) 'Contrast and Stability of the Axon Diameter Index from Microstructure Imaging with Diffusion MRI', 721(2013), pp. 711–721. doi: 10.1002/mrm.24501.

Hanicke, W. (1991) 'Diffusion Imaging Using Stimulated', 239, pp. 233–239.

Heidemann, R. M. *et al.* (2010) 'Diffusion Imaging in Humans at 7T Using Readout-Segmented EPI and GRAPPA', 14(February), pp. 9–14. doi: 10.1002/mrm.22480.

Hutter, J. *et al.* (2018) 'Quiet echo planar imaging for functional and diffusion MRI', *Magnetic Resonance in Medicine*, 79(3), pp. 1447–1459. doi: 10.1002/mrm.26810.

Kato, H. *et al.* (2005) 'Composition of MRI phantom equivalent to human tissues', *Medical Physics*, 32(10), pp. 3199–3208. doi: 10.1118/1.2047807.

Lundell, H., Alexander, D. C. and Dyrby, T. B. (2014) 'High angular resolution

diffusion imaging with stimulated echoes : compensation and correction in experiment design and analysis', (December 2013), pp. 918–925. doi: 10.1002/nbm.3137.

Malyarenko, D. I., Ross, B. D. and Chenevert, T. L. (2014) 'Analysis and correction of gradient nonlinearity bias in apparent diffusion coefficient measurements', *Magnetic Resonance in Medicine*, 71(3), pp. 1312–1323. doi: 10.1002/mrm.24773.

Marks, P. *et al.* (1996) 'Acute and Chronic Stroke: Navigated Spin-Echo Diffusion-weighted MR Imaging', pp. 403–408.

Method, S. and Diffusion, R. (2003) 'Use of the Stimulated Echo in NMR Diffusion Studies', 2523(September). doi: 10.1063/1.1673336.

Michaeli, S. *et al.* (2002) 'Proton T2 relaxation study of water, N-acetylaspartate, and creatine in human brain using Hahn and Carr-Purcell spin echoes at 4T and 7T', *Magnetic Resonance in Medicine*, 47(4), pp. 629–633. doi: 10.1002/mrm.10135.

Pierpaoli, C. and Basser, P. J. (1996) 'Toward a quantitative assessment of diffusion anisotropy', *Magnetic Resonance in Medicine*, 36(6), pp. 893–906. doi: 10.1002/mrm.1910360612.

Pooley, R. A. (2005) 'AAPM/RSNA physics tutorial for residents: fundamental physics of MR imaging.', *Radiographics : a review publication of the Radiological Society of North America, Inc*, 25(4), pp. 1087–1099. doi: 10.1148/rg.254055027.

Tournier, J., Mori, S. and Leemans, A. (2011) 'Diffusion Tensor Imaging and Beyond', 1556, pp. 1532–1556. doi: 10.1002/mrm.22924.

Welvaert, M. and Rosseel, Y. (2013) 'On the definition of signal-to-noise ratio and contrast-to-noise ratio for fMRI data', *PLoS ONE*, 8(11). doi: 10.1371/journal.pone.0077089.

# Chapter 8

# Chapter-8 Diffusion MRI monitoring of specific structures in the irradiated mouse brain

## 8.1 Introduction:

Radiotherapy is widely used for the treatment of primary brain tumours or metastasis (Constanzo *et al.*, 2018). However, the patient's quality of life may be affected by radiotherapy treatment, leading to potentially severe cognitive impairment (Pérès *et al.*, 2018). Unfortunately, cognitive deficits have been reported in 50-90% of patients who were suffering from brain tumours and survived more than six months after partial or whole brain irradiation (Brown *et al.*, 2016). Hence, treatment planning must be improved (Ostrom *et al.*, 2015) as fewer than 5% of glioblastoma patients survive more than 5 years and patients with brain metastasis have a median survival time of 5 to 25 months (Agboola *et al.*, 1998),(Nieder and Mehta, 2009). In fact, with the exception of the radiation dose, the location of the tumour and the volume to be irradiated, there is very limited knowledge available on the likelihood of behavioural alteration and brain damage. Consequently, such considerations are not included in treatment planning. For example, Stereotactic Radiosurgery (SRS) consists of the delivery of a high single or hypo-fractionated dose targeting a small tumour or metastasis in the brain region. However, clinical complications, such as delayed formation of oedema in the irradiated volume area and, in some cases, necrosis development, are often reported (Constanzo *et al.*, 2017),(D. *et al.*, 2013).

Therefore, we sought to identify the negative impact of acute, early delayed and late or chronic radiation-induced changes in normal brain tissues. To accomplish this, we irradiated half of the mouse brain hemisphere with a 20 Gy single dose, which is the minimum amount of radiation for inducing changes in healthy mouse brain tissues (Liu *et al.*, 2010). We investigated the ability of traditional DTI and a novel variant, to detect and monitor any microstructural and pathological changes at different time points post-irradiation. To investigate the impact of long observation times, Δ, we used the modified stimulated echo DTI sequence, that was described in section 7.3.1,Chapter-7. In that process, we modified the amount of crusher gradient used to overcome any artefacts during scanning to improve the sequence stability. The study by Dyrby et al. (2014), suggested the need for

long observation times, particularly with the Stimulated Echo Acquisition Mode (STEAM), probe large axon diameters (Dyrby *et al.*, 2014).

## 8.2 Aim:

Significant side effects causing decreased quality of life can be the result of the targeting the human brain with irradiation. Consequently, preclinical studies are needed to adequately investigate structural and functional alterations after brain irradiation. A SARRP was used as a robust standardised method of targeted irradiation on small regions of the mouse brain. The use of diffusion MRI to analyse the properties of mesoscopic and biological structures in the brain post-radiation therapy remains challenging. Hence, this study aimed to investigate the consequences of unwanted doses on healthy tissues when assessing radiation-induced brain damage of living mice, by comparing DTI with histopathology. Several DTI measures were quantified and compared with histopathology, focusing on the cortex, corpus callosum, hippocampus, fimbria, and thalamus. Different ROI's were selected to understand the biological effect of radiation exposure in the CNS. Different WM regions were selected because of the WM changes observed in the study presented in Chapter-5. It has been proposed that WM in the brain is more vulnerable to IR than GM due to its fewer capillaries (McDonald and Hayes, 1967). Further, GM regions like the hippocampus, thalamus and cortex were also selected because of their involvement in various essential cognitive functions such as the production of memory, awareness, learning and motor functions. Ionising radiation effects can hamper these pathways causing permanent damage (Watve *et al.*, 2018). Therefore, we sought to determine the impact of radiation-induced changes in the different brain regions, at different time points post-IR. To accomplish this, we conducted a longitudinal study, using histology to confirm any changes detected by diffusion MRI. It is generally agreed that histopathology is the gold standard for characterising diseased tissue and for validating imaging biomarkers.

## 8.3 Methods:

### 8.3.1 Experimental design and animal model

All studies were performed in compliance with relevant procedures of The University of Glasgow and approved by the Home Office Local Ethical Review Panel. C57 BL/6 mice (n=31) were irradiated with a 20 Gy single dose targeting the right brain hemisphere with a SARRP machine, while (n=5) mice received 0 Gy and were used as a control (Figure 8.1).

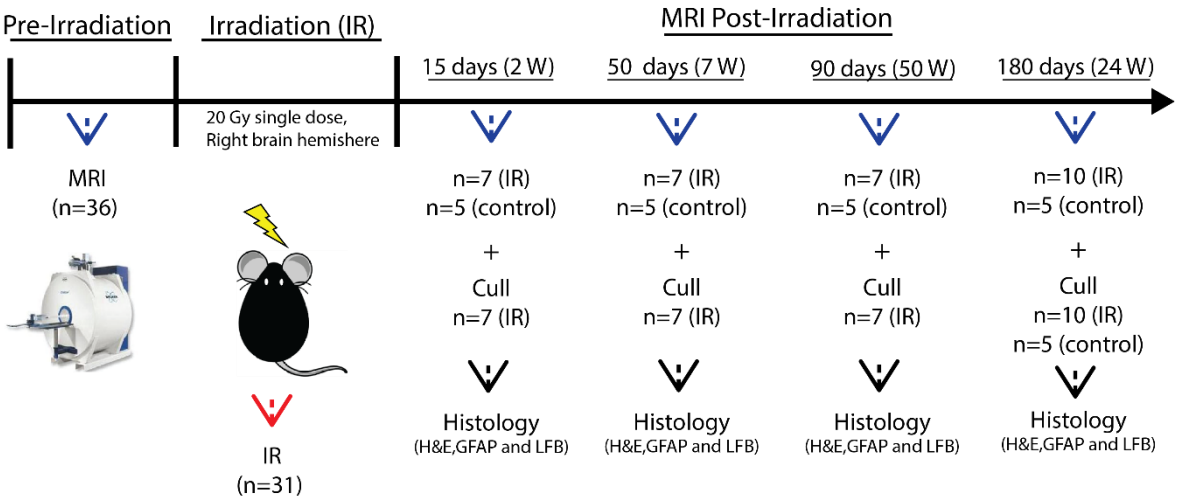


**Figure 8.1: Experimental design and timeline.**

### 8.3.2 Irradiation protocols

#### 8.3.2.1 Small Animal Radiation Research Platform (SARRP)

For precision irradiation, a new system, known as SARRP, has been designed to allow targeted irradiation studies on small animals. It has been used with beam sizes as small as approximately 0.5 mm and is guided by a radiation on CBCT (Matinfar *et al.*, 2009), which provides a quick and efficient beam size with minimal scatter of radiation to the surrounding tissues. As in clinical irradiation therapy, treatment planning is needed (Gutierrez, Descamps and Vanhove, 2015), hence, the SARRP has an integrated X-ray CT scanner. Using a beam collimator for

the radiation, we can use the CT image to precisely localise the radiation beam in the brain. Hence, the collimator plays a vital role in adjusting the X-ray field to irradiate only the target area and minimise the dose to other tissues, thus mimicking a clinical situation.

#### 8.3.2.2 Radiation Therapy Treatment Planning

Two single fraction exposures of the mouse's right brain hemisphere were performed as feasibility studies. In planning our research, CT scans were acquired and used as described above. The first experiment involved the delivery of the beam to target a region of interest of 10 x 10 $mm^2$ inside the right brain hemisphere. For CT image acquisition, animals were moved to a SARRP using the in-house based multimodality bed to maintain a fixed mouse head position. The cone beam was acquired with the following parameters: 220 KV, 13 mA and 409 seconds. One mouse brain hemisphere received an absorbed dose of 20 Gy. The system in Glasgow requires the use of fixed collimators of various sizes that restricts conformality to some extent, while still achieving excellent tumour coverage using the SARRP. Consequently, the ability of SARRP to deliver accurate doses to small volumes provides confidence in the clinical relevance of pre-clinical radiation studies (Rutherford *et al.*, 2019).

### 8.3.3 MRI techniques

#### 8.3.3.1 Experimental set up

All mice (n = 36) were scanned with MRI pre-IR and at each time point post-IR. Experimental mice (n = 7) and controls (n = 5) were scanned using a small animal 7T MRI scanner with a dedicated brain receiver mouse coil at 15 (n=7), 50 (n=7), 90 (n=7) and 180 (n=10) days post-IR. In addition, for each MR sequence, the first and second slices were located between the interface of the olfactory bulb and the brain and were visible on the tripilot images with a sagittal view. DTIs were acquired using a multi-slice (S=7) SE-DTI sequence with 30 diffusion gradient directions and a *b*-value of 700 $s/mm^2$. A reference $b_0$ image was also acquired, $b_0$= 0.612455 $s/mm^2$. Other imaging parameters were: $\Delta$ = 20 ms, $\delta$ = 4 ms, TR/TE 3800 ms/ 36.06 ms, slice thickness 1mm and number of averages = 4. Stimulated Echo multi-slice (n=7) DTIs (STE-DTI) were acquired with the following

parameters: Δ = 20, 200 and 400 ms, TR/TE = 3800, 30.95, *b* value 700 s/mm$^2$ and 4 averages. Matrix= 96 x 96, FOV= 2.00 cm and spatial resolution=0.0208 cm/pixel.

T2 weighted high resolution images were obtained using the following parameters: TR = 5000 ms, effective echo time TE $_{eff}$ = 46 ms, 4 averages, 1 echo, number of slices = 14, slice thickness = 0.5 mm, field of view = 20 mm.

## 8.3.4 MRI Data acquisition

### 8.3.4.1 Anatomical MRI

T2 weighted MRI scans were used to calculate whole, right and left brain volumes by manual segmentation of all acquired slices (S=14) using a MATLAB code programmed in-house. Matlab code was used for analysing both T2 weighted images from different slices and DTI images. Matlab code was programmed for the simultaneous analysis of both T2 weighted and DTI images with different observation times. The programme thresholds the MD images to identify voxels containing the CSF, namely, the ventricles, and removes these voxels from the analysis, thus avoiding contamination by partial volume effects.

### 8.3.4.2 Artefact correction

On each DTI, the field homogeneity was maximised by acquiring a field map image then using Bruker "Mapshim" to calculate shim values, hence minimising artefacts (Figure 8.2).

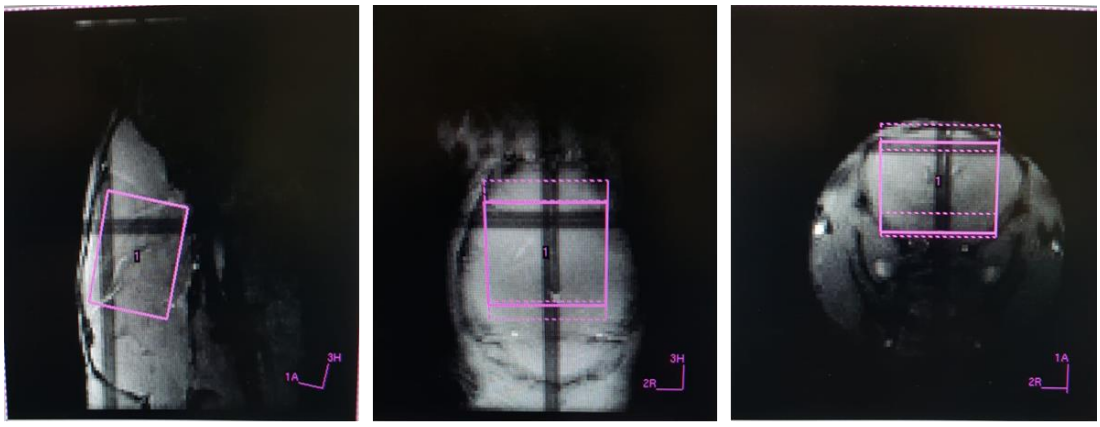


(a) (b) (c)

**Figure 8.2: Image shows an example of map shimming, from different positioning, for one mouse.**

In addition, a diffusion weighted spoiler gradient (Dw GSP) was increased from 0 % to 20 %, which is effective in reducing artefacts without simultaneously affecting the diffusion parameters (see Chapter-7,section 7.3.1).

#### 8.3.4.3 MRI slices

To make sure the same brain slices for each mouse were longitudinally scanned, post-IR slice positions were matched and checked with the pre-IR localiser scans (Figure 8.3). As the effect we are seeking was expected to be subtle, care was taken in positioning slices.

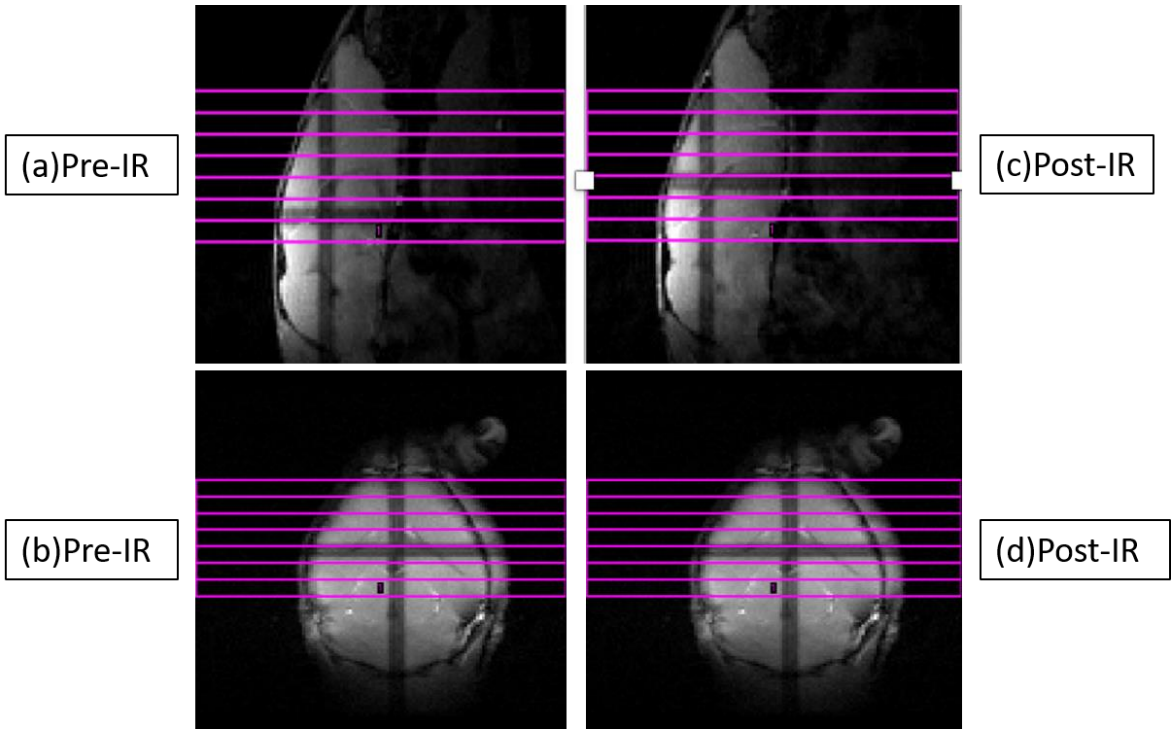


**Figure 8.3: Image shows slices matched before MRI scanning between pre-IR (a and b) and post-IR (c and d).**

## 8.4 Histopathology

A total of 36 mice, including 5 control mice at the last time point, were euthanised for histological pathology observation at 4 different time points (15 days n=7, 50 days n=7, 90 days n=7 and 180 days n=10) post-irradiation. The mice were transcardially perfused using 4% PFA in 0.1 M phosphate buffer (PBS; pH 7.4) under

deep anaesthesia. The brains were removed and post-fixed for 24 h in PFA before being Paraffin embedded using aTissue Tek Vacuum Infiltration Processor. The whole brains were then re-embedded in paraffin wax, mounted onto a wooden block and coronally sectioned on a microtome (Leica RM 2135) at 6 µm throughout the brain. The sections were collected on poly –L-lysine coated slides for histological staining.

## 8.5 Diffusion MRI pre-processing steps

MRI data were exported in DICOM format for post processing and then converted to the NifTI format using MATLAB in-house code. Gradient values and vectors were also extracted from Paravision software 5.0 and imported to FSL software 5.0.10 to re-generate the DTI parameters map (FA, MD and axial and radial diffusivity). The reference image ($b_0$ image) that was acquired before each DTI acquisition scan was also extracted as a DICOM format and converted to the NifTI format using MATLAB in-house code. This T2 weighted image was registered to an FA image to select some ROIs, which are not as visible on an FA image, such as the hippocampus and thalamus. The corrected *b*-values that were acquired based on the water phantom experiment, (Chapter-7,section 7.6), were used instead of the *b*-values from the Paravision software.

## 8.6 ROI based method

DTI and T2 weighted high resolution images that were generated from 36 mice pre-irradiation and at all time points post-irradiation, were randomised before we started ROI selection. The mouse brain was divided into two main anatomical areas. The right (irradiated) and the left (non-irradiated) hemispheres. DTI parameters, with different imaging sequences and modalities, were measured for specific ROIs in each of these structures, including the cortex, hippocampus, fimbria, thalamus and corpus callosum (Figure 8.4). The ROI's were determined using MATLAB and drawn manually on both SE-DTI and STE-DTI. The Mean Diffusivity (MD) was then thresholded on Matlab to remove CSF voxels, such as the ventricles, preventing CSF contamination. This is especially problematic in regions prone to CSF contamination such as the fimbria (Metzler-Baddeley *et al.*, 2012). A threshold was applied to the MD values to identify CSF. Similarly, a lower threshold was applied to FA values, to identify voxels that cannot be within WM

tracts, such as the fimbria. In calculating whole and half brain volumes, based on T2 high resolution images, MATLAB was used and ROIs drawn manually on both right and left brain hemispheres.

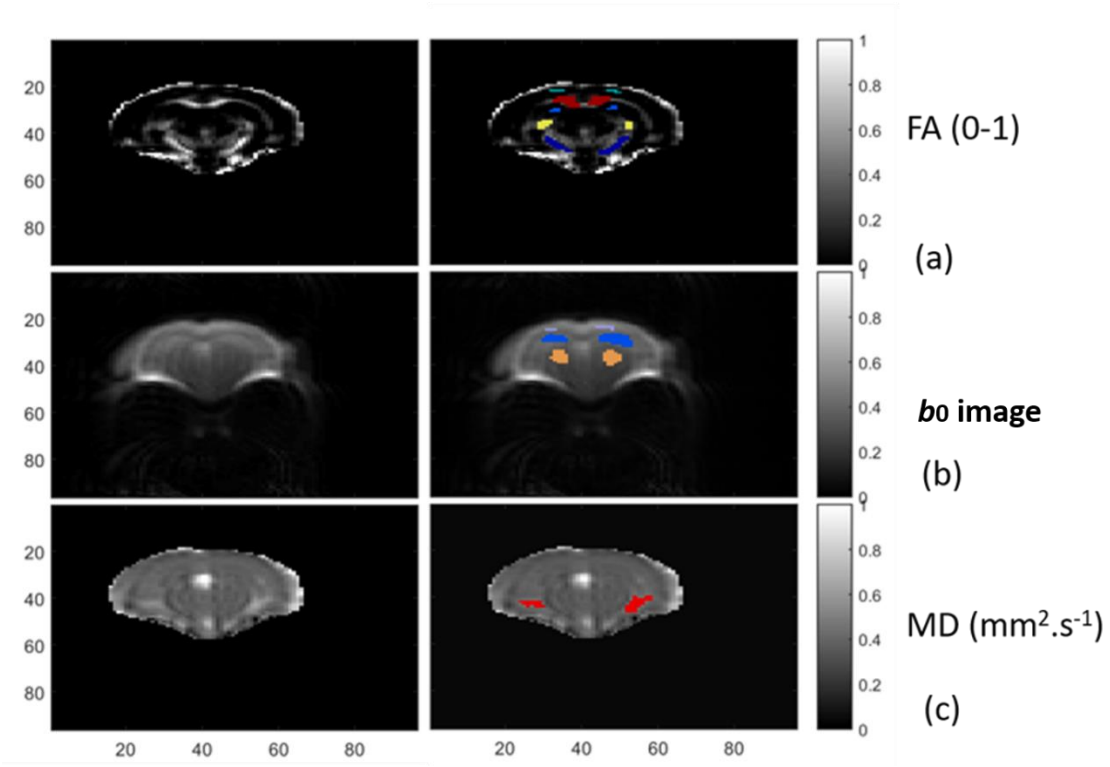


**Figure 8.4: (a) FA image and ROI selection. (b) $B_0$ image used to select thalamus and re-select some ROIs, such as the cortex and hippocampus in addition to the FA image, due to its resolution. (c) MD images show the ventricle's threshold to avoid its contamination of fimbria.**

## 8.7 Statistical analysis

For quantitative diffusion MRI analysis, measurements on both irradiated and non-irradiated mouse brain hemispheres of five ROIs were performed on every animal, including the control mice, at each time point pre- and post-irradiation. Data are expressed as median ± SD, except for the weight monitoring test, which is expressed as mean standard error of the mean (±SEM). All statistical analyses were carried out using GraphPad Prism software version 7.0. Statistical analysis: two-tailed, unpaired t-tests. N.S.= not significant. A *P*-value ≤0.05 was considered to be significant.

## 8.8 Results

### 8.8.1 Survival and behavioural monitoring of mice after exposure to 0 Gy and 20 Gy doses of radiation

Daily follow-up of mice did not reveal any paralysis or any locomotor deficit. However, while all irradiated mice (n = 31) exhibited loss of weight in the first week post-IR, they were back to normal weight from week two post-IR and started gaining weight thereafter. The control mice, however, continued gaining weight and had no weight reduction (Figure 8.5). In addition, from week 5 post-IR, all IR mice started losing hair from the ROI targeted with radiation in the right brain hemisphere.

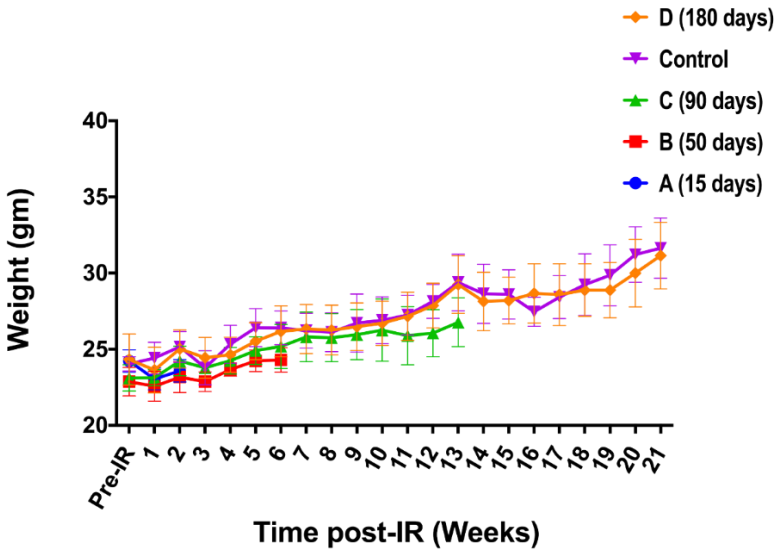


**Figure 8.5: Weight of mice pre-IR and at different week's post-IR. Data are presented as the mean ± standard deviation (SD). All statistical analyses were carried out using GraphPad Prism software version 7.0.**

## 8.8.2 MRI

### 8.8.2.1 T2 weighted high resolution image

No noticeable anatomical lesions such as oedema or necrosis were observed by T2 weighted high resolution image MRI scans at any time points post-irradiation (Figure 8.6). Furthermore, right (IR) and left (non-IR) brain volume assessment from anatomical MRI revealed no significant differences between them, meaning that there was no long lasting radiation-induced atrophy (Figure 8.7).

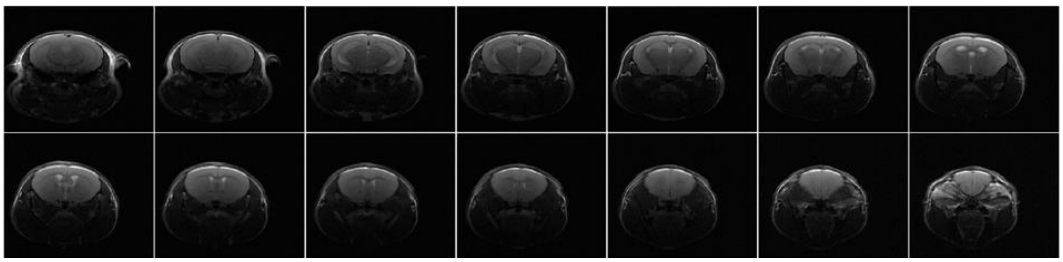

**Figure 8.6: Example of T2 weighted high resolution images acquired from different slices.**

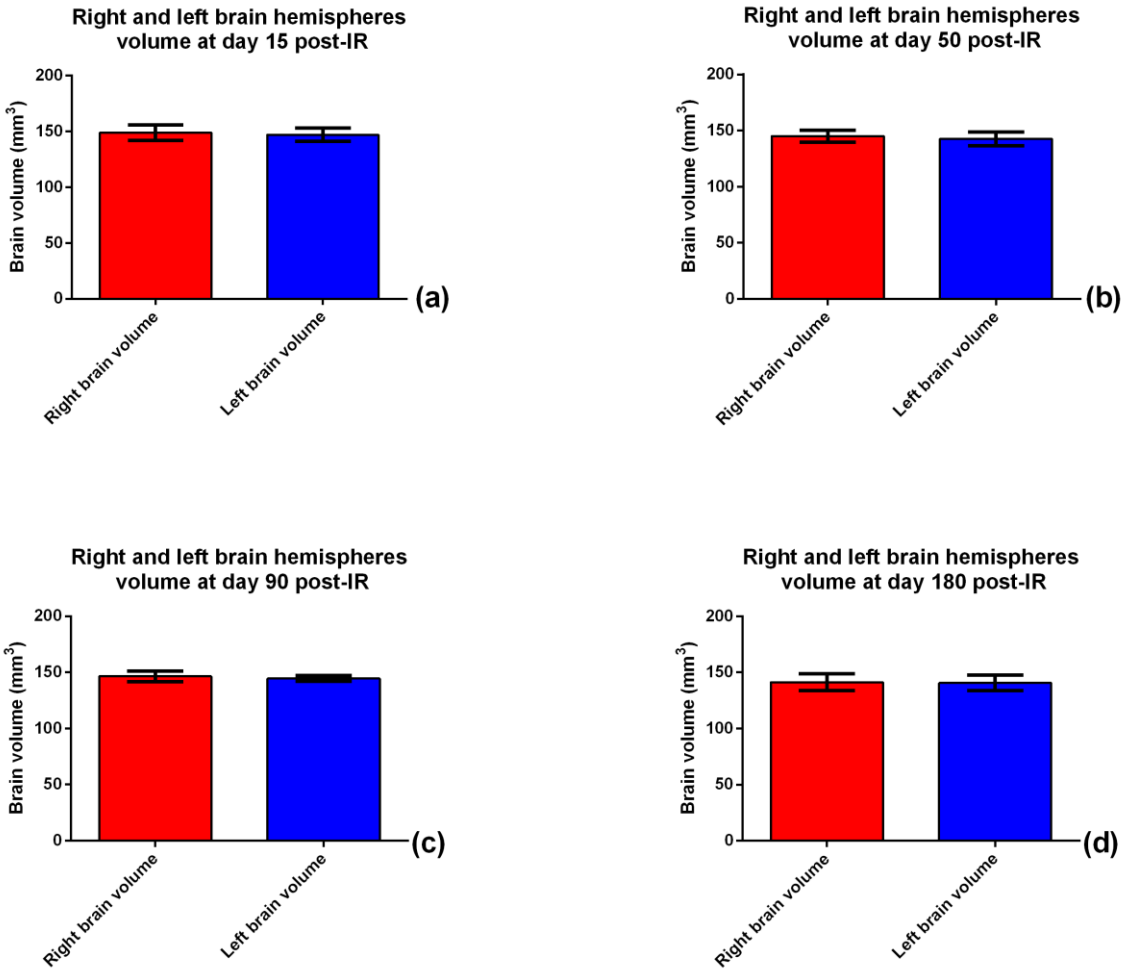


**Figure 8.7: Right (IR) and left (non-IR) brain volumes measured based on T2-weighted high resolution images at all time points post-Irradiation. (a) At day 15, (b) at day 50, (c) at day 90 and (d) at day 180. Data are presented as the mean ± standard deviation (SD). All statistical analyses were carried out using GraphPad Prism software version 7.0. Statistical analysis: two-tailed, unpaired t-tests. N. S.=not significant, significantly different (P<0.05).**

### 8.8.2.2 DTI

DTI measurements were taken from different ROIs pre-irradiation and all time points post irradiation (Figure 8.8). However, the comparison and statistical analysis were done only between controls (left-right) and irradiated (left-right) at each time point post-irradiation (15, 50, 90 and 180 days) for different ROIs. Data are presented as the median ± standard deviation (SD). All statistical analyses were carried out using Graph Pad Prism. Statistical analysis: two-tailed, unpaired t-tests. N.S=not significant, significantly different (P<0.05).

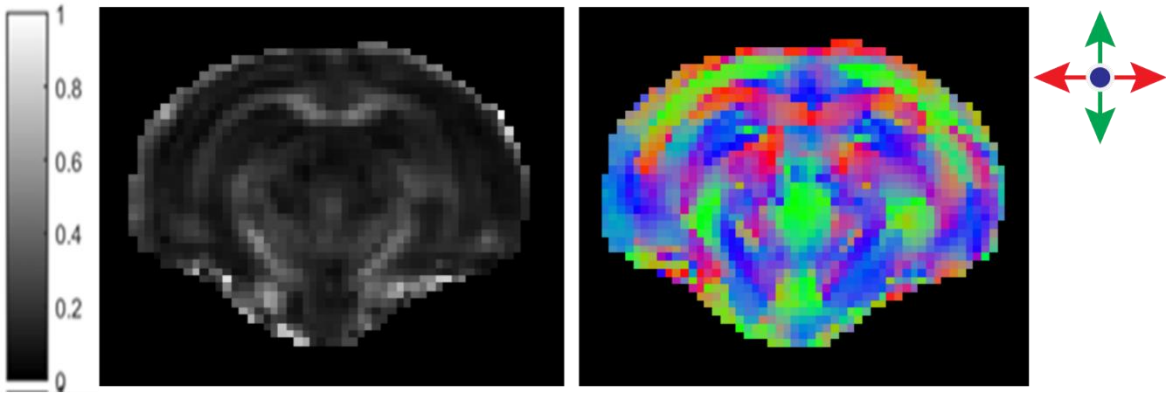


**Figure 8.8:Example DTI images showing examples of (a) FA image and (b) a representative DTI colour map image, that indicates the principle diffusion direction (red = x axis (left-right), green = y axis (anterior-posterior) and blue = z-axis (inferior-superior), which were generated by the FSL software.**

Furthermore, the Mean Diffusivity (MD) measurements that were acquired from the fimbria ROI from control mice showed that there was a reduction in MD with increased observation time, as was expected from the findings in the literature (Seland *et al.*, 2000). Therefore, the sequence has been validated in-vivo and hence allows further brain structures to be probed (Figure 8.9).

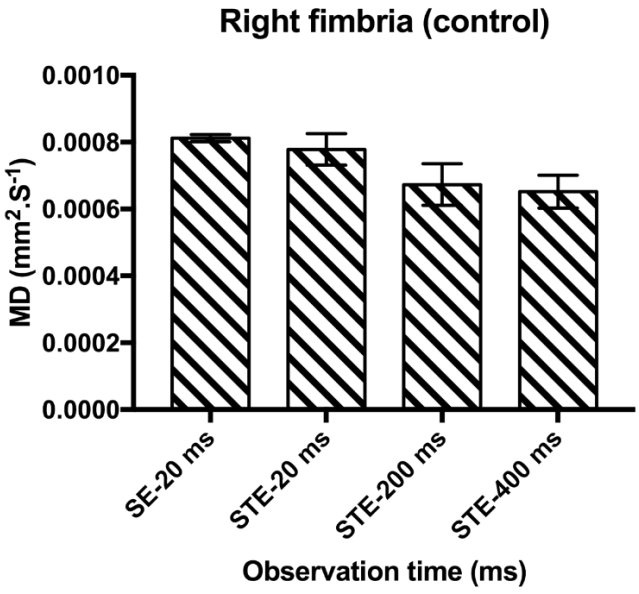


**Figure 8.9: Mean Diffusivity (MD) reduction with increased observation time for the controls' right fimbria.**

### 8.8.2.3 Fimbria changes following irradiation

Figure 8.10 and Figure 8.11 show DTI measures in the Fimbria as a function of time using a short observation time sequence (SE-20ms) and long observation time sequences (STE-200ms). FA, MD, AD and RD values of the fimbria are shown in Table 8.1 and Table 8.2. Our first observation is that in the control animals, the fimbria had very stable values of FA, MD, RD, and AD from days 15 to 90, which provide confidence that our scanner performance was constant with a short observation time. On day 180, with a short observation time (SE-20ms), the control fimbria metrics for FA values showed a significant increase. This explains why there was no significant difference at this time point for AD and RD, despite the fact that AD with a short observation time sequence (SE-20ms) was consistent with FA over time. AD, which is the principle direction of diffusion, generally corresponds to the FA during DTI measurements.

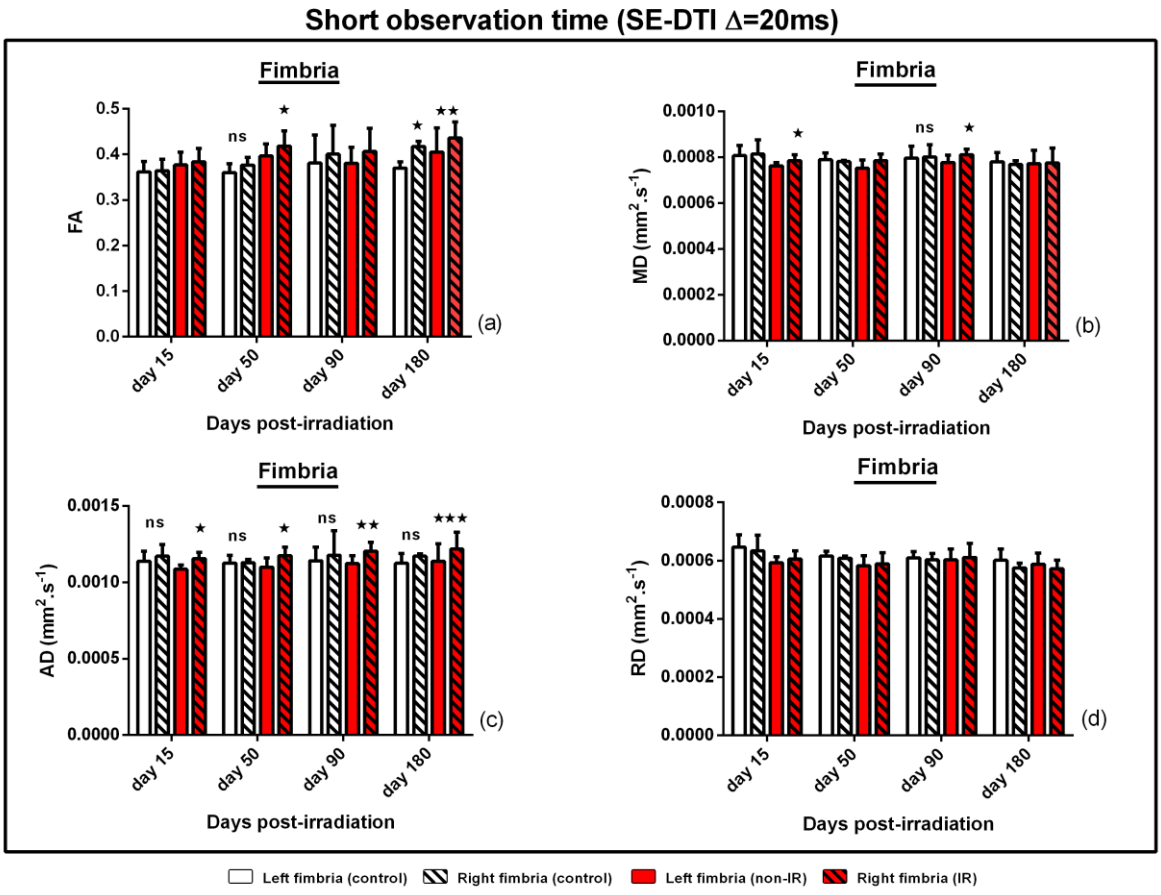


**Figure 8.10: Standard measures calculated from fimbria ROI using a short observation time (SE-20ms). Control corresponds to the contralateral hemisphere (solid pattern), and IR corresponds to the irradiated hemisphere (hatched pattern). All statistical analyses were**

**carried out using GraphPad Prism. Statistical analysis, two tailed, unpaired t-tests. N.S. = not significant. Significantly different (P≤0.05).**

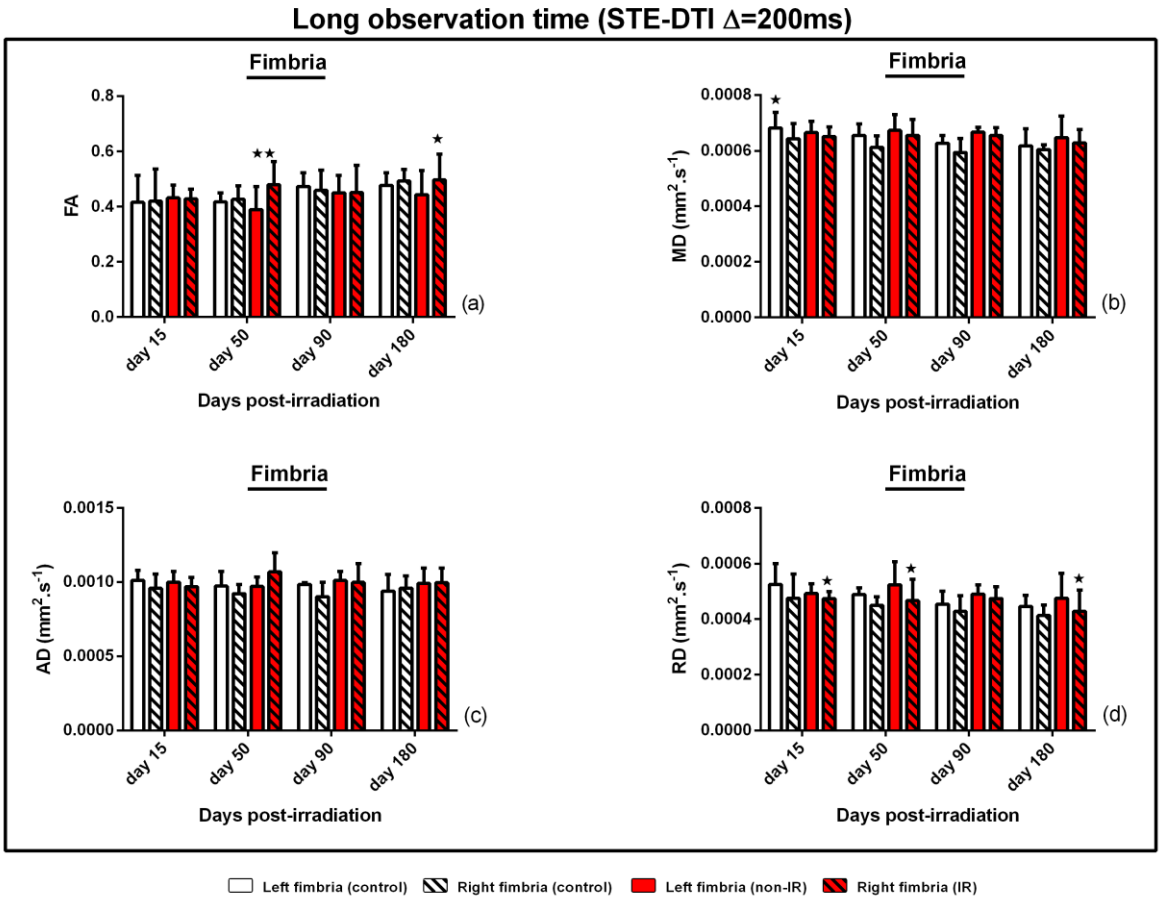


**Figure 8.11: Standard measures calculated from fimbria ROI using a long observation time (STE-200ms). Control corresponds to the contralateral hemisphere (solid pattern), and IR corresponds to the irradiated hemisphere (hatched pattern). All statistical analyses were carried out using GraphPad Prism. Statistical analysis, two tailed, unpaired t-tests. N.S. = not significant. Significantly different (P≤0.05).**

**FA**: Using both short and long observation time, there was a significant increase in FA measurements within irradiated fimbria (right) at days 50 and 180 post-IR compared with the control fimbria (left) for the same mice. However, the differences did not reach statistical significance at all time points. Comparing the fimbria contralateral (left) to irradiation (right) at day 50 post-irradiation, the FA values increased for fimbria (*P*=0.0493) for SE-20ms and (***P*=0.0060) for STE-200ms. MD also increased and reached significance with SE-20ms at days 15 and 90 with (*P*= 0.0372) and (*P*= 0.022), respectively. Whereas MD values that were acquired at a long observation time did not show any significant differences at all time points, the RD decreased only at longer observation times at days 15, 50 and 180 with (*P*=0.029), (*P*= 0.014) and (*P*= 0.019),respectively (Figure 8.11 d)). The MD significantly increased at a short observation (SE-20ms) at day 90 in the irradiated fimbria (*P*=0.0225). With a long observation time, MD was stable at all time points post-irradiation, however, the RD decreased significantly, which seems due to more structure being probed. That, in turn, shows consistency between FA and RD measurements with both short and long observation times.

**Table 8.1: FA, MD, AD and RD in irradiated and control sides of fimbria acquired at a short observation time (SE-20ms).**

| Time points (days) | SE-20ms | | | |
|---|---|---|---|---|
| | Irradiated mean (Right) (SD) | Control mean (Left) (SD) | Control mean (Right) (SD) | Control mean (Left) (SD) |
| **FA** | | | | |
| 15 | 0.384 (0.029) | 0.376 (0.028) | 0.364 (0.025) | 0.361 (0.361) |
| 50 | 0.418 (0.033) | 0.396 (0.026) | 0.376 (0.017) | 0.360 (0.019) |
| 90 | 0.406 (0.051) | 0.380 (0.035) | 0.400 (0.063) | 0.381 (0.061) |
| 180 | 0.436 (0.034) | 0.405 (0.053) | 0.417 (0.011) | 0.370 (0.013) |
| **MD ($mm^2.s^{-1}$)** | | | | |
| 15 | 0.0007 (0.00002) | 0.0007 (0.00001) | 0.0008 (0.0006) | 0.0008 (0.00004) |
| 50 | 0.0007 (0.00002) | 0.0007 (0.00003) | 0.0007 (0.000005) | 0.0007 (0.00002) |
| 90 | 0.0008 (0.00002) | 0.0007 (0.00003) | 0.0008 (0.00005) | 0.0007 (0.00005) |
| 180 | 0.0007 (0.00006) | 0.0007 (0.00005) | 0.0007(0.00001)) | 0.0007 (0.00005) |
| **AD ($mm^2.^{s-1}$)** | | | | |
| 15 | 0.0010 (0.00004) | 0.001 (0.00002) | 0.001 (0.00007) | 0.001 (0.00006) |
| 50 | 0.0010 (0.00005) | 0.001 (0.00006) | 0.001 (0.00002) | 0.001 (0.00004) |
| 90 | 0.0011 (0.00005) | 0.001 (0.00005) | 0.001 (0.00015) | 0.001 (0.00009) |
| 180 | 0.0011 (0.00011) | 0.001 (0.00011) | 0.001 (0.00001) | 0.001 (0.00006) |
| **RD ($mm^2.^{s-1}$)** | | | | |
| 15 | 0.00060 (0.00002) | 0.00059 (0.00002) | 0.00063 (0.00005) | 0.00064 |
| 50 | 0.00058 (0.00003) | 0.00058 (0.00003) | 0.00060 (0.00007) | 0.00061 |
| 90 | 0.00061 (0.00004) | 0.00060 (0.00003) | 0.00060 (0.00002) | 0.00060 |
| 180 | 0.00057 (0.00002) | 0.00058 (0.00003) | 0.00057 (0.00001) | 0.00060 |

**Table 8.2: FA, MD, AD and RD in irradiated and control sides of fimbria acquired with a long observation time (STE-200ms).**

| Time points (days) | STE-200ms | | | |
|---|---|---|---|---|
| | Irradiated mean (Right) (SD) | Control mean (Left) (SD) | Control mean (Right) (SD) | Control mean (Left) (SD) |
| **FA** | | | | |
| 15 | 0.427 (0.036) | 0.431 (0.046) | 0.419 (0117) | 0.415 (0.097) |
| 50 | 0.478 (0.083) | 0.388 (0.083) | 0.425 (0.049) | 0.416 (0.032) |
| 90 | 0.450 (0.098) | 0.450 (0.062) | 0.458 (0.072) | 0.472 (0.049) |
| 180 | 0.495 (0.094) | 0.442 (0.087) | 0.493 (0.042) | 0.476 (0.045) |
| **MD ($mm^2.s^{-1}$)** | | | | |
| 15 | 0.00065 (0.00003) | 0.00066 (0.00004) | 0.00064 (0.00005) | 0.00068 (0.00005) |
| 50 | 0.0006 (0.00005) | 0.00067 (0.00005) | 0.00061 (0.00004) | 0.00065 (0.00004) |
| 90 | 0.00065 (0.00002) | 0.00066 (0.00001) | 0.00059 (0.00004) | 0.00062 (0.00002) |
| 180 | 0.00062 (0.00004) | 0.00064 (0.00007) | 0.00060 (0.00001) | 0.00061 (0.00006) |
| **AD ($mm^2.s^{-1}$)** | | | | |
| 15 | 0.00096 (0.00006) | 0.00099 (0.00007) | 0.00095 (0.00009) | 0.00101 (0.00006) |
| 50 | 0.00106 (0.0001) | 0.00097 (0.00006) | 0.00092 (0.00006) | 0.00097 (0.00009) |
| 90 | 0.00099 (0.0001) | 0.00101 (0.00006) | 0.00090 (0.00009) | 0.00098 (0.00001) |
| 180 | 0.00099 (0.00009) | 0.00099 (0.0001) | 0.00095 (0.0009) | 0.00093 (0.0001) |
| RD ($mm^2.s^{-1}$) | | | | |
| 15 | 0.00047 (0.00002) | 0.00049 (0.00003) | 0.00047 (0.00008) | 0.0005 (0.00007) |
| 50 | 0.00046 (0.00007) | 0.00052 (0.00008) | 0.00044 (0.00003) | 0.00048 (0.00002) |
| 90 | 0.00047 (0.00004) | 0.00049 (0.00003) | 0.00042 (0.00005) | 0.00045 (0.00004) |
| 180 | 0.00042 (0.00007) | 0.00047 (0.00009) | 0.00041 (0.00003) | 0.00044 (0.00003) |

### 8.8.2.4 Corpus callosum changes following irradiation

The corpus callosum is characterised by a complex shape, due to fibres crossing neurons, that may lead to lower signals in DTI measurements. FA measurements show a significant increase between left (non-IR) and right (IR) brain hemispheres. At days 15 and 180 at a short observation time, there was a significant increase in FA values in the irradiated brain hemisphere with ($P$=0.005) and ($P$=0.003), as MD significantly increased at day 15 with ($P$=0.024). At day 15, there was also a significant increase in AD compared with the controls ($P$=0.004) (Figure 8.12). However, no DTI measurements at a long observation time (STE-200ms) reached significance at any time points post-irradiation (Figure 8.13).

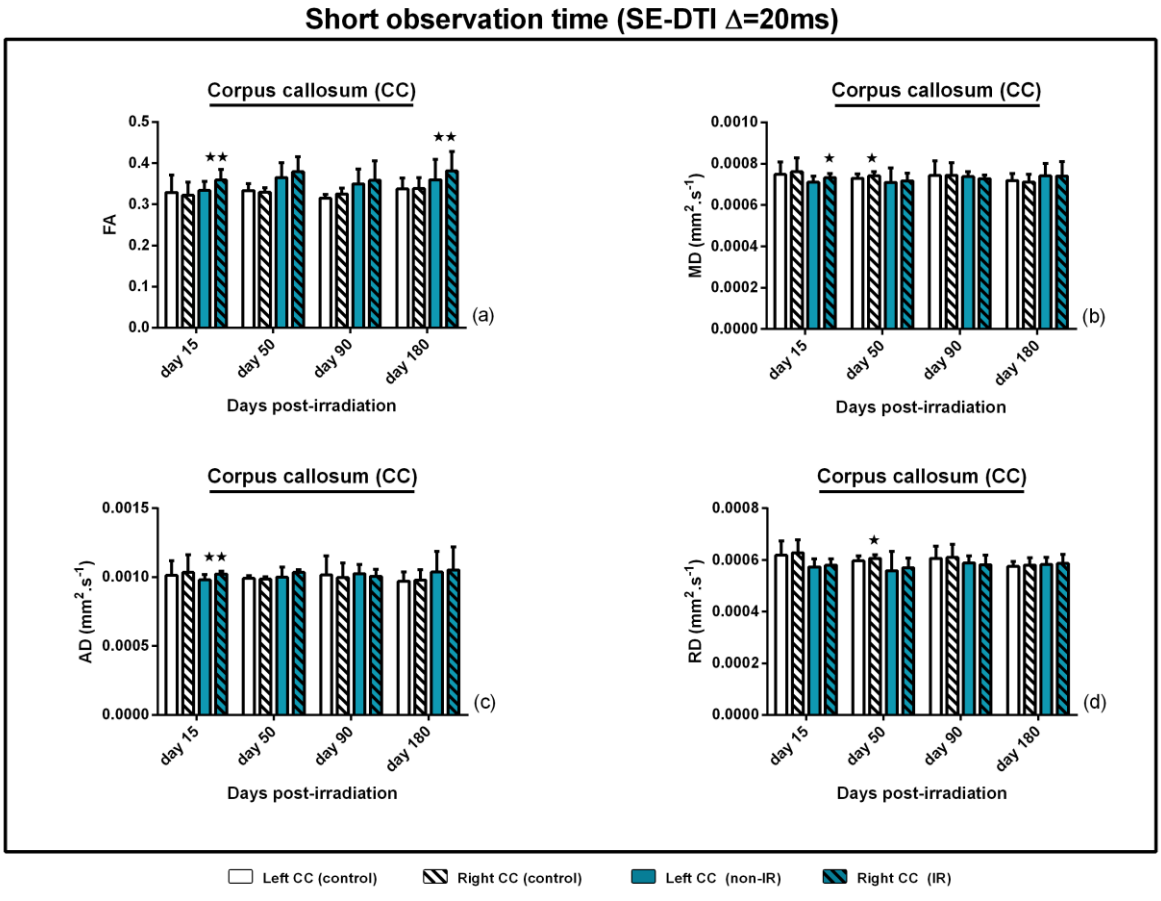


**Figure 8.12: Standard measures calculated from the corpus callosum ROI using a short observation time (SE-20ms). Controls correspond to the contralateral hemisphere (solid pattern), and IRs correspond to the irradiated hemisphere (hatched pattern). All statistical analyses were carried out using GraphPad Prism. Statistical analysis, two tailed, unpaired t-tests. N.S. = not significant. Significantly different (P≤0.05).**

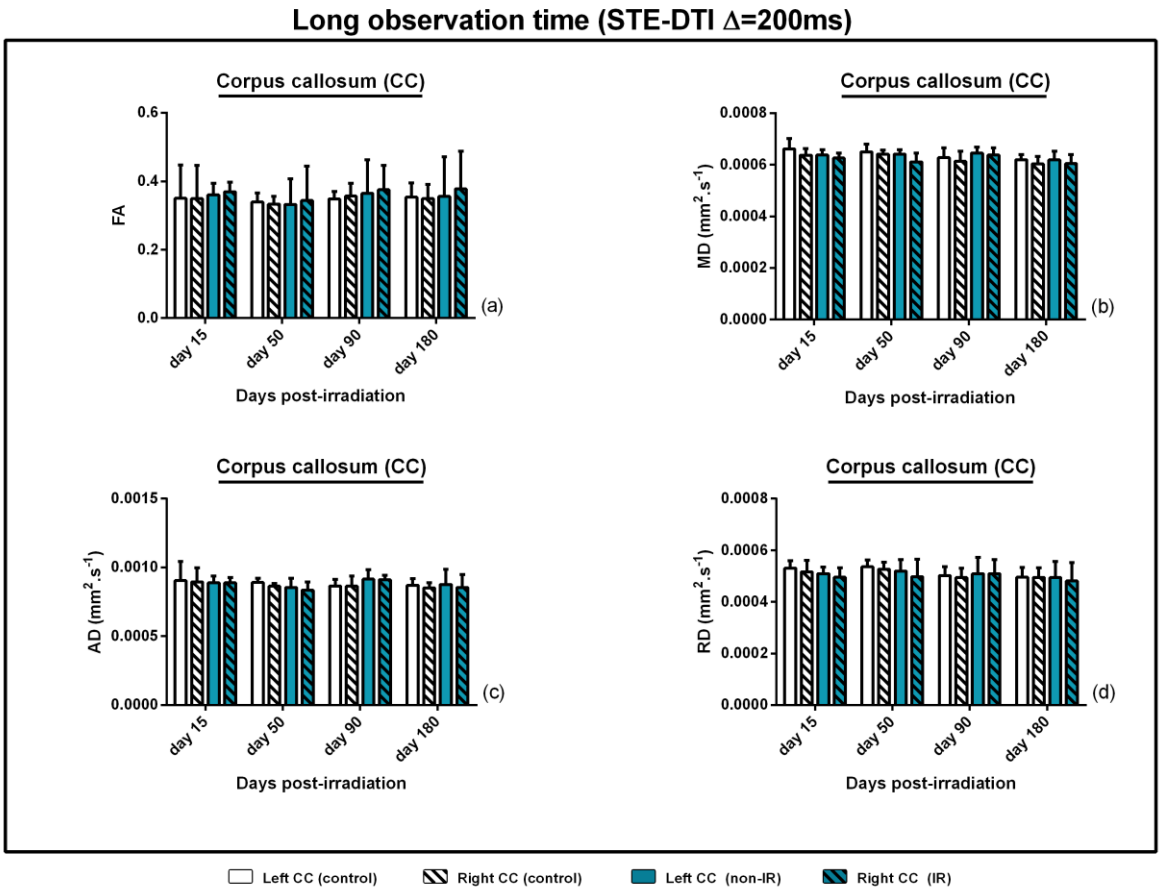


**Figure 8.13: Standard measures calculated from the corpus callosum ROI using a long observation time (STE-200ms). Controls correspond to the contralateral hemisphere (solid pattern), and IRs correspond to the irradiated hemisphere (hatched pattern). All statistical analyses were carried out using GraphPad Prism. Statistical analysis, two tailed, unpaired t-tests. N.S = not significant. Significantly different (P≤0.05).**

### 8.8.2.5 Hippocampus changes following irradiation

Measurements acquired from the hippocampus using a short observation time at day 15 show that, there was a decrease in FA measurement in the irradiated compared with the non-irradiated hemisphere, but significance was not reached. Furthermore, there was a statistically significant increase in MD and RD at day 15 post-irradiation, compared with the contralateral in the irradiated groups. AD showed a slight increase at day 15 post-irradiation but did not reach significance (Figure 8.14). Both short and long observation times show that there is a significant decrease in FA at day 50 post- irradiation in the ipsilateral hippocampus. At day 50 post-irradiation a long observation time also shows a decrease in FA value consistent with the short observation time for the same time points post-irradiation. No significant differences were observed with the long observation time sequence between right (IR) and left (non-IR), except at day 50 with FA, as mentioned previously (Figure 8.15).

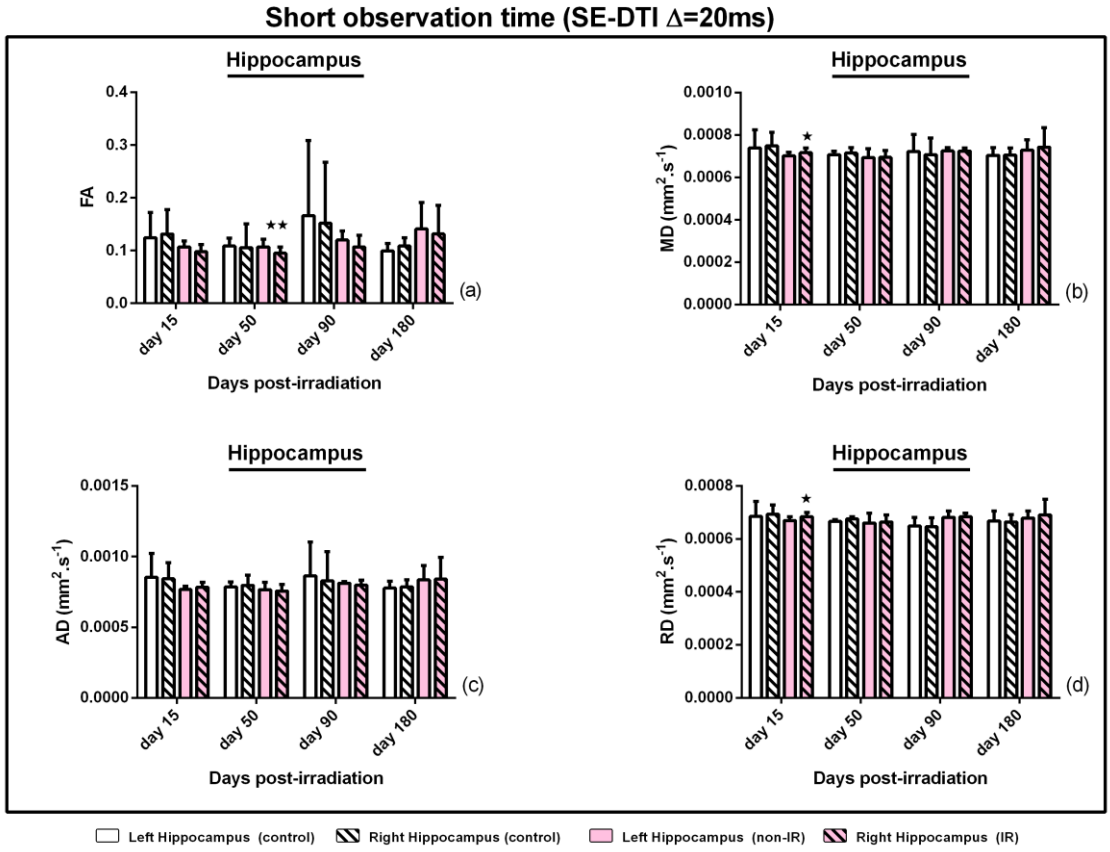


**Figure 8.14: Standard measures calculated from Hippocampus ROI using a short observation time (SE-20ms). Controls correspond to the contralateral hemisphere (solid pattern), and IRs correspond to the irradiated hemisphere (hatched pattern). All statistical analyses were carried out using GraphPad Prism. Statistical analysis, two tailed, unpaired t-tests. N.S. = not significant. Significantly different (P≤0.05).**

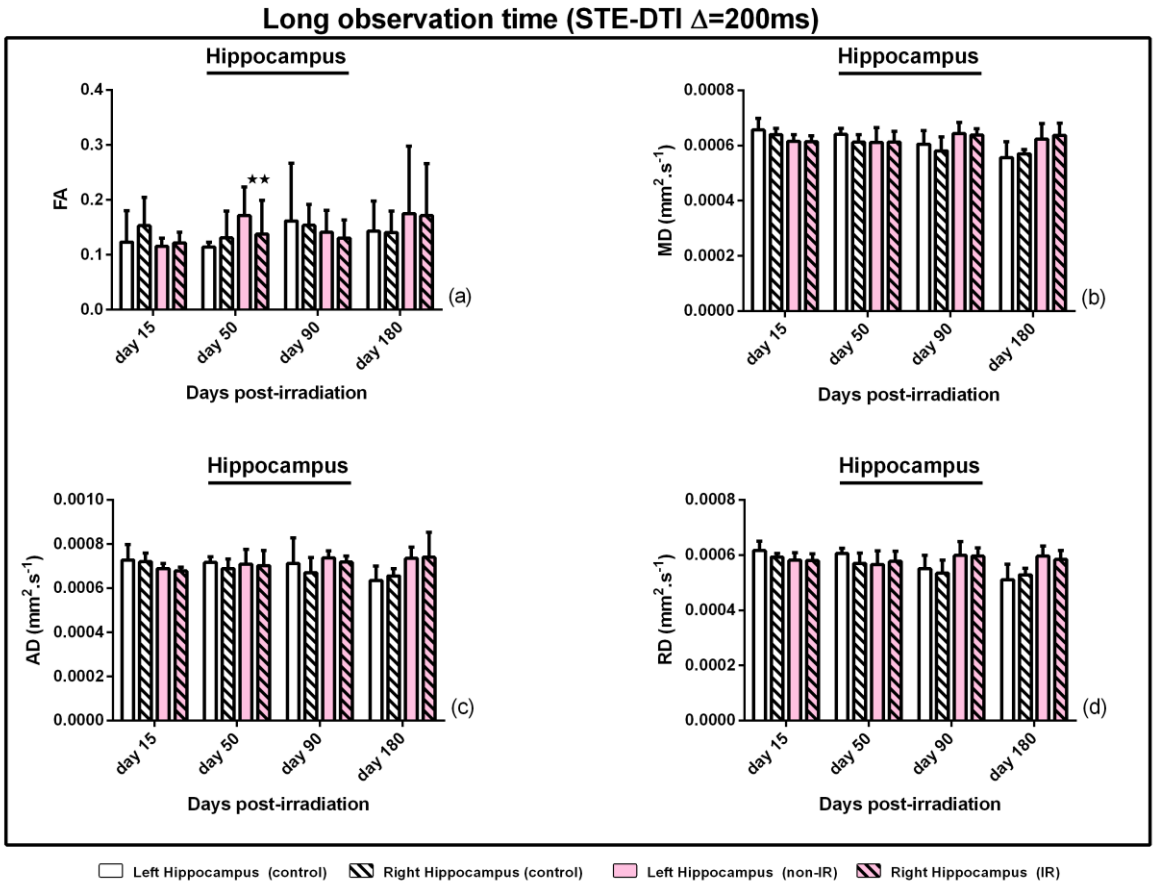


**Figure 8.15: Standard measures calculated from Hippocampus ROI using a long observation time (STE-200ms). Controls correspond to the contralateral hemisphere (solid pattern), and IRs correspond to the irradiated hemisphere (hatched pattern). All statistical analyses were carried out using GraphPad Prism. Statistical analysis, two tailed, unpaired t-tests. N.S. = not significant. Significantly different (P≤0.05).**

### 8.8.2.6 Cortex changes following irradiation

DTI measurements that were acquired from the cortex using a short observation time (SE-20ms) show that there was a significant increase in FA at day 15 post-irradiation between left (non-IR) and right (IR). Similarly, a long observation time shows an increase in FA measurement for this time point, but it did not reach significance. Significant increases in FA measurements were also observed at days 50 and 180 post- irradiation between ipsilateral and contralateral for the same groups of mice.

However, significant differences were also observed at days 50 and 90 post-irradiation with AD and RD respectively between left and right brain hemispheres for the control group with a short observation time (SE-20ms) (Figure 8.16). No significant differences were observed between ipsilateral and contralateral in FA, MD, AD and RD using a long observation time (STE-200ms) (Figure 8.17). In the cortex, it seems that long observation time measurements were more consistent than short observation times, which we believe is due to the consistency in the increase and decrease between FA and AD measurements with a long observation time.

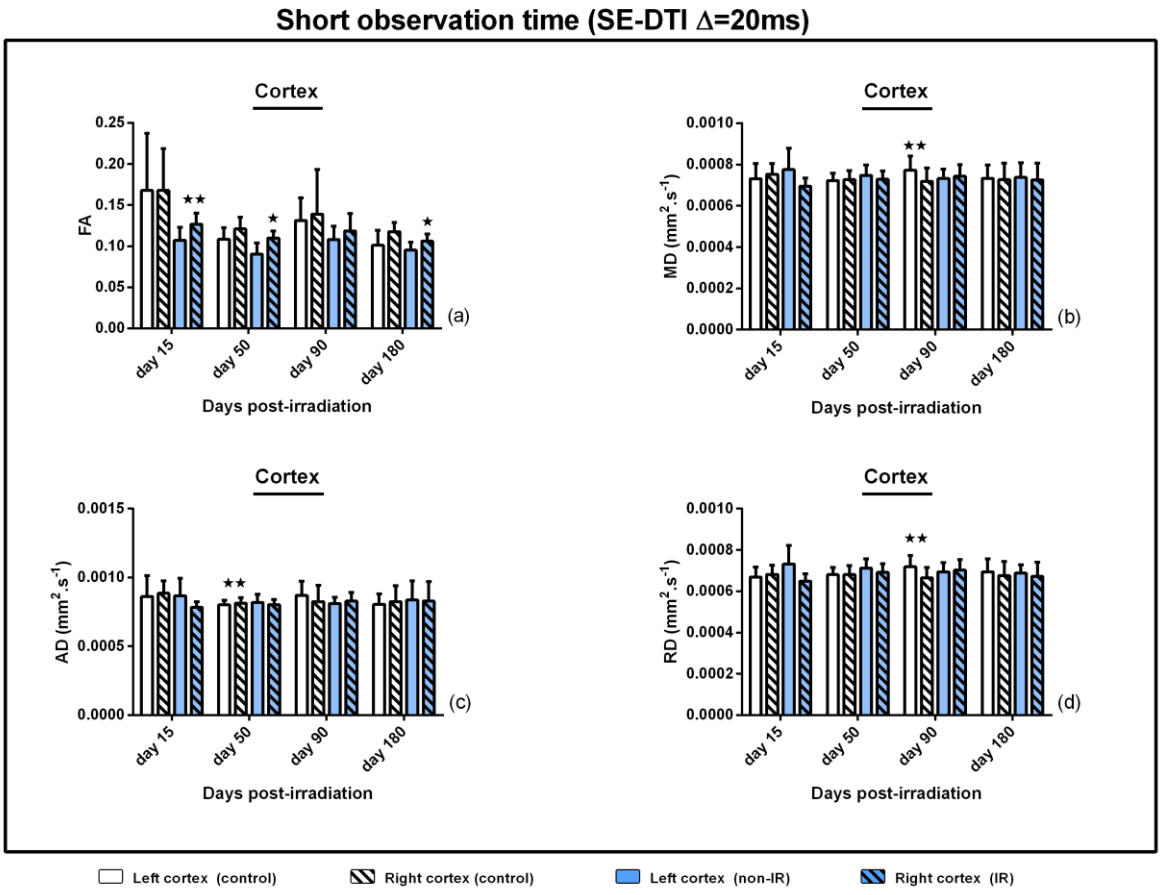


**Figure 8.16: Standard measures calculated from cortex ROI using a short observation time (SE-20ms). Controls correspond to the contralateral hemisphere (solid pattern), and IRs correspond to the irradiated hemisphere (hatched pattern). All statistical analyses were carried out using GraphPad Prism. Statistical analysis, two tailed, unpaired t-tests. N.S. = not significant. Significantly different (P≤0.05).**

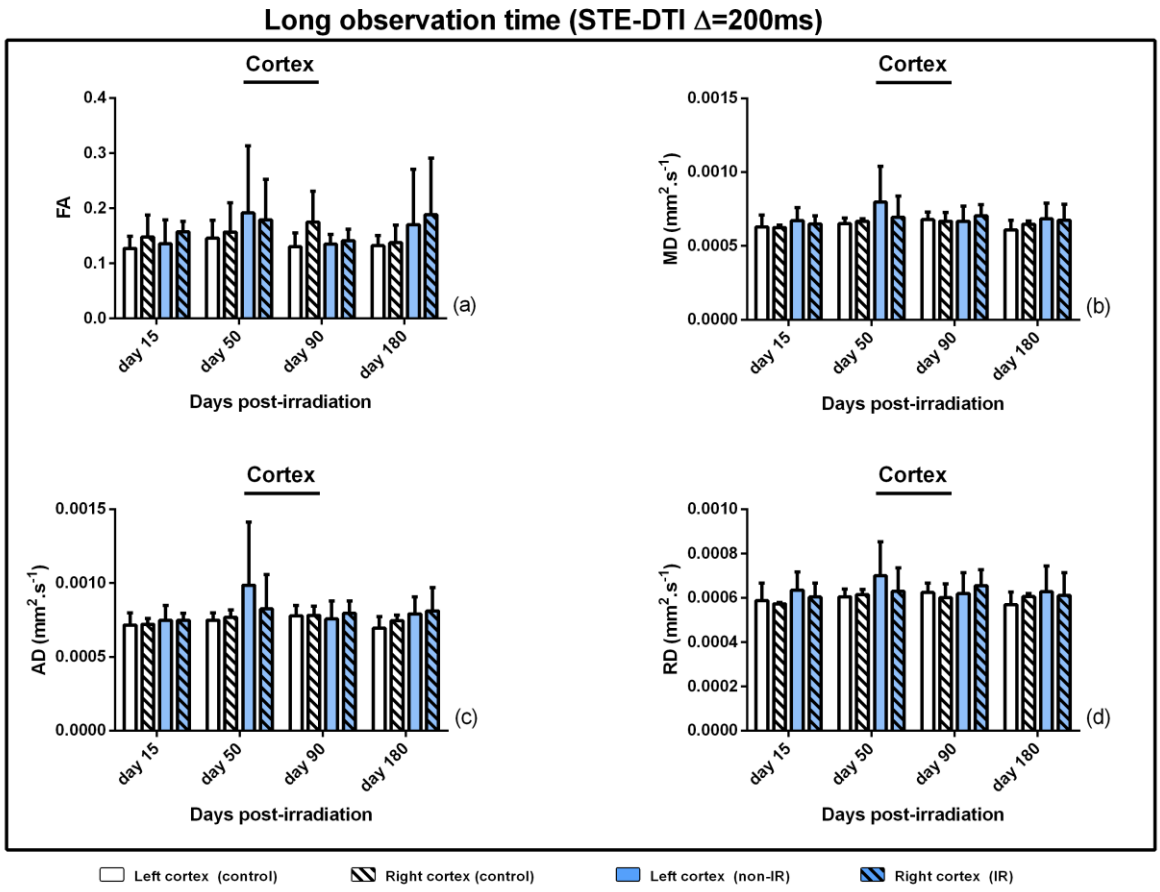


**Figure 8.17: Standard measures calculated from cortex ROI using a long observation time (STE-200ms). Controls correspond to the contralateral hemisphere (solid pattern), and IRs correspond to the irradiated hemisphere (hatched pattern). All statistical analyses were carried out using GraphPad Prism. Statistical analysis, two tailed, unpaired t-tests. N.S. = not significant. Significantly different (P≤0.05).**

### 8.8.2.7 Thalamus changes following irradiation

DTI measurements from the thalamus using the $B_0$ image, registered to the FA image, acquired with a short observation time (SE-20ms), show a slight increase in FA value at day 15 post-irradiation, but did not reach significance. However, AD shows a significant difference for this time point between ipsilateral and contralateral hemispheres with ($P$=0.024). No significant differences between ipsilateral and contralateral hemispheres was observed for this time point with MD and RD. At day 90, RD shows a significant increase with ($P$=0.017), while FA shows a reduction, but it did not reach significance (Figure 8.18). Data acquired with a long observation time sequence (STE-200ms) show stable measurement over time with a reduction in both FA and AD within the irradiated hemispheres at day 50, but they did not reach significance (Figure 8.19).

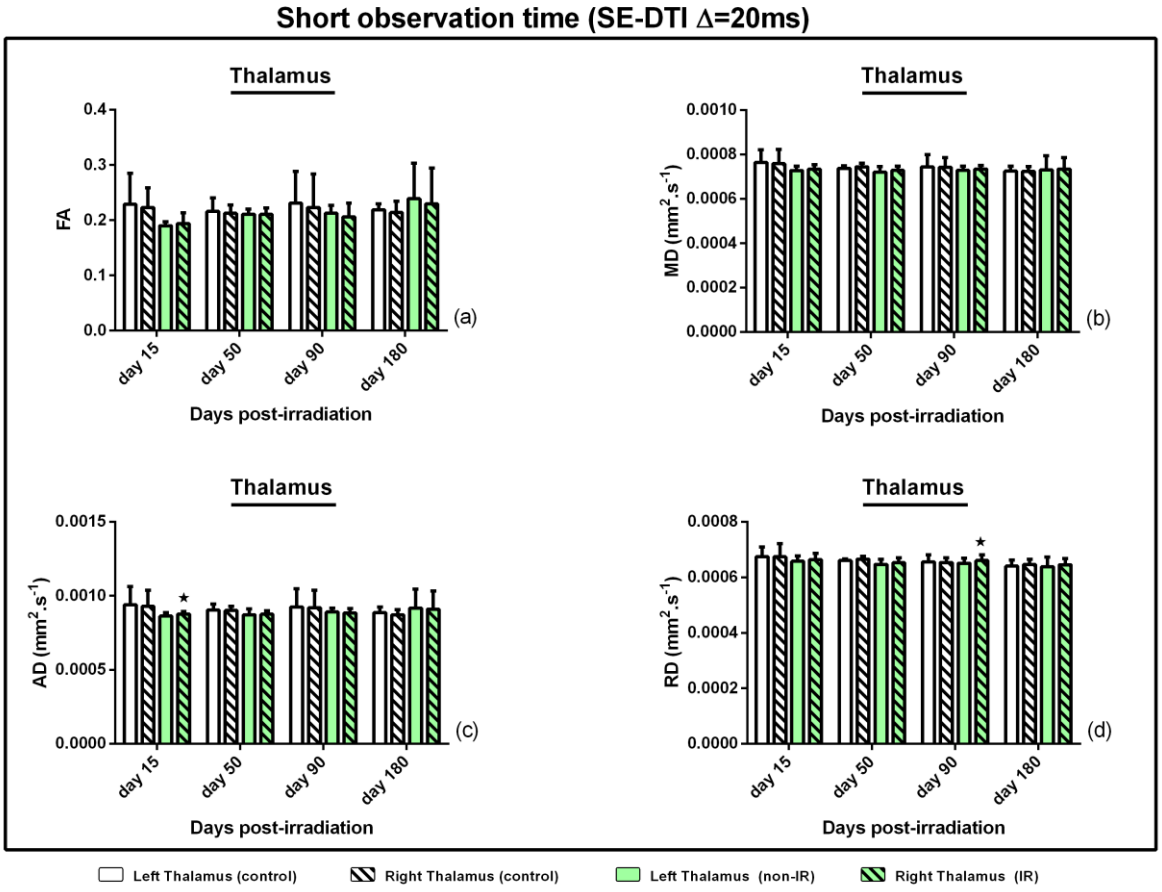


**Figure 8.18: Standard measures calculated from thalamus ROI using a short observation time (SE-20ms). Controls correspond to the contralateral hemisphere (solid pattern), and IRs correspond to the irradiated hemisphere (hatched pattern). All statistical analyses were carried out using GraphPad Prism. Statistical analysis, two tailed, unpaired t-tests. N.S. = not significant. Significantly different (P≤0.05).**

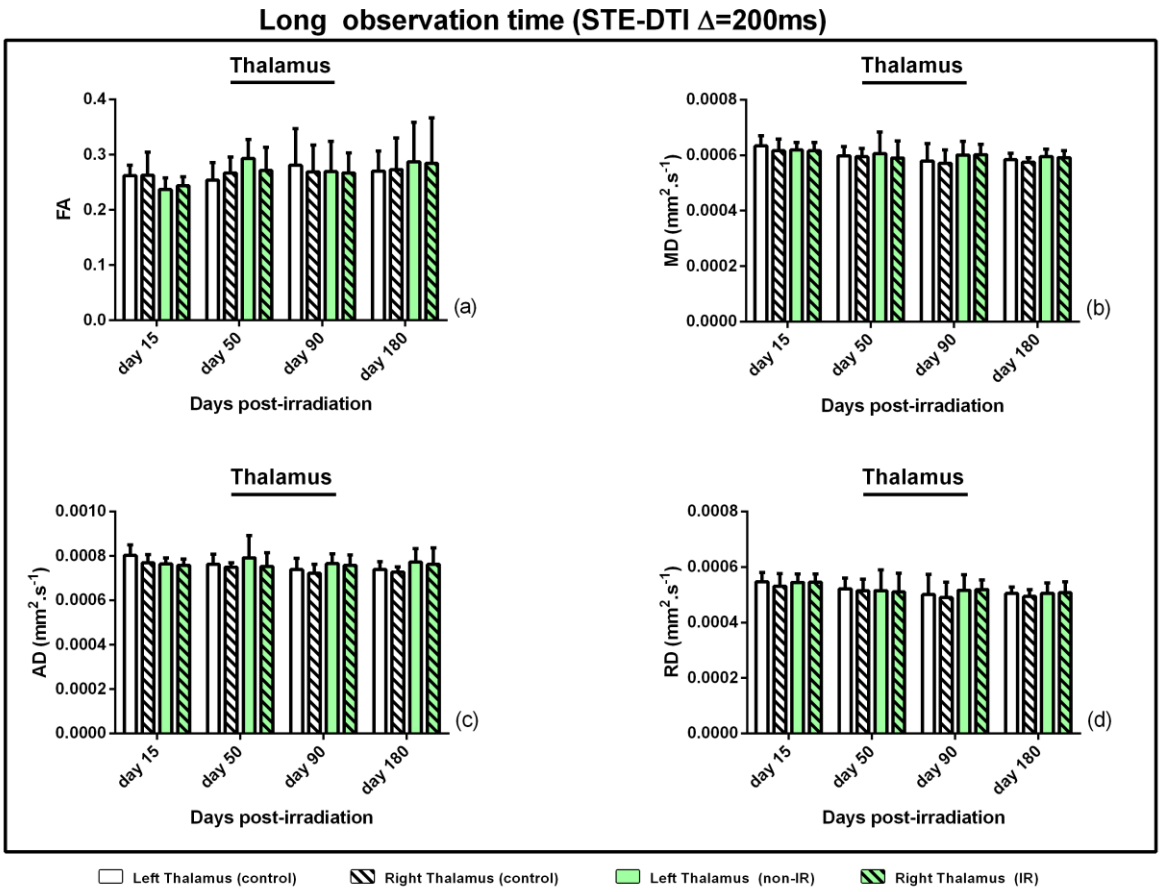


**Figure 8.19: Standard measures calculated from thalamus ROI using a long observation time (STE-200ms). Controls correspond to the contralateral hemisphere (solid pattern), and IRs correspond to the irradiated hemisphere (hatched pattern). All statistical analyses were carried out using GraphPad Prism. Statistical analysis, two tailed, unpaired t-tests. N.S. = not significant. Significantly different (P≤0.05).**

### 8.8.3 Histology

Histopathological analysis has not yet been completed. It is currently being undertaken by a post-doctoral researcher (Dr David Walker) for all time points post-irradiation. Irradiated mouse brains will be analysed at multiple time points post-irradiation (15, 50, 90 and 180 days). The comparison will be between right (IR) and left (non-IR) brain hemisphere ROIs for all time points post-irradiation, except the last time point (180 day). The comparison will also be made between irradiated (n=10) and control groups (n=5). Various histology stains will be used to determine radiation-induced changes for all selected ROI's: H&E to stain cell nuclei and the extracellular matrix will be used to examine general morphology; Cresyl violet to stain the Nissl body of neurons; LFB to stain the myelin sheath. WM injury will be examined using LFB to identify any changes consistent with changes in RD, which is believed to predict myelin pathology such as demyelination; as GFAP antibodies are the most popular marker for astrocytes, these will be used to count astrocyte cell numbers, as well as to assess their sizes and locations.

## 8.9 Discussion

Diffusion MRI is a particularly effective technique to quantify the diffusive motion of water molecules in living biological tissues (Le Bihan, 2007). The direction and extent of water diffusion in brain structures is dependent on the tissues' microstructure and organisation. Consequently, DTI is widely used to map brain architecture, for example, when characterising the effect of aging and disease on the WM (Budde and Frank, 2012),(Shimmyo *et al.*, 2008). DTI metrics, such as FA and MD, are promising non-invasive tools for characterising microstructural changes in brain tissue, hence, DTI has been used in a wide range of CNS applications, such as detecting early cognitive changes due to irradiation (Kumar *et al.*, 2013). An often overlooked parameter in Diffusion MRI experiments is the observation time, $\Delta$, which normally takes the shortest value. However, longer observation times allow the water molecules to diffuse further and to experience longer range structures and experience more exchange across a permeable barrier, such as myelin. Consequently, diffusion time is potentially a key parameter that determines the sensitivity of diffusion MRI to microstructures of at different spatial dimensions. Hence, we hypothesised that long observation

time diffusion MRI could be used as a non-invasive imaging biomarker of radiation induced brain damage.

Our animal model received a low radiation dose and was monitored at early and late time points post-irradiation as we looked for any microstructural changes. To confirm this hypothesis, serial DTI experiments were performed on healthy mice by delivering low dose hemisphere irradiation. The aim of this study was to extract quantitative longitudinal information from DTI metrics of different brain anatomical regions and to compare it with histopathological analysis at each time point post-irradiation.

**Fimbria:** In this study, we found the FAs of the ipsilateral fimbria increased compared with the contralateral side at all time points, and significantly at days 50 and 180 post- irradiation, with both short and long observation times, see (Figure 8.10 (a)) and (Figure 8.11 (a)). This suggests a high sensitivity to degeneration in these fimbrial structures due to irradiation damage. This is consistent with our previous MRI result inChapter-5, which showed that the fimbria of the hippocampus was more sensitive to radiation. This was confirmed by our initial histological analysis at day 80 post-irradiation, which increases in FA. It seems that FA increases due to the increase in AD because both of them show a significant increase in the irradiated fimbria at days 50 and 180 post-irradiation.

The scenario for the fimbria was similar with a long observation time. There was a significant increase in FA at days 50 and 180 with ($P$=0.027) and ($P$=0.005), respectively. However, the FA increase seems to be due to the significant reduction in RD measurements that showed a significant reduction in the irradiated hemisphere of the fimbria compared with the control hemisphere, see (Figure 8.11 (d)). The reduction in MD measurements, see (Figure 8.11 (b)) is also consistent with previous hypothesis reports of hindered diffusion (Chris A. Clark,Hedehus Maj and Moseley E. Michael., 2001),that allowing more time for diffusion increases the opportunity to probe more structures.

**Corpus callosum:** The significant increase in FA for the corpus callosum that was observed with a short observation time (SE-20ms) is consistent with the significant increase that was shown by MD and AD with ($P$ =0.02) ($P$ =0.004) at day 15 post-irradiation, see (Figure 8.12 (a, c)). A possible reason for this increase in MD, is

the free water in the extracellular space which may be due to vasogenic oedema. These MD increases are consistent with the result of Wang et al. (2009) (Wang *et al.*, 2009), who irradiated half a rat brain hemisphere with a 30 Gy single dose and observed an increase in MD and AD in the external capsule at 48 weeks post-irradiation. However,it did not reach significance. Our finding is consistent with this result, but at an earlier time point. No significant difference was observed between irradiated and non-irradiated corpus callosum at any time points with a longer observation time (STE-200ms). Thus, we concluded there was no additional information to be found by probing more tissue structures with the long observation sequences.

**Hippocampus**: In the irradiated hippocampus, at day 15 there was a significant increase in MD and RD with ($P$=0.043) and ($P$=0.047) respectively, see (Figure 8.14 (b, d)). Constanzo et al. (2018), recently performed a longitudinal DTI study of late WM injury resulting from specific brain irradiation in a rat model study. They showed a significant increase in MD, RD and AD between days 90 and 180 post-irradiation on the hippocampus (Constanzo *et al.*, 2018). Our result is partially consistent with their findings, however, we observed this effect on the hippocampus at an earlier time point post-irradiation (15 days) and only in MD and RD, but not at a later time point. In the study by Constanzo et al. (2018), FA was constant until the last time points post-irradiation (110 days). However, our result shows that there was a significant reduction in FA value at day 50 post irradiation, which was observed with both short and long observation times, see (Figure 8.14 and Figure 8.15 (a)). The reduction in FA at day 15 is consistent with the significant RD increase (see (Figure 8.14 (d)). This effect in the hippocampus was also observed by Perez-Torres *et al.*, (2015) 12 weeks post-irradiation, when necrosis and oedema were also observed following a 50 Gy mouse brain irradiation. However, with a longer observation time at day 15, there was an increase in FA, which did not reach significance and there was no corresponding increase in RD for this time point (Figure 8.15 (d)).

The most likely explanation for our results was the effect of necrosis or haemorrhage and oedema, this will be assessed with future analysis of the histology. FA reduction may corresponds to axonal damage due to necrosis. Our result also shows a reduction in AD but it did not reach significance. However, oedema is related to MD and RD increases that were already observed in this study

and reached significance at an early time point post-irradiation. In other studies, tissues surrounding a necrotic area are usually characterised by the presence of inflammation in tandem with increased MD due to reduction in anisotropy, (Constanzo *et al.*, 2018), which was already observed in our study.

**Cortex**: Lower FA values were expected to be seen in the cortex due to the lower anisotropy of grey matter, see (Figure 8.16 and Figure 8.17 (a)). FA values show a significant increase between left (non-IR) and right (IR) cortex at days 15 and 180, which is consistent with RD reductions, but they do not reach significance. This result was consistent with the study of Constanzo *et al,* who observed an increased in FA value at day 10 post-IR which did not reach significance. However, their irradiation dose was 41 Gy targeting the primary motor cortex of the right brain hemisphere (Constanzo *et al.*, 2018).

The control group showed large variability at these time points (days 50 and 90). The control group also showed significant differences at days 50 and 90 with MD and AD and RD at day 90 post- irradiation. FA values also showed significant differences between the left and right hemispheres at day 50 with AD, and at day 90 for MD and RD. FA values also showed a significant increase between the ipsilateral and contralateral hemispheres for the last time point post-irradiation (day180), however, the other DTI metrics were stable. This result was observed only with a short observation time, while longer observation time sequence did not show any difference at any time points post-irradiation. This result was not consistent with the study of Constanzo *et. al,* in which observed a reduction in FA into the primary motor cortex was observed for the most of the time points of their study (54, 90 and 110 days post-IR, with the exception of day 10).

**Thalamus**: DTI measurements from the thalamus that were acquired with a short observation time (SE-20 ms) show a significant increase in AD in the irradiated thalamus (right), see (Figure 8.18 (c)). This increase is consistent with the FA increase for the same time point post-irradiation (day 15), but it does not reach significance. MD and RD show stable values, except at day 90 where RD shows a significant difference between the irradiated (right) and non-irradiated (left) thalamus with stable MD, see (Figure 8.18 (d)). FA values show a slight reduction at the last two time points, but they were not significant. Long observation time

(STE-200ms) show consistent reduction in both FA and AD at day 15 post-irradiation, but did not reach significant, see (Figure 8.19 (a, c)).

## 8.10 Conclusion

In this study, we compared the radiation-induced microstructural changes in the irradiated mouse brain using a T2 weighted high resolution image and DTI measures, with histopathology (still ongoing) for each time point post-irradiation. T2 weighted high resolution images indicated no significant changes between brain hemispheres at all time points post-irradiation. However, from day 15 post-irradiation, the fimbria of the hippocampus start showing changes in AD and FA that are consistent with our previous result, showing more diffusion in the principal direction, namely, the axial direction (AD). Changes were also observed in the fimbria at all time points post-irradiation with both sequences. Our study confirmed the high sensitivity of fimbria to radiation. A decrease in FA values was observed in the hippocampus at day 50 post irradiation with both DTI sequences, meaning there may be axonal damage due to necrosis or haemorrhage. A significant increase was also observed with MD and RD, suggesting that there may be demyelination. Overall, DTI shows potential to non-invasively obtain a better picture of post-irradiation microstructural changes. However, we found no evidence that long observation time DTI, performed better than short observation time DTI in identifying microstructural changes. This may provide useful information to guide the development of irradiation protocols in clinic for brain tumour patients. Consequently, DTI can be used as a biomarker for the non-invasive evaluation of radiation induced-brain injury. Current clinical radiation therapy strategies to minimise radiation damages include the reduction of the radiation dose and fractionated doses.

## 8.11 References

Agboola, O. *et al.* (1998) 'Prognostic factors derived from recursive partition analysis (RPA) of Radiation Therapy Oncology Group (RTOG) brain metastases trials applied to surgically resected and irradiated brain metastatic cases', *International Journal of Radiation Oncology Biology Physics*, 42(1), pp. 155–159. doi: 10.1016/S0360-3016(98)00198-9.

Le Bihan, D. (2007) 'The "wet mind": Water and functional neuroimaging', *Physics in Medicine and Biology*, 52(7). doi: 10.1088/0031-9155/52/7/R02.

Brown, P. D. *et al.* (2016) 'Effect of radiosurgery alone vs radiosurgery with whole brain radiation therapy on cognitive function in patients with 1 to 3 brain metastases a randomized clinical trial', *JAMA - Journal of the American Medical Association*, 316(4), pp. 401–409. doi: 10.1001/jama.2016.9839.

Budde, M. D. and Frank, J. A. (2012) 'Examining brain microstructure using structure tensor analysis of histological sections', *NeuroImage*, pp. 1–10. doi: 10.1016/j.neuroimage.2012.06.042.

Clark A.Chris,Hedehus Maj and Moseley E. Michael. (2001) 'Diffusion time dependence of the apparent diffusion tensor in healthy human brain and white matter disease.', *Magnetic resonance in medicine*, 45(6 PG-1126–9), pp. 1126–1129. Available at: NS -.

Constanzo, J. *et al.* (2017) 'Understanding the continuum of radionecrosis and vascular disorders in the brain following gamma knife irradiation: An MRI study', *Magnetic Resonance in Medicine*, 78(4), pp. 1420–1431. doi: 10.1002/mrm.26546.

Constanzo, J. *et al.* (2018) 'Diffusion MRI monitoring of specific structures in the irradiated rat brain', *Magnetic Resonance in Medicine*, 80(4), pp. 1614–1625. doi: 10.1002/mrm.27112.

D., B. *et al.* (2013) 'Bevacizumab as a treatment for radiation necrosis of brain metastases post stereotactic radiosurgery', *Neuro-Oncology*, 15(9), pp. 1257–1263. Available at:

http://www.embase.com/search/results?subaction=viewrecord&from=export&id=L369685047%5Cnhttp://dx.doi.org/10.1093/neuonc/not085%5Cnhttp://sfx.ub.rug.nl:9003/sfx_local?sid=EMBASE&issn=15228517&id=doi:10.1093%2Fneuonc%2Fnot085&atitle=Bevacizumab+as+a+treatme.

Dyrby, T. B. *et al.* (2014) 'Contrast and Stability of the Axon Diameter Index from Microstructure Imaging with Diffusion MRI', 721(2013), pp. 711–721. doi: 10.1002/mrm.24501.

Gutierrez, S., Descamps, B. and Vanhove, C. (2015) 'MRI-Only Based Radiotherapy Treatment Planning for the Rat Brain on a Small Animal Radiation Research Platform (SARRP)', *Plos One*, 10(12), p. e0143821.

Kumar, M. *et al.* (2013) 'Early cognitive changes due to whole body γ-irradiation: A behavioral and diffusion tensor imaging study in mice', *Experimental Neurology*. Elsevier Inc., 248, pp. 360–368. doi: 10.1016/j.expneurol.2013.06.005.

Liu, Y. *et al.* (2010) 'An experimental study of acute radiation-induced cognitive dysfunction in a young rat model', *American Journal of Neuroradiology*, 31(2), pp. 383–387. doi: 10.3174/ajnr.A1801.

Matinfar, M. *et al.* (2009) 'Image-guided small animal radiation research platform: Calibration of treatment beam alignment', *Physics in Medicine and Biology*, 54(4), pp. 891–905. doi: 10.1088/0031-9155/54/4/005.

McDonald, L. W. and Hayes, T. L. (1967) 'The role of capillaries in the pathogenesis of delayed radionecrosis of brain.', *American Journal of Pathology*, 50(5), pp. 745–764.

Metzler-Baddeley, C. *et al.* (2012) 'How and how not to correct for CSF-contamination in diffusion MRI', *NeuroImage*. Elsevier Inc., 59(2), pp. 1394–1403. doi: 10.1016/j.neuroimage.2011.08.043.

Nieder, C. and Mehta, M. P. (2009) 'Prognostic indices for brain metastases - Usefulness and challenges', *Radiation Oncology*, 4. doi: 10.1186/1748-717X-4-10.

Ostrom, Q. T. *et al.* (2015) 'CBTRUS Statistical Report: Primary Brain and Central Nervous System Tumors Diagnosed in the United States in 2008-2012', *Neuro-oncology*, 17(July), pp. iv1–iv62. doi: 10.1093/neuonc/nov189.

Pérès, E. A. *et al.* (2018) 'Longitudinal Study of Irradiation-Induced Brain Microstructural Alterations With S-Index, a Diffusion MRI Biomarker, and MR Spectroscopy', *International Journal of Radiation Oncology Biology Physics*, 102(4), pp. 1244–1254. doi: 10.1016/j.ijrobp.2018.01.070.

Perez-Torres, C. J. *et al.* (2015) 'Perilesional edema in radiation necrosis reflects axonal degeneration', *Radiation Oncology*, 10(1), pp. 10–13. doi: 10.1186/s13014-015-0335-6.

Rutherford, A. *et al.* (2019) 'Evaluation of four different small animal radiation plans on tumour and normal tissue dosimetry in a glioblastoma mouse model', *British Journal of Radiology*, 92(1095). doi: 10.1259/bjr.20180469.

Seland, J. G. *et al.* (2000) 'Diffusion Measurements at Long Observation Times in the Presence of Spatially Variable Internal Magnetic Field Gradients', *Journal of Magnetic Resonance*, 146(1), pp. 14–19. doi: 10.1006/jmre.2000.2101.

Shimmyo, Y. *et al.* (2008) 'Multifunction of Myricetin on Ab: Neuroprotection Via a Conformational Change of Ab and Reduction of Ab Via the Interference of Secretases', *Journal of neuroscience research*, 86, pp. 368–377. doi: 10.1002/jnr.

Wang, S. *et al.* (2009) 'Longitudinal diffusion tensor magnetic resonance imaging study of radiation-induced white matter damage in a rat model', *Cancer Research*, 69(3), pp. 1190–1198. doi: 10.1158/0008-5472.CAN-08-2661.

Watve, A. *et al.* (2018) 'Longitudinal changes in gray matter regions after cranial radiation and comparative analysis with whole body radiation : a DTI study', *International Journal of Radiation Biology*. Informa UK Limited, trading as Taylor & Francis Group, 94(6), pp. 532–541. doi: 10.1080/09553002.2018.1466064.

# Chapter 9

# Chapter-9 General discussion and conclusion

## 9.1 Discussion

The focus of this thesis was to investigate the ability of several established and modified MRI sequences to detect radiation-induced microstructural changes in the rodent brain. T2 weighted images were used to probe the effects of radiotherapy treatment on tumour cells infiltration by measuring tumour volumes. DTI imaging modalities commonly use a short observation time to reduce signal loss due to rapid transverse relaxation. This short observation time limits the diffusion of water molecules to short distances, thus, permitting only short range tissue structures to be observed. It was decided, therefore, to investigate the potential use of longer observation times, probing longer range structures, to detect microstructural changes post-IR. To avoid substantial MR signal losses, we implemented a STE-DTI sequence which stores the net magnetization along the z-axis during the long observation times. This has the advantage that MR signal loss then occurs via T1 relaxation, rather than faster T2 relaxation, for SE-DTI sequences. It is widely accepted that histology is the gold standard to characterise the microscopic structure, function and pathology of biological tissues. Hence, we aimed to use histology to validate potential MR imaging biomarkers.

In Chapter-3, T2 weighted high resolution images were used to assess the ability of MRI to probe the effect of ionising radiation treatment on the invasiveness of an infiltrative rodent G7 glioma model. GBM is a highly aggressive brain tumour with a very poor prognosis, and multi-modal treatments are available (Hanif *et al.*, 2017). The G7 model that was used in this experiment was provided by our collaborators from Cambridge University (Collin Watts lab) and is characterised by being highly invasiveness, at the tumour margins. Because G7 cells are human in origin, it is simple to discriminate between the replicating tumour cells and the normal cells of the mouse brain (Birch *et al.*, 2018). This study aimed to assess the ability of MRI to investigate the behaviour of G7 tumour cell invasion after treatment (days 7 and 14). While there was tumour growth at 7 days, no significant differences were found between groups (IR and non-IR). However, the IR group showed a significant increase in tumour volume at day 14 by comparison with the non-IR group, that was potentially due to the increased infiltration. Histology, using a Ki67 stain, was used longitudinally in this study to indicate the presence

of G7 tumour cells by using a Ki67 stain. Histological analysis also showed there was more infiltration of tumour cells, from the IR hemisphere to the non-IR hemisphere, in the treatment groups by comparison with the control groups (non-IR).

In Chapter-4, we described our aim to reproduce results previously obtained by our group. These previous results indicated that quantitative T2 mapping could be used to detect the acute effect of radiation, via the multi-exponential decay of the MR signal. Consistent with this previous study, we found no significant differences in actual T2 values measured between IR and non-IR brain hemispheres at 24 hours post-IR. However, unlike the previous results, we found all signal decays to be exponential, with no significant difference in the Paravision 'standard deviation of the fit' parameter.

Due to the lack of agreement with the previous study, the data were investigated further using an in-house Matlab program, which used an $R^2$ value for determining the goodness of the fit, which is independent of the magnitude of the MR signal. This showed all signal decays to be mono-exponential. Upon further investigation it was discovered that the Paravision 'standard deviation of the fit' parameter, was dependent on the magnitude of the MR signal. As the MRI experiments were performed using a volume transmit coil with a receiver surface coil, the magnitude of the MR signal was dependent on the position of the mouse head, resulting in the Paravision 'standard deviation of the fit' parameter being unsuitable.

In addition to the above T2 mapping measurements, scoping experiments were performed using various permutations of multiple *b*- value, long observation time DWI. These scoping experiments sought to identify deviations from normal Gaussian behaviour due to microstructural changes post-IR. Multiple *b*-value SE-DWI with short observation times showed no deviation from normal Gaussian behaviour. However, there was an indication that long observation time STE-DWI (200ms) did show a deviation from normal Gaussian behaviour post-IR.

In Chapter-5, based on the previous scoping experiments from Chapter-4, we described how this study aimed to relate changes in long observation time STE-DWI to any post-IR microstructural changes seen in histology. However, these experiments showed no significant deviations from Gaussian behaviour between

irradiated and non-irradiated brain hemispheres. Following inspection of the individual images from day 60 post-IR, SE-DWI showed no significant changes in any gradient directions. However, STE-DWI with long observation time showed that there was a noticeable drop in the signal in the fimbria with the gradient applied along the X axis. This result was supported by the greatly increased standard deviation of diffusion coefficient between right (IR) and left (non-IR) fimbria. Further investigations confirmed that these observations were not due to artefacts during imaging. To better investigate these WM effects, a long observation time STE-DTI sequence was implemented. Before this sequence was applied in-vivo, the decision was made to first validate the sequence using phantoms, which subsequently highlighted problems with the sequence.

In Chapter-6, given the noticeable problems during the development of the long observation time STE-DTI sequence, a gradient calibration was performed using a diffusion MRI method. We then conducted a full series of diffusion measurements was performed on the phantom, with both SE-DWI and STE-DWI, for a range of observation times and diffusion gradient strengths. These measurements highlighted a problem with the long observation time STE-DWI sequence, where large errors in the measured diffusion coefficients were observed when the diffusion gradients were applied in the +slice or -slice gradient direction.

In Chapter-7, we described our investigation of various imaging parameters that may lead to errors from the long observation time STE-DTI sequence and also how these errors could be minimised. To better match future in-vivo applications, the phantom was doped to match the MR signal relaxation times of brain tissue at 7T. It was found that the errors increased with longer observation time, thinner slice thickness and larger diffusion gradients. The sequence was then optimised to minimise errors in future in-vivo studies. Further, the performance of the STE-DTI sequence was improved by modifying the application of the crusher gradients of the stimulated echo.

Following implementation of the results of Chapters 6 and 7, an in-vivo DTI study, described in Chapter-8, was performed. This study aimed to validate whether SE-DTI and STE-DTI sequences could be used to detect the acute, early delayed and late delayed effects of ionising radiation. Histology was conducted longitudinally with MRI for all time points post-IR longitudinally with MRI. At all-time points post-

IR, T2 weighted high resolution images did not show any noticeable anatomical lesions such as oedema or necrosis. In addition, irradiated half brain volume assessment from anatomical MRI revealed no significant, long-lasting irradiation-induced brain atrophy by comparison with the contralateral hemisphere. DTI metrics such as FA, and AD start showing changes commencing from day 15 post-irradiation in the fimbria of the hippocampus. This is consistent with our previous result, showing more diffusion in AD which is the principle direction of diffusion. FA also showed a reduction in the fimbria of the hippocampus at day 50 post-irradiation, suggesting the possibility of the axonal damage due to haemorrhage or necrosis. We plan to compare DTI results with brain alterations detected by using immunohistochemistry.

## 9.2 Limitations

In hindsight and on reflection, a number of limitations have been identified in this study:

1- In Chapter-3, we stated that the number of mice that were injected with G7 was *n*=32. However, before the experiment started, we lost *n*=13 mice and the experiment commenced with *n*=19. We did not consider that the rapid spread of the G7 tumour model would cause the death of so many mice before the experiment began. However, this experience has subsequently helped another researcher in our group better plan their drug treatment experiment using the same tumour model.

2- As described in Chapter-8, one of the limitations in this study was not to consider adding another control group of mice for histology at each MRI scan time points post-IR, as in an MRI study. Histology at different time points would have provided concrete evidence of the various morphological and functional changes occurring at time points post-IR. Unfortunately, we noticed this problem only at the end of the experiment. Furthermore, due to the lack of time and the hard deadline for thesis submission, this thesis was submitted while the histological analysis was still ongoing.

## 9.3 Conclusion

The main aim of this thesis was to investigate the potential for MRI to detect the early stage effects of radiotherapy treatment and validate this with histology. The ability to better detect these effects may lead to improvements in radiotherapy planning, assessment of drug treatments and identifying patients that may experience future complications. Several established and modified MRI sequences were tested for their ability to detect microstructural changes at different time points post-IR. We identified several problems with the use of the long observation time STE-DTI sequence and these errors were reduced by optimising and modifying the sequence.

In this thesis we proposed several scientific contributions to detect the effects of radiotherapy treatment on tumours and healthy brain tissues. These are summarised below.

Firstly, in Chapter-3, this study identified the relationship between ionising radiation treatment and tumour infiltration. At the time of these experiments, there was no available estimate of the G7 model attrition rate. Hence, the thesis highlighted the estimate of the G7 model attrition rate. Consequently, our attrition rate data was used by another researcher in our group, that led them to double the number of experimental mice used from n=32 to n=64.

Histology is recognised as the gold standard for assessing the effects of many diseases, including brain tumours, and radiotherapy effects. Therefore, we decided to use different MRI sequences longitudinally with histology and tested the ability of the STE-DTI sequence with long observation times to form the basis of the development of a new MRI technique.

Thirdly, we highlighted the importance of technical issues such as gradient calibration and MRI scanner stability and their roles during scanning. This was particularly important to avoid technical errors when scanning using long observation times.

## 9.4 Future directions

Potential future directions of development in the detection of tumour cells beyond the treatment margins and the effect of ionising radiation on healthy brain tissues are listed below:

1- Investigate further whether MRI can significantly increase the accuracy of tumour cell detection beyond treatment margins.

2- MRS may provide useful metabolic information about abnormal tissues. This would be useful for tumour diagnosis and understanding radiation therapy effects on healthy tissues as well.

3- Behavioural testing of mice could provide an assessment of cognitive deficits following irradiation. This would provide additional valuable information when conducted longitudinally with MRI and histology.

4- Use of rats, not mice, as rats have more and larger areas of WM.

## 9.5 References

Birch, J. L. *et al.* (2018) 'A novel small-molecule inhibitor of MRCK prevents radiation-driven invasion in glioblastoma', *Cancer Research*, 78(22), pp. 6509–6522. doi: 10.1158/0008-5472.CAN-18-1697.

Hanif, F. *et al.* (2017) 'Glioblastoma multiforme: A review of its epidemiology and pathogenesis through clinical presentation and treatment', *Asian Pacific Journal of Cancer Prevention*, 18(1), pp. 3–9. doi: 10.22034/APJCP.2017.18.1.3.

# Selected Conference Proceedings

1- Early delayed radiation-induced brain injury in mice: preliminary findings using magnetic resonance imaging

Mr Abdulrahman Qaisi, Dr Antoine Vallatos, Dr Katrina Stevenson, Mrs, Lindsay Gallagher, Dr Rodrigo Gutierrez-quintana, Dr Apostolos Zarros, Dr Lesley Gilmour, Prof Anthony J Chalmers, Dr William Holmes

Neuro-Oncology, Volume 20, Issue suppl_5, 1 October 2018, Pages v356–v357, https://doi.org/10.1093/neuonc/noy130.059

Published: 03 October 2018

**Paper poster presentation:**

1- Investigation of MRI biomarkers for detecting effects of ionizing radiation, European Society for Magnetic Resonance in Medicine and Biology (ESMRMB 2017), 34th Annual Scientific Meeting, Oct. 19- Oct. 21, Barcelona/ES.

**Conference posters:**

1- Investigation of magnetic resonance imaging biomarkers for detecting effect of ionizing radiation on healthy tissue. British Chapter ISMRM meeting, University of Leeds,2016.

2- Early delayed radiation-induced brain injury in mice: preliminary findings using magnetic resonance imaging. BRITISH NEURO-ONCOLOGY SOCIETY ANNUAL MEETING 2018. 4th – 6th JULY 2018, University of Winchester, Sparkford Road, Winchester, Hampshire SO22 4NR

3- Minimizing observation time related errors for stimulated echo DTI, British Chapter ISMRM meeting, University of Sheffield,2019.